THE COMPUTATIONAL MODELING OF ORGANOMETALLIC COMPOUNDS AND REACTIONS INSPIRED BY HYDROGENASES

A Dissertation

by

SHENGDA DING

Submitted to the Office of Graduate and Professional Studies of
Texas A&M University
in partial fulfillment of the requirements for the degree of

DOCTOR OF PHILOSOPHY

Chair of Committee,	Michael B. Hall
Co-Chair of Committee,	Marcetta Y. Darensborg
Committee Members,	Perla B. Balbuena
	Timothy R. Hughbanks
Head of Department,	Simon W. North

December 2017

Major Subject: Chemistry

ABSTRACT

Hydrogenases are enzymes capable of catalyzing, reversibly, coupling of protons and electrons into dihydrogen. The active sites of both [NiFe]- and [FeFe]-hydrogenases feature a M_2S_2 core, where two first-row transition metals are tightly held together by two bridging thiolates. In this manner, two "one-electron" metals, in the aspect of redox activity, cooperate to facilitate the "two-electron" H_2 production.

Such a delicate apparatus from Nature inspired molecular models composed of two base metals and a dithiolate chelating ligand. Using 1,3-propanedithiolate (pdt) or N,N-bis(2-mercaptoethyl)-1,5-diazacyclohexane/octane (N_2S_2) to hinge metal fragments, these models share a common formula M-(μ-S)$_2$-M' and a variety of reactions can be initiated on them. Computational chemistry studies of geometries, electronic structures, reaction energetics and spectral simulations were used to investigate the mechanisms of the following reactions:

<u>H_2 production.</u> A Lewis acid-base pair is generated on the electro-catalysts M-(N_2S_2)-M' (M = Ni^{2+}/$Fe(NO)^{2+}$, M' = $Fe(CO)Cp^{+}$/$Fe(NO)^{2+}$) by reductively dissociating the S-M' bond during the catalytic cycle. The pair holds a proton and a hydride before their coupling into H_2. The tri-nitrosyl complex Fe(NO)-(N_2S_2)-$Fe(NO)_2^{+}$ is special with multiple electron-buffering $Fe(NO)_x$ units such that it can generate two hydrides on irons, which reductively eliminate into H_2.

<u>CO_2 reduction.</u> Ni(N_2S_2) metalloligand replaces the redox-active bipyridine of the proven electro-catalyst (bpy)$Re(CO)_3Cl$ to create Ni(N_2S_2)$Re(CO)_3Cl$. In addition to the

electron buffer role in the mechanism, the Ni also stabilizes the up-taken carbon dioxide by establishing a dative O-Ni bond.

C-H bond activation. $(CO)_3Fe(\mu\text{-}Me_2\text{-}pdt)Fe(CO)(P_2N_2)$ undergoes intramolecular C-H bond activation under oxidation conditions. The strategically placed amine on the second coordination sphere cleaves the proton from the C-H bond and serves as a proton shuttle, reproducing the role of the pendant amine of [FeFe]-hydrogenase.

Ligand isomerization. The trimetallic complex $Cp(CO)_2Fe\text{-}NC\text{-}Fe(CO)_2(\mu\text{-}pdt)Fe(CO)_3$ and derivatives were used to simulate the linkage cyanide isomerization processes during the maturation of [FeFe]-hydrogenase. The energetics of cyanide linkage isomerization is controlled by the oxidation and spin states of the cyanide-bound metals.

The computational studies herein confirm the versatility of complexes containing the M_2S_2 core and suggest the ligands and the metals to be of equal importance in contributing to the activity of these organometallic compounds.

DEDICATION

This dissertation is dedicated to my parents who brought me up and educated me.

ACKNOWLEDGEMENTS

I would like to thank my research advisors for their helpful guidance, both for the research and the life. They are more than generous to use their wisdom and experience to coach me, a young scientist and young adult.

Thanks also go to my collaborators including my peer group members as well as domestic and international chemists. Their experimental work literately forms the foundation of my research and the subjects of this dissertation. Fruitful outcomes crystallize from helpful advices and comments given by, as well as engaging discussions even debates with, my intelligent coworkers.

Generous help from the friendly faculty and staff of the Department of Chemistry has turned my Ph.D. study into a rewarding experience; thank you.

Finally, thanks to my parents for their continuous investment in my education.

CONTRIBUTORS AND FUNDING SOURCES

Contributors

This work was supervised by a dissertation committee consisting of Professors Darensbourg [co-advisor], Hall [co-advisor] and Hughbanks of the Department of Chemistry and Professor Balbuena of the Department of Chemical Engineering.

The experimental work in this dissertation includes contributions from Nattamai Bhuvanesh (Chapter III, IV, VI and VII), Ryan D. Bethel (Chapter VI), Christopher C. Beto (Chapter V), Rachel B. Chupik (Chapter IV), Matthew A. Cohan (Chapter VII), Danielle J. Crouthers (Chapter IV and VI), Jason A. Denny (Chapter VI and VII), Ozlen F. Erdem (Chapter IV and V), Pokhraj Ghosh (Chapter III and IV), Kristina F. Goldstein (Chapter VII), Chung-Hung Hsieh (Chapter IV and VI), Tianbiao Liu (Chapter IV), Allen M. Lunsford (Chapter III, V and VII), Chengbing Ma (Chapter VI),Charles C. L. McCrory (Chapter IV), Codrina V. Popescu (Chapter IV), Manuel Quiroz (Chapter IV), Joseph H. Reibenspies (Chapter IV), Licheng Sun (Chapter VI), Mei Wang (Chapter IV), Ning Wang (Chapter III and VI), Lubitz Wolfgang (Chapter IV), Dehua Zheng (Chapter VI).

All computational work conducted for the dissertation was completed by the student independently under the advisement of the committee.

Funding Sources

This work was made possible in part by the National Science Foundation under Grant Numbers CHE-0910552, CHE-1266097, CHE-1300787, CHE-1664866, CHE-1665258 and the Welch Foundation under Grant Numbers A-0648, A-0924.

Its contents are solely the responsibility of the authors and do not necessarily represent the official views of the funding agencies.

NOMENCLATURE

adt	2-aza-1,3-dithiolate
apo-HydA	[FeFe]-hydrogenase less the $[Fe_2S_2]$-sub-cluster
bdt	Benzene-1,2-dithiolate
BS	Broken symmetry
bpy	Bipyridine
Cp	Cyclopentadiene
Cp*	Pentamethylcyclopentadiene
CV	Cyclic voltammetry
C (step)	Chemical (step) / proton addition
cyclam	1,4,8,11-tetraazacyclotetradecane
DFT	Density Functional Theory
dmpdt	2,2-dimethyl-1,3-propane-dithiolate
dppv	1,2-bis(diphenylphosphino)ethylene
dppe	1,2-bis(diphenylphosphino)ethane
E-F	Enemark–Feltham
EPR	Electron paramagnetic resonance
ET	Electron transfer
E (step)	Electrochemical (step) / electron addition
edt	Ethane-1,2-dithiolate
en	Ethylenediamine

F_8-tpp	Tetrakis(2,6-difluorphenyl)porphyrinate
GEDIIS	Energy-represented direct inversion in the iterative subspace
GGA	Generalized gradient approximations
HER	Hydrogen evolution reaction
HF	Hartree-Fock
HP	Hydride protonation
HydE/F/G	Hydrogenase synthase E/F/G
ICF	Inhomogeneity correction factor
IR	Infrared
IRC	Intrinsic reaction coordinate
KS	Kohn-Sham
LSDA	Local spin density approximations
Me_5dien	1,1,4,7,7-pentamethyldiethylenetriamine
$MeNpy_2$	Bis(2-(2-pyridylethyl))methylamine
MO	Molecular orbital
LCAO	Linear combination of atomic orbitals
m-GGA	Meta-generalized gradient approximations
NMR	Nuclear magnetic resonance
N_2S_2	N,N-bis(2-mercaptoethyl)-1,4-diazacyclohexane or N,N-bis(2-mercaptoethyl)-1,5-diazacyclooctane
NPy_3	Tris(2-pyridylmethyl)amine
NBO	Natural bond orbital

OP	Over-potential
oep	Octaethylporphyrin
PB	Prussian Blue
pc	Phthalocyaninato
Ph_4-porphorin	Tetraphenylporphyrin
P_2N_2	1,5-diaza-3,7-diphosphacyclooctane
P_2C_5	1,4-diphosphacycloheptane
PCET	Proton coupled electron transfer
PES	Potential energy surface
PT	Proton transfer
pdt	Propane-1,2-dithiolate
py	Pyridine
RE	Reductive elimination
RFO	Rational function optimization
SCF	Self-consistent field
STQN	Transit-guided quasi-Newton
TFA	Trifluoracetic acid
TOF	Turn-over frequency
tp	Trispyrazolylborate
TS	Transition state
(Me_3)tacn	N, N' ,N''-trimethyl-1,4,7-triazacyclononane
tmphen	3,4,7,8-tetramethyl-1,10-phenanthroline

XANES	X-ray absorbance near-edge spectrum

A	Hyperfine coupling constant
E	Electronic energy
E_{x}	Exchange energy
E_{c}	Correlation energy
$E_{1/2}$	Reduction potential at equilibrium
e	Charge of an electron; Euler's number
F	Fock integral; Faraday constant
$\hat{f}$	Fock operator
G	Gibbs free energy
g	Inhomogeneity correction factor; Lande g factor
H	Heat
$\hat{H}$	Hamiltonian operator
$\hat{h}$	Hartree operator
$\hbar$	Planck constant
J	Coulomb integral
K	Exchange integral
k_{B}	Boltzmann constant
m	Mass
N	Electric potential energy
p	Pressure

pK_a	Acid dissociation constant
Q	Overall partitioning function
q	Partitioning function for a particular motion
$\boldsymbol{r}$	Position vector
S	Overlap integral; Spin; Entropy
$\hat{S}$	Spin operator
T	Kinetic energy; Temperature
V	Volume
∇^2	Laplace operator
δ	Chemical shift
ΔE_q	Quadrupole splitting
μ	First derivative of density function
ρ	Density function
χ	Atomic orbital or basis function
φ	Molecular orbital
ψ	Wavefunction (of a molecule)
ω	Frequency; Second derivative of density function

TABLE OF CONTENTS

Page

LIST OF FIGURES

Page

LIST OF TABLES

Page

CHAPTER I

INTRODUCTION

The development of computational methods

In 1998, the Nobel prize in Chemistry was awarded to John Pople for "his development of computational methods in quantum chemistry" and Walter Kohn for "his development of the density-functional theory". They and other scientists paved the way for the two branches of computational chemistry: the *ab initio* wavefunction theory and the density functional theory, that are used to investigate the electronic structure and the energy of a molecule.

The electronic energy of a molecule. The important quest of computational chemistry for studying reaction mechanisms is to predict, by modeling, transient species that are too reactive to be accurately characterized in the experimental chemistry. Reliable modeling begins with an accurate value of the electronic energy (E) of a given species, represented by the solution (ψ) of the time-independent Schrodinger equation with the Hamiltonian ($\widehat{H}$) operator for a multi-atom molecule:

$$\widehat{H}\psi = E\psi$$

$$E = T_N + V_{NN} + T_E + V_{NE} + V_{EE}$$

$$\widehat{H} = -\frac{\hbar^2}{2}\sum_{\alpha}\frac{1}{m_\alpha}\nabla_\alpha^2 + \sum_{\alpha}\sum_{\beta>\alpha}\frac{Z_\alpha Z_\beta e^2}{r_{\alpha\beta}} - \frac{\hbar^2}{2}\sum_{i}\frac{1}{m_e}\nabla_i^2 - \sum_{\alpha}\sum_{i}\frac{Z_\alpha e^2}{r_{\alpha i}} + \sum_{i}\sum_{j>i}\frac{e^2}{r_{ij}}$$

The symbol α and β run over all atoms and i and j run over all electrons. The symbols $\hbar$, m, and Z are the reduced Planck constant, the mass, and the nuclear charge. ∇^2 is the Laplace operator. The Hamiltonian operator above has five summations, which relate to the five items in the electronic energy: the kinetic energy of nuclei (T_N), the electronic repulsion between nuclei (V_{NN}), the kinetic energy of electrons (T_E), the electronic attraction between nuclei and electrons (V_{NE}) and the electronic repulsion between electrons (V_{EE}), respectively. Considering the mass difference between a nucleus and an electron, T_N can be omitted, *i.e.*, the nuclei can be treated as stationary with respect to the motion of the electrons (the Born-Oppenheimer approximation[1]). Therefore, V_{NN} also becomes constant at a given geometry. Thus, the "pure electronic" energy is solely dependent on the distribution of electrons and only has three items:

$$E_e = T_E + V_{NE} + V_{EE}$$

The wavefunction and molecular orbitals. The exact solution of the Schrodinger equation for any one-electron molecule yields a wavefunction that spans the entire molecule and has high amplitudes near each nucleus; such a wavefunction is called a molecular orbital. Each molecular orbital (also called a spatial orbital) can accommodate one α and one β electron. Alternatively, a molecular orbital can be recognized as constituted by two spin orbitals, one α and one β, each of which can accommodate an electron of the corresponding spin. The wavefunction of a multi-electron molecule, should contain all the individual spin orbitals occupied by electrons, with the satisfaction of Pauli exclusion principle;[2] *i.e.*, two electrons cannot occupy the same spin orbital, and the wave function must be anti-symmetric with respect to electron exchange (an intrinsic property

of fermions and electrons are fermions). Thus, the wavefunction of a multi-electron molecule is represented as a Slater determinant (and its shorthand):[3]

$$\psi = \frac{1}{\sqrt{i!}}\begin{vmatrix} \varphi_1(1) & \varphi_2(1) & \cdots & \varphi_i(1) \\ \varphi_1(2) & \varphi_2(2) & \cdots & \varphi_i(2) \\ \vdots & \vdots & \ddots & \vdots \\ \varphi_1(i) & \varphi_2(i) & \cdots & \varphi_i(i) \end{vmatrix} = |\varphi_1 \quad \varphi_2 \quad \cdots \quad \varphi_i|$$

In this Slater determinant, each row and each column involve the same electron and the same spin orbital, respectively. If two columns (*i.e.* two spin orbitals) are the same, then this determinant vanishes. If two rows or columns swap with each other, then the determinant changes the sign. By using the Slater determinant as a representation of the wavefunction, one non-classic (quantum) electron interaction is introduced: the exchange energy, which is part of V_{EE}. V_{EE}, on SCF level, can be further divided into two items: the classic Coulomb integral (J) and the non-classic exchange integral (K). These integrals can be represented in the "bra-ket" notations in the following equations.

$$V_{EE} = \sum_{i}^{occ}\sum_{j>i}^{occ}(J_{ij} - K_{ij})$$

$$V_{EE} = \sum_{i}^{occ}\sum_{j>i}^{occ}(\langle\varphi_i(1)\varphi_j(2)\left|\frac{e^2}{r_{12}}\right|\varphi_i(1)\varphi_j(2)\rangle - \langle\varphi_i(1)\varphi_j(2)\left|\frac{e^2}{r_{12}}\right|\varphi_j(1)\varphi_i(2)\rangle)$$

The indices i and j run over occupied spin orbitals in the Slater determinant. Note φ_i and φ_j are spin orbitals, the exchange integral K_{ij} vanishes when they have opposite spins. *i.e.* the exchange integral is only applicable to spin orbitals of the same spin. The Coulomb integral runs over all the spin orbitals regardless of the direction of the spin. A

single spin orbital φ_i, occupied or unoccupied, is the eigenfunction of the Fock operator $\hat{f}$ and can be represented as

$$\hat{f}\varphi_i = E_i\varphi_i = \hat{h}\varphi_i + \sum_j^{occ}(J_{ij} - K_{ij})\varphi_i = [-\frac{\hbar^2}{2m_e}\nabla^2 - \sum_\alpha \frac{Z_\alpha e^2}{r_{\alpha i}} + \sum_j^{occ}(J_{ij} - K_{ij})]\varphi_i$$

The eigenvalue of the Fock operator is the molecular orbital energy. In the equation, $\hat{h}$ is the historic Hartree operator calculating the kinetic energy of the electron and the electron-nuclei attraction. K_{ij} also vanishes when two spin orbitals have different spins.

LCAO-MO scheme and the algorithm of SCF theorem. A molecular orbital can be constructed as a linear combination of atomic orbital (MO-LCAO scheme[4]) or basis functions. The radial parts of basis functions are usually Gaussian functions or "contracted" (*i.e.* the sum of a few) Gaussian functions with fitted coefficients and exponentials, to simulate the atomic orbitals of hydrogen-like atoms. The angular parts of the basis functions are spherical harmonics. The Gaussian-type functions were introduced by Boys[5] to replace the Slater-type functions (although Slater-type functions better resemble the atomic orbitals); Hehre, Steward, and Pople contracted these Gaussian type functions.[6] Both improvements reduce the computational cost of integrals significantly and make calculations practical. Gaussian later became the name of the most popular computational chemistry package.

A molecular orbital (the discussion is based on spatial orbitals instead of spin orbitals from now on) can be represented as

$$\varphi_i = \sum_k a_{ik}\chi_k$$

The symbols φ and χ represent the molecular orbitals and basis functions, with i and k being their indices, respectively. a_{ik} is the normalized coefficient. To obtain the wavefunction, the constant a_{ik} in each molecular orbital in the Slater determinant must be determined. This is done by the variation theorem; *i.e.*, the coefficients are veried until the lowest energy is obtained and a lower energy indicates the trial wavefunction is closer to the real wavefunction. At the minimal energy, the optimized coefficient a_{ik} (k is arbitrary) would satisfy:

$$\frac{\vartheta E_i}{\vartheta a_{ik}} = 0$$

The orbital energy E_i can also be written in the bra-ket form:

$$E_i = \frac{\langle \sum_n a_{in}\chi_n \left| \hat{f} \right| \sum_n a_{in}\chi_n \rangle}{\langle \sum_n a_{in}\chi_n \mid \sum_n a_{in}\chi_n \rangle} = \frac{\sum_n a_{in}^2 F_{nn} + 2\sum_n \sum_m^{n\neq m} a_{in}a_{im}F_{nm}}{\sum_n a_{in}^2 S_{nn} + 2\sum_n \sum_m^{n\neq m} a_{in}a_{im}S_{nm}}$$

Here, F_{nm} and S_{nm} are defined to be integrals over basis function(s):

$$F_{mn} = \langle \chi_m \left| \hat{f} \right| \chi_n \rangle$$

$$S_{mn} = \langle \chi_m | \chi_n \rangle$$

Expand the partial derivative equation above:

$$\frac{\vartheta E_i}{\vartheta a_{ik}} = \frac{(2a_{ik}F_{kk} + 2\sum_n^{k\neq n} a_{in}F_{kn}) \langle \sum_n a_{in}\chi_n \mid \sum_n a_{in}\chi_n \rangle}{\langle \sum_n a_{in}\chi_n \mid \sum_n a_{in}\chi_n \rangle^2}$$

$$- \frac{(2a_{ik}S_{kk} + 2\sum_n^{k\neq n} a_{in}S_{kn}) \langle \sum_n a_{in}\chi_n \left| \hat{f} \right| \sum_n a_{in}\chi_n \rangle}{\langle \sum_n a_{in}\chi_n \mid \sum_n a_{in}\chi_n \rangle^2} = 0$$

Simplify the equation:

$$\frac{\sum_n a_{in}F_{kn}}{\sum_n a_{in}S_{kn}} = \frac{\langle \sum_n a_{in}\chi_n \,|\hat{f}|\, \sum_n a_{in}\chi_n \rangle}{\langle \sum_n a_{in}\chi_n \,|\, \sum_n a_{in}\chi_n \rangle} = E_i$$

$$\sum_n a_{in}F_{kn} = (\sum_n a_{in}S_{kn})E_i$$

$$\sum_n a_{in}(F_{kn} - E_i S_{kn}) = 0$$

The above equation is valid for any arbitrary k and a system of N linear homogeneous equations can be established:

$$\begin{pmatrix} F_{11} - E_i S_{11} & \cdots & F_{n1} - E_i S_{n1} \\ \vdots & \ddots & \vdots \\ F_{1n} - E_i S_{1n} & \cdots & F_{nn} - E_i S_{nn} \end{pmatrix} \begin{pmatrix} a_{i1} \\ \vdots \\ a_{in} \end{pmatrix} = 0$$

The linear equation system ("secular equation") has non-zero solutions. It can be interpreted as:

$$\begin{bmatrix} F_{11} - E_i S_{11} & \cdots & F_{n1} - E_i S_{n1} \\ \vdots & \ddots & \vdots \\ F_{1n} - E_i S_{1n} & \cdots & F_{nn} - E_i S_{nn} \end{bmatrix} = 0$$

For a system with N basis function, N solutions of E_i (including degenerate solution(s)) can be obtained from the above determinant. Once an E_i is determined, plugging it back to the linear equation system generates the optimized coefficients for the corresponding molecular orbital.

An initial set of coefficients for each occupied orbital must be available to get the electron-electron repulsion specified in the Fock integrals F_{mn}; they are usually generated through some simple algorithms (for example, Harris functional[7]). Then, the second set of orbital coefficients can be obtained by solving the secular equation. The iteration continues with the newer set of coefficients until two sets of coefficients are very close to

each other when the self-consistent field is achieved. The algorithm to obtain the wavefunction through the self-consistent field was systematically organized by Roothaan[8] and was named after Hartree[9] and Fock[10] for their historic contributions. This method is often abbreviated as HF or HFR method.

The negligence of electron correlation energy in HF/SCF theorem. The accuracy of HF/SCF theorem is satisfactory for simple organic systems if the change of bonds is not involved, *e.g.*, the calculation of energy differences of isomers.[6, 11] By expanding the size of the basis set, HF/SCF can reproduce 99.5% ("HF limit") of the electronic energy and the remaining error is attributed to the negligence of the correlation, which can be further divided into two parts, the dynamic correlation, and the static (non-dynamic) correlation. The causes of the error are traced back to the design of HF/SCF wavefunction, in which a particular electron under investigation is influenced by the static/spatially averaged electronic field created by other electrons without knowing their exact positions. In reality, these electrons do know where the other electrons are and they move accordingly to avoid close contacts, but with the HF/SCF wavefunction two electrons may approach each other to a physically unreasonable extent in the calculations, which results in too high an electronic energy and incorrect electron distributions. Most of the correlation energy is related to the movement of electrons described about and is classified as dynamic correlation. The application of the Slater determinant, fortunately, eliminates this problem between electrons of the same spin, as the Slater determinant tends to vanish if two spin orbitals are too similar, creating the "Fermi hole". But the dynamic correlation of

electrons of opposite spins (*i.e.* the implementation of the "Coulomb hole") is not taken care of in the HF/SCF calculation.

The static correlation, is related to the electron movement, but in a different, more implicit way, as it relates to the appropriateness of using one Slater determinant to represent the wavefunction. Each Slater determinant is linked to a (pre-determined) configuration, *i.e.*, the bundle of orbitals that is occupied. Multiple determinants sometimes are necessary to describe a system whose unoccupied and occupied orbitals are relatively close to each other. The error, classified as static correlation, accumulates if the wavefunction fails to count the additional contributing determinants. The static correlation is particularly dominant for diradical systems and molecules containing the first-row transition metals.

The development of high-level / post-HF wavefunction methods tries to introduce the correlation energy by correcting the wavefunction beyond one Slater determinant. With a more and more complicated wavefunction, it is on the ultimate route to approach the answer but the required computation resources increase exponentially. Therefore, the applications of high-level wavefunction methods are limited to relatively small systems.

DFT theorem. Another way to address the correlation problem is to use Density Functional Theory (DFT), for which Hohenberg and Kohn[12] proved that the exact non-relativistic energy for a non-degenerate ground state of a molecule is a functional of the density (note the exact functional exists but it is not known). Thus, they proved that this energy can be computed without the necessity of solving the Schrodinger Equation for the exact wavefunction. In DFT the spatial distribution of electron density $\rho(x, y, z)$ or $\rho(\boldsymbol{r})$,

where $\boldsymbol{r}$ is a vector, may be exploited to derive the energy with an energy function that can process the function $\rho(\boldsymbol{r})$, hence a functional. Still applying the Born-Oppenheimer approximation, the pure electronic energy, as a functional of $\rho(\boldsymbol{r})$ can be represented as the sum of three contributing terms:

$$E_e[\rho(\boldsymbol{r})] = T_E[\rho(\boldsymbol{r})] + V_{NE}[\rho(\boldsymbol{r})] + V_{EE}[\rho(\boldsymbol{r})]$$

The meanings of these three items are exactly the same as those in SCF theorem and their values are dependent on the density function. The electronic interaction between electrons may be further represented as

$$V_{EE}[\rho(\boldsymbol{r})] = J[\rho(\boldsymbol{r})] + E_X[\rho(\boldsymbol{r})] + E_C[\rho(\boldsymbol{r})]$$

The item J is the Coulomb integral, while E_X and E_C stand for two remaining electron-electron interactions: exchange and correlation, respectively. The correlation is explicitly evaluated with a specific operator/functional E_C in DFT.

Hohenberg and Kohn[12] also proved that the variation principle is applicable to the electron density; *i.e.* a trial electron density that resembles the real electron density better would lead to a lower electronic energy. The orbital-free DFT methods vary the density function $\rho(\boldsymbol{r})$ itself and are capable of processing very large systems as the time-consuming orbital generation is eliminated, but their performance is not good enough for molecular systems.[13]

Kohn and Sham proposed a fictitious reference system with non-interacting electrons where the pseudo-wavefunction with the correct density is described by a Slater determinant that consists of Kohn-Sham (KS) orbitals[14] that are expanded in a basis set exactly like the MOs in the HF/SCF approach. Despite the theoretical deviation, the

algorithm of SCF methods (*vide supra*) can be adapted to KS orbitals. In this manner, T_E, V_{NE} and J item of V_{EE} can be directly evaluated with KS orbitals. However, there is an unknown error in the kinetic energy as the exact functional for T_E is unknown and the remaining exchange-correlation E_{XC} (E_X + E_C) functional is also unknown. Thus, practitioners of DFT have developed approximate functionals through trial and error approaches, which contribute to a diversity of functionals.

Generations of DFT functionals. The designs of functionals, particularly E_{XC}, are heavily dependent on meeting certain constraints about simple systems that do have exact solutions and fitting other parameters in the functional to experimental values in training sets. The development of the DFT methods is best represented by "Jacob's ladder", Figure I-1, which progressively incorporates higher derivatives of the density, though it is not rigidly proven that the performance will be improved with each rung. The first generation of the exchange-correlation functional is called local spin density approximations (LSDA). The exchange functional is derived from an infinite uniform electron gas[15] and only uses the local values of alpha and beta electron densities:

$$E_{x,LSDA} = -\frac{3}{2}\left(\frac{3}{4\pi}\right)^{1/3} \sum_{\sigma}^{\alpha,\beta} \int \rho_{\sigma}^{4/3} \mathrm{d}\boldsymbol{r}$$

This LSDA exchange functional is analytic while its correlation functional contains a few fitted parameters. The representative functional is SPW92.[16] Unfortunately, the performance of functionals based on this idealized model is not good enough for realistic chemical systems, see Table I-1.

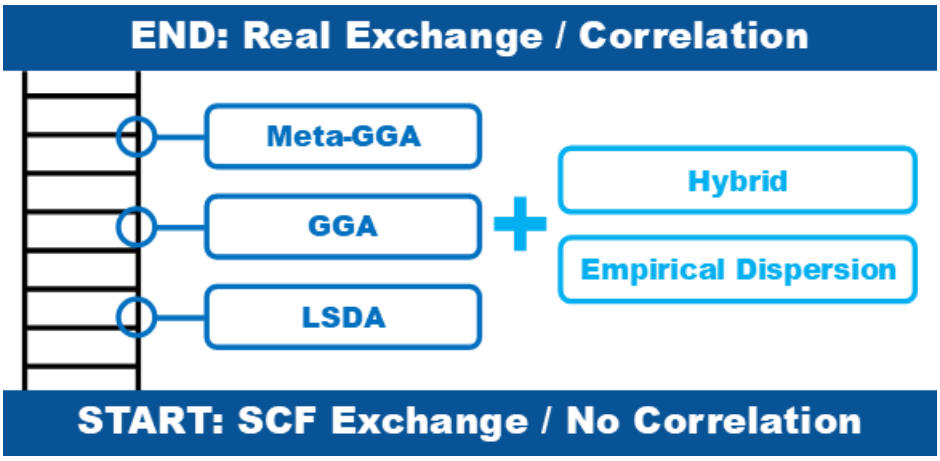

Figure I-1 Jacob's ladder with modifications.[17] The generations of DFT functionals based on using information from the density, its derivatives, and other function of the density.

Compared to the generally parameterized correlation functionals, a seemingly systematic way exists to optimize the exchange functional from LSDA.

$$E_{x,GGA/m-GGA} = -\frac{3}{2}\left(\frac{3}{4\pi}\right)^{1/3}\sum_{\sigma}^{\alpha,\beta}\int g_\sigma \rho_\sigma^{4/3}\mathrm{d}\boldsymbol{r}$$

The inhomogeneity correction factor (ICF, g_σ)[18-19] was introduced and this factor is a (truncated) Taylor series expanded over the electron density gradient or another quantity that can be derived from the density gradient:

$$g_{\sigma,GGA} = \sum_{i}^{N} c_i \mu_\sigma^i$$

In the above equation, c_i is the Taylor series coefficient and μ_σ is related to the α and β density gradients. These gradient corrected exchange-correlation functionals are

classified as generalized gradient approximations (GGA) and they start to give reasonable predictions for chemical systems, a representative example is PBE,[20] see Table I-1.

The second order derivative of the density, either in the form of Laplacian of the density or kinetic energy density, can also be included in the design of the ICF, which now is represented as a (truncated) two-dimensional Taylor series expanded over two variables μ_σ and ω_σ, related to the first derivative and the second derivative of the density, respectively.

$$g_{\sigma,m-GGA} = \sum_{i}^{N}\sum_{j}^{M} c_{i,j}\mu_\sigma^i \omega_\sigma^j$$

These functionals utilizing the second order derivative of densities are classified as meta-GGA (m-GGA) functionals. They can generally outperform GGA functionals. The representative example is TPSS, see Table I-1.[21]

The definition of the albeit well-tuned ICF is arbitrary, which inevitable conflicts with knowledge of the exact exchange obtained from the exchange integrals *K* of SCF theorem. A large part of the difference or error is attributed to self-interaction.[22] The electron may interact with itself in the Coulomb integral and this self-interaction is completely cancelled by the exact HF exchange. However, the approximate exchange functionals cannot cancel it to the full extent. The complete substitution of the DFT exchange functional by the exact HF exchange failed to produce great results as the DFT correlation functional was not accurate enough to balance the exact exchange to yield satisfactory energetics. However, a fractional mixture[23-24] of DFT exchange and HF exchange (*i.e.* a hybrid) gives unexpected accuracy, perhaps due to the cancellation of

errors. Almost all GGA or m-GGA functionals can be used to construct hybrid functionals, among which B3LYP[24] becomes the *de facto* standard of DFT calculations. The representative examples for energetic comparison in Table I-1 are PBE0 (hybrid GGA)[25] and TPSSh (hybrid m-GGA).[26] The fraction of the HF exchange is usually fixed in hybrid functionals. The on-going trend is to introduce a variable controlling the fraction of the HF exchange, dividing the exchange functional into the short-ranged and long-ranged parts in the range-separated functionals.[27-28] Another attempt to improve the functionals is to add empirical dispersion which accounts for long-range correlation, as DFT functionals only use local density information. The most prevailing dispersion correction is three-parameter D3 from Grimme with various damping algorithms.[29-30] Table I-1 summarizes the performance of HF and a few representative density functionals belonging to different generations on the most challenging systems for energetics. A significant improvement is present between SPW92(LSDA) and PBE(GGA)/TPSS(m-GGA). TPSS slightly outperforms PBE and the hybridization of HF exchange can reduce the error moderately. In the original Jacob's latter, hybrid functionals were actually recognized as the fourth rung above m-GGA functionals.[17] The addition of D3-BJ dispersion improves the energetics of systems whose interactions are dominated by dispersion but may introduce errors to other systems.

Table I-1 Benchmarking data for HF and representative density functionals. Mean signed error (MSE) and mean absolute deviations (MAD) in kcal/mol were calculated based on three sets of experimental data describing challenging scenarios for energetics: 124 atomization energies (AE), 12 dispersion-bound (DB) alkane dimers and 38 hydrogen-bonded (HB) water clusters.[31]

Method	HF	SPW92[16]	PBE[20]	TPSS[21]	PBE0[25]	TPSSh[26]
Generation	-	LSDA	GGA	m-GGA	GGA	m-GGA
Hybrid	-	N	N	N	Y (25%)	Y (10%)
Without empirical dispersion D3-BJ[30]						
AE MSE	112.79	-58.11	-12.17	-2.72	1.12	1.46
DB MSE	6.01	-1.10	3.36	4.67	3.37	4.55
HB MSE	18.29	-30.74	-1.26	3.21	0.20	3.52
AE MAD	112.79	58.11	13.61	4.40	3.22	4.37
DB MAS	6.01	1.11	3.36	4.67	3.37	4.55
HB MAD	18.29	30.74	1.30	0.67	0.67	3.52
With empirical dispersion D3-BJ[30]						
AE MSE	-	-	-13.13	-3.91	0.31	0.39
DB MSE	-	-	-0.11	0.23	-0.02	0.18
HB MSE	-	-	-5.86	-2.44	-3.86	-1.77
AE MAD	-	-	14.32	5.15	3.37	4.40
HB MAS	-	-	0.11	0.30	0.10	0.29
HB MAD	-	-	5.86	2.45	3.86	1.80

The weakness of DFT functional is the static correlation. The design of DFT theorem rejects the expansion of the reference wavefunction with multiple determinants, which are necessary for multi-reference systems. Training sets containing multi-reference systems may be used to fit the empirical parameters in certain functionals, at the cost of (much) worse performance over single-reference systems.[32] However, the functionals with low or zero percentage of HF exchange often provide acceptable performance for systems with the multi-reference properties.[31] In addition to the hybrid exchange, a double

hybrid scheme was also proposed to substitute some DFT correlation with the correlation from post-HF methods, *e.g.* MP2.[33]

The application of DFT methods in the mechanistic study of transition metal complexes. The transition metals as molecular catalysts are versatile by having flexible coordination modes, multiple oxidation states and the high angular momentum *d* orbitals to mediate chemical reactions. However, the less than fully occupied *d* orbitals brought a challenge to the HF/SCF theorem. Without the appropriate correlation energy, the HF exchange almost always prefers a high-spin electronic structure. DFT methods that have the correct balance between exchange and correlation can circumvent this problem and provide correct ground states compared to the experimental evidence. DFT modeling, if well tuned, is ubiquitously applicable to any homogenous molecular catalyst containing transition metals as extensively reviewed in the special issues of Chemical Review[34] and Coordination Chemistry Reviews.[35] The computationally investigated reactions include those for organic synthesis (C-H activation, functionalization, and coupling reaction), N_2 fixation, water oxidation, catalytic polymerization *etc*. The standard routine of computational mechanistic study is to survey the potential energy surface (PES) for stationary points (including intermediates and transition states) to reasonably connect the reagent and the product, with minimal thermodynamic and kinetic cost and to provide insight on the factors controlling reaction routes. *Vide infra* for some examples.

A large part of the DFT investigation covered by this dissertation primarily is about one simple reaction: the coupling of electrons and protons into dihydrogen. This electrochemical reaction is catalyzed by hydrogenase enzymes in Nature, as well as

heterogeneous and homogeneous catalysts under artificial conditions. The active sites of Hydrogenases, also inspired many organometallic compounds whose reaction mechanisms are covered in the dissertation.

The mechanistic study of [FeFe]-hydrogenase and its mimics

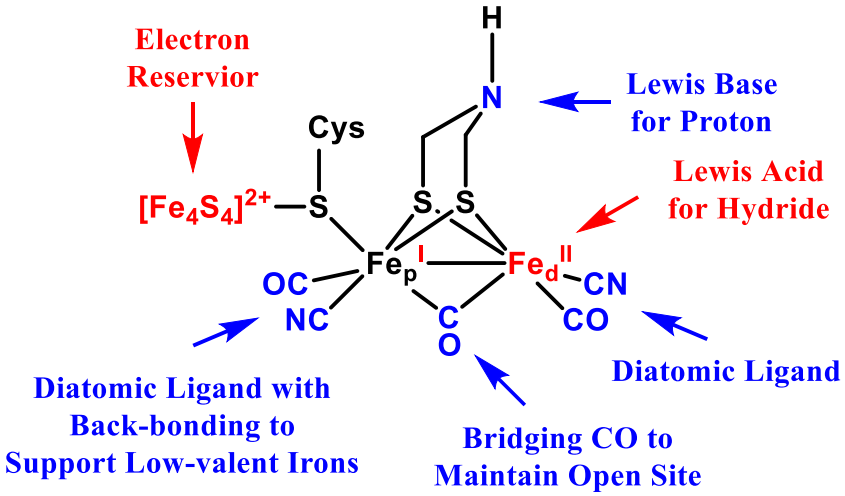

Figure I-2 The H-cluster of [FeFe]-hydrogenase and the structure-function analysis.

The active site of [FeFe]-hydrogenase. The hydrogenases are a family of enzymes that catalyze the reversible coupling of protons and electrons. Depending on the metals in the active site, the hydrogenases can be classified as [FeFe]-hydrogenase, [NiFe]-hydrogenase and [Fe]-hydrogenase. Utilizing base metals like iron and nickel only, they can achieve performance on par with noble metal (platinum and palladium) based artificial catalysts. Among the hydrogenases, [FeFe]-hydrogenase is typically found in biological systems requiring the production of H_2, *i.e.*, the prototypical hydrogen evolution reaction (HER).

The earliest isolated forms of [FeFe]-hydrogenase are the CO-inhibited (deactivated) oxidized state $\mathbf{H_{CO}}$ and the activated oxidized state $\mathbf{H_{ox}}$.[36-37] The $\mathbf{H_{ox}}$ state

was examined by X-ray crystallography to obtain its structure.[38-39] It was determined that the active site of [FeFe]-hydrogenase is a [Fe_6S_6] cluster (the H-cluster, Figure I-2), which can be further divided into one [Fe_4S_4] sub-cluster and one [Fe_2S_2] sub-cluster. The [Fe_4S_4] sub-cluster is an electron reservoir and can be treated as a redox active ligand as unity to the [Fe_2S_2] sub-cluster, which interacts with the substrate(s).

The [Fe_4S_4] sub-cluster is a cubane-like species and binds into the protein by four cysteine residues. With the overall charge of 2+, it features two high-spin Fe(II) and two high-spin Fe(III); these are antiferromagnetically coupled to form a diamagnetic unit (S = 0). The [Fe_4S_4] sub-cluster serves as an electron reservoir that picks up and buffers electron(s) from the electron transport channel, which consists of a series of additional [Fe_xS_x] clusters (F-clusters). The [Fe_4S_4] sub-cluster within the H-cluster stores the electron(s) at a short distance for transferring on call to the [Fe_2S_2] sub-cluster. The two irons in the [Fe_2S_2] sub-cluster are brought together by two bridging thiolates within a dithiolate and one bridging carbonyl. Each iron in the [Fe_2S_2] sub-cluster has multiple diatomic π-acid ligands to stabilize the possible low-valence iron (Fe^I) during the catalytic cycle. These diatomic ligands are further stabilized by the second coordination sphere with multiple hydrogen bonds from side chains of amino-acid residues. These two irons are differentiated by the mixed oxidation level (Fe^I-Fe^{II}). The sixth coordination site of the proximate iron. Fe_p^I, is bound to the [Fe_4S_4] sub-cluster via a cysteine residue sulfur; The other iron, the distal iron Fe_d^{II}, adopts a "rotated" conformation (Figure I-2) at the cost of, or benefiting from, a bridging carbonyl. The rotation of Fe_d^{II} puts the vacant site (along with appropriate vacant *d* orbitals) opposite to the bridgehead of the dithiolate. The vacant

site works as a Lewis acid and can accommodate incoming electron(s) and a hydride generated on site; H_2 evolves from that site as well. For an isolated [Fe_2S_2] sub-cluster, it would be more stable for Fe_d to adopt the unrotated conformation so that Fe_p and Fe_d can form a (partial) metal-metal bond. The protein matrix, *i.e.* the second coordination sphere of the H-cluster, must contribute to stabilizing the rotated Fe_d to keep the active structure

The unique bridging dithiolate is distinguished by an amine on the bridgehead, which is an apparent Lewis base and serves as a proton shuttle, responsible for accepting and temporality storing the "feedstock" protons form C169, the end of the proton transport channel through a series of groups of basicity. The bridgehead amine hangs over this vacant site of Fe_d so that the proton on it can travel to the vacant site easily. The identity of the bridgehead atom was actually confirmed much later[40] than the initial crystallographic report that recognized the difficulty of unambiguous assignment of the light bridgehead atom to carbon, oxygen, or nitrogen.[39]

The overall sophisticated, well-tuned design of the H-cluster enables the coupling of proton and electrons into H_2 at a high rate, *i.e.*, a TOF of up to 9000 s^{-1}.[41]

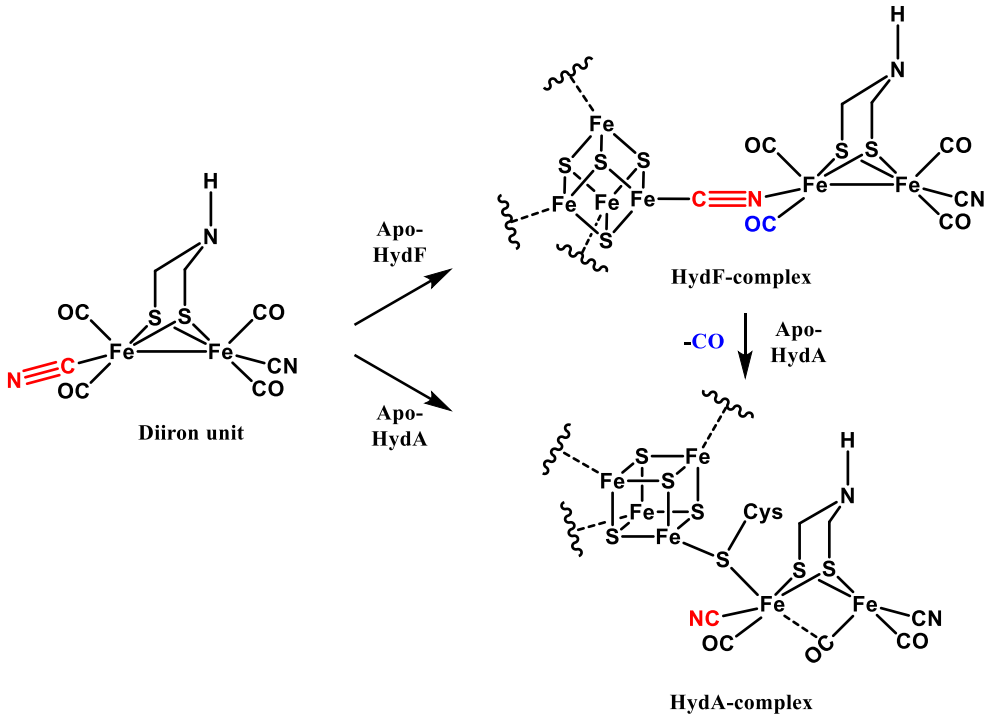

Figure I-3 The artificial maturation process of [FeFe]-hydrogenase. Note the flipping of the cyanide in the bridging orientation. [42-43]

The (artificial) maturation of [FeFe]-hydrogenase. The precursor of the $[Fe_2S_2]$ sub-cluster of [FeFe]-hydrogenase is the symmetric $(\mu\text{-adt})[Fe(CN)(CO)_2]_2$, likely synthesized by enzymes HydE and HydG.[36] This precursor would lose one carbonyl from one iron and convert another carbonyl on the other iron into a bridging ligand during the maturation process. (Figure I-3) This process is facilitated by the maturase, HydF,[42] which is likely a vehicle to transport the diiron precursor. The precursor uses its cyanide to bind to the anchor point, a $[Fe_4S_4]$-cluster of HydF, in so doing the cyanide flips, *i.e.*, the N-terminal on the $[Fe_2S_2]$ unit while the C-terminal on the $[Fe_4S_4]$ unit, as evidenced by hyperfine coupling constants from N and C by EPR experiments.[36] In fact our computational study

doubts the validity of the flip given a higher energy for the flipped structure. Generally speaking, the carbon end of a cyanide is softer in the hard-soft acid-base theory and prefers a metal with a low-spin, low-oxidation state, in order to maximize the back-bonding; in contrast the nitrogen end is harder and prefers a high oxidation state. The flip indeed coordinates the carbon end to a high-spin Fe^{II} or Fe^{III} of the $[Fe_4S_4]$ unit of HydF, instead of the low-spin Fe_p^{I} of the $[Fe_2S_2]$ sub-cluster. After that, the diiron unit is passed from HydF to apo-HydA (apo-HydA contains the $[Fe_4S_4]$ sub-cluster but not the $[Fe_2S_2]$ sub-cluster),[44] to fully assemble the active enzyme. This final step releases a CO ligand and the bridging cyanide flips back.[45]

Artificial *in vitro* maturation actually does not need the involvement of HydF because apo-HydA has access to the diiron unit from the solution and can uptake it without further assistance.[43] Apo-HydA is also tolerant to diiron units that are not native, including those with modified bridgehead atoms as well as modified substituents and ligands.[46] But the natural activity can only be achieved by the small molecule match of the native diiron unit, which contains adt bridging ligands, *i.e.* the N-base at the bridgehead in required adt. Protein crystallography reveals that the difference between the natural [FeFe]-hydrogenase and semi-synthetic [FeFe]-hydrogenase is minimal.[47] Albeit, these inert semi-synthetic models provide an opportunity to pause the fast turn-overs of [FeFe]-hydrogenase and is used as a platform to capture short-lived intermediates, *vide infra*.

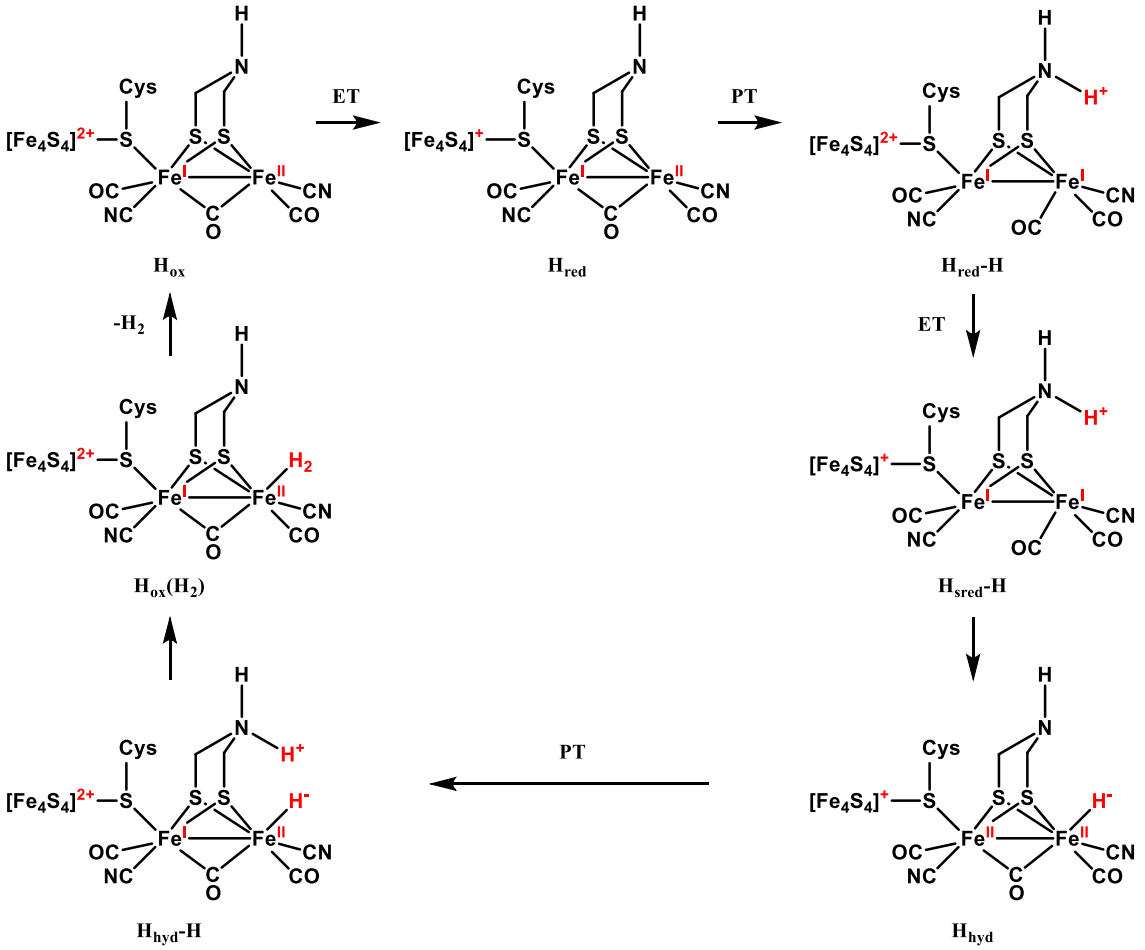

Figure I-4 The consensus catalytic cycle of the hydrogen evolution reaction on [FeFe]-hydrogenase.[48]

The catalytic cycle of [FeFe]-hydrogenase. Proposed by Lubitz and coworkers, the catalytic cycle (Figure I-4) of [FeFe]-hydrogenase starts with a one-electron reduction. At high-pH, the reduction is localized to the [Fe4S4] sub-cluster from $[Fe_4S_4]^{2+}$ to $[Fe_4S_4]^{+}$ without immediate protonation, rendering the reduced states, **H**$_{red}$. By lowering the pH, protonation at the bridgehead amine of **H**$_{red}$ generates **H**$_{red}$**-H**.[48] This proton transfer is coupled with an intramolecular electron transfer from the [Fe4S4] sub-cluster to the [Fe2S2]

sub-cluster, resulting in an oxidation state of $[Fe_4S_4]^{2+}$-Fe_p^{I}-Fe_d^{I}; *i.e.*, this is a proton-coupled electron transfer (PCET) process.[49] The $[Fe_4S_4]^{2+}$ of **H_{red}-H** is ready for the next incoming electron and a second reduction makes the super-reduced state **H_{sred}-H**, with two equivalences of reduction power accumulated on the $[Fe_4S_4]$ sub-cluster and the $[Fe_2S_2]$ sub-cluster, respectively.[50]

The internal proton transfer from the amine to the open site of Fe_d consumes the stored reduction power and converts the proton into a hydride in the **H_{hyd}** state. This was very recently verified by spectroscopic evidence.[48, 51] A more inert diiron unit featuring an oxygen bridgehead, is applied in this case to preserve the hydride-bearing species. It is noted that the two electrons for the hydride come from Fe_p and Fe_d respectively. The $[Fe_4S_4]^{+}$ sub-cluster of **H_{hyd}** remains in the reduced state $[Fe_4S_4]^{+}$ until another PCET process of intramolecular electron transfer from the $[Fe_4S_4]$ sub-cluster to the $[Fe_2S_2]$ sub-cluster is triggered by the second protonation on the pendant amine in **H_{hyd}-H** state.[49] Finally, the proton and the hydride couple with each other to form the H_2 in the σ-complex **H_{ox}-(H_2)** and soon regenerates the oxidized state **H_{ox}** by releasing H_2. Only three nominal reduction levels, **H_{ox}** (with zero equivalent of reduction power stored), **H_{red}** (with one equivalent) and **H_{sred}** (with two equivalents), are involved, but the distribution of the reduction power is more flexible between three versatile redox centers, $[Fe_4S_4]^{2+/1+}$, $Fe_d^{II/I}$ and $Fe_p^{II/I}$. Among them, the $Fe_d^{II/I}$ directly interacts with the added protons and hydride. (Note: **H_{hyd}** has its reduction power depleted by the newly formed hydride so that it is treated as a special case of **H_{ox}**.)

Computational chemistry[52] precisely predicted the role of the pendant amine,[53-54] long before the confirmation of its existence. The computational catalytic cycle, developed without the [Fe_4S_4] sub-cluster, provided some *a priori* support before the ultimate experimental data became available.[55-56] The [Fe_4S_4] sub-cluster was also modeled[57-59] with Noodleman's broken-symmetry scheme[60-61] but the focus was on the electronic structures rather than the mechanistic properties.

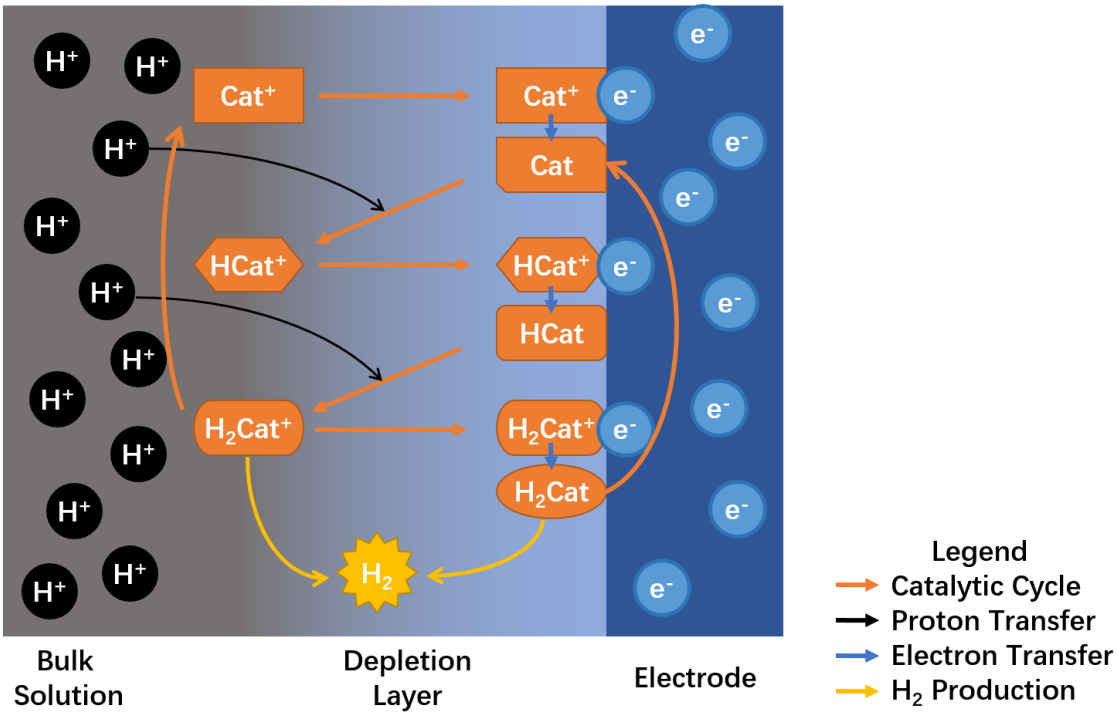

Figure I-5 Cartoon illustration of the general mechanism of an electro-catalyst for HER. Note that electron transfer only happens when the catalyst "hits" the electrode surface while the proton transfer could happen anywhere between the electrode surface and the bulk solution, depending on the level of proton (substrate) depletion.

Mechanisms of model complexes inspired by [FeFe]-hydrogenase. Unlike hydrogenase with exclusive protein domains to transport the "feedstock", protons and electrons, and the product, H_2, for HER; the artificial catalyst must pick up the substrate, i.e. protons from solution, and then combine them with the electrons provided by the electrode.

Figure I-5 illustrates the general working mechanism of a homogenous electro-catalyst for HER. The build-up of reduction power and protons on the catalyst, is generally stepwise in alternate order of proton transfers (PT, chemical/C step) and electron transfers (ET, electrochemical/E step) to prevent the accumulation of like charge, but two successive PT or ET steps are also possible on certain catalysts. The electro-catalyst, which is responsible for collecting electrons and protons, must shuttle through the electrode double layer for multiple times and run back and forth between the electrode surface for electrons and the bulk solution for protons, as the protons are quickly depleted and become unavailable in the double layer when the catalytic turn-over proceeds.

The production of one molecule of H_2 requires two electrons and two protons, therefore the catalyst may either have [ECEC] or [CECE] catalytic cycles, or even a mixture of both, assuming C and E events are alternate. Figure I-5 shows a sequence of five events ECECE, after the first four events, the catalyst has the option to yield the product H_2; However, before H_2 is released over the barrier, the catalyst still has the chance to pick up the third electron when it travels back to the electrode surface. In this case, the catalytic cycle is E[CECE] and the first E event may be treated as the activation of the catalyst.

Certain PT and ET steps are thermodynamically disfavored, as the acceptance of a proton depletes the electron density of the recipient while the acceptance of an electron increases the electron crowdedness. But the coupling of PT and ET, so called proton-coupled electron transfer (PCET) (Figure I-6), may alleviate the thermodynamic problem. The energy released during the coupling of the proton and the electron can help drive the reaction and can reduce the overall barrier for such processes. Therefore, the potential required by a PCET process depends on the pH of the environment, represented by a diagonal line in Figure I-6.

A **B**

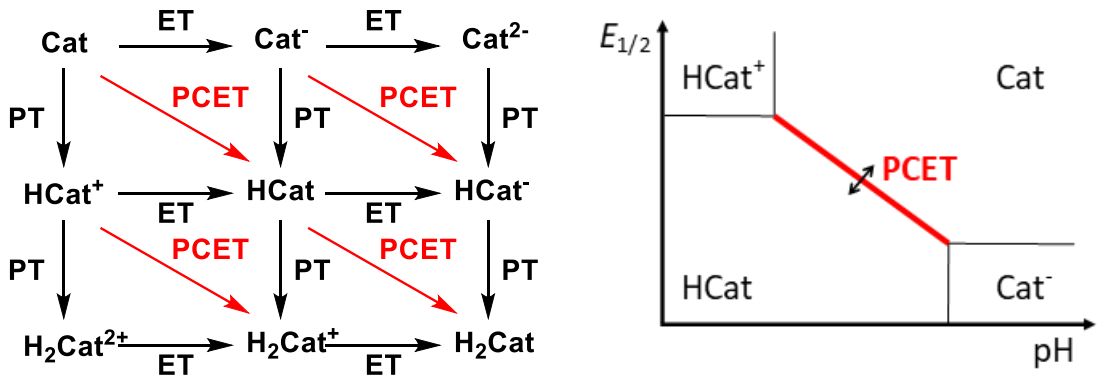

Figure I-6 The PCET matrix and the Pourbaix diagram. **A**) PCET matrix shows PT and ET are coupled to lower thermodynamic and kinetic barriers for each individual step. B) Pourbaix diagram shows the applicable range of a PCET step.

The computational study can treat the thermodynamics of the ET and PT steps by introducing the standard reference couples: a conjugate acid-base couple and a redox couple. The thermodynamic preferences are quantified as ΔpK_a and $E_{1/2}$, comparable with

experimental data. Therefore, the computational modeling helps locate the most stable intermediates after a given number of protonations and reductions are introduced to the electro-catalyst. The kinetics of the PT steps, can also be treated with regular computational methods but the solvation correction is necessary to obtain reasonable barriers; this is because the protonation process by a (neutral) acid essentially involves the separation of the positively charged proton and negative charged conjugate base, and the solvation is necessary to shield the Coulomb interaction to provide stabilization to charged species. Marcus theory describes the kinetics or the calculation of barriers for ET steps in the molecular systems,[62] but is less applicable to the process involving both the electrode and the molecular catalyst in solution, *i.e.* a heterogeneous electron transfer.

The HER mechanism of (μ-pdt)[Fe(CO)$_3$]$_2$. Two representative examples of the computational mechanistic study of mimics of [FeFe]-hydrogenase are provided below. One is based on the first generation of model complexes, those without the strategically placed pendant amine to transport the protons. Examples are (μ-pdt)[Fe(CO)$_3$]$_2$,[63] (μ-edt)[Fe(CO)$_3$]$_2$[63] and (μ-bdt)[Fe(CO)$_3$]$_2$.[64] The emergence of this series of model complexes was partially led by the uncertain identity of the bridge-head (which was modelled to be C instead of N in early days, *vide supra*) of Fe_2S_2 sub-cluster of the H-cluster in [FeFe]-Hydrogenase as well as its structure simplicity. The HER mechanism[65] of (μ-pdt)[Fe(CO)$_3$]$_2$ is given here as a representative mechanism.

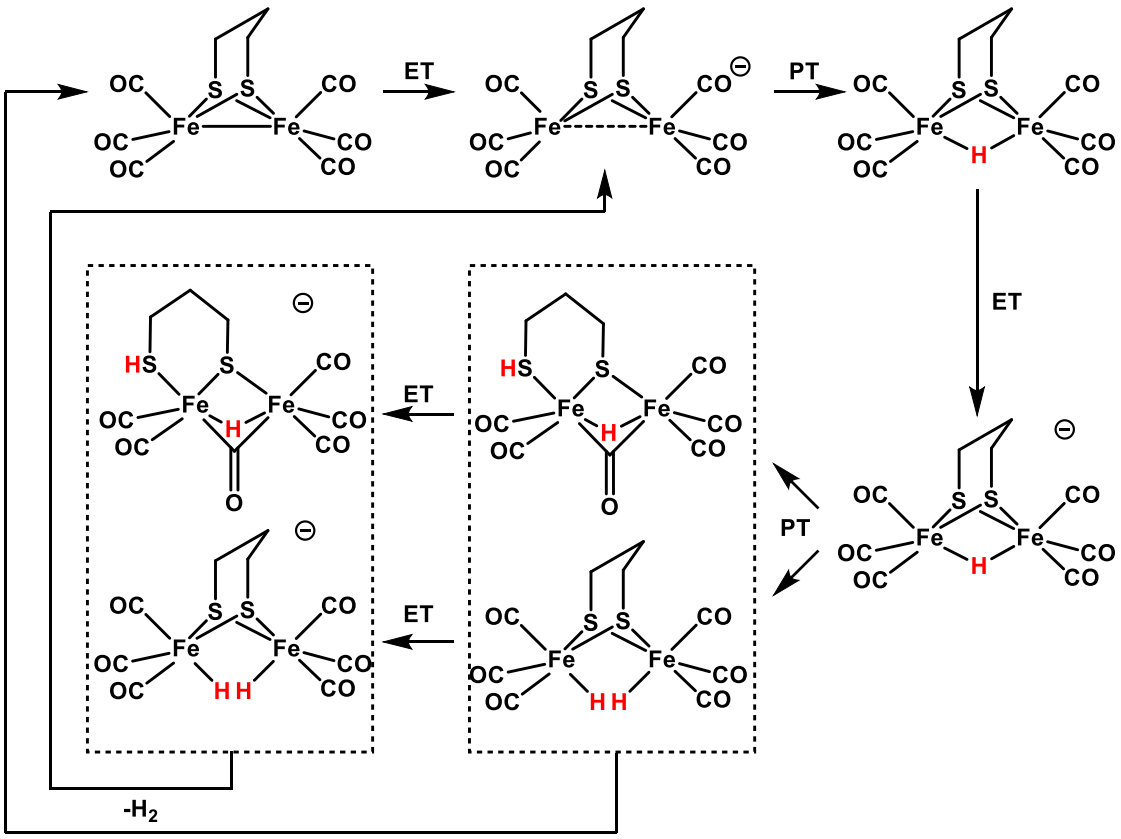

Figure I-7 An early computational H_2 production catalytic cycle of (μ-pdt)[Fe(CO)$_3$]$_2$.[65]

Both irons in (μ-pdt)[Fe(CO)$_3$]$_2$ are relatively reduced (Fe^{I}), which coincides with the oxidation state of **H$_{red}$** of [FeFe]-Hydrogenase. However, the depletion of electron density on the irons by six π-acid carbonyls is so great that a reduction is required before the complex can accept a proton. The added proton is accommodated as a bridging hydride and was calculated to be more stable than a terminal hydride or a protonated S. In other words, it is disadvantageous for one of two irons to adopt the rotated conformation, as one sees in Fe$_d$ (Figure I-2) and to create a bridging carbonyl.

The second reduction follows the protonation and restores the oxidation state of both irons to Fe^{I}. However, the second protonation is tricky on this model as no vacant site is available. One of the bridging sulfurs might accommodate it, but to do so the sulfur must break one S-Fe dative bond to withdraw enough electron density to support the newly formed S-H bond. Meanwhile, one carbonyl on the other iron becomes bridging to the iron cleaved from the S-Fe bond to fill the vacancy due to the loss of S donation. In the resting state after two protonations and two reductions, the two irons are bridged by one thiolate, one hydride, and one carbonyl; and another external proton rests on the thiol. At this point the hydride and the proton can directly couple into H_2. A thermodynamically less stable (by 14.6 kcal/mol) isomer possesses two iron-hydrides and the H_2 production is through the coupling of two hydrides, though this coupling is kinetically hindered. Introducing a third electron into the system can accelerate the rate-determined coupling reaction, but the dihydride is still less stable than the proton-hydride pair-bearing species. Both coupling routes, at this stage, have comparable barriers and are lower than those species without a third electron. In summary, the event sequence of the catalytic cycle of $(\mu\text{-pdt})[Fe(CO)_3]_2$ is either [ECEC] or E[CECE].

The first-generation models, although capable of performing catalytic HER, have quite a few aspects to be optimized. First, they generally have quite high over-potentials and low turn-over frequencies. Second, these models prefer to have the bridging hydride instead of terminal hydride and won't have a bridging carbonyl as one sees in the active site of [FeFe]- Hydrogenase. But a bridging hydride is generally more stable than a terminal hydride and is less active towards HER. Lastly, they are flawed in the structural

design without an intramolecular pendant base to assist the reaction, the most delicate state of the art design by Nature. However, they tend to generate their own "pendant base" by dissociating one of the thiolates throughout the catalytic cycle, at the cost of a chemical bond.

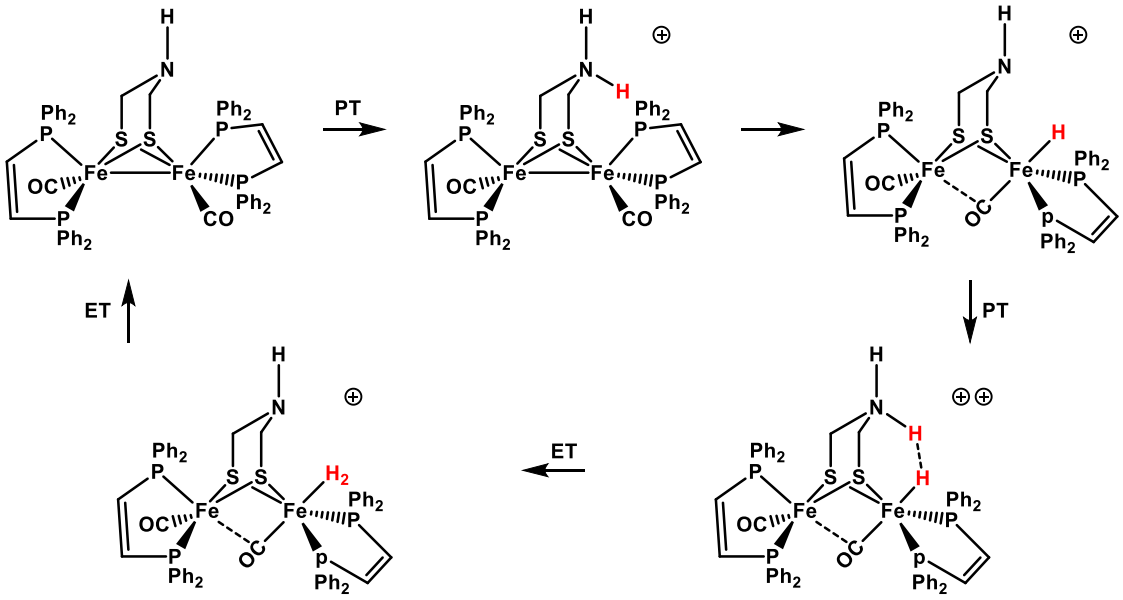

Figure I-8 The H_2 production catalytic cycle of (μ-adt)[Fe(CO)(dppv)]$_2$ from available experimental evidence. [72]

The HER mechanism on (μ-adt)[Fe(CO)(dppv)]$_2$. The second generation model complex starts to incorporate azadithiolate to bridge irons[66] and strategically added bulky groups[67-70] to stabilize the rotated iron conformation with a bridging carbonyl, which makes a terminal hydride possible. Stronger donors are also introduced to make the system overall more basic to incoming protons for easier protonation and hydride generation:

phosphine,[71] diphosphine,[72] nitrosyl[73] are used to replace the carbonyl in the models. The representative example of mechanistic study shown here is (μ-adt)[Fe(CO)(dppv)]$_2$. [72]

Both irons of (μ-adt)[Fe(CO)(dppv)]$_2$ are Fe(I), sharing the same oxidation states as the previous example (μ-adt)[Fe(CO)$_3$]$_2$ and **H$_{red}$**. The existence of the pendant amine and the general rich electron density by the donation from dppv ligands enables the protonation and the successive conversion into a hydride, before the introduction of external electrons. The proton is accepted by the pendant amine first, which acts as a proton shuttle and then is transferred to one of the irons, creating a terminal hydride. This conversion is also accompanied by the geometric rearrangement that one carbonyl on the affected iron adopts a bridging position. At room temperature, this newly formed terminal hydride may isomerize into a bridging hydride, with two possible geometries to lower the energy. After the hydride is generated, the amine now is vacant again and can accept the second proton, again without the introduction of external electrons, provided that a strong acid is present. The successive protonation creates a hydride-proton pair. This pair is stabilized by the mutual interaction and the terminal hydride is no longer prone to convert into a bridging hydride; therefore, the crystal structure was obtained.[72] However, the coupling between the proton and the hydride must be initiated by the addition of an external electron to generate the σ-H$_2$ complex, as η^2-H$_2$ is a significantly weaker ligand compared to a hydride. The second incoming electron kicks the H$_2$ away and regenerates the catalyst. The catalytic cycle is summarized as [CCEE] for (μ-adt)[Fe(CO)(dppv)]$_2$.

Summary. The [Fe$_2$S$_2$] sub-cluster is highly integral itself, as it is connected to the rest part of the enzyme with only one covalent bond, in additional to multiple weak interactions

like hydrogen bonds. The model complexes may reproduce the structural features of the active site, especially the [Fe_2S_2] sub-cluster of the [FeFe]-Hydrogenase to a considerable extent. This raises the optimistic hope they are going to reproduce the activity as well, even without the supporting protein matrix of the enzyme. But these model complexes may still suffer certain drawbacks: they operate with stronger acids only and are significantly less efficient (lower turn-over-frequency and higher over-potentials) than the hydrogenases. The computational mechanistic study on these models tries to illustrate the details of the catalytic cycle, in which most intermediates are not observable experimentally. A clear picture of the catalytic cycle of the models themselves, as well as the hydrogenase, can help discover possible direction, in which the optimization of the model can be pursued. In addition, the delicate design the active site of hydrogenase also inspired organometallic compounds that are capable of intermediating reactions beyond H_2 production.

The content of this dissertation. The body of this dissertation focuses on the mechanistic study of model complexes / electrocatalysts inspired by the active site of hydrogenases. The common structural feature is that two (first-row) transition metals are bridged by two thiolates. The applied methodology is introduced in Chapter II. Chapter III discusses the hemi-lability of the bridging thiolate in these electrocatalysts and the contribution that such a feature might make to catalytic activity. Chapter IV investigates another kind of diatomic actor ligand brought into the model studies; *i.e.*, the nitrosyl(s) perform the role of an electron acceptor or donor depending on the electronic environment it experiences. Chapter V describes the mechanistic study of cyanide isomerization on small

organometallic models, as an effort to clarify the maturation process of hydrogenase. Chapter VI illustrates the mechanisms of a couple of reactions occurring on the bridging thiolates (C-H bond activation reactions as well as isomerization reactions) in the diiron models and Chapter VII shows the mechanism of CO_2 reduction by a Ni-Re complex featuring a similar core design M_2S_2 as the hydrogenase active site.

CHAPTER II

METHODOLOGY

Software packages

Most calculations are executed in Gaussian 09, Version D01.[74] Some spectral calculations (Mossbauer parameters, EPR parameters) are done with ORCA.[75]

Functionals and basis sets

The functionals of choice are B3LYP[24] and TPSS[21]. The former is used ubiquitously throughout different projects in this dissertation while the latter, a pure functional (without the addition of any Hartree-Fock exchange), was previously benchmarked[76] to perform better with the strongly correlated $Fe(NO)_x$ systems. Other functionals M06,[77] M06L,[77] PBE,[20] TPSSh,[26] ωB97X[78] are also used and specifically noted.

The basis set of choice is the Triple-ζ 6-311++G(d,p) for all non-metal atoms (up to Cl)[79-81] and Wachters-Hay basis set with diffuse and polarization functions for first-row transition metals, under the designation 6-311++G(d,p). Effective core potentials SDD[82] are used for certain heavier metals and are be noted specifically in the relevant chapters.

Geometry optimization and frequency calculations

The computational optimization of a molecule's structure is aimed at exploring the potential energy surface (PES) to locate stationary points, where the energy gradient (the

first-order derivative of the energy with respect to any arbitrary geometric parameter) is zero. In other words, no internal forces exist and the geometry will be stationary unless a perturbation is introduced. The vibrational analysis, converts the 3*N* degrees of freedom of an *N*-atom molecule into 3*N* normal modes, including 3 translational motions, 3 rotational motions, and 3*N*-6 vibrational motions. Each vibrational motion is described by a set of internal coordinates (the relative movement of atoms) and a force constant. When its force constant is positive, the vibrational mode has a real frequency; in contrast, a negative force constant produces an imaginary number as its frequency. The calculated real frequencies may help assign the IR spectrum while the number of imaginary frequencies indicates the property of the corresponding stationary point (0 for local minimums (reactants, products, and intermediates) and 1 for transition states, 2+ for higher-order saddle points). Every optimized geometry should be verified to have negligible forces and the desired number of imaginary frequencies.

For the optimization of local minimums, the available crystal structures, are imported as the starting geometries. The starting coordinates of other species are guessed by modifying available experimental and/or computational geometries. The optimization is carried out with GEDIIS algorithm[83] as guided by energy gradients with redundant coordinates for efficiency. For tough situations, the calculation of partial or full analytical Hessian matrix can be included.

The transition states, are generally optimized by a two-step process. First, a relaxed scan is performed by scanning one appropriate geometric parameter, *i.e.*, it is frozen to a set of fixed values that can guide the desired transformation from the reactant

to the proposed product, *vice versa,* while other geometric parameters are free to change. The "crude" geometry of the transition state is indicated by a maximum on the energy scan curve and a minimum on the force scan curve. In the second calculation, this "crude" geometry is imported again in the transition state search with RFO algorithm to have one imaginary frequency.[84] Eigenvector check is usually turned off as the "crude" geometry may indeed have multiple imaginary frequencies at the beginning. For some difficulty transition states, in addition to the crude geometry, the coordinates of the guessed reactants and products are also introduced in the calculations and the optimization uses STQN algorithm.[85-86]

The molecular motion associated with the imaginary frequency in the optimized transition state must be inspected. The transition state is manually displaced by following the imaginary frequency and re-optimized to validate the proposed reaction coordinate. The re-optimization process may reveal the existence of overlooked intermediates and multiple transition states are sometimes needed to connect the reactant and the product, through a few intermediates.

Manual adjustment of electronic structures

The wavefunction automatically generated is usually good enough for the optimization. An important exception is the open-shell singlet, which has the same number of α and β electrons but not all electrons are exactly paired, also called a spin-polarized or broken-symmetry solution. The computational code prefers to pair up electrons in the singlet calculations and the spin polarization must be initiated manually,

either by swapping occupied and unoccupied spin orbitals, often by calculating the triple state first, or generating the initial wavefunction from fragments which are assigned localized unpaired electrons. Due to the single determinant nature of DFT calculations (see Chapter I), the broken-symmetry wavefunction is only one component of the correct wavefunction, and the calculated broken-symmetry energy is missing an exchange integral and may also be contaminated by high-spin state(s). The energy can be corrected approximately by the Yamaguchi correction:[87]

$$E_{BS,Corrected} = E_{BS} + (E_{BS} - E_{HS})\frac{S_{BS}^2 - S_{CS}^2}{S_{HS}^2 - S_{BS}^2}$$

E_{BS} stands for the optimized electronic energy of the broken symmetry singlet and E_{HS} is the energy of the corresponding high-spin state. For example, if one α and one β electron are not paired, the corresponding high-spin state should be the triplet; the quintet for two α and two β unpaired electrons. S^2 is the calculated expectancy value of the operator $\widehat{S^2}$ for the open-shell singlet or the high-spin state. S_{CS}^2 for the closed-shell singlet is always 0.

Solvation

Since most reactions studied happen in the solution, a solvation model is necessary to accurately model them. The solvation effect is implicitly simulated by the solute cavity created in the polarizable continuum representing the solvent field. The parameters from the SMD model[88] is used unless otherwise specified. The solvation correction is generally

calculated with the optimized structure in the vacuum without re-optimization and adds to the electronic energy E directly. Exceptions are specifically indicated.

Gibbs free energy

The optimized structure comes with its electronic energy (see Chapter I for the definition). However, the thermodynamics and kinetics are directly associated with the Gibbs free energy instead. The frequency calculation is used to generate zero-point energy (E_{ZPE}), then additional information from this calculation, namely translations and rotations, are used with the vibrational frequencies and electronic degeneracy to produce thermal corrections which are used to calculate the enthalpy (H) and entropy (S). Finally, the Gibbs free energy (G) at the standard condition (1 atm and 298.15 K) can be calculated.

$$G = H - ST = (E + E_{ZPE}) + pV - k_B T ln Q = E_{0\mathrm{K}} + pV - k_B T ln Q$$

In the above equation p, V, T are the pressure, the molar volume and the temperature, respectively; k_B is the Boltzmann constant. Q stands for the partition function describing the contributions from the different excited states of electronic, translational, rotational, and vibrational motions. Note that imaginary vibrational motion(s) are omitted in the calculation of Q as well as G as their frequencies are imaginary numbers, as the distribution over imaginary vibration(s) lacks a physical definition. The symbols G' and Q' are specifically used in this context when the imaginary vibrations are included. Thermodynamic stability comparisons between two species are straightforward by comparing their Gibbs free energy: the lower, the more stable.

Rate constant

The reactant or an intermediate species must climb the potential energy surface (PES) to reach a transition state before it spontaneously goes downhill on the PES to convert into the product or another intermediate. The free-energy barrier is defined to be the Gibbs free-energy difference between the transition state and the most stable species (the reactant or an intermediate) in front of it in the reaction coordinate. A chemical reaction can involve multiple barriers and the chemical process associated with the highest barrier is the rate determining step.

For a simple example reaction with only one transition state (also the rate determining step):

$$\mathrm{A} \rightarrow \mathrm{TS} \rightarrow \mathrm{B}$$

By applying the Boltzmann distribution, the fraction of the reactant at the transition state is

$$\frac{[\mathrm{TS}]}{[\mathrm{A}]} = \exp\left(\frac{-(G'_{\mathrm{TS}} - G_{\mathrm{A}})}{k_B T}\right) = \frac{Q'_{\mathrm{TS}}}{Q_{\mathrm{A}}} \exp\left(\frac{-\left(E_{0\mathrm{K,TS}} - E_{0\mathrm{K,A}}\right)}{k_B T}\right)$$

Please specifically note the real Gibbs free energy G'_{TS} instead of the computational Gibbs free energy G is used here for the transition state. The transition state has 3N-7 real vibrations and one imaginary vibration ω_{TS}. And the partition function for this motion can be separated from Q'_{TS} and is written as:

$$q_{\mathrm{TS}} = \sum_{k=0}^{\infty} e^{\frac{-kh\omega}{k_B T}} = \frac{1}{1 - e^{\frac{-h\omega_{\mathrm{TS}}}{k_B T}}} \approx \frac{k_B T}{h\omega_{\mathrm{TS}}}$$

$$\frac{[\mathrm{TS}]}{[\mathrm{A}]} = \frac{q_{\mathrm{TS}} Q_{\mathrm{TS}}}{Q_{\mathrm{A}}} \exp\left(\frac{-\left(E_{0\mathrm{K,TS}} - E_{0\mathrm{K,A}}\right)}{k_B T}\right) \approx \frac{k_B T}{h\omega_{\mathrm{TS}}} \frac{Q_{\mathrm{TS}}}{Q_{\mathrm{A}}} \exp\left(\frac{-\left(E_{0\mathrm{K,TS}} - E_{0\mathrm{K,A}}\right)}{k_B T}\right)$$

The reaction rate can be written in two ways, with respect to [A] or [TS]:

$$\frac{d[\mathrm{A}]}{dt} = k[\mathrm{A}] = k_{\mathrm{TS}}[\mathrm{TS}] = k_{\mathrm{TS}}\frac{k_B T}{h\omega_{\mathrm{TS}}}\frac{Q_{\mathrm{TS}}}{Q_{\mathrm{A}}}\exp\left(\frac{-\left(E_{0\mathrm{K,TS}} - E_{0\mathrm{K,A}}\right)}{k_B T}\right)[\mathrm{A}]$$

k_{TS} is defined to be the rate constant that the molecule departs from the transition state and it happens to be the frequency of the imaginary vibrational motion, so that

$$k = \frac{k_B T}{h}\frac{Q_{\mathrm{TS}}}{Q_{\mathrm{A}}}\exp\left(\frac{-\left(E_{0\mathrm{K,TS}} - E_{0\mathrm{K,A}}\right)}{k_B T}\right)$$

At this moment, the contribution from the imaginary vibration has been cancelled. The remaining Q_{TS} is the partition function used in the computational calculations of the Gibbs free energy of the transition state. The Eyring equation[89] used to theoretically calculate the rate constant thus appears as

$$k = \frac{k_B T}{h}\exp\left(\frac{-(G_{\mathrm{TS}} - G_{\mathrm{A}})}{k_B T}\right) = \frac{k_B T}{h}\exp\left(\frac{-\Delta G_{\mathrm{TS}}}{k_B T}\right)$$

The rate constant of a chemical reaction can solely be evaluated by the calculated barrier of the rate determining step. Note that the Gibbs free energy is calculated at the standard condition (1 atm and 298.15 K) in the gas phase and the corresponding concentration is approximately 0.0409 mol/L. For the solution reaction, the standard condition is 1 mol/L, so that a factor of 1.89 kcal/mol (at 298.15 K) is added to G of every species to account the concentration difference. This factor affects ΔG_{TS} except unimolecular reactions and ensures that the Eyring equation is ubiquitously applicable to elementary reactions of different molarities.

Protonation and reduction

Protonations and reductions are two special types of reactions:

$$\mathrm{Cat} + e^- = \mathrm{Cat}^-$$

$$\mathrm{Cat} + \mathrm{H}^+ = \mathrm{HCat}^+$$

The special aspect is that one reactant is either an electron or a proton. Considering their relatively small sizes and high charge densities compared to molecules, the calculation of their free-energies by the procedures above will incur extraordinary errors in the absolute values. A way to circumvent this problem is to introduce references to cancel errors.:

$$\mathrm{Cat} + \mathrm{Red} = \mathrm{Cat}^- + \mathrm{Ox}^+$$

$$\mathrm{Cat} + \mathrm{HAcid} = \mathrm{HCat}^+ + \mathrm{Base}^-$$

A redox couple (Ox^+/Red, specifically the couple used here is ferrocenium and ferrocene $Fc^{+/0}$) is introduced to provide the electron and the thermodynamic reference for this reduction reaction. The standard reduction potential, $E_{1/2}$, is calculated by the following equation:

$$E_{1/2} = -\frac{G(\mathrm{Cat}^-) - G(\mathrm{Cat}) + G(\mathrm{Ox}^+) - G(\mathrm{Red})}{nF}$$

G is the calculated Gibbs free energy, n is the equivalents of electrons transferred, F is the Faraday constant.

Similarly, a conjugate acid and base pair (usually the acid used in the corresponding experimental work) is introduced to serve as the proton donor/acceptor.

The thermodynamic preference of a protonation reaction is indicated by the relative acidity ΔpK_a calculated by the following equation.

$$\Delta pK_a = pK_a\,(\mathrm{CatH}) - pK_a\,(\mathrm{HAcid})$$

$$= \log_{10}(e) \times \frac{G(\mathrm{Cat}^-) - G(\mathrm{CatH}) + G(\mathrm{HAcid}) - G(\mathrm{Base}^-)}{RT}$$

e is the Euler's number here (not the charge of an electron).

The kinetic aspect of an electron transfer reaction can be described by the classic Marcus theory,[62] but for molecular processes only. No mature theory is available to model the kinetics of electron transfers from the electrode to the molecular catalyst involved in the electro-catalysis. The kinetics of proton transfers may be modeled by the transition state theory. However, the optimization of the transition state must be done in the solvation model as the protonation involves the charge separation between the proton and the conjugate base, which is shielded by solvents.

Sometimes, the electron(s) and the proton(s) are transferred at the same time in the so-called proton-coupled electron transfer (PCET). Its thermodynamic preference can be estimated by combining the Gibbs free energies of these two individual steps. In this manner, the reduction potential is mutually dependent on the acidity of the proton source. This mutual dependence is graphically represented by a diagonal line in the Pourbaix diagram (*i.e.* a potential / pH diagram, see Figure I-6).

The standard potential $E_{1/2}$ (vs. $Fc^{+/0}$) of a PCET process was calculated with the following equation:

$$\mathrm{Cat} + \mathrm{Red} + \mathrm{Hacid} = \mathrm{Hcat} + \mathrm{Ox}^+ + \mathrm{Base}^-$$

$$E_{1/2} = -\frac{G(\mathrm{Hcat}) - G(\mathrm{Cat}) + G(\mathrm{Ox}^{+}) - G(\mathrm{Red}) + G(\mathrm{Base}^{-}) - G(\mathrm{Hacid})}{nF}$$

Though the above equations may give arbitrary numbers for $E_{1/2}$ with various acids, it is only applicable to the defined range, indicated by the red line in Figure I-6B. A very strong acid would initiate a PT step instead of a PCET process; on the other hand, a very weak acid cannot initiate a PCET process instead of an ET step.

Orbital analysis

Visual representations of molecular orbitals, electron density, and spin density are extracted from the optimized wavefunction. Atom-wise and orbital-wise numerical electron densities and spin densities are generated by Mulliken population analysis. Such evidence helps assign/localize the redox events. NBO analysis (version 3.1)[90] incorporated in Gaussian is applied to get natural bonding orbitals, which give Lewis bonding structures.

EPR and Mossbauer parameters

They are calculated by ORCA. EPR parameters include the *g*-tensor and hyperfine coupling *A*-tensors of paramagnetic species. The *A*-tensors contains isotropic contribution and anisotropic contributions form dipoles and spin-orbital couplings. The Mossbauer parameters, namely the isomer shift and the quadrupole splitting, are determined from the electron density and the electron gradient at nuclear with fitted calibration curves.[91]

CHAPTER III

HEMI-LABILE BRIDGING THIOLATES AS PROTON SHUTTLES IN BIO-INSPIRED H_2 PRODUCTION ELECTROCATALYSTS

Introduction

As mentioned in the introductory chapter, the use of thiolate-sulfurs to bridge transition metals are ubiquitous in metalloenzymes, for example, in the active sites of the [FeFe]- and [NiFe]-Hydrogenase and Acetyl CoA Synthase.[36, 92] The efforts to create model complexes were stimulated and inspired by the organometallic nature of such active sites featuring base metals and their capacity to conduct organometallic-like reactions, with the optimistic hope to gain the desired reactivity. On the other hand, the simplified models offer opportunity to explore the intricate unresolved reaction mechanisms on the enzymes.

One major objective of such biomimetics is to reproduce the active site structure of hydrogenases to design electro-catalysts for H_2 production or oxidation.[93] While current attempts have helped assign spectroscopic features, fully functional models are elusive. The most important lesson people learnt from the active site of the [FeFe]-hydrogenase is that the availability of a Lewis base, *i.e.*, the so-called "pendant amine" adjacent to the exposed vacant site of the distal iron, is of crucial importance for the H_2-

---

This chapter is reproduced with permission from Ding, S.[#]; Ghosh, P.[#]; Lunsford, A. M.[#]; Wang, N.; Bhuvanesh, N.; Hall, M. B.; Darensbourg, M. Y. *J. Am. Chem. Soc.* **2016,** *138*, 12920-12927. ([#]Equal contributions. The author of this dissertation primarily contributed the computational mechanistic studies.)

production activity.[2] This idea was actually exploited by Dubois, *et al.* in the design of the P_2N_2 or P_2N ligands,[93-98] which chelate to a nickel atom to generate a series of monometallic catalysts. Liu *et al.* used this P_2N_2 ligand on an iron-based complex, (η^5-$C_5H_4R)Fe^{II}(P_2N_2)^+$ and was able to capture a hydride (on iron) - proton (on nitrogen) pair that is stable enough to be examined by neutron diffraction. [99-101]

An interesting contrast is that the [NiFe]-Hydrogenase active site does not have an apparent pendant base at all; however, high-resolution protein crystallography of Ni-R, one state of [NiFe]-Hydrogenase, shows a proton is bound to a terminal cysteine residue on Ni,[102-103] which serves as a "pendant base" and was actually predicted as early as two decades ago by computations.[104] Besides the clear function of the pendant base, the roles of, and the fine interplay between, the two transition metals in the active sites of [FeFe]- and [NiFe]-hydrogenase are more or less ambiguous. It is the topic of the work in this chapter and is explored by the investigation into the bimetallic complexes presented in this work.

A family of bimetallics can be generated by combining one metalloligand and one metal receiver fragment. The metalloligand consists of a tetradentate, cis-dithiolate ligand $E_2S_2^{2-}$ (E = N, P, S) and the central metal M chelated by four claws; it further binds to the M' receiver fragment with its excess lone pairs on the thiolates.[105-106] Our lab is particularly specialized in the $M(N_2S_2)$ metalloligands (M= $[Fe(NO)]^{2+}$, $[Co(NO)]^{2+}$, Ni^{2+} and many other transition metals). As for the receiver unit M', the combination of Fe/Ru and cyclic polyhapto ligands, *e.g.* η^5-cyclopentadienyl and η^6-benzene is widely use,[105, 107-112] for both H_2 and O_2 activation.[113-116] However, their application in H_2 production

electrocatalysts is less explored, with only one example exploiting the S'_2NiS_2 metalloligand.[108, 110]

A

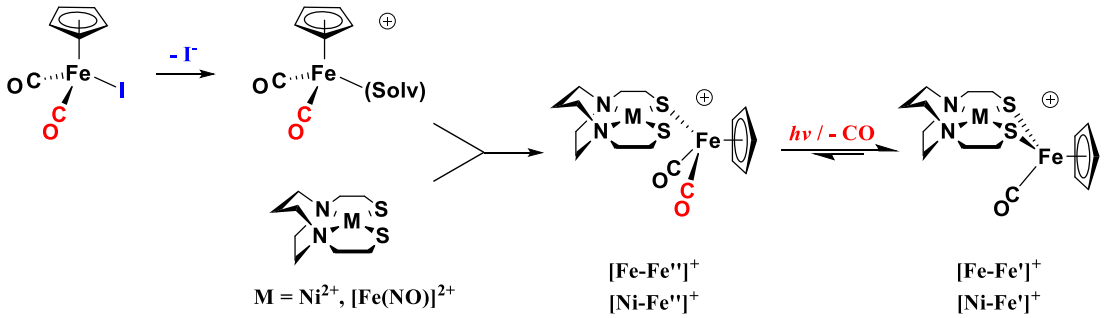

B **C** **D**

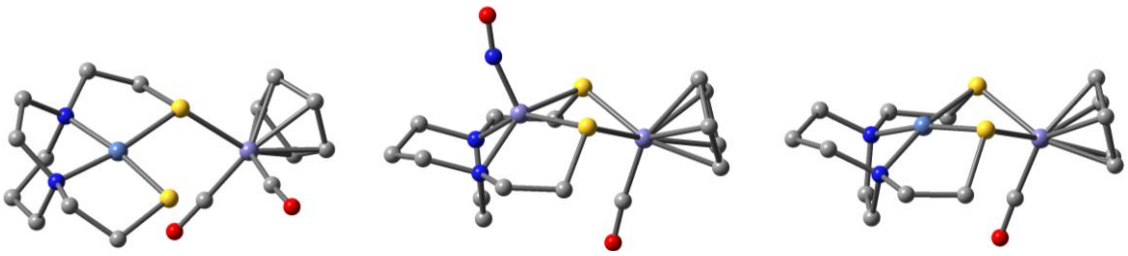

Figure III-1 The synthetic route and relevant structures. **A**) The synthetic route to dicarbonyl species **[Fe-Fe'']**$^+$, **[Ni-Fe'']**$^+$ and moncarbonyl species **[Fe-Fe']**$^+$, **[Ni-Fe']**$^+$. The crystal structures of **B**) **[Ni-Fe"]**$^+$, **C**) **[Fe-Fe']**$^+$, and **D**) **[Ni-Fe']**$^+$ with omission of counter ion(s). Note: the product of I^- removal by $AgBF_4$ in panel A has a labile ligand site, occupied by a solvent molecule or a weakly ligated BF_4^-.

In the work described within this chapter, the fragment $Fe(CO)Cp^+$, is introduced to our mature $M(N_2S_2)$ (M = $[Fe(NO)]^{2+}$ and Ni^{2+}) metalloligand platform, generating the bimetallics **[Fe-Fe']**$^+$ and **[Ni-Fe']**$^+$ as presented in Figure III-1. Experimental and

computational work was done to primarily address their activities as H_2-producing electro-catalysts with emphasis on the electron / proton up-take order and the functional analysis of the two metal centers and the hemi-labile ligand; *i.e.*, how do reaction centers appear and work throughout the catalytic cycles.

Summary of experiments

Synthesis and characterization. The bimetallics are synthesized by combining the metallodithiolate ligand $M(N_2S_2)$ ($M = Ni^{2+}$ and $[Fe(NO)]^{2+}$) and the precursor of the monometallic receiver unit $CpFe(CO)_2I$, whose iodide is removed *in situ* by $AgBF_4$, Figure III-1A. The combination generates dicarbonyl intermediates **[Fe-Fe'']**$^+$ and **[Ni-Fe'']**$^+$, the latter of which was separated and subjected to X-ray diffraction analysis, Figure III-1B. UV photolysis-induced CO removal, reversible under CO atmosphere, further generates the bidentate, monocarbonyl species **[Fe-Fe']**$^+$ and **[Ni-Fe']**$^+$, for which crystal structures are available, Figure III-1C and D. The bimetallics **[Fe-Fe']**$^+$ and **[Ni-Fe']**$^+$ feature a butterfly-shaped M_2S_2 core with two transition metals chelated by the dithiolate hinge. However, the M-M' distance (3.203 and 3.016 Å for **[Fe-Fe']**$^+$ and **[Ni-Fe']**$^+$ respectively) is out of the range for a metal-metal bond. The **[Fe-Fe']**$^+$ is paramagnetic ($S = 1/2$), with the unpaired electron inherited from the metalloligand $Fe(NO)N_2S_2$, and has an E-F electron count[117] of $\{FeNO\}^7$.[118-119] Paramagnetism is evidenced by the isotropic g value of 2.04 with hyperfine coupling constant of 15.3 G from ^{14}N of the nitrosyl in the room-temperature EPR spectrum, resembling the signal of the free metalloligand.[120] The **[Ni-Fe']**$^+$ complex is diamagnetic.

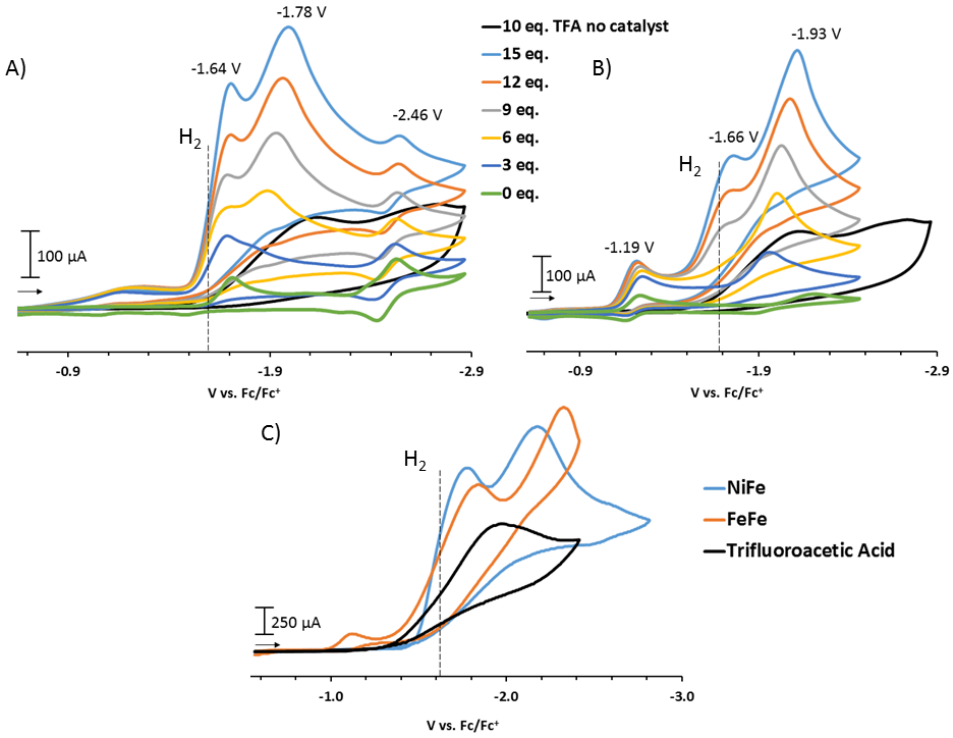

Figure III-2 CV scans of the catalysts with and without the presence of trifluoroacetic acid (TFA). CV of 2 mM **A**) **[Ni-Fe']**$^+$ and **B**) **[Fe-Fe']**$^+$ under Ar in CH_3CN solutions containing 0.1 M [^{t}Bu$_4$N][PF_6] as supporting electrolyte with addition of equivalents of trifluoroacetic acid. **C**) An overlay of **[Ni-Fe']**$^+$ and **[Fe-Fe']**$^+$ in the presence of 50 equivalents of TFA as well as 50 equivalents of TFA in the absence of either catalyst. The dotted line denotes the potential applied during bulk electrolysis, -1.56 V.

Electrochemistry. Two reductions were revealed by the CV scans of **[Fe-Fe']**$^+$ and **[Ni-Fe']**$^+$ (in MeCN), initiated in cathodic direction, Figure III-2A and B. The first, quasi-reversible event of **[Fe-Fe']**$^+$ at -1.19V is assigned to the {Fe(NO)}$^{7/8}$ redox couple. The second, more negative, irreversible reduction event is assigned to the Fe'$^{II/I}$ couple, and its

irreversibility is related to a reduction-induced S-Fe' bond breakage. In contrast, the first, irreversible event of **[Ni-Fe']**$^{+}$ at -1.64 V is initially assigned to the $Ni^{II/I}$ couple but is accompanied by an immediate intramolecular electron transfer to the $Fe'^{II/I}$ couple along with the concomitant S-Fe' bond cleavage, which is further addressed in the computational section below. After the structural rearrangement in the first irreversible event, the second reduction event is likely on the now restored $Ni^{II/I}$ couple, again. In both complexes, the $Fe(CO)Cp^{+}$ moieties bound to the N_2S_2 metalloligands act as electron withdrawers, depleting the electron densities of its attached metalloligand. A positive shift of the reduction event is observed in these bimetallic complexes, compared to the corresponding free metalloligands.[119, 121]

The CV scans of **[Fe-Fe']**$^{+}$ and **[Ni-Fe']**$^{+}$ in the presence of increasing equivalents of trifluoracetic acid (TFA) show significant current enhancement of the above-mentioned events. The current enhancement of the first reduction event at -1.19 V of **[Fe-Fe']**$^{+}$ is saturated after the addition of 12 equivalents of TFA, Figure III-2B and a new peak appears and grows at ~ -1.66 V only with more than 6 equivalents of TFA. In contrast, the current continues to grow for the first reduction event of **[Ni-Fe']**$^{+}$ at -1.64 V with additional equivalents of TFA, Figure III-2A.

The current enhancement at ~ -1.6 V is attributed to electro-catalytic H_2 production for both electrocatalysts, verified by H_2 collection and analysis, in addition to the spontaneous reduction of TFA. More detailed mechanistic analysis is given in the computational section below. Their inherent catalytic capacities were tested with 50 equivalents of FTA, Figure III-2C, with the turnover frequencies quantified to 69 s^{-1} and

52 s^{-1}, and overpotentials of 938 and 942 mv for **[Fe-Fe']**$^+$ and **[Ni-Fe']**$^+$, respectively, by the published approach.[122-125] The experimental barriers were estimated to 14.9 and 15.1 kcal/mol at 298.15 K by Eyring equation accordingly. With d_1-TFA, TOFs show a normal kinetic isotope effect. The ratio (k_H/k_D) are 1.46 and 1.56, respectively for **[Fe-Fe']**$^+$ and **[Ni-Fe']**$^+$. These numbers, relative close to 1, indicate the possible involvement a metal-hydride throughout the mechanism.[126 127]

Long-term (30 min) bulk electrolysis was applied to both catalysts with 50 equivalents of TFA, generating enough H_2 for quantitative analysis by GC. Under the set-up used, the complex **[Fe-Fe']**$^+$ has a turn-over number (TON) of 0.26 ± 0.01 with a Faradaic efficiency of 96.0 ± 2.9 % for H_2 production while the TON of **[Ni-Fe']**$^+$ is 0.33 ± 0.02 with a Faradaic efficiency of 77.2 ± 7.9 %.

Computational investigation: assignment of redox events and mechanistic studies

General strategy. The complexities of the cyclic voltammograms of the **[Ni-Fe']**$^+$ or **[Fe-Fe']**$^+$ complexes in the presence of added acid, which indicate the existence of protonated and/or rearranged species, stimulated computational studies as complements to electrocatalytic proton reduction studies. A minimum of two chemical steps (C steps, *i.e.* protonation) and two electrochemical steps (E steps, *i.e.* reduction) is required to produce H_2 from protons and electrons. The exact order of C and E steps depends on the pK_a of the acid vs. catalyst and the redox potential of the catalyst, respectively; they often take place in an alternating order to prevent the accumulation of charges.[128] To computationally construct the E and C steps in catalytic cycles, structures of the precursor complexes from

x-ray diffraction were compared to the calculated structures as validity checks; the redox potentials (E^0 vs. $Fc^{+/0}$) and relative acidities ($\Delta pK_a = pK_a\ (CatH) - pK_a\ (CF_3COOH)$) of components were predicted by calculations. Alternative sites for location of the added protons were carefully examined to determine which sites were lowest in energy. The functional B3LYP[24] was used for this project.

Computational approaches to electrocatalytic proton reduction mechanisms have become fairly standard,[52, 128-129] especially for biomimetics of the hydrogenase active sites. From protein crystallography the features of the protein ensconced molecular catalysts and second coordination spheres are readily apparent but their roles are just beginning to be firmly established.[36] Hence, our starting points for the predicted mechanisms lie in paths deemed reasonable for the biocatalysts and for previous studies of biomimics; structures are accepted or rejected according to comparative energies (E^0 and pK_a) and activation barriers between structures. The bimetallic constitution of our complexes, **[Fe-Fe']**$^+$ and **[Ni-Fe']**$^+$ enables them to buffer electrons, with additional stabilization from the non-innocent ligands, particularly NO in the case of **[Fe-Fe']**$^+$.[120] At some point, typically after reduction(s), a complex must be able to accept a proton, convert it into a hydride on the metal, be poised to react with an additional proton, located on some basic site, to yield H_2. Our model complexes, however, lack an obvious built-in pendant base to serve as a proton reservoir, a role played by the bridgehead amine in [FeFe]-Hydrogenase, [36, 52, 54-56] or a terminal thiolate in the [NiFe]-Hydrogenase active site.[36, 102-103] Instead, the hemi-labile bridging thiolates on **[Fe-Fe']**$^+$ and **[Ni-Fe']**$^+$ may dissociate one of two Fe'-S bonds; the veracity of such a mono-dentate S-bridging species is supported by the isolated **[Ni-**

Fe"]$^{+}$ shown in Scheme 1. Such dissociation creates reactive sites both on S and Fe'; *i.e.*, a Lewis acid-base pair that can be used as proton and hydride storage depots is generated. Interestingly, the possibility of conversion of a bridging thiolate into an available proton base was inspired by the early theoretical studies of the [FeFe]-Hydrogenase.[52-53] The advent of semi-synthetic approaches to biohybrids in recent years that unambiguously identified a bridgehead amine in the S to S linker of the diiron unit in [FeFe]-Hydrogenase has established the pivotal role of this pendant base in proton transfer, thus negating the requirement for Fe-S bond cleavage in such functionalized dithiolates.[43, 45-47]

The HER mechanism on [Fe-Fe']$^{+}$**.** Figures 3-3 and 3-4 display the calculated electrocatalytic cycles for H_2 production with **[Fe-Fe']**$^{+}$ and **[Ni-Fe']**$^{+}$, respectively, as electrocatalysts. A description of the former is as follows. In the absence of added acid, the CV scans of **[Fe-Fe']**$^{+}$ show two reduction events; the first quasi-reversible one was calculated to be -1.11 V (exp. -1.19V) and is assigned to the Fe(NO) unit, i.e., the redox couple $\{Fe(NO)\}^{7/8}$-Fe'^{II}. Such an assignment was confirmed by the IR shifts of the diatomic ligands (exp.: -57 and -23 cm^{-1}; calc'd -84 and -31 for NO and CO respectively). The resulting neutral **Fe-Fe'** has a linear triplet $\{Fe(NO)\}^{8}$ moiety, formed by high spin Fe^{II} antiferromagnetically coupled to high-spin NO^{-}.[120, 130] It may be further reduced irreversibly, calculated at - 1.99 V (exp. - 2.07 V), to **[Fe-Fe']**$^{-}$, in which one S-Fe' bond dissociates to accommodate the added electron on Fe' with a final redox level of $\{Fe(NO)\}^{8}$-Fe'^{I}.

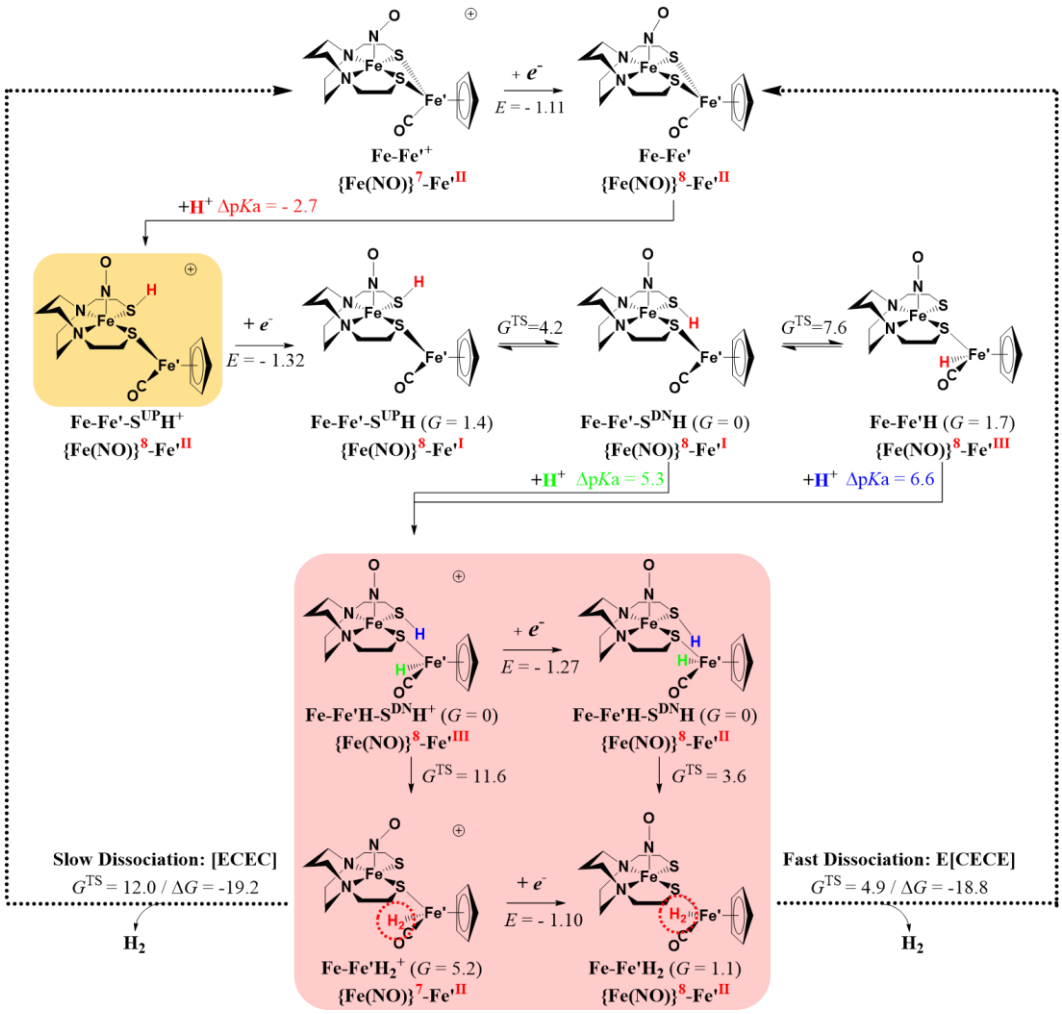

Figure III-3 The calculated electrocatalytic cycles for H_2 production on **[Fe-Fe']$^+$** in the presence of TFA. The relative Gibbs free energies are provided in kcal/mol and the reference point (G = 0) resets after every reduction or protonation. The redox potentials (E) are reported in V with reference to the standard redox couple $Fc^{+/0}$ and the relative acidities (ΔpK_a) are reported with reference to TFA. Note: superscripts DN and UP on S refer to the positioning of the proton in S-protonated species.

In the presence of TFA the first reduction event at -1.19 V in the cyclic voltammogram was observed to increase in current without shifting position. This behavior is explained by the reaction of TFA with the reduced **Fe-Fe'** state and its depletion, thus enhancing diffusion of **[Fe-Fe']**$^+$ into the double layer at the electrode. By calculations, the thiolate S was determined to be the optimal protonation site. Other possibilities were considered, including the iron-bound NO which would produce the HNO ligand. It was found however to be thermodynamically less likely and also non-productive for subsequent H_2 formation as a metal-hydride is needed for the H^+/H^- coupling. Upon protonation on sulfur the bond cleavage at Fe'-S immediately follows, stabilizing the system by 3.7 kcal/mol. The ΔpK_a (vs. TFA) values for ring-closed (**[Fe-Fe'-S*H]**$^+$) and ring-opened (**[Fe-Fe'-S^{UP}H]**$^+$) sulfur-protonated species are -5.6 and -2.7, respectively, indicating slightly unfavorable thermodynamic processes. Thus, excess acid is needed to drive the protonation of **Fe-Fe'**, explaining why the observed saturation of current enhancement requires multiple equivalents (> 12 equiv.) of added acid and rules out the possibility of an immediate second protonation on **[Fe-Fe'-S^{UP}H]**$^+$ (to **[Fe-Fe'H-S^{DN}H]**$^{2+}$, ΔpK_a = -14.3). Despite the increase in current response, the electrochemical event at -1.11 V (-1.19 V exp.) is not catalytic as this reduction potential is insufficient (*vide infra*) to pass a second electron and close the catalytic cycle.

A second current enhancement, which appears in CV scans with added acid at -1.66 V (shifted by 0.41 V from - 2.07 V in the absence of acid), suggests reactions of new species, **[Fe-Fe'-S^{UP}H]**$^+$, generated by protonation. One should be reminded that the production of **[Fe-Fe'-S^{UP}H]**$^+$ is energetically unfavorable such that the reduction event

of **[Fe-Fe'-S^{UP}H]$^+$** observed at -1.66 V becomes dominant only with the presence of more than 6 equiv. of TFA. The reduction of **[Fe-Fe'-S^{UP}H]$^+$** has a calculated potential of -1.32 V, changing the Fe^{II} of Fe' to Fe^{I} , a redox state capable of converting a proton into a hydride. The direct product of reduction, **Fe-Fe'-S^{UP}H** (G =1.4 kcal/mol) may transform into a hydride-bearing species **Fe-Fe'H** (G =1.7 kcal/mol) via the S-H inversion species **Fe-Fe'-S^{DN}H** (G = 0 kcal/mol) traversing two low-lying transition states (G = 4.2 and 7.6 kcal/mol). The **Fe-Fe'H** species is at the $\{Fe(NO)\}^8$-Fe'^{III} redox level as the electrons forming the iron-hydride are donated by Fe^{I} of the reduced Fe'.

There are two pathways shown in Figure III-3 for addition of the second proton. Although **Fe-Fe'-S^{DN}H** is the dominant species, the next protonation step, either on S of **Fe-Fe'H** or on Fe' of **Fe-Fe'-S^{DN}H**, produces the same thiol-hydride, **[Fe-Fe'H-S^{DN}H]$^+$** and both protonations are thermodynamically favored, with ΔpK_a values of 6.6 or 5.3 kcal/mol, respectively. The spatial positioning of the hydride and the proton on **[Fe-Fe'H-S^{DN}H]$^+$** allows the coupling reaction over a barrier of G = 11.6 kcal/mol. The resulting H_2 σ-complex **[Fe-Fe'H$_2$]$^+$** then overcomes another barrier at G = 12.0 kcal/mol to dissociate H_2 and to regenerate the catalyst **[Fe-Fe']$^+$**. This catalyst cycle thus closes with an [ECEC] mechanism. This mechanism uses the thiolate sulfur as a proton relay. One may argue TFA may directly deliver the proton to the hydride of **Fe-FeH'** to accomplish an intermolecular coupling to form **[Fe-FeH$_2$]$^+$**, skipping the intermediate **[Fe-FeH-S^{DN}H']$^+$**. The relatively high barrier at 16.2 kcal/mol renders this possibility less likely. In contrast the delivery of proton into the sulfur open site only incurs a negligible barrier.

Alternatively, **[Fe-Fe'H-S^{DN}H]$^+$** may accept a third electron at a redox potential of - 1.27 V and the highest reaction barrier for H_2 formation dramatically drops to 4.9 kcal/mol. In this case the reduced **Fe-Fe'** is regenerated instead of **[Fe-Fe']$^+$** and closes an E[CECE] working catalytic cycle, in which the first reduction event essentially serves as an activation step. According to the calculations, the current enhancement associated with the second reduction event at -1.32 V (calc'd; observed at -1.66 V) is considered to be catalytic and productive in either the slow or fast catalytic cycle as subsequent reduction events are all calculated to be less negative than -1.32 V.

The HER mechanism on [Ni-Fe']$^+$. The nickel species **[Ni-Fe']$^+$** has mechanisms similar to those of **[Fe-Fe']$^+$** with a few exceptions, Figure III-4. The first reduction of **[Ni-Fe']$^+$** is initially localized on the NiN_2S_2 moiety with its four-membered Ni(μ-SR)$_2$Fe' unit intact as was that of **Fe-Fe'**. However, the four-coordinate nickel lacks the electronic flexibility of Fe(NO) in **Fe-Fe'** and can only accommodate the added electron on nickel's highly destabilized antibonding d_{x2-y2} orbital, achieving an oxidation state of Ni^{I}-Fe'^{II} in **Ni-Fe'***. As a result the calculated redox potential rises significantly to -2.00 V (exp. -1.64 V). Following the reduction, one S-Fe bond of the Ni(μ-SR)$_2$Fe' core breaks to open the Ni-S$_2$-Fe' ring. The electron previously added to the nickel is concomitantly transferred to the unsaturated (16-e^-) Fe' with bond cleavage, bringing the electron counts back to a 16-e^- Ni^{II} and a 17-e^- Fe^{I}. This arrangement stabilizes the ring-opened species **Ni-Fe'** by 1.0 kcal/mol, accounting for observed irreversibility of the CV event. The experimental IR shift, -157 cm^{-1}, upon the reduction of **[Ni-Fe']$^+$**, confirms **Fe-Fe'** (calc'd shift: -127 cm^{-1}) is the reduced product, rather than **Fe-Fe'*** (calc'd shift: -43 cm^{-1}).

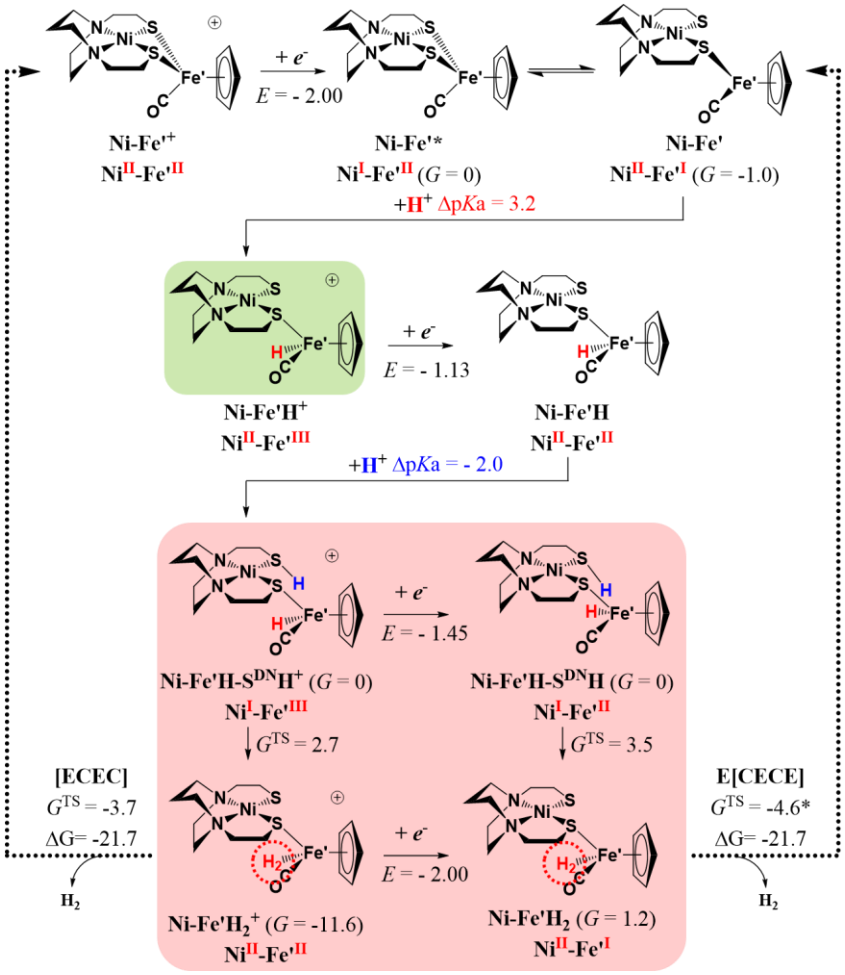

Figure III-4 The calculated electrocatalytic cycles for H_2 production on **[Ni-Fe']**$^+$ in the presence of TFA. See caption of Figure III-3 for additional description. The Gibbs free energy of the barrier between **Ni-Fe'H$_2$** and **Ni-Fe'**, G = -4.6 kcal/mol, as marked with an asterisk, is lower than that of **Ni-Fe'H$_2$**, G = 1.2 kcal/mol. This is caused by the preference of solvation correction over the transition state. This transition may be accepted as barrierless.

In the absence of acid, following the ring-opening process and intramolecular charge transfer, the successive reduction on **Ni-Fe'** puts the second electron again within the $Ni^{II/I}$ couple. The calculations also affirm that the first redox potential is more negative than that of any subsequent steps in the catalytic cycles in the presence of TFA (Figure III-4), so that the CV current enhancement at -1.64 V is acknowledged as catalytic. The follow-up protonation on **Ni-Fe'** goes directly to the reduced Fe' rather than S as the Fe^{I} has sufficient electron density to convert the proton into a Fe^{III}-hydride. The next steps are similar to those of **[Fe-Fe']**$^{+}$ in Figure III-3. The **[Ni-Fe']**$^{+}$ may also have two working catalytic cycles, either [ECEC] or E[CECE] depending on the occurrence of a non-mandatory, third reduction event.

The homoconjugation of TFA,[122, 131] *i.e.*, the stabilization of the conjugate base TFA^{-} by another molecule of H-TFA, was evaluated by calculations to enhance the the acidity by - 5.6 pK_a units (exp. -3.9)[122] on standard conditions. The acidity increase, though less significant when the acid concentration is low, may further facilitate these protonation processes outlined in Figure III-3 and 3-4 at the cost of faster depletion of the available acid on the electrode surface. However, it may not be able to activate another route. An immediate second protonation requires a much stronger acid, *vide supra*.

By proceeding along the predicted mechanistic pathway, the mono-dentate species, **[Ni-Fe"]**$^{+}$, breaks its single Fe-S bond upon reduction and the complex decomposes, as experimentally observed. The cleaved fragment, the •$FeCp(CO)_2$ radical, is also catalytically active for H_2 production before its fast deactivation by dimerization.[132]

Discussion

This work provides a paradigm for deconvoluting electrocatalytic proton-reduction mechanisms in dithiolate bridged bimetallics. Salient points to be made regarding the mechanistic features of the two $[MN_2S_2{\cdot}CpFe(CO)]^+$ electrocatalysts are as follows:

The initial electron uptake is at the M in the N_2S_2 pocket, rather than the $CpFe'(CO)^+$, for both M = Ni^{II} and $\{[Fe(NO)\}^7$; the latter however presents a softer, delocalized landing for the electron, without permitting subsequent Fe-H formation, as the iron is not adequately basic. Another key difference lies in the fact that the added electron is stored on the $\{[Fe(NO)\}^8$ unit (within the $Fe(NO)N_2S_2$ metallo-ligand) throughout the catalytic cycle rendering that unit a "redox-active, spectator ligand"[133] to the reactive center, the CpFe(CO) unit, in the preferred E[CECE] path. In contrast, the first-formed $Ni^IN_2S_2$ readily transfers its electron to Fe', with Ni^{II}-(μ-SR)$_2$-Fe'^I ring opening in advance of protonation. Thus, the Ni^{II} in the mono-dentate NiN_2S_2 metalloligand cannot accept a proton to form a Ni-H bond resembling the recent NMR characterized Ni-bound hydride in a Ni-R model, which contains a non-innocent ligand with Ni to buffer the electron.[134] Besides, Fe is also protected from the proton by open sites on S and on reduced Fe'.

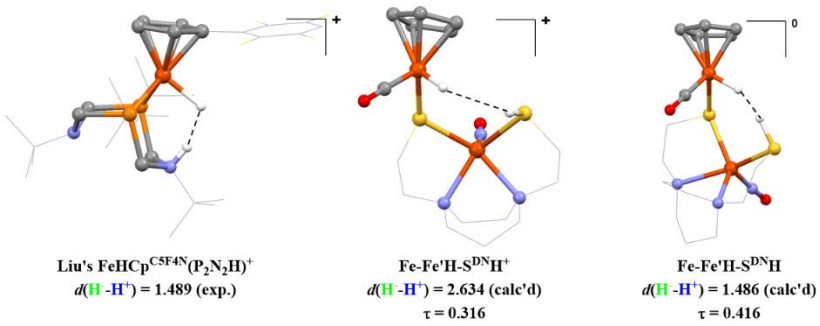

Figure III-5 Species featuring proximate proton-hydride pairs and the comparisons of H^+-H^- distances. The τ value, a measure of square pyramid (τ = 0) vs. trigonal bipyramid (τ = 1) geometry in the $Fe(NO)N_2S_2$ unit.

The hemi-lability of the MN_2S_2 metallo-ligand, necessary for producing an open site on the active iron of the CpFe' unit (a site that is occupied by CO in the **[Ni-Fe"]**$^+$ congener or procatalyst**)**, as well as an available S-base site, is facilitated by reduction of the dithiolate bridged bimetallic. A further role for this hemi-lability is displayed in the mono-dentate bridging thiolate bound to the Fe'^{III}-hydride in **[Fe-Fe'H-S^{DN}H]**$^+$. The Fe'^{III} with a formal electron count of 17 is able to accept partial donation from an available π-donor pair on S, serving as a σ+π ligand, while Fe'^{II} in **[Fe-Fe'H-S^{DN}H]**$^+$ is completely saturated and the S is merely a σ-donating ligand. This additional π bonding in the oxidized **[Fe-Fe'H-S^{DN}H]**$^+$ species is exemplified by its short Fe'-S bond distance at 2.230 Å that elongates to 2.342 Å upon reduction to the **Fe-Fe'H-S^{DN}H** species.

The H_2 evolution from the di-protonated, doubly or triply reduced species requires optimally oriented protonated thiol and iron hydride. In this regard it is instructive to compare H^+---H^- distances in our calculated intermediate thiol-hydrides with experimental

data from the doubly protonated $P_2N_2FeCpR(CO)$ complex of Liu, *et al.*,[100] Figure III-5, finding concurrence in the reduced **Fe-Fe'H-S^{DN}H** form (1.486Å) with that found in the amine pendant base complex (1.489 Å). Note that reduction of **[Fe-Fe'H-S^{DN}H]$^+$** shortens the H^+---H^- distance from 2.634Å to 1.486Å via structural shifts in the $Fe(NO)N_2S(SH)$ metalloligand, involving both a rotation around the Fe'-S bond as well as a small change in the τ parameter[135] that defines the extent of square pyramid vs. trigonal bipyramid character in the $Fe(NO)N_2S(SH)$ unit. These changes push the proton-hydride pair into a close position, creating an early transition state according to Hammond's postulate,[136] amenable for H_2 elimination via the E[CECE], low barrier path. In contrast at 2.634Å the H^+/H^- coupling following the [ECEC] mechanistic path must surmount a much higher barrier. Note that the H^+---H^- coupling distance in the Fan and Hall calculated mechanism for proton reduction in the [FeFe]-Hydrogenase active site is 1.472Å, remarkably consistent with the experimental value from structure I, and the calculated value (1.486Å) for our reduced diprotonated intermediate **Fe-Fe'H-S^{DN}H** in Figure III-5.[36] Notably, the proton/hydride pair recently characterized in the Ni-R state of the [NiFe]-Hydrogenase active site is at 2.45Å,[102] a distance related to the intermediate in our slow route for H_2 production, and perhaps consistent with the [NiFe]-Hydrogenase enzyme's bias towards H_2 uptake and oxidation rather than production.

In conclusion, the well-studied P_2N_2 ligand of Dubois, et al.[94] has control of optimal proton placement via the chair/boat interconversion of the six-membered FeP_2C_2N cyclohexane-like ring described in Figure III-5,[100] a feature that was exploited in the design and development of further generations of the $Ni(P_2N_2)_2$ catalyst(s) and presaged

by Nature's azadithiolate bidentate bridging ligand in the [FeFe]-Hydrogenase active site.[36] The heterobimetallics explored herein demonstrate the possibility for very stable bidentate ligands based on metallodithiolates (a metal-tamed S-donor or Nature's version of a phosphine P-donor) that respond to an electrochemical event by switching a coordinate covalent bond into a Lewis acid-base pair and concomitantly placing a proton and hydride within an optimal coupling distance. Easily accessible molecular motions and coordination sphere distortions are available to render the tethered thiolate into a pendant base of greater activity for proton delivery to the metal-hydride. The opportunities for tuning catalysts according to this approach lie both on the metal responsible for the hydride activity and, as we have also shown, the metal that holds and orients the pendant base. Our future plans are to optimize the catalysts via the bidentate S-M-S angle and to pursue experimental evidence for the thiol-hydride pair.

CHAPTER IV

LIGANDS IN ACTION: A COMPUTATIONAL STUDY OF THE INTERPLAY OF HEMI-LABILITY AND REDOX-ACTIVITY IN MODELS OF HYDROGENASE ACTIVE SITES

Introduction

Dihydrogen is currently a candidate for energy storage to alleviate problems from electricity produced intermittently by photovoltaic cells or wind turbines.[137] Hydrogenases[36, 52] are Nature's masterpiece enzymes for H_2 production and its use as an energy vector or chemical substrate; they use abundant base metals in their catalytic active sites. An array of enzymatic and spectroscopic probes, crowned by modern protein X-ray diffraction technology,[36, 138] provide opportunities for structure-function analysis of the intricate Hydrogenase active site molecular machinery. Strategically placed acid and base functionalities in the active site guide and store protons and electrons for their efficient processing into H_2, or the reverse, H_2 oxidation, reaction. Currently favored mechanisms are based on earlier proposals from computational modeling of [FeFe]-[52-56] and [NiFe]-Hydrogenase.[52, 104, 139-141]

This chapter is primarily reproduced with permission from the accepted manuscript: Ding, S.; Ghosh, P.; Darensbourg, M. Y.; Hall, M. B. *Proc. Natl. Acad. Sci. U.S.A.*, **2017**, 10.1073/pnas.1710475114. Some content of this chapter is taken from two other manuscripts with permission: Hsieh, C.-H.; Ding, S.; Erdem, O. F.; Crouthers, D. J.; Liu, T.; McCrory, C. C. L.; Lubitz, W.; Popescu, C. V.; Reibenspies, J. H.; Hall, M. B.; Darensbourg, M. Y. *Nat. Commun.* **2014,** *5*, 3684. Ghosh, P.; Ding, S.; Chupik, R. B.; Hsieh, C.-H.; Bhuvanesh, N.; Hall, M. B.; Darensbourg, M. Y. *Chem. Sci.*, **2017**, DOI: 10.1039/C7SC03378H, to which two manuscripts the author of this dissertation contributed the computational studies.

In the active site of [FeFe]-Hydrogenase (Figure IV-1A), a diiron unit takes up protons via an amine base strategically placed to hold and transfer that proton to the available open site on a reduced iron to create an iron-hydride, whose existence was recently spectroscopically confirmed;[48, 51] the amine then accepts another proton.[50] Importantly, the H^+/H^- components of H_2 are positioned within a convenient distance for coupling over a low barrier (Figure IV-1A).[54] A similar strategy appears to be operative in the [NiFe]-Hydrogenase active site; whether a guanidine base from R509,[142] which hovers over the NiFe core and is required for full enzyme activity, is the proton delivery agent itself, or a cysteine (C546) thiolate sulfur, bound to the Ni,[143] facilitates the ultimate H^+/H^- coupling, is not firmly established. Structural evidence from recent high resolution X-ray diffraction indicates the arrangement shown in Figure IV-1B, finding a thiol-proton nearby a hydride accommodated in a bridge position between Ni and Fe,[143] remarkably predicted by DFT calculations two decades ago.[104, 139] Thus, in both hydrogenases the hydride-protonation mechanism (**HP**, *a.k.a.* heterolytic coupling) accounts for H_2 production.[52]

Interestingly, while the major function of nitrogenase (N_2-ase) is nitrogen fixation, it is known that a molecule of H_2 is an obligatory side product as one molecule of N_2 is fixed into NH_3.[144] Four equivalents of electrons and four protons are required before the H_2 is released and the N_2 is initially fixed;[145-146] this is Nature's creative mechanism whereby the N_2-ase active site can build up sufficient reduction power, stored as hydrides within the expanded Fe-S cluster, to reductively activate the strong triple bond of N_2. Hoffman, Seefeldt, Dean, *et al.* proposed that such H_2 release goes through a reductive

elimination mechanism (**RE**, *a.k.a.* homolytic coupling of two H•) from two hydrides, thus leaving two electrons localized within the cluster to fix N_2 (Figure IV-1C).[147-149] [Note: The **HP** mechanism is also applicable to the H_2 production on N_2-ase in the absence of N_2, nevertheless the capacity for N_2 fixation requires the **RE** mechanism.] [146]

The questions crucial to the development of molecular electrocatalysts are 1) what conditions lead to the preference for **RE** *vs.* **HP** mechanisms for H_2 production assisted by Fe-S clusters, and 2) can these conditions be replicated in small biomimetics of these active sites, using alternate redox active ligands.

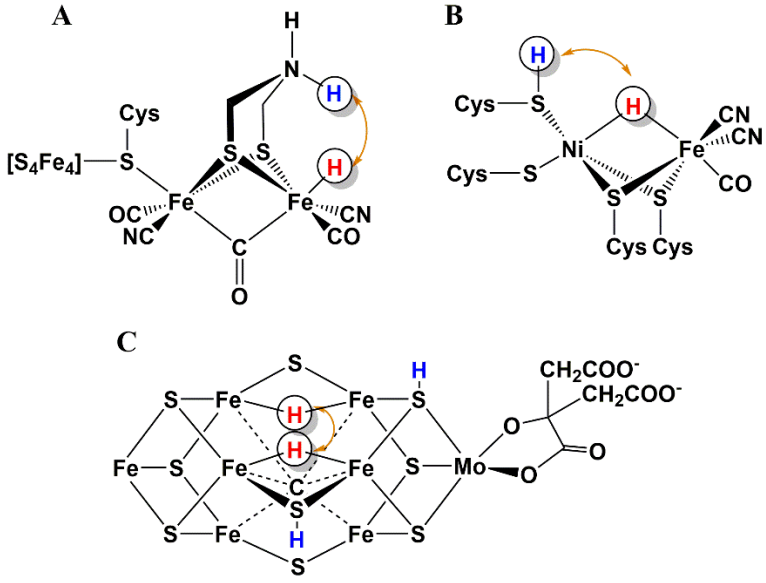

Figure IV-1 The active sites of enzymes related to H_2 production. **A**) [FeFe]-hydrogenase (H_{hyd} state), **B**) [NiFe]-hydrogenase (Ni-R state) and **C**) the H_2-producing intermediate of nitrogenase (E_4/H_4 state that fixes N_2 following **RE** of H_2), displayed with bound H and indicating coupling routes. Charges are not explicitly assigned. Hydrides and protons are colored red and blue, respectively.

Synthetic analogues. The organometallic characteristics of the hydrogenase active sites have led to a rich area of synthetic chemistry aiming to reproduce core features and delineate structure/function relationships in bimetallic complexes that are electrocatalysts for H_2 production.[36, 150-151] Even without the enzymatic intricate positioning of proton and electron relay functions, many model complexes show positive responses to appropriate E/C conditions (E = electron addition; C = proton addition). Developed from systematic alterations in such bimetallics is a series shown in Figure IV-2 of minimal synthetic analogues containing dithiolate-bridged Fe-Fe or Ni-Fe cores derived from MN_2S_2 metalloligands; all are at least modest electrocatalysts for proton reduction/hydrogen production. The MN_2S_2 metalloligand[106, 152] provides a variable platform according to the carbon connectors within the N_2S_2 tetradentate ligand, as well as the M itself. The M, as Ni^{2+}, or particularly in the form of $[Fe(NO)]^{2+}$ and $[Co(NO)]^{2+}$, may tune the donor properties of the thiolates. The nitrosyl, NO, attached to metal, facilitates redox events because it features π^* orbitals close in energy to a metal's *d* orbitals. The energetic proximity enables orbital admixtures so that the $M(NO)_x$ moiety shares the electrons during redox activities while the delocalization enables the electrons to flow between M and NO easily. Such orbital mixing creates electronic flexibility in the $M(NO)_x$ unit during redox processes, but it prohibits the clear assignments of electrons; this ambiguity was defined to be "non-innocence" by Jørgensen.[153] The Enemark–Feltham (E-F) electron count (the metal *d* electrons plus NO π^* electrons)[117] was introduced to circumvent the partitioning of electrons between the metal and the nitrosyl(s). The receiver groups, *i.e.*,

the second metal (all are iron in our series) bound to the metalloligand MN_2S_2, may also be modulated to test and verify the results via structure-function analysis.

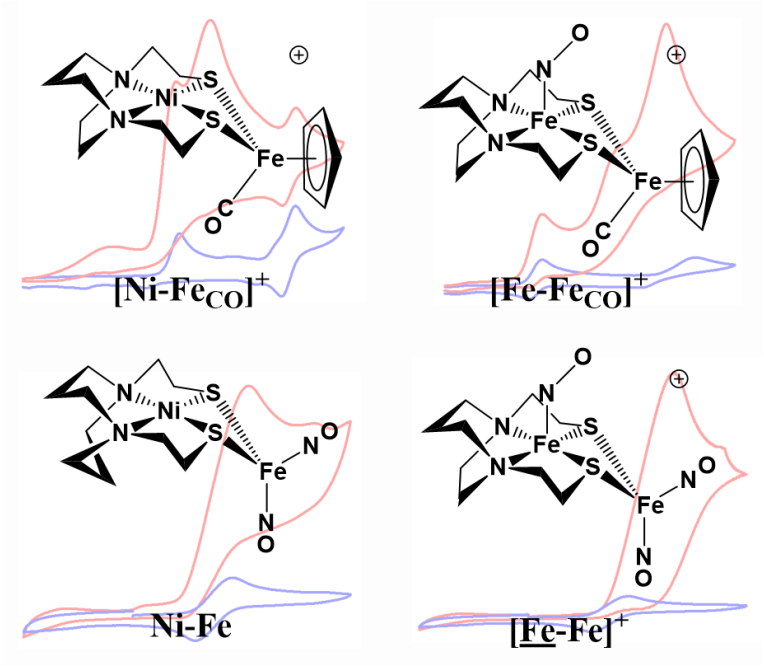

Figure IV-2 Structural representations of electrocatalysts for proton reduction: **[Ni-Fe$_{CO}$]$^+$**, **[Fe-Fe$_{CO}$]$^+$**,[154] **Ni-Fe**,[155] **[Fe-Fe]$^+$**.[156] The background of each species shows the cyclic voltammograms before (blue) and after (red) the addition of acid. The current enhancement in the red scan is determined to relate to H_2 production. For Ni-Fe, the CV's were obtained from dimeric **[Ni-Fe]$_2^{2+}$** which was calculated to dissociate into **[Ni-Fe]$^+$** in solution.

Notably, the hemi-lability, originally defined by Rauchfuss for P-O bidentate ligands,[157] of the metallodithiolate ligands, *i.e.*, their ability to dissociate one arm of the bidentate ligand while maintaining integrity of the bimetallic, was previously determined to contribute to the catalytic activity of complexes $[NiN_2S_2{\bullet}Fe(CO)Cp]^+$ (**[Ni-Fe$_{CO}$]$^+$**, Cp

= η^5-C_5H_5) and $[Fe(NO)N_2S_2•Fe(CO)Cp]^+$ (**[Fe-Feco]$^+$**), Figure IV-2.[154] The dissociation of one S-Fe(CO)Cp dative bond, cleaves the S-donor (Lewis base) and creates a metal open site (Lewis acid). If the components coexist within a convenient distance, the base and acid sites can be used to assist chemical reactions. *In fact, reaction-created Lewis acid-base pairs, such as this one, handle the hydrides and the protons, respectively, throughout the catalytic cycle, and account for the catalytic activity of bimetallic models which do not contain obvious build-in Lewis bases as proton shuttles*.[154] To stabilize the Lewis pair and to avoid the reinstatement of the dative bond, the pair is protected either by reduction of the Lewis acid or protonation on the Lewis base.

As shown in Figure IV-2, multiple electron-buffering NO ligands have been introduced into the N_2S_2-based bimetallic models, in attempts to reproduce the electron-buffering function of the $[Fe_4S_4]$ sub-cluster of [FeFe]-hydrogenase.[156, 158-160] The electronic flexibility introduced by NO raises the optimistic expectation that buffer ligands might convert first row transition metals that are 1-e^- catalysts into 2-e^- catalysts.[133, 161] Another prospect is that such electron-buffering ligands prevent dramatic structural reorganization or a change in coordination number during redox activities, consistent with the structurally constrained active sites of enzymes; in this way, they might contribute to catalyst longevity. Precisely how such delocalization might affect the mechanistic behavior or the individual steps/events of our models remains a question, and is the topic of this report.

In this work, two bimetallic complexes known to be electrocatalysts for proton reduction, $[Fe(NO)N_2S_2•Fe(NO)_2]^+$ (**[Fe-Fe]$^+$**)[156] and $[NiN_2S_2•Fe(NO)_2]$ (**Ni-Fe**),[155]

Figure IV-2, were investigated via computational chemistry as they contain potentially hemi-labile bridging thiolates as well as multiple electron-buffering NO ligands. (For clarity, the two irons in **[<u>Fe</u>-Fe]**$^+$ are differentiated as follows: the former **<u>Fe</u>** (underlined as shown in Figure IV-2) refers to the iron in $Fe(NO)N_2S_2$, and the latter **Fe** refers to the receiver unit, $Fe(NO)_2$.) These reaction mechanisms are compared to a previous theoretical study of **[Ni-Fe**$_{CO}$**]**$^+$ and **[Fe-Fe**$_{CO}$**]**$^+$.[154] The detailed computational mechanistic study described below delineates sequences of protonation and reduction of the bimetallics and the consequent coupling of electrons and protons to H_2. Importantly, the increased electron-buffering capacity conveyed by NO was found to influence the hemi-lability of the bridging thiolates and essentially change the working mechanism, especially controlling how H_2 is produced: hydride protonation, **HP,** or reductive elimination, **RE**. The connections between these two categories of actor ligands, *i.e.* hemi-labile and redox active ligands, provide insight to the question as to why Nature settled on the unique configurations that are found in redox-active, metalloenzyme active sites.

General computational methodology.

All structures were fully optimized with the crystal structures of **Ni-Fe**, **[<u>Fe</u>-Fe]**$^+$ and the reduced form **<u>Fe</u>-Fe**, imported as geometric starting points in the computational investigations by density functional theory (DFT), with the functional TPSS.[21] Natural bonding orbital (NBO), was applied to certain species for bonding analysis. Further details of the methodology and optimized coordinates are provided in the SI. The comparison of experimental and computed metric data for **Ni-Fe**, **[<u>Fe</u>-Fe]**$^+$ and **<u>Fe</u>-Fe**

validate the calculations. The bond distance error is generally less than 1% with the maximum less than 2%. One exception is the metal-metal distance as here there is no covalent bond between them. It is noteworthy that the oxidized state of **Ni-Fe**, crystallizes in the dimeric form $\mathbf{[Ni\text{-}Fe]_2^{2+}}$, but the dimer was calculated to dissociate in solution; hence the oxidized monomer $\mathbf{[Ni\text{-}Fe]^+}$ is considered as part of the catalytic cycle and its structure is calculated to be analogous to the reduced monomer **Ni-Fe**.

To stoichiometrically produce a molecule of H_2 on an electrocatalyst, two protons (*i.e.* chemical, C, steps) and two electrons (*i.e.* electrochemical, E, steps) must be introduced to the catalytic site. After each reduction, any immediate geometric reorganization is treated as part of the corresponding E step, *i.e.* a so-called "concerted"[162] E step. Generally, the E and C steps alternate in order to avoid the accumulation of like charges.[128, 154] The likelihood of each C step is evaluated in our computations by comparing the acidities of the protonated species vs. the proton provider $HOEt_2^+$ (as the acid is HBF_4•OEt_2 or $HOEt_2$•BF_4).[155-156] A positive ΔpK_a (ΔpK_a = pK_a(CatH) - $pK_a([HOEt_2]^+)$, indicates a thermodynamically favorable C step. Each E step has a calculated redox potential, $E_{1/2}$ (*vs.* Fc^+/Fc), which is compared to the experimentally applied electrode potential derived from cyclic voltammetry. As a result, the mechanisms will be presented as a set of equilibrium values ($G/\Delta G$, ΔpK_a and $E_{1/2}$) for evaluating the thermodynamic preference of each step. In addition, transition state barriers (G^{TS}) for steps other than proton and electron transfers are calculated to determine whether such a step is kinetically allowed. The geometric representations of species within these electrochemical cycles were based on the optimized structures.

The mechanisms for H_2 production by **Ni-Fe** and **Fe-Fe**, as described below, start in parallel with the previous study of **[Ni-Fe$_{CO}$]$^+$** and **[Fe-Fe$_{CO}$]$^+$**.[154] But the mechanisms soon diverge as the effects of multiple redox active NO ligands on **Ni-Fe** and **Fe-Fe** appear to redirect the protonations and the reductions to different recipients.

The divergent or convergent orientation of S lone pairs of MN_2S_2 metalloligand and influences on structures of $M(N_2S_2)$•M' heterobimetallics.

Traditional bidentate ligands such as diphosphines, diamines and bipyridyls have a single lone pair on each donor site. These lone pairs are positioned on orbitals originating from *sp*^{x}-hybridization and are highly directional.[163] They provide fixed binding orientations that match the coordination preference of traditional metal receivers.

In contrast, the binding between the sulfurs of the metallothiolate MN_2S_2 and an exogeneous metal are more geometrically flexible with different binding orbitals. Take NiN_2S_2 as an example, the NBO bonding analysis indicates the sulfur in the metalloligand is found to use *p* orbitals for bonding.[164-165] For example, in a free NiN_2S_2, 83% and 86% of the S contributions in the S-Ni bonds and S-C_α bonds (C_α and C_β refer to the C_2H_4 linker connecting S and N where C_α is directly bound to S, Figure IV-3A, are of *p* character, leaving one lone pair on a *p* orbital and another on an *s*-dominated orbital, on each S. As the receiver group, *i.e.* a $Fe(NO)_2$ unit, in our case, providing the monomer **Ni-Fe** and dimer **[Ni$_2$-Fe$_2$]$^{2+}$** (Figure IV-3C and D) adds to the NiN_2S_2 metalloligand, it may use either lobe of the *p* lone pair(s) for bonding; a diversity of structures results,[106, 152] and the

orientation of the bound receiver group is determined by the directionality of the *p* lone pair.

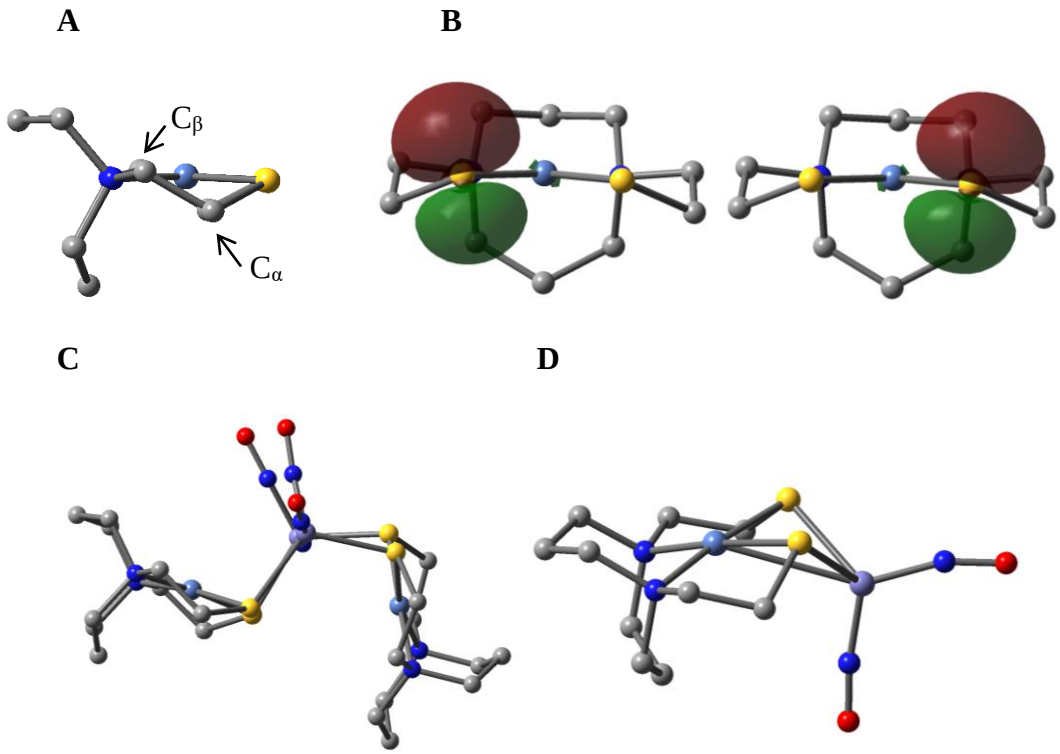

Figure IV-3 Illustrations of the converging and diverging lone pairs. **A**) The geometry of a free metalloligand Ni(N_2S_2) and **B**) its two 3*p* lone pairs, one on each sulfur (contour plots at isovalue = 0.05 a.u. by NBO analysis). Note the relative positions of the S-C_α / S-Ni bonds and the 3*p*-lone pair. The crystal structures of **C**) **[Ni_2-Fe_2]$^{2+}$** and **D) Ni-Fe.**

Note that the Ni-S-C_α-C_β-N five-membered rings inside the NiN_2S_2 metalloligands are not coplanar, *i.e.*, they adopt the envelope conformation of cyclopentane. The C_α carbon (the "flap" of the envelope conformation) of the C_2H_4 linkers puckers towards one side of N_2S_2 plane, Figure IV-3C and D. The solid structure of the reduced monomer **[Ni-**

Fe]^{0} shows the $Fe(NO)_2$ fragment is on the same side as the flap; while in the oxidized dimer **[Ni$_2$-Fe$_2$]$^{2+}$** the flap and the $Fe(NO)_2$ fragment(s) appear on different sides of each N_2S_2 plane. As seen in Figure IV-3B, the orientations of the *p*-lone pair on each sulfur of a free NiN_2S_2 is correlated to the orientations of the S-Ni and S-C_α bonds. Due to the puckering within the C_2H_4 linkers between N and S, a small intersection angle is created between the NiN_2S_2 and the C_α-S-Ni planes. Therefore, the S is slightly twisted by the N to S hydrocarbon linker, the S-C_α bond and the S-Ni bond of the NiN_2S_2 scaffold; thus its remaining 3*p* lone pair is tilted from the normal to the N_2S_2 plane, Figure IV-3B. This tilt causes two *p*-orbital lobes (green lobes) to **converge** on the side to which the flap puckers, while the red lobes **diverge** on the opposite side. The orientation of the added $Fe(NO)_2$ receiver unit(s), will be thus determined by such directional property of the donor *p* lone pairs.

The result of the analysis above is that converging lobes of the *p* donor lone pairs maximize contact to the $Fe(NO)_2$ unit in the monomer **Ni-Fe**, while the diverging lobes are preferred by two bridging $Fe(NO)_2$ units between two metalloligands in the dimer **[Ni$_2$-Fe$_2$]$^{2+}$**. The latter arrangement apparently lessens the steric repulsion between $Fe(NO)_2$ units. In summary, the binding position of the $Fe(NO)_2$ unit with respect to the flap of the C_2H_4 linkers in the Ni-S-C_α-C_β-N five-membered rings are correlated by the competition between chemical bond directionality of the binding sulfurs and steric repulsion of the receiver units.

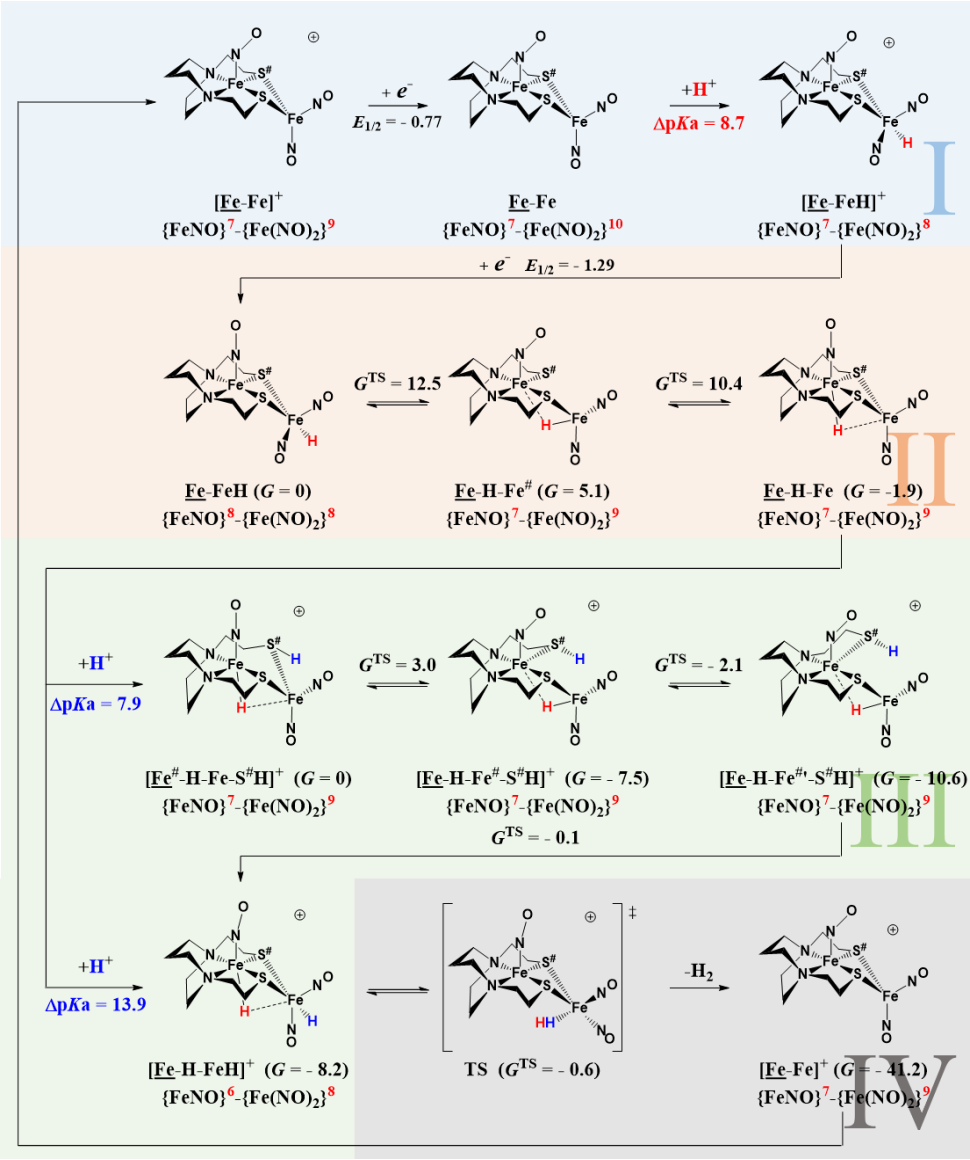

Figure IV-4 The computational mechanism of electrocatalytic H_2 production on **[Ni-Fe]$^+$** in the presence of HBF_4•OEt_2. The Gibbs free energies in kcal/mol are scaled to the reference point (G = 0), which resets after every reduction or protonation. The reduction potentials ($E_{1/2}$) are reported in V with reference to the standard redox couple $Fc^{+/0}$ = 0.0 and the relative acidities (ΔpKa) are reported versus $[HOEt_2]^+$.

The mechanism of H_2 production on the Ni-Fe model complex.

The first reduction and the first protonation. Figure IV-4-I shows the first reduction at -0.77 V (exp. -0.72 V) on the oxidized monomer **[Ni-Fe]$^+$**, dissociated from the dimer **[Ni-Fe]$_2^{2+}$** in solution, and the successive protonation. The $Fe(NO)_2$ moiety of **[Ni-Fe]$^+$** accepts the electron and increases the E-F electron count from $\{Fe(NO)_2\}^9$ to $\{Fe(NO)_2\}^{10}$. Although **[Ni-Fe]$^+$** itself cannot be protonated by HBF_4•OEt_2.[155] The reduced species **[Ni-Fe]** accepts a proton (ΔpK_a = 12.9 with respect to HBF_4•OEt_2). Protonation reduces the E-F electron count of the $Fe(NO)_2$ moiety to 8 as two electrons are consumed by the Fe-H bond, but the overall electron count of **[Ni-FeH]$^+$** remains at 18. The **[Ni-FeH]$^+$**, with reduced basicity after the first protonation, cannot accept a second proton.

The second reduction and associated geometric and electronic reorganization. The reduction of **[Ni-FeH]$^+$** at -1.28V and its further geometric changes are reported in Figure IV-4-II. The incoming electron is initially shared by both metals of **Ni-FeH**, as Ni's only vacant orbital d_{x2-y2}, is heavily destabilized and Fe already has 18 electrons. Nevertheless, the electron-buffering effect of NO ligands in the $Fe(NO)_2$ moiety, along with the electron depletion by the hydride, facilitates the acceptance of the second electron at a moderate potential. However, to lower the energy of this electron species, the hemi-labile bridging thiolate easily dissociates the S-Fe bond with a concomitant shift of the added electron to $Fe(NO)_2$, now a 17-electron species, **Ni-Fe$^{\#}$H** ($S^{\#}$ denotes the S of the S-Fe bond that will be broken and, in the text, $Fe^{\#}$ denotes the Fe with the broken S-Fe bond). The **Ni-Fe$^{\#}$H** then rotates the hydride beneath the Ni and Fe, creating a semi-bridging hydride, *d*(Ni-H) = 1.691 Å and *d*(Fe-H) = 1.587 Å and inverting the C_2 linker, to produce **Ni-H-Fe$^{\#}$'** ('

indicates the inverted C_2 linker). The nickel in **Ni-H-Fe$^{\#}$'** has a distorted trigonal bipyramidal (TBP) geometry ($\tau = 0.48$),[135] which stabilizes a high-spin state and results in the antiferromagnetic coupling between the high-spin $Ni^{II}(d^8)$ and the $\{Fe(NO)_2\}^9$ The bridging hydride on the mimics of [NiFe]-Hydrogenase has long been featured in the literature[52, 105, 166-168] with a recent interpretation of a model with the hydride closer to Ni, as it appears to be in the enzyme.[169] After these geometric changes, the second reduction is fully assigned to $Fe(NO)_2$ as the concomitant actuation of hemi-lability facilitates the accommodation of the incoming electron, as in the case of **[Fe-Fe$_{CO}$]$^+$**.[154]

The second protonation and the production of H_2. The second protonation on **Ni-H-Fe$^{\#}$'** and successive H_2 production are presented in Figure IV-4-III. The $S^{\#}$ of **Ni-H-Fe$^{\#}$'** is an ideal target for protonation (ΔpK_a of 14.4) producing **[Ni-H-Fe$^{\#}$'-S$^{\#}$H]$^+$**. The thiol-hydride pair in **[Ni-H-Fe$^{\#}$'-S$^{\#}$H]$^+$** is already in spatial proximity (2.773 Å) and they exothermally couple to H_2 over a barrier of 7.4 kcal/mol without formation of a σ-complex (η^2-H_2) intermediate. The H_2 release restores the Fe-S$^{\#}$ bond in **[Ni-Fe']$^+$** and the inverted C_2 linker reverses to regenerate the catalyst **[Ni-Fe]$^+$**. Thus, the [ECEC] catalytic cycle in Figure IV-4-III closes with an **HP** step.

The calculations predict that second reduction event at -1.28 V (calc'd) should produce the catalytic wave. However, this catalytic wave appears experimentally at – 0.70 V and the current increases with additional equivalents of HBF_4•OEt_2.[155] The early appearance of the catalytic wave indicates that the second reduction in the mechanism is a proton coupled electron transfer (PCET) as in an [EC<u>E</u>C] cycle. The calculated standard potential of this proton-coupled reduction from **[Ni-FeH]$^+$** (Figure IV-4-I) to the resting

state **[Ni-H-Fe$^{\#}$'-S$^{\#}$H]$^{+}$** (Figure IV-4-III) is -0.32 V, less negative than the calculated potentials for a simple ET step at -1.28 V.

Of course, the resting state **[Ni-H-Fe$^{\#}$'-S$^{\#}$H]$^{+}$** differs from **[Ni-FeH]$^{+}$** significantly, thus the actual PCET to **[Ni-FeH]$^{+}$** cannot generate **[Ni-H-Fe$^{\#}$'-S$^{\#}$H]$^{+}$** without geometric reorganizations over barriers (Figure IV-4). And the actual potential should not go below -0.77 V, before the first reduction event occurs. The calculations essentially set a reasonable range, from -0.77 V to -1.28 V, for the reduction potential for a PCET process to **[Ni-FeH]$^{+}$**; thus the existence of an unresolved PCET process may explain the appearance of the catalytic wave at a less negative potential than that calculated.

The intermolecular protonation by the acid on the hydride of **Ni-H-Fe$^{\#}$'** of Figure IV-4-II to produce H_2 directly from the added acid is ruled out by a barrier ca. 10 kcal/mol higher than that of the protonation on S$^{\#}$. As in the previous work with **[Ni-Fe$_{CO}$]$^{+}$**,[154] a third electron could be added to **[Ni-H-Fe$^{\#}$'-S$^{\#}$H]$^{+}$**, before it releases H_2, which would render an E[CECE] catalytic cycle. However, for this particular catalyst **[Ni-Fe]$^{+}$**, the third electron would not appear to accelerate the catalytic cycle.

The geometric and electronic structures of [<u>Fe</u>-Fe]$^{+/0/-}$.

The **[<u>Fe</u>-Fe]$^{+}$** complex, described here with NO ligands on both irons, is also an effective electro-catalyst for H_2 production with HBF_4•OEt_2.[156] In the absence of a proton source, **[<u>Fe</u>-Fe]$^{+}$** displays two reversible reduction events, $E_{1/2}$ = -0.78 V and -1.41 V, respectively.[156] The spin densities of **[<u>Fe</u>-Fe]$^{+/0/-}$** are provided in Figure IV-5 and Table IV-1. The oxidized complex **[<u>Fe</u>-Fe]$^{+}$** was previously described to have a closed-shell

singlet ground state.[76] The re-optimization discovers an open-shell singlet with one unpaired α electron on {Fe(NO)}^{7} and one unpaired β electron on {Fe(NO)$_2$}^{9}, and they are antiferromagnetically coupled to an open-shell singlet. This singlet is lower in energy and the optimized Fe-Fe distance (closed-shell singlet: 2.659 Å; open-shell singlet: 2.710 Å) is in better agreement with the crystal data (2.786 Å). The diradical property of **[Fe-Fe]$^+$** is also indicated by the optimized total spin *S* value of 0.269.

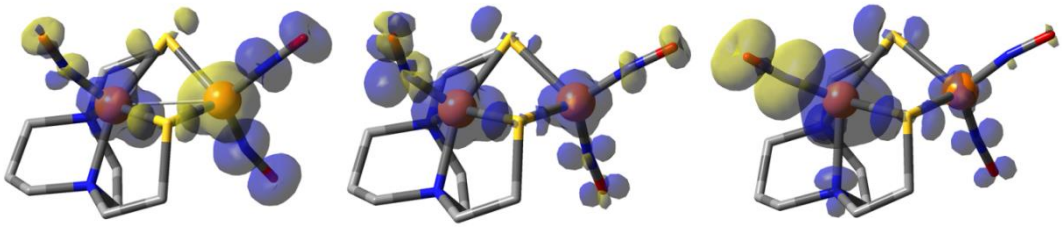

[Fe-Fe]$^+$ **[Fe-Fe]^0** **[Fe-Fe]$^-$**

Figure IV-5 Visualizations of the spin densities of complex **[Fe-Fe]$^+$**, **Fe-Fe** and **[Fe-Fe]$^-$**. The blue shading represents positive spin density (excess α spin) and the yellow shading, negative spin density (excess β spin). The color of the shading changes on Fe of Fe(NO)$_2$, when comparing **[Fe-Fe]$^+$** and **[Fe-Fe]^0** because the excess β spin density on Fe of Fe(NO)$_2$ is offset by adding an α electron during the first reduction. The second reduction enlarges the blue shaded area on Fe of Fe(NO), indicating the increase of α spin density.

The reduction of **[Fe-Fe]$^+$** to **Fe-Fe**, is localized to the {Fe(NO)$_2$}$^{9/10}$ couple with a calculated potential of - 0.77 V (DCM solvation model in CH_2Cl_2). The added α electron neutralizes the β spin density on the Fe(NO)$_2$ unit and some excessive *α* spin density

appears on the $Fe(NO)_2$ moiety, while the most unpaired spin density is still attributed to the unpaired α electron of $\{Fe(NO)\}^7$ in the overall doublet ground state. Though the configuration of the $\{Fe(NO)\}^7$ moiety does not change after the first reduction, the calculated Fe-N-O angel of the Fe(NO) unit changes from 164.0° to 148.8° (exp: 165.8° to 154.7°), likely attributed to a stronger back-bonding between Fe and its bound NO due to the delocalization of the added electron from $Fe(NO)_2$ unit to the Fe(NO) unit.

Table IV-1 The numerical spin densities of two irons and corresponding NO ligands in complexes **[Fe-Fe]$^+$**, **[Fe-Fe]^0**, **[Fe-Fe]$^-$**.

Complexes	Multiplicity	*S* value	Spin density			
			Fe	Fe(NO)	Fe	$Fe(NO)_2$
[Fe-Fe]$^+$	BS Singlet	0.269	0.539	0.543	-0.752	-0.454
[Fe-Fe]^0	Doublet	0.512	0.683	0.716	0.251	0.203
[Fe-Fe]$^-$	Triplet	1.078	2.142	1.619	0.068	0.088

The successive reduction then adds the second electron to the $\{Fe(NO)\}^7$ unit, as the $\{Fe(NO)_2\}^{10}$ unit now is saturated. Either an α electron can be introduced to form a triplet **[Fe-Fe]$^-$** or a β electron to make a singlet **[Fe-Fe]$^-$**. The former is the ground state. If all nitrosyls are treated as NO^+ in electron counting, the configuration of $\{Fe(NO)\}^7$ can be written as $(d_{x2-y2})^2(d_{xz})^2(d_{yz})^2(d_{z2})^1$. Note the non-conventional layout of Cartesian coordinates in Figure IV-6. When the Fe-N-O angle of the Fe(NO) moiety is linear, d_{xz} and d_{yx} can contact π^*_x and π^*_y orbitals of NO to initiate π-back-bonding, respectively. [170] In contrast, a bent (presumably toward *x*-axis) Fe-N-O angle, replaces the d_{xz}-π^*_x π-back-bonding with d_{z2}-π^*_x σ-back-bonding.[170] Therefore, d_{xz} and d_{yz} prefer a linear NO while

d_{z2} prefers a bent NO and the preference from orbitals take effects when these individual *d* orbitals are occupied by electrons. The singlet **[Fe-Fe]**$^{-}$ has a doubly occupied $(d_{z2})^2$ orbital (configuration: $(d_{x2-y2})^2(d_{xz})^2(d_{yz})^2(d_{z2})^2$) and shows a very bent (124.8°) Fe-N-O angel, consistent with the classic description of $\{Fe(NO)\}^8$ systems. In this case, the triplet is lower in energy and is the ground state, with the configuration of $(d_{x2-y2})^2(d_{xz})^2(d_{yz})^2(d_{z2})^1(d_{xy})^1$. The singly occupied d_{z2} orbital cannot provide as strong back bonding as the doubly occupied d_{xz} or d_{yz} orbital especially when the electron crowdedness of the $\{Fe(NO)\}^8$ unit demands effective back-bonding. In other words, the preference of the d_{z2} orbital is overwhelmed. In addition to that, the two unpaired α electrons on Fe of FeNO also initiate the spin-polarization in the back-bonding orbitals, *i.e.*, the bonding orbitals constituted by Fe's d_{xz}, d_{yx} and NO's π^*_x, π^*_y, Figure IV-6. The other α electrons (in addition to the two unpaired electrons on the d_{z2} and d_{xy} orbitals) tend to localize on Fe (with a spin density larger than 2) and the β electrons concentrate on its attached NO to take advantage of exchange energies of local spin density, see the obital sketches in Figure IV-6.

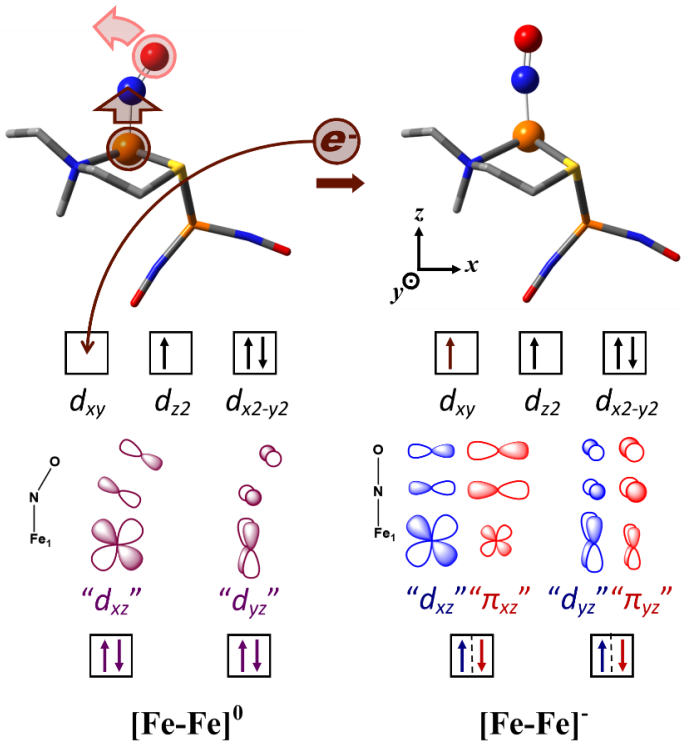

Figure IV-6 The sketch of relevant geometric and electronic structure changes of the reduction of **Fe-Fe** to **[Fe-Fe]**$^{-}$. The orbitals are represented by sketches in corresponding colors.

Another relevant geometric change predicted by the computational chemistry is the displacement of the Fe(NO) unit from the chelating N_2S_2 metalloligand plane. The d_{xy} orbital is heavily destabilized by the donation from N_2S_2 ligand. (The Cartesian coordinates are non-conventional, see Figure IV-6). The occupancy of this orbital in the triplet **[Fe-Fe]**$^{-}$ motivates the Fe(NO) moiety to go out of the N_2S_2 plane to reduce the anti-bonding orbital overlapping. This displacement of Fe(NO) from the N_2S_2 plane increases form 0.52 Å (**[Fe-Fe]**^{0}) to 0.87 Å (**[Fe-Fe]**$^{-}$) with elongated Fe-S and Fe-N bonds.

The mechanism of H_2 production on the Fe-Fe model complex.

The first and second reduction and the roaming of the first proton. Figure IV-7-I depicts the first two steps of the mechanism, the reduction and protonation of the $\{Fe(NO)_2\}^9$ moiety in the **[Fe-Fe]**$^+$, consistent with our earlier experimental and theoretical study.[156] Figure IV-7-II shows the second reduction event and associated geometric changes. The second electron reduces the iron-mononitrosyl in **[Fe-FeH]**$^+$ to $\{Fe(NO)\}^8$. Next, hydrogen in **Fe-FeH** migrates from the iron-dinitrosyl to the iron-mononitrosyl while an electron migrates in the opposite direction, which results in the intermediate **Fe-H-Fe** with a semi-bridging hydride. The six-coordinate iron in the$\{Fe(NO)\}^7$ has a vacant d_{z2} orbital due to the strong axial hydride ligand thus the nitrosyl has no tendency to bend (175.7°) to mix its π^* orbital with Fe d_{z2}.

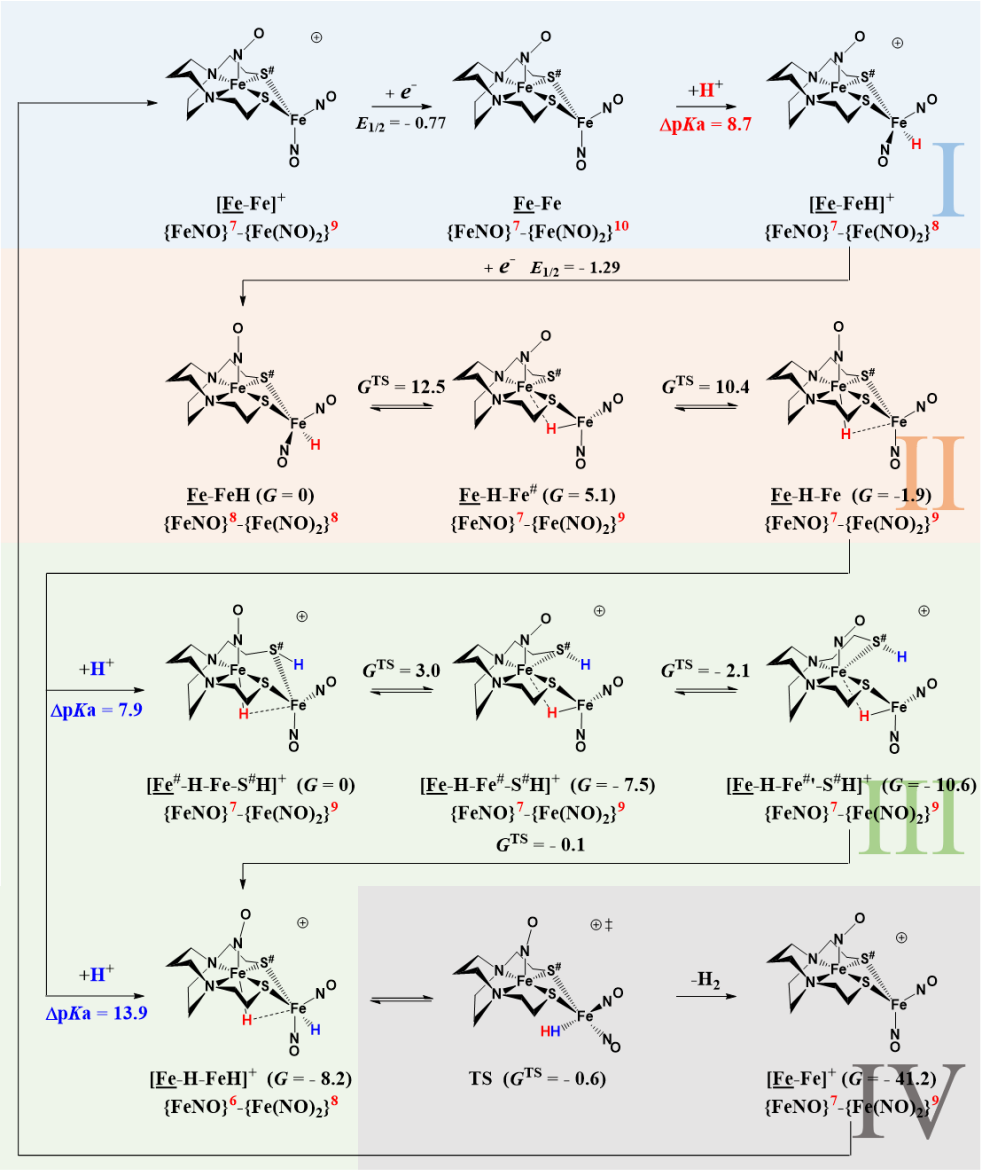

Figure IV-7 The computational mechanism of electrocatalytic H_2 production on **[Fe-Fe]$^+$** in the presence of HBF_4•OEt_2. Note that one transition state was marked with a star as its Gibbs free energy is lower than its immediate precursor, which is caused by the error of solvation and thermal corrections. See the caption of Figure IV-4 for more explanation.

The second protonation and the production of H_2. The second protonation step is summarized in Figure IV-7-III. Protonation on one of the two bridging thiolates (ΔpK_a = 7.9) of **Fe-H-Fe**, initially breaks the $S^{\#}$-Fe(NO) bond but this species rearranges by breaking the $S^{\#}$-$Fe(NO)_2$ bond, restoring the $S^{\#}$-Fe(NO) bond and inverting the C_2 linker. The product, **[Fe-H-Fe$^{\#}$'-S$^{\#}$H]$^+$**, does not couple thiol-hydride to generate H_2 but transfers the proton on S to the $Fe(NO)_2$ to create the intermediate **[Fe-H-FeH]$^+$**, featuring one terminal and one (semi-)bridging hydride. This dihydride may also be created by the direct protonation of **Fe-H-Fe** on $Fe(NO)_2$, ΔpK_a = 13.9. Either protonation has a negligible barrier and leads to the same productive process.

Figure IV-7-IV shows the final step, the reductive elimination of H_2 from two hydrides on **[Fe-H-FeH]$^+$** over a low barrier. The **[Fe-Fe]$^+$** is regenerated after the exothermic release of H_2 and this [ECEC] catalytic cycle closes with an **RE** step. The reduction of **[Fe-FeH]$^+$** (at - 1.29V, calc'd) is expected to produce a catalytic wave. With only a few equivalents of added acid, the experimental catalytic wave appears as early as -0.8 V, which overwhelms the shoulder peak at approximately - 0.7 V representing the first electron reduction.[156] Again, the discrepancy may be attributed to a PCET process. This standard reduction potential is -0.28 V from **[Fe-FeH]$^+$** (Figure IV-7-I) to the resting state **[Fe-H-Fe$^{\#}$'-S$^{\#}$H]$^+$** (Figure IV-7-III), if the necessary geometric reorganizations in-between are ignored. Therefore the real PCET could have a potential between -0.77 V and - 1.29 V. The addition of a third electron to **[H-Fe-Fe-H]$^+$** before H_2 release is also possible, yielding an E[CECE] catalytic cycle, as in the previous report of **[Fe-Fe(CO)]$^+$**. [154]

Discussion

The factors controlling the actuation of hemi-lability. The conditions wherein the hemi-lability can be triggered in these bimetallics with bridging thiolates as core structures provide interesting comparisons. As summarized in Figure IV-8, as few as one and as many as four steps may be required. Here, we note that the number of steps correlates with the number of NO ligands installed on the catalyst. In the **[Ni-Feco]$^+$**, Figure IV-8, the Ni^{II} (d^8) within the metalloligand is unable to hold onto the incoming electron, resulting in an internal electron transfer to the 6-coordinate, 18-electron Fe^{II} (d^6) in $[Fe(CO)Cp]^+$, which concomitantly breaks one of the two S-Fe^{I}(CO)Cp bonds to reduce the 19 electron count for iron to 17, as indicated by an irreversible reduction event in the absence of the acid.[154] This type of reduction-actuated, hemi-lability of a multidentate ligand has precedent in the tridentate trispyrazolborate ligand of $[Rh(CO)(PPh_3)Tp^{Me2}]^{+/0}$ and derivatives by Connelly, Geiger, *et al*.[162, 171-172]

The complex **[Fe-Feco]$^+$**, Figure IV-8, places the incoming electron on $\{Fe(NO)\}^7$ in the N_2S_2 site, which has electron-buffering capacity and does not initiate bond dissociation. Here a second step, the protonation of S, which is quite basic after the reduction, removes electron density from S, reduces the donation to $[Fe(CO)Cp]^+$, and leads to the S-Fe bond rupture. [154] NBO analysis shows both the S-Fe bond (before the protonation) and the S-H bond (after the protonation) primarily use the 3*p* orbital of the three-coordinate S, while the remaining lone pair is dominated by the less accessible 3*s* orbital.

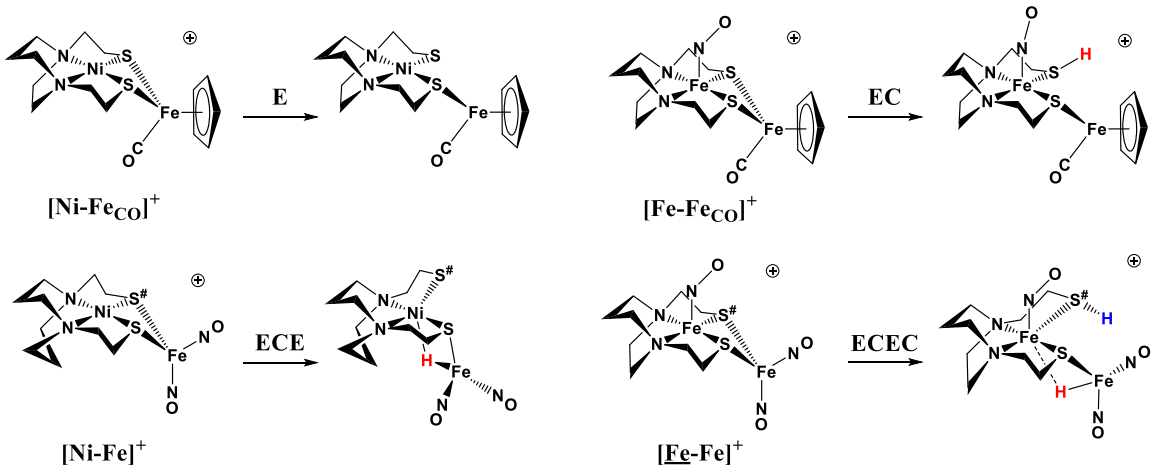

Figure IV-8 Conditions required to realize the hemi-lability of the bridging thiolates on different models. **E** indicates an electrochemical step (reduction); and **C**, a chemical step (protonation).

In contrast to **[Ni-Fe$_{CO}$]$^+$** and **[Fe-Fe$_{CO}$]$^+$**, the **[Ni-Fe]$^+$** and **[Fe-Fe]$^+$** complexes, whose H_2 production mechanisms are presented in this work, require additional electrons and protons to dissociate the S-Fe$(NO)_2$ bond. The reason lies in the nitrosyl ligand's electron-buffering capacity. In both **[Ni-Fe]$^+$** and **[Fe-Fe]$^+$**, the $\{Fe(NO)_2\}^9$ moiety accepts the first electron to produce $\{Fe(NO)_2\}^{10}$; this reduction does not require the dissociation of a S-Fe$(NO)_2$ bond to accommodate the incoming electron. Since the NO's electron-buffering capacity supports the electron-rich Fe, the first proton goes to the $\{Fe(NO)_2\}^{10}$ moiety to create an iron hydride, rather than to the sulfur. Still these two steps do not elicit the S-Fe$(NO)_2$ bond dissociation. However, the second reduction to **[Ni-Fe]$^+$** triggers the S-Fe$(NO)_2$ bond dissociation as neither the now-saturated, five-coordinate $\{Fe(NO)_2\}^8$-hydride nor the square-planar Ni^{II} can accept the electron easily.

Thus, the S-Fe$(NO)_2$ bond now cleaves after three steps, ECE, so that the FeH$(NO)_2$ moiety becomes 4-coordinate and has the vacancy for the second incoming electron. Since for **[Fe-Fe]**$^+$ the second electron is again buffered by the Fe(NO), as one saw in the first reduction of **[Fe-Feco]**$^+$, a fourth step, the second protonation, which occurs on thiolate sulfur this time, is needed for the S-Fe$(NO)_2$ cleavage, as in the first protonation for **[Fe-Feco]**$^+$.

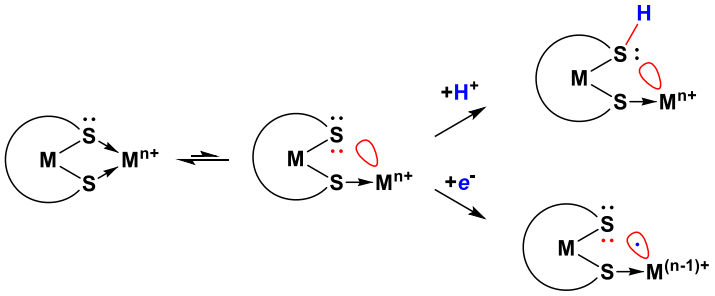

Figure IV-9 The actuation of the hemi-lability of the thiolate. Either the reduction on the dissociated metal, or the protonation on the dissociated sulfur, finalizes the dative bond dissociation and preserves the reactive sites.

The Lewis acid-base pair generated from the cleavage of the S-Fe bond. Figure IV-9 summarizes the key mechanistic aspects of the actuation of the hemi-lability of the bridging thiolate in the reactive centers to assist the electrocatalytic process of H_2 production. The first reaction on the left of Figure IV-9 shows a simple dative-bond disruption, which would be expected to be short lived as it is thermodynamically advantageous to reestablish the dative bond. In our mechanistic study, it was discovered that this bond dissociation is synergic with either reduction or protonation. In other words, either of these manipulations modulates the electron density on the Lewis acid or the

Lewis base to quench their acidity or basicity and prevent the reformation of the dative bond, on the right of Figure IV-9.

Inspection of the correlation between the number of steps to trigger the hemi-lability and the number of NO ligands (Figure IV-8), leads to the conclusion *that the electron-buffering capacity demonstrated by NO ligand prevents an earlier S-Fe bond dissociation as it interferes with either endeavor to make the bond dissociation irreversible, by redirecting the reduction or protonation. The more nitrosyls the complex has, the more electron-buffering capacity it receives such that more reduction/protonation steps are needed before the dative bond dissociation occurs.*

H_2 production step: hydride protonation (HP) vs. reductive elimination (RE). The increasing number of nitrosyls on the model also makes formation of the hydride(s) easier. For **[Fe-Fe]$^+$**, two external electrons are enough to reduce two protons and create two hydrides, one on each iron of **[Fe-H-Fe-H]$^+$**, with the two additional internal electrons coming from the $Fe(NO)_x$ fragments buffered by NO π^* orbitals. In comparison, other [FeFe]-Hydrogenase models, such as (μ-pdt)$[Fe(CO)(dppv)]_2$[173-174] and (dppv)(CO)Fe(μ-edt)$Fe(CO)_3$, (edt = ethane-1,2-dithiolate) [175] that lack an electron reservoir such as NO, only achieve a dihydrido derivative by the addition of an exogenous hydride.

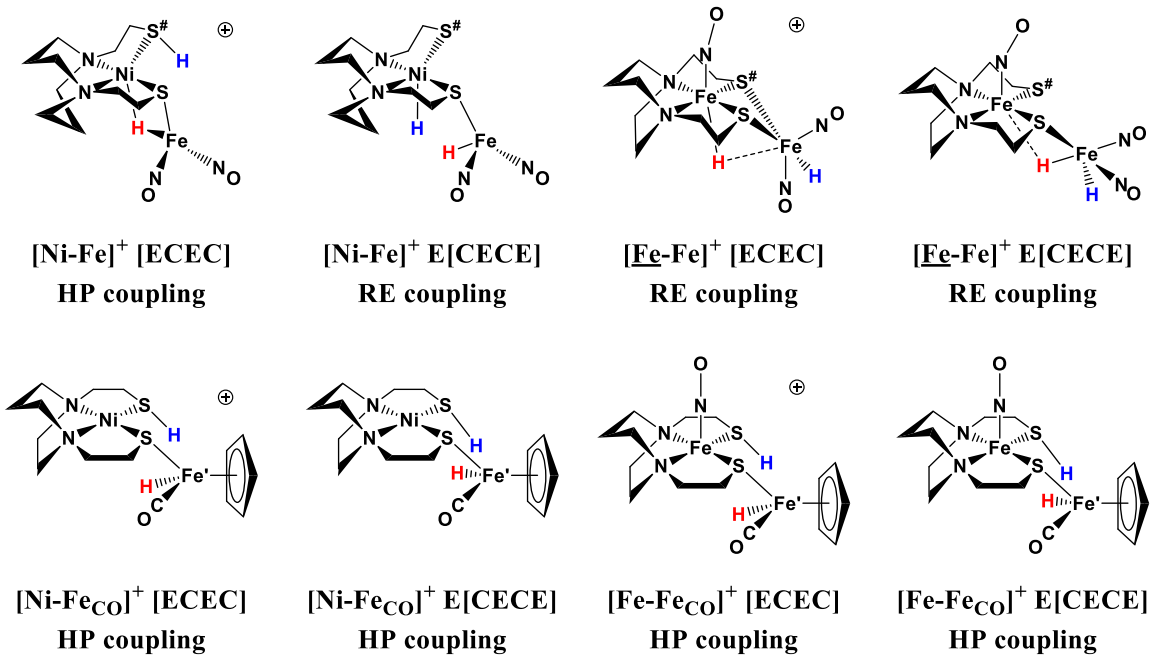

Figure IV-10 H_2 production by either **HP** or **RE** coupling and their immediate precursors.

The coupling to produce H_2 varies mechanistically. The hydride protonation (**HP**) mechanism only needs one hydride, which means it can occur on less electron-rich metal complexes, while the reductive elimination (**RE**) needs two hydrides to produce H_2. Thus, the **HP** process operates in the [ECEC] and E[CECE] cycles of both **[Ni-Fe$_{CO}$]$^+$** and **[Fe-Fe$_{CO}$]$^+$**.[154] For **[Ni-Fe]$^+$**, the [ECEC] cycle involves the **HP** coupling, while with one more electron in the E[CECE] cycle **[Ni-Fe]$^+$** switches to the **RE** coupling process. In other words, the **RE** coupling is made possible by the electronic flexibility of NO ligands attached to metals. Finally the **RE** mechanism takes over completely in either the [ECEC] cycle or the E[CECE] cycle of the trinitrosyl species **[Fe-Fe]$^+$**. Figure IV-10 summarizes the H_2 production steps and corresponding immediate precursors of all four electrocatalysts. From the aspect of structure-function analysis, the **RE** coupling requires

one more Lewis acid to park the additional hydride while eliminating the necessity of a Lewis base to store the proton, which is however required by **HP** coupling. Though the hemi-lability of the thiolate may still be important in molecular isomerization and the resting states, the Lewis base required to hold a proton is no longer mandatory for **[Fe-Fe]**$^{+}$, as the incoming proton can always be stored as a hydride, whose production uses the electrons held by the irons and their nitrosyl(s).

The relevance between electron availability and H_2 coupling mechanism is also present in the enzymes: [NiFe]-Hydrogenase (with no immediate buffering) and [FeFe]-Hydrogenase (with the $[Fe_4S_4]$ sub-cluster to buffer one electron) can provide two and three electrons on the most reduced Ni-L and H_{sred} states, respectively. In other words, they are unable to generate two hydrides, even if there are enough vacant sites for two hydrides; therefore, they can only proceed through the **HP** mechanism.[36] Intriguingly, nitrogenase, whose electron-buffering can be attributed to the extensive delocalization of the FeS cluster (Figure IV-1), takes in four electrons to create two hydrides on the E_4 state and it can execute a **RE** step to produce H_2 concomitantly with N_2 fixation. This **RE** step strategically deposits two reduction equivalences needed for the initial uptake and activation of N_2 in the nitrogenase FeMo-cofactor.[145, 147-149] The E_4 state of nitrogenase can actually be discharged with a **HP** step to produce H_2, but in the absence of N_2.[146] In conclusion, such electron delocalization is a strategy used by Nature to enable non-noble metals to do multi-electron chemistry.

Summary

Our theoretical investigation highlights the role of the hemi-lability of the bridging dithiolate and the electron-buffering capacity of ligands such as NO in bimetallic electrocatalysts. Upon the actuation of the hemi-lability by dative-bond dissociation, Lewis acid and base sites are created and serve as reactive centers. To maintain the availability of the Lewis acid-base pair, it must be protected from reformation of the dative bond. The protection for our systems is achieved by the modification of the electron densities either on the acid (by reduction) or on the base (by protonation) to prohibit a stable donation from the base to the acid.

The electron-buffering by the NO provides metal sites with electron capacity such that the protonation and reduction are directed to sites other than the potential Lewis base and acid sites. The realization of the hemi-lability of the bridging thiolate is modulated by its interplay with the NO ligand. Thus, NO can interfere with the early (upon reduction) hemi-lability of the MN_2S_2 ligand and postpones the creation of the Lewis acid-base pair. The electron-buffering NO ligands also provide electron–rich metal site that facilitates conversion of protons to hydrides, pivoting the mechanism from **HP** to **RE** as multiple hydrides become available. The ultimate role of NO in the models is recognized to be a bifunctional electron reservoir and it (at least partially) reproduces the function of the $[Fe_4S_4]$ sub-cluster of [FeFe]-Hydrogenase active site.

CHAPTER V

CYANIDE LINKAGE ISOMERIZATION MECHANISM

Linkage cyanide isomerization in [FeFe]-hydrogenase active site mimics

Introduction. As mentioned in Chapter I, the artificial maturation of [FeFe]-hydrogenase involves two linkage cyanide isomerization processes, which occur when the di-iron complex enters the transferase HydF and when the di-iron unit is transferred into the apo-hydrogenase apo-HydA.[45, 176] As such linkage cyanide isomerizations are not common (a more detailed literature review is provided in the next section), we were interested in constructing a few simple organometallic complexes to simulate such processes.

Synthetic models. The synthetic models were constructed with two fragments: the diiron fragment and the mono-iron fragment (Figure V-1), representing the $[Fe_4S_4]$ sub-cluster and the $[Fe_2S_2]$ sub-cluster of the active site of [FeFe]-hydrogenase, respectively. To make a cyanide bridge in the target tri-iron models, a terminal cyanide is installed on one fragment and a labile ligand (either THF or CO) is present on the other fragment. Four model complexes **A-D** (Figure V-2) form as the N end of the cyanide substitute the labile ligand on the receiver fragment. The refined crystal structures indicate that the M-C-N-M' orientations are completely pre-determined by the reagents used, consistent with Zhu and Vahrenkamp's study of many pairs of linkage isomers.[177] Unfortunately, It is not

---

This chapter is partially reproduced from two manuscripts with permission: Lunsford, A. M.; Beto, C. C.; Ding, S.; Erdem, O. F.; Wang, N.; Bhuvanesh, N.; Hall, M. B.; Darensbourg, M. Y. *Chem. Sci.* **2016,** *7*, 3710-3719 (to which the author of this dissertation primarily contributed the computational study); Ding, S.; Darensbourg, M. Y.; Hall, M. B. *Manuscript in preparation.*

possible to synthesize the linkage isomer of **A** by combining the fragments **2** and **z**, as the nitrogen end of the cyanide on **z** does not replace the solvent THF on **2**.

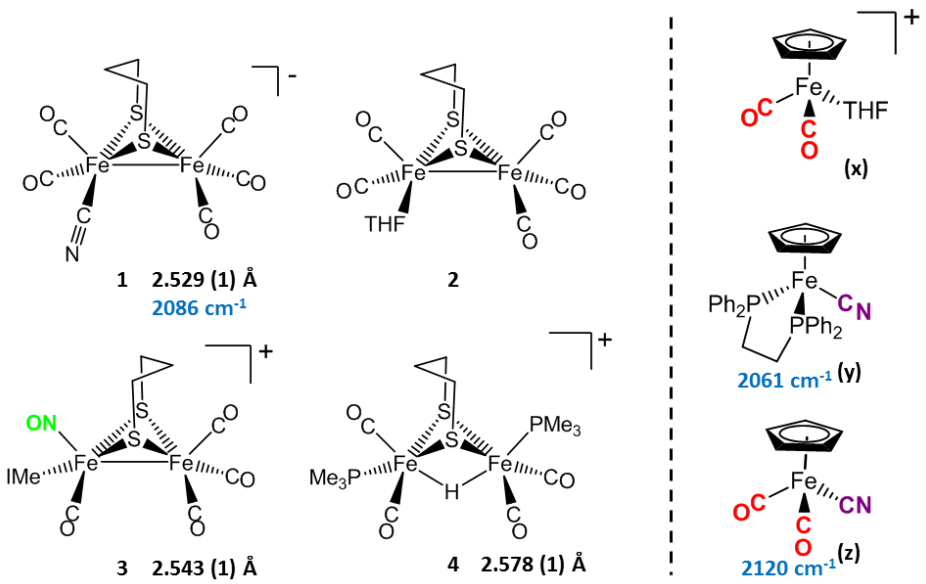

Figure V-1 The bimetallic and monometallic fragments used in the synthesis.

The mechanism of cyanide linkage isomerization is largely an unexplored area and our trimetallic complexes could be good representative examples to explore the energetics of the possible linkage isomerization by Density Functional Theory computations.

Computational protocols. Metric data from the x-ray diffraction analyses of complexes **A-D** were imported as the initial geometries of the experimentally observed isomers. The calculated metric data that compares with experimental values with an approximately 1-2% error, provides confidence to the validity of the computations. The initial geometries of their cyanide-flipped isomers were created by computationally exchanging the positions of C and N in the crystallographic structures. Geometric optimizations were done with B3LYP functional[24] and Gaussian 09, as well as thermal and solvation corrections.

Transition states were initially generated through relaxed scans with educated guesses and successively optimized. The Intrinsic Reaction Coordinate (IRC) calculations were applied to certain transition states, to trace the reaction paths following the imaginary vibrational frequency, until a local minimum on the potential energy surface was achieved.

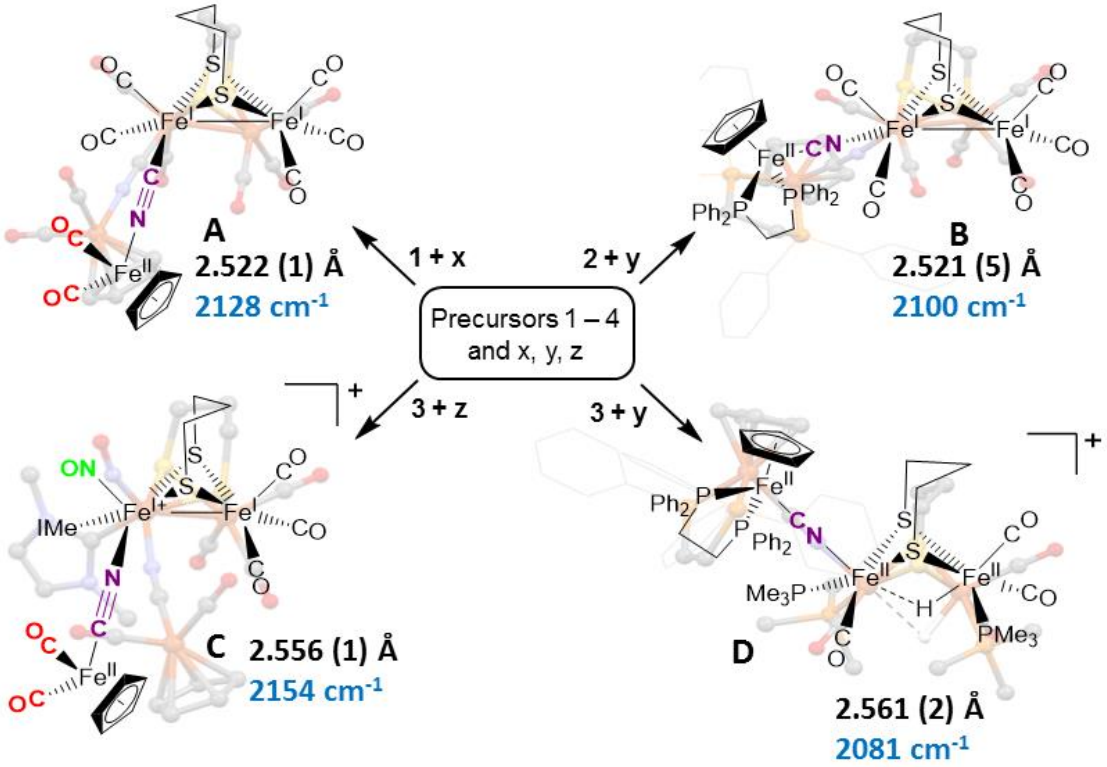

Figure V-2 The trimetallic complexes. The Fe-Fe distances in the bimetallic units and the NO vibrational frequencies are noted.

Isomers. Despite the fact that the orientation of cyanide in these synthesized complexes is predetermined by the precursors, the calculations showed that it is always energetically advantageous for the carbon to coordinate to the mono-iron moiety in the four complexes.

The Gibbs free energy differences between two isomers of complexes **A**-**D** were determined to be 1.0, 2.0, 3.2 and 4.4 kcal/mol, respectively.

Isomerization mechanism and associated barriers. Complex **A**, the simplest structure, was investigated as a representative example to search for a cyanide-flipping mechanism. The C-Fe and N-Fe bond energies of the linkage isomers were calculated (Figure V-3A) finding that the carbon, rather than nitrogen, end of CN forms the stronger bond to either Fe^{II} or $Fe^{I}Fe^{I}$, see **A'** and **A** of Figure V-3A. The imaginary vibrational frequency of **A-TS**, located as the likely transition state connecting the isomers (see Figure V-3A), is associated with a wagging motion that initiates the asymmetric concomitant slide from one CN end to the other. The motion is indicative of an intramolecular transfer mechanism rather than a dissociation-association mechanism. The Gibbs free energy of **A-TS** was calculated to be 38.7 kcal/mol above the more stable isomer **A'**, a barrier unlikely to overcome at room temperature, and thus consistent with the experimental observation of only one isomer.

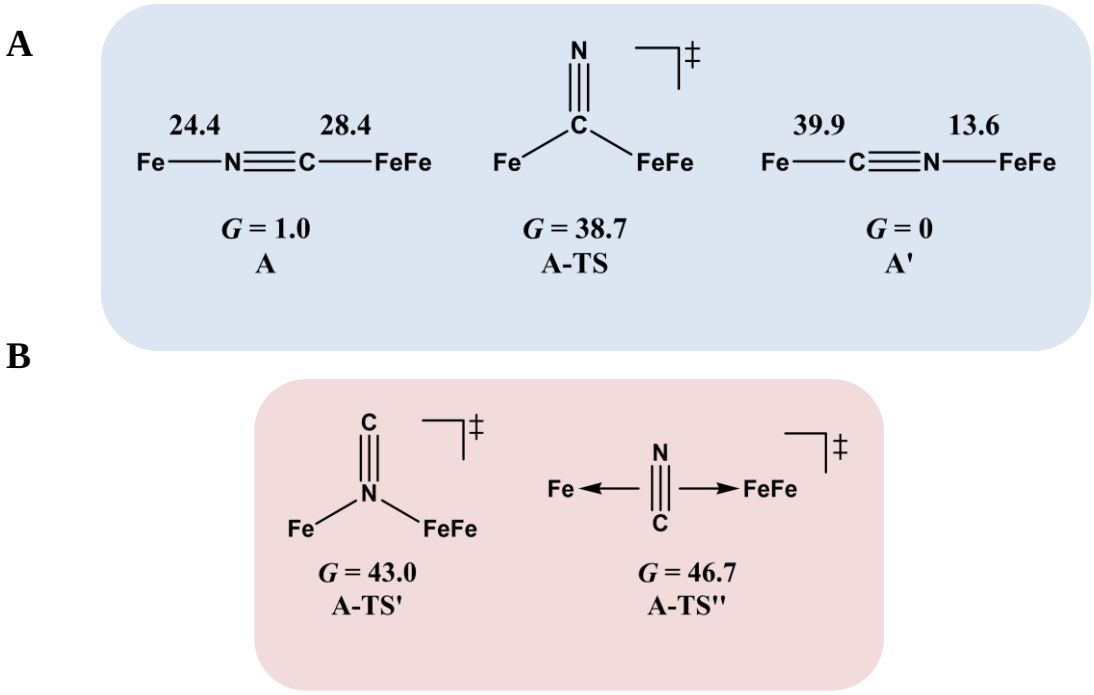

Figure V-3 The transition states connecting isomers. **A**) Cyanide-flipped isomers of complex **A** and a possible transition state connecting them. Gibbs free energies ΔG of bond rupture of these species are given in kcal/mol with thermal and solvation corrections (solvent: acetonitrile). **B**) Other transition states that were optimized.

While many features of the enzyme active site are mimicked in our model complexes, one blatantly obvious difference is the lack of an aza-dithiolate linker connecting the two sulfur atoms. Erdem, *et al.* have shown that the central atom of this linker, in their case NH, is electronically influenced by the ligands attached to the iron.[178] Presumably, the reverse would be true, *i.e.*, changing the atom from NH to CH_2 may be expected to alter the electronics of the Fe-CN unit to some extent, and consequently the energy of cyanide isomerization. The replacement of the bridgehead in **A**, **A'** and **A-TS**

by azadithiolate (adt, -SCH_2NHCH_2S-), *i.e.*, the N bridgehead in [FeFe]-hydrogenase, does not change the energetics significantly. The **Adt-A'** with an Fe-CN-FeFe sequence is still more stable, by 1.2 kcal/mol, than **Adt-A** with an Fe-NC-FeFe sequence. The corresponding transition state **Adt-A-TS**, is 38.6 kcal/mol less stable than **Adt-A'**, similar to the 38.7 kcal/mol seen above.

Internal reaction coordinate and reaction trajectory. The reaction trajectory involving **A-TS** was obtained by intrinsic reaction coordinate (IRC) calculations and is presented in Figure V-4. The reaction coordinate is explained in the following sentences, taking the path from **A-TS** to **A'** as an example. **A-TS** follows the wagging imaginary vibrational motion first until the FeFe moiety approaches the nitrogen (Pts #5-15). In this manner, the FeFe moiety gradually shifts from C to N and ultimately the N-C-Fe angle continues to increase until it is completely linear (Pt #28). After that, the bridging cyanide continues to rotate to align the C-N-FeFe angle and the N-C-Fe re-bends slightly as a side effect until it reaches Pt #50. Finally, both N-C-Fe and C-N-FeFe angles adjust to completely linear as the energy ultimately drops to the local minimum **A'**. As the reaction coordinate is traced downhill, the C-N-FeFe angle increases monotonically. The other branch of the reaction coordinate, *i.e.*, from **TS-A** to **A**, has exactly the same features and the validity of the transition state is confirmed. Such a route is partially related to the mechanism developed for HCN ⇆ CNH isomerization with spectroscopic evidence of the transition state.[179] A similar transition state **D-TS** for complex **D**, which features more bulky substituents on both iron moieties, was estimated to have an even higher barrier of 51.0 kcal/mol**.**

In **D-TS,** both iron moieties are dragged together by the bridging carbon and severe steric repulsion develops. Other trials to locate transition states, including a N-bridged **A-TS'** or a side-on / η^2-bridged **A-TS''** of complex **A**, were attempted but yielded higher barriers, G = 43.0 and 46.7 kcal/mol, respectively (Figure V-3B).

A recent paper[180] expounded on the fact that the nitrogen end of the cyanide anion has a stronger affinity to H-bond than the carbon end. Thus an interesting question is whether properly arranged H-bond providers can compensate the loss of N-M bond and facilitate the flipping. Thus, we tested the effects of one or two waters, one urea and one protonated pyridine as H-bond providers. However, none of them significantly stabilize the transition state.

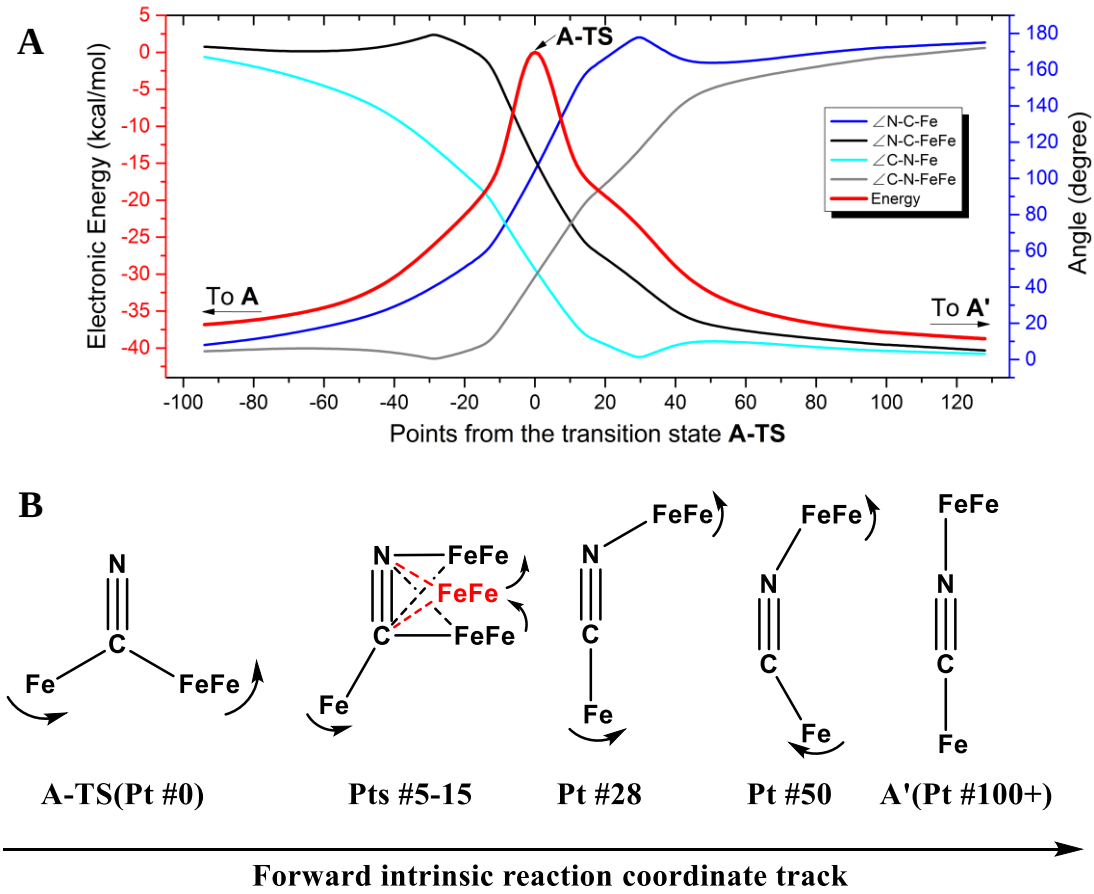

Figure V-4 The intrinsic reaction coordinate of the cyanide linkage isomerization. **A**) Electronic energy and selected metric data plot of the intrinsic reaction coordinate (IRC) connecting **A** and **A'** through **A-TS**. (The left (red) *y*-axis is for energy, and the right (blue) *y*-axis is for bond angles.) **B**) The geometries of selected points on the IRC; the motions are indicated by arrows. The shifting of the FeFe moiety on CN is reflected by the sketches of Pts # 5-15.

To assess the possibilities of intermolecular mechanisms, the isomerization of fragment **1** (Figure V-1A) in complex **A** was first evaluated computationally. The

isomerized species **1'**, with a N-bound terminal cyanide, is 14.6 kcal/mol less stable than **1**. The barrier is 28.2 kcal/mol and the transition state **1-TS** features a side-on cyanide. On top of that, it takes 24.4 kcal/mol to dissociate fragment **1** from **A** (Figure V-3A). Alternatively, a $(CO)_2Fe(NC)$ fragment (**z'**) may be cleaved from complex **A**. The barrier is 14.1 kcal/mol for **z'** to isomerize into fragment **z** (Figure V-1), which is further stabilized by 15.9 kcal/mol compared to **z'**. Such an isomerization is also overwhelmed by the bond rupture energy of 28.4 kcal/mol (Figure V-3A). Therefore the intermolecular mechanisms are actually more difficult to access than the intramolecular one presented above.

Summary. The calculations show that high kinetic barriers prevent the isomerization of the bridging cyanide. These high barriers are attributed to the (partial) rupture of two bonds (M-C and M'-N bonds) at the same time. Unfortunately, both C-Fe and N-Fe bonds are strong in these tri-iron complexes. The reason for such strong dative bonds is that the irons are either low-spin Fe^{I} or low-spin Fe^{II} and have ample vacant orbitals to accept donation from either the C end or the N end of the cyanide. In addition, low valence irons with rich electron densities are also able to provide back-bonding to reinforce the Fe-C bond, and to a smaller extent, the Fe-N bond.

Linkage cyanide isomerization in the models of the cytochrome c oxidase heme-copper active site

Introduction. As indicated by the previous mechanistic study, it is necessary to break, or at least weaken both the C-M bond and the N-M' bond in the M-CN-M' moiety, in order to flip the bridging cyanide. Therefore, a condition to facilitate this process is to have

weak linkage cyanide-metal bonds. Though the trimetallic complexes do not show cyanide linkage isomerization, a survey of the literature revealed several *bona fide* examples of linkage cyanide isomerization either during the formation of the cyanide bridge or immediately after that. The most classic examples are analogs of Prussian Blue (PB, $Fe^{III}_4[Fe^{II}(CN)_6]_3 \cdot xH_2O$): $Fe^{II}_3[Cr^{III}(CN)_6]_2$,[181-183] $Fe^{II}_3[Mn^{III}(CN)_6]_2$,[184]. The linkage cyanide isomerization of $Fe^{II}_3[Cr^{III}(CN)_6]_2$ was discovered in the 1960s, by the IR band changes after heating a sample for hours. [181-183] The reaction indeed is more complex as the Mössbauer spectra identified an Fe^{III}-N-C-Cr^{II} intermediate and indicated that the intramolecular charge transfer between Fe^{II} and Cr^{III} accompanies the linkage isomerization.[185] Subsequent studies reveal the isomerization can also be controlled by the pressure[186-187] and the size of nanoparticles.[188] Though the PB analogs continue to receive attention.[189-190] These cyanide coordination polymers involving an infinite network are essentially not molecular systems and are difficult to model by quantum chemistry methods.

A few molecular complexes were reported to have linkage cyanide isomerization as well and partly reviewed in a 2009 book chapter.[191] One example is a series of molecular models of PB: the cyanide flips during the formation of $[Fe^{II}(tmphen)_2]_3 \cdot [Cr^{III}(CN)_6]_2$,[192] $[Co^{II}(tmphen)_2]_3 \cdot [Cr^{III}(CN)_6]_2$,[193] $[Co^{II}_3(dppe)_4(MeCN)] \cdot [Cr^{III}(CN)_6]_2$,[194] and $[Cu^{II}(Me_3tacn)]_3 \cdot [Fe^{III}(CN)_3(Me_3tacn)]_2$.[195] Each of them features two IR bands corresponding to two kinds of bridging cyanides. Simpler trimetallic examples are also known. Such as the partial isomerization during the synthesis of $Cp(dppe)Fe^{II}$-(μ-CN)-$Fe^{III}Pc$-(μ-CN)-$Fe^{II}Cp(dppe)$ from $[Fe^{III}Pc(CN)_2]^-$ (Pc

= phthalocyaninato) and Cp(dppe)Fe^{II}-Br. The bridging cyanide gradually converts to the sequence Fe^{II}-CN-Fe^{III} over time, as monitored by IR. Similar linkage isomerization is observed if the analogous starting materials Cp(PPh_3)Ru^{II}-Cl and $[Fe^{II}Pc(CN)_2]^{2-}$ are used in the synthesis.[196] Other trinuclear examples are $\{[Cr^{II}(cyclam)(CN)_2]_2 \cdot [(Ru^{II})(bpy)_2]\}^{4+}$ [197] and $\{[Cu^{II}(tpa)_2]\ [(F_8\text{-tpp})Fe^{II}(CN)_3]\}^{3+}$,[198] in which the central metal is pinched by two cis- or trans- bridging cyanides. The magnetic moment measurement and geometric parameters, *i.e.*, M-C and M-N bond lengths, were used to validate the cyanide flipping in the larger tetradecanuclear clusters $\{[L_3M^{III}]_8[Ni^{II}(CN)_4]_6\}^{12+}$ [199-201] M = Cr, Mo and L = tacn, Me_3tacn.

To our knowledge, a limited number of binuclear systems, best suited for computational modeling, show the linkage cyanide isomerization. One example is the reaction between a d^{10} heavy-metal cation Ag^+, Hg^{2+} and various chromium cyano-complexes: $[Cr^{III}CN(H_2O)_5]^{2+}$,[202-203] $[Cr^{III}CN(NH_3)_5]^{2+}$,[204] $[Cr^{III}CN(H_2O)_4(NO)]^{+}$,[205] $[Cr^{III}(CN)_2(H_2O)_4]^{+}$,[203] $[Cr^{III}(CN)_2(NH_3)_4]^{+}$,[204] $Cr^{III}(CN)_2(H_2O)_3(NO)$[206], *cis*-$[Cr^{III}(CN)_2(en)_2]^{+}$[207] and $Cr^{III}CN_3(NH_3)_3$.[203] The linkage isomers Cr-CN-Hg/Ag (the presumed intermediate) and Cr-NC-Hg/Ag (the final product) were established by UV-Vis spectra and polarographic analyses. Direct solid state/crystal structure information is limited for this series. The structural refinement of the complex *cis*-$[(en)_2Cr^{III}(NCAgCN)_2]^{+}$ synthesized from *cis*-$[Cr^{III}(CN)_2(en)_2]ClO_4$ and $AgClO_4$ found the flipped Cr-NC-Ag sequence is more reasonable.[208]

Another example involving two transition metals, $(Tp^{t\text{-}Bu})Zn^{II}$-NC-$Ni^{II}(S'_3)$ was synthesized from $(Tp^{t\text{-}Bu})Zn^{II}$-CN and $[Ni^{II}(S'_3)]_2$, in which S'_3 is bis(2-

mercaptophenyl)sulfide. The linkage isomerization in the product was confirmed by an alternative synthetic route from $[Ni^{II}(S'_3)CN]$ and $(Tp^{t\text{-}Bu})Zn^{II}\text{-}NCCH_3$.[209]

The most interesting examples come from Holm and coworkers, as a couple of the $Cu^{I}\text{-}Fe^{III}$ complexes $[(oep)Fe^{III}\text{-}NC\text{-}Cu^{I}(MeNPy_2)]^{+}$ [210] and $[(oep)Fe^{III}\text{-}NC\text{-}Cu^{I}(Me_5dien)]^{+}$,[211] oep = Et_8-porphyrin. The cyanide from $(oep)Fe^{III}(CN)(py)$ flips when the Cu^{I} unit is added to the system and the bimetallic complexes form, Figure V-5. In contrast, the Cu^{II} analog added to $(oep)Fe^{III}(CN)(py)$ will not initiate a similar isomerization, Figure V-5.[210-211] Another associated species is $[(oep\text{-}CH_2\text{-}CN)Fe^{III}\text{-}NC\text{-}Cu^{I}(NPy_3)]^{+}$;[210] in addition to the cyanide flipping, one molecule of the solvent, acetonitrile, undergoes C-H bond activation, and forms a C-N bond with a nitrogen on the porphyrin. The trimetallic analogue $\{[(NPy_3)Cu^{II}(NC)]_2[Fe^{III}(F_8\text{-}tpp)]\}^{3+}$, does the isomerization as well when synthesized from $\{(NPy_3)Cu^{II}(CN)\}^{+}$ and $(F_8\text{-}tpp)Fe^{III}(PF_6)$, F_8-tpp = F_8- tetraphenylporphyrin.[198]

These Fe-Cu complexes are actually molecular models of the heme-copper active site of the cytochrome c oxidase,[212-213] which features a high-spin Fe(III) coordinated by a porphyrin and a histidine residue (*i.e.*, heme a_3) and a Cu(I) coordinated by three histidine residues. In the molecular models, the bridging cyanide is added to connect the two metals, which lack the support from the protein network.

Specifically, DFT computations address the factors controlling the linkage cyanide isomerization in these bimetallic Cu-Fe complexes in the following paragraphs.

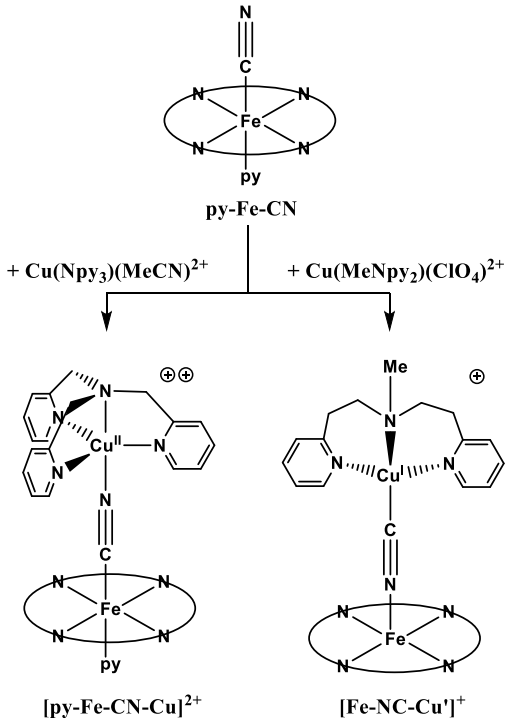

Figure V-5 The selective cyanide isomerization introduced by Cu^{I} moiety.

Methodology. The structures from X-ray diffraction analyses of the Fe precursor (py)(oep)Fe^{III}(CN) (**py-Fe-CN**), the F^{eIII}-Cu^{II} complexes $[(py)(oep)Fe^{III}(CN)Cu^{II}(Npy_3)]^{2+}$ (**[py-Fe-CN-Cu]$^{2+}$**) and the Fe^{III}-Cu^{I} complexes $[(oep)Fe^{III}(NC)Cu^{II}(MeNpy_2)]^{+}$ (**[Fe-NC-Cu']$^{+}$**) were imported as geometric references for optimizations. To simplify the calculations, eight ethyls on oep were replaced by hydrogens. For Cu, Fe, N and the C of the cyanide, 6-311++G(d,p) was used; for the remaining C and H double-ζ basis set 6-31G was used to save resources. Six common functionals B3LYP, M06, M06L, PBE, TPSS, ωB97X, were selected for screening with solvation corrections (SMD model, acetonitrile) and thermal corrections (based on gas-phrase structures). Three criteria were utilized to check the effectiveness of the functionals:

a) the experimental spin states, *i.e.* **py-Fe-CN** (low-spin Fe^{III}), **[py-Fe-CN-Cu]$^{2+}$** (low-spin Fe^{III}) and **[Fe-NC-Cu']$^{+}$** (intermediate- or high-spin Fe^{III}); b) the thermodynamic preferences over experimentally isomerized **[Fe-NC-Cu']$^{+}$** and un-isomerized **[py-Fe-CN-Cu]$^{2+}$**; and c) the thermodynamic preferences of the pyridine dissociation from **[py-Fe-NC-Cu']$^{+}$** and **[py-Fe-CN-Cu]$^{2+}$**.

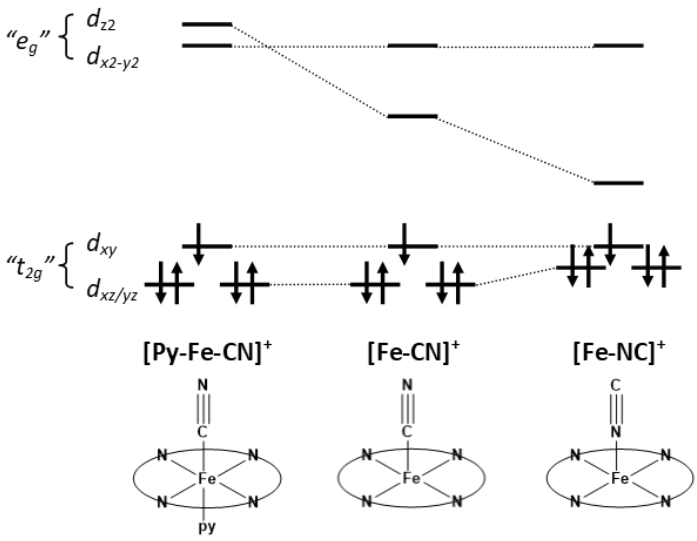

Figure V-6 The orbital line-up of the Fe^{III} depending on its coordination environment. For better comparisons, the iron is set to be doublet.

Screening of functionals by spin states. The precursor **py-Fe-CN** features a low-spin Fe^{III} in the pseudo-O_h coordinate environment. The σ-donations from the coordinating N or C atoms, along with the back-bonding into the porphyrin, pyridine, and cyanide, create a gap between "t_{2g}" and "e_g" sets of the Fe's *d* orbitals and prevent the occupations of either d_{x2-y2} or d_{z2}. (Figure V-6) All functionals attempted reproduced the correct spin states of **py-Fe-CN**, except M06 with a relatively high (27 %) Hartree-Fock exchange. (Table V-1)

The addition of a Cu^{II} fragment $[Cu(Npy_3)]^{2+}$ to the nitrogen end of **py-Fe-CN** does not trigger the linkage cyanide isomerization (Figure V-5) thus it does not dramatically change the coordination environment around the iron; nevertheless, Cu^{II} (d^9) has an unpaired electron and is also a spin center; therefore it couples with the low-spin Fe^{III}, either ferromagnetically or antiferromagnetically to form an overall triplet or singlet, which are rather close in energy.

Table V-1 The relative electronic energies of different spin states by various functionals.

Multiplicity	B3LYP	M06	M06L	PBE	TPSS	ωB97X
			py-Fe-CN			
Doublet	**0.0**	0.0	**0.0**	**0.0**	**0.0**	**0.0**
Quarter	16.9	8.6	15.7	24.9	26.6	27.7
Sextet	13.8	**-4.4**	6.1	33.5	34.3	42.1
			[py-Fe-CN-Cu]$^{2+}$			
Singlet(BS)	**0.0**	0.0	0.0	0.0	0.0	0.0
Triplet	**0.0**	-0.1	**-0.3**	**-0.9**	**-0.4**	**-0.1**
Quintet	7.2	0.7	9.9	20.6	20.5	7.9
Septet	12.4	**-6.2**	4.2	33.4	33.3	11.1
			[Fe-CN-Cu']$^{+}$			
Doublet	0.0	0.0	0.0	**0.0**	**0.0**	0.0
Quartet	-1.4	-8.0	1.5	9.7	9.5	-1.5
Sextet	1.2	-16.8	-6.5	20.2	20.3	0.0
			[Fe-NC-Cu']$^{+}$			
Doublet	2.2	2.8	3.8	5.2	3.4	3.0
Quartet	-7.5	-15.5	-5.6	3.5	3.6	**-7.7**
Sextet	**-5.3**	**-24.0**	**-13.3**	15.3	14.0	-7.3

In contrast, the addition of the closed-shell **Cu'** (Cu^{I}, d^{10}) unit $[Cu(MeNpy_2)]^{+}$ causes the cyanide flipping, Figure V-5. The coordination environment of the iron in the resulting **[Fe-NC-Cu']$^{+}$** is dramatically changed. The iron loses its axial pyridine and the remaining axial ligand, the N-bound cyanide, is much weaker σ-donor than a C-bound

cyanide, leading to a relatively low-lying d_{z2} orbital, Figure V-6. The back-bonding from the iron to the cyanide is also weakened with the flip (CN can be a weak pi-donor in this case), which results in a slight rise of the energy of Fe's d_{xz} and d_{yz} orbitals. Experimentally, evidence from EPR rules out the possibilities of a low-spin Fe with g_{pend} = 5.81 and g_{para} = 2.00.[210] Pure functional TPSS failed to reproduce this experimental spin state and prefer to have a doublet ground state for **[Fe-NC-Cu']**$^+$. Both pure functionals TPSS and PBE predicted the **[Fe-CN-Cu']**$^+$ is more stable than the flipped, experimental product **[Fe-NC-Cu']**$^+$ and failed the test, Table V-1. B3LYP and ωB97X predicted an intermediate-spin Fe while M06 and M06L, high-spin Fe for **[Fe-NC-Cu']**$^+$. The functionals B3LYP, M06, and ωB97X passed the first round of screening, among which ωB97X was selected to evaluate the kinetics of the linkage isomerism on **Fe-NC-Cu'**$^+$. It was revealed the functionals B3LYP and M06 incorrectly predict the thermodynamics of the pyridine dissociation from these complexes (*vide infra*).

***The isomerization of [Fe-NC-Cu']*$^+$.** The cyanide-isomerized complex, **[Fe-NC-Cu']**$^+$ is synthesized with the procurers **py-Fe-CN** and **Cu'**. Besides the isomerism process, the pyridine on the iron is also cleaved before or after the isomerism. The Gibbs free energies of the isomer pairs of **[py-Fe-CN-Cu']**$^+$, **[py-Fe-NC-Cu']**$^+$, and **[Fe-CN-Cu']**$^+$, [**Fe-NC-Cu']**$^+$ in different spin states were calculated by ωB97X and tabulated in Table V-2. The ground state of the presumed immediate product from two precursors, **[py-Fe-CN-Cu']**$^+$ was determined to be a doublet with a low-spin iron, and its quartet and sextet states are higher in energy by 6.0 and 9.0 kcal/mol respectively. In contrast, the cyanide-isomerized product **[py-Fe-NC-Cu']**$^+$ has a quartet ground state and is lower by 1.6 kcal/mol with a

more stable d_{z2} orbital, compared to the doublet counterpart. It is thermodynamically feasible to have the linkage cyanide isomerization, even with the axial pyridine attached.

The removal of the pyridine from the un-isomerized **[py-Fe-CN-Cu']**$^+$ changes the ground state of the resulting **[Fe-CN-Cu']**$^+$ complex to a quartet, though this ligand cleavage is thermodynamically unfavored by 3.1 kcal/mol. In contrast, the cyanide cleavage from the flipped, quartet **[py-Fe-NC-Cu']**$^+$ is thermodynamically favored, by 1.7 kcal/mol. It is clear by either switching the axial binding atom of the cyanide from C to N or removing the axial N-binding pyridine, the iron tends to change from the low-spin state to the intermediate-spin state, with the now less destabilized d_{z2} orbital singly occupied, Figure V-6. In other words, the quartet ground state (See Figure V-7 for spin densities) of the experimentally observed product **[Fe-NC-Cu']**$^+$ is determined by the synergic effects of the cyanide isomerization and the pyridine removal. The final product **[Fe-NC-Cu']**$^+$ is more stable than the two possible intermediate **[py-Fe-CN-Cu']**$^+$ or **[Fe-CN-Cu']**$^+$ by 3.3 and 6.4 kcal/mol, respectively, and is the most stable species. In conclusion, the calculated thermodynamic parameters indicate an inverted Fe^{III}-NC-Cu^{I} sequence, regardless of the coordination of the axial pyridine.

Table V-2 Relative Gibbs free energies (kcal/mol) of isomers of **[(py-)Fe-NC-Cu']$^+$** with different multiplicities. Energetics were calculated by ωB97X.

Multi-plicity	**[py-Fe-CN-Cu']$^+$**	**[py-Fe-NC-Cu']$^+$**	**[Fe-CN-Cu']$^+$**	**[Fe-NC-Cu']$^+$**
Doublet	0.0	-0.4	5.8	8.9
Quartet	6.0	-1.6	3.1	**-3.3**
Sextet	9.0	1.3	3.3	-2.6

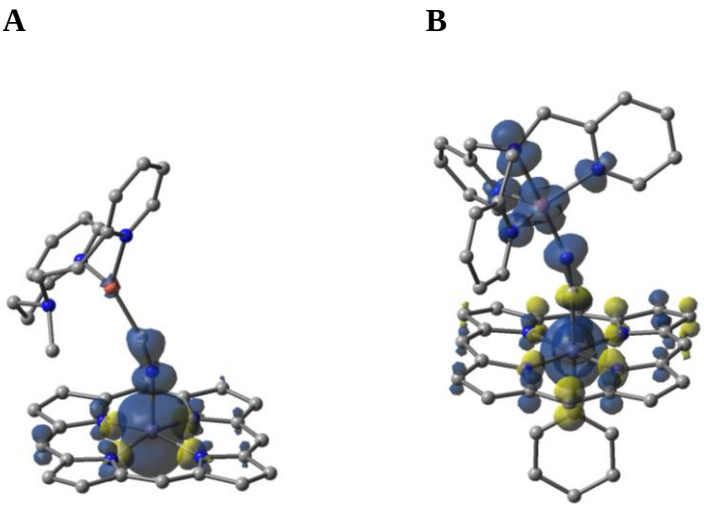

Figure V-7 The spin densities of cyanide-bridged species. **A**) quartet **[Fe-NC-Cu']$^+$** and **B**) triplet **[py-Fe-CN-Cu]$^{2+}$** (by ωB97X).

The isomers of [py-Fe-CN-Cu]$^{2+}$. Similarly, the relative Gibbs free energies of the relevant isomers were tabulated in Table V-3. The **Cu** (Cu^{II}, d^9) moiety is open-shell with one unpaired electron. Therefore, the overall multiplicity of each individual complex is determined by ferromagnetic or antiferromagnetic coupling of Fe^{III}(d^5) and Cu^{II}(d^9). The ground state of **[py-Fe-CN-Cu]$^{2+}$** is a triplet, *i.e.* ferromagnetic coupling of a low-spin Fe^{III} and a Cu^{II} (See Figure V-7 for spin densities). The corresponding broken-symmetry

singlet featuring antiferromagnetic coupling is 0.7 kcal/mol higher. The quintet and the septet, created by ferromagnetically coupling an intermediate- and high-spin Fe^{III} and Cu^{II}, are still higher in energy by 4.4 and 6.4 kcal/mol respectively.

Though **[py-Fe-CN-Cu]$^{2+}$** is most stable with a low-spin iron on the triplet ground state before isomerization, the cyanide isomerization and the pyridine removal favor the iron in the intermediate-spin, which would then create an overall quintet as the ground state by ferromagnetic coupling with Cu^{II}. The product, cyanide-isomerized, pyridine-cleaved **[Fe-NC-Cu]$^{2+}$** (quintet) indeed is more stable, but only by -0.5 kcal/mol compared to the un-isomerized, pyridine-retained **[py-Fe-CN-Cu]$^{2+}$** (triplet). The small energy difference indicates the carbon end of the cyanide shows less preference over Cu^{II}, in contrast to Cu^{I}. The Cu^{II} unit may not provide a similar level of back-bonding. However, the X-ray diffraction of **[py-Fe-CN-Cu]$^{2+}$** showed no proof of the isomerism at all. Therefore, some other factors must have overridden the thermodynamics, *vide infra*.

The product **[Fe-NC-Cu]$^{2+}$** may also have various multiplicities resulted from different coupling modes between Fe and Cu. Specifically for its singlet and triplet states, the moiety of [Fe(porphyrin)] does have an overall spin S = 0.5, coupled to Cu^{II} antiferromagnetically or ferromagnetically. However, the population analysis revealed a formal oxidation state of Fe^{II}-(porphyrin)$^{-}$, resulted from a ligand-metal charge transfer (LMCT) from porphyrin^{2-} to Fe^{III}. (Figure V-6) The transferred electron is accepted by the d_{z2} as it is low in energy. Then the iron has a configuration of $(d_{xz})^2(d_{yz})^2(d_{xy})(d_{z2})$. The intermediate-spin Fe^{II} (S = 1) and porphyrin^{-} (S = 0.5) are further anti-ferromagnetically coupled.

Table V-3 Relative Gibbs free energies (kcal/mol) of isomers of **[(py-)Fe-NC-Cu]$^{2+}$** with different multiplicities. Energetics were calculated by ωB97X.

Multi.	**[py-Fe-CN-Cu]$^{2+}$**	**[py-Fe-NC-Cu]$^{2+}$**	**[Fe-CN-Cu]$^{2+}$**	**[Fe-NC-Cu]$^{2+}$**
Singlet (AF[a])	0.7	3.4	8.1	9.0[b]
Triplet (F[a])	0.0	2.6	7.4	8.4 [b]
Quintet (F[a])	4.6	-0.2	2.7	**-0.5**
Septet (F[a])	6.6	2.4	5.0	2.6

a. F and AF refer to ferromagnetic and antiferromagnetic coupling respectively.

b. LMCT occurs inside the [Fe(porphyrin)] moiety, see text.

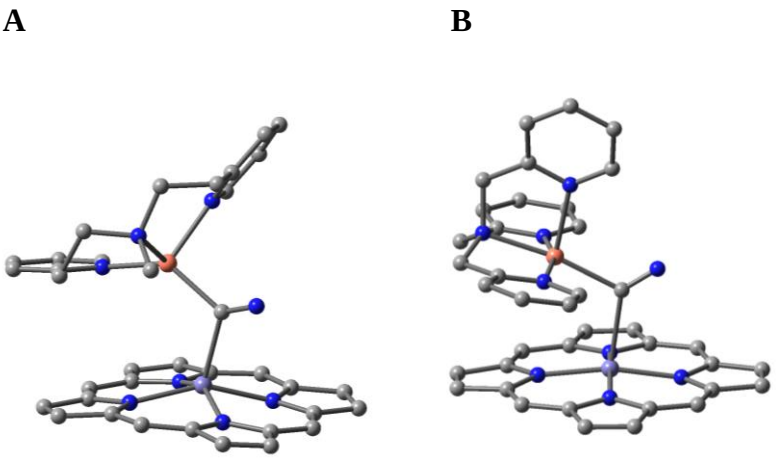

Figure V-8 Representative transition state geometries during cyanide isomerization. **A**) the sextet transition state between **[Fe-CN-Cu']$^{+}$** and **[Fe-NC-Cu']$^{+}$**; **B**) the quintet transition state between **[Fe-CN-Cu]$^{2+}$** and **[Fe-NC-Cu]$^{2+}$**.

Isomerization mechanism. According to this DFT approach, CN linkage isomerism in the Cu^{I}-Fe^{III} and Cu^{II}-Fe^{III} complexes goes through a transition state featuring a C-bound bridging cyanide, which was determined to be the most accessible transition state in the

study of the trimetallic compounds in the previous section. Though the geometries of these transitions states (see Figure V-8 for representative geometries) are similar on the potential energy surfaces (PES) for different multiplicities, the barrier heights (Table V-4) vary depending on the spin states of Fe and the oxidation states of Cu. This behavior arises because the transition state for cyanide isomerization requires weakening, if not complete rupture, of both the Fe-C and the Cu-N bonds, whose strength is relevant to the properties of the metals. The relative barrier between the doublet TS and the doublet **[py-Fe-CN-Cu']**$^{+}$ is 22.9 kcal/mol, approximately two times the barriers of the quartet (9.2 kcal/mol) and the sextet (8.8 kcal/mol) transition states. The intermediate-spin and high-spin Fe^{III} have one of the unpaired electrons on the d_{z2} metal-axial ligand antibonding orbital and can dramatically reduce the Fe-C bond strength by a half, Figure V-6. However, the extra unpaired electron of a high-spin Fe^{III}, excited from either d_{xz} or d_{yz} to the d_{x2-y2} metal-axial ligand antibonding orbital, only has a marginal effect on the barrier height, as it has little effects on the Fe-CN bond strength. The same explanation is also applicable to the transition state of the pyridine-free **[Fe-CN-Cu']**$^{+}$. However, the absolute heights of quartet and sextet TS of **[Fe-CN-Cu']**$^{+}$ are actually lower than those of **[py-Fe-CN-Cu']**$^{+}$, whose quartet and sextet are destabilized by the axial σ donation from the pyridine, *vide supra*. The lowest absolute barrier for **[Fe-CN-Cu']**$^{+}$ to isomerize is 12.4 kcal/mol on the sextet PES, while the quartet PES barrier of 13.4 kcal/mol follows closely, indicating a kinetically allowed isomerization process in the Fe^{III}-Cu^{I} complex.

Table V-4 The height of the transition state featuring a C-bound bridging cyanide. Both absolute height and relative height (in parenthesis, with respect to its immediate precursor in the same spin state) are presented in kcal/mol.

Multi-plicity	**[Py-Fe-CN-Cu']$^+$** **[Py-Fe-NC-Cu']$^+$**	**[Fe-CN-Cu']$^+$** **[Fe-NC-Cu']$^+$**	Multi-plicity	**[Py-Fe-CN-Cu]$^{2+}$** **[Py-Fe-NC-Cu]$^{2+}$**	**[Fe-CN-Cu]$^{2+}$** **[Fe-NC-Cu]$^{2+}$**
Doublet	22.9 (22.9)	22.9 (17.1)	Singlet	24.7 (24.0)	23.9 (15.8)
Quartet	24.2 (9.2)	13.4 (10.3)	Triplet	24.1 (24.1)	23.5 (16.1)
Sextet	17.8 (8.8)	**12.4 (9.1)**	Quintet	16.4 (11.9)	**16.1 (13.4)**
			Septet	19.5 (12.9)	17.8 (12.8)

Another observation from the absolute barrier heights is that the linkage cyanide isomerization of **[py-Fe-CN-Cu]$^{2+}$** is less favored kinetically, regardless of its marginal thermodynamic advantage. The absolute heights of the lowest barriers are 16.4 and 16.1 kcal/mol, with or without the pyridine on the quintet PES. Such barriers indicate a slower reaction at room temperature and help explain the absence of the experimental isomerized product, in addition to the absence of a strongly favored thermodynamic preference. The barrier difference between **[(py)-Fe-CN-Cu']$^+$** and **[(py)-Fe-CN-Cu]$^{2+}$** is rooted in the N-Cu bonding. The Cu^I, possessing a fully filled *3d* subshell, can only accept σ donations by its high-energy 4*s* / 4*p* sub-shells. Therefore, the bond formed is relatively unstable and is subject to dissociation easily. The Cu^{II} with one singly occupied *d* orbital is more prone to establish a stronger dative bond with the coordinating nitrogen, but on the other hand, the strong bond contributes to a higher barrier in the linkage cyanide isomerization.

Pyridine removal. As shown in Table V-2, the loss of axial pyridine from either **[py-Fe-CN-Cu']$^+$** or **[py-Fe-NC-Cu']$^+$** stabilizes intermediate- and high-spin irons. Therefore, the isomerization barrier on the quartet PES of **[Fe-CN-Cu']$^+$** becomes accessible. It turns

out the pyridine loss is essential before the isomerization can take place, though this dissociation leads to a small energy rise and is likely reversible if the linkage isomerization does not follow immediately. After the isomerization, the pyridine re-association becomes endothermal, at which moment the loss of pyridine is finalized, as observed in the crystal structure of **[Fe-NC-Cu']**$^+$. The change of thermodynamic preferences is again attributed to the ground spin state and the occupancy of the d_{z2} orbital, which is discussed earlier. As a result, cyanide isomerization and pyridine removal, are mutually stranded on Holm's Fe^{III}-CN-Cu^I systems. The functional M06L failed here as it predicted that **[py-Fe-NC-Cu']**$^+$ is more stable than the experimental product **[Fe-NC-Cu']**$^+$. The B3LYP also failed because it incorrectly predicted pyridine dissociation from the experimentally stable product **[py-Fe-CN-Cu]**$^{2+}$.

The evaluation of the kinetics of pyridine loss requires special handling. The dissociation curves (electronic energy, w/ or w/o solvation corrections) of the Fe-N(py) bond from relaxed scans (with additional restrains added to keep the pyridine plane perpendicular to the porphyrin plain) are provided in Figure V-9. The dissociation curves are monotonically increasing on the gas-phase PES of all three multiplicities and do not have local maximums. A major negligence in these dissociation curves is the entropy gain in the dissociation. The application of the SMD solvation model partially relieves the problem by including solvent enthalpy but still fails to create local maximum(s) (see the caption of Figure V-9 for an exception). The enthalpy from the molecular motions is a necessary component of the Gibbs free energy but ultimately very few mature algorithms (*e.g.* variational transition state theory)[214] are available for non-stationary points (*i.e.*, the

points in the relaxed scans) on the PES and they can hardly process organometallic compounds to a satisfactory extent. This portion of enthalpy is expected to increase monotonically with extending bond lengths and to reduce the overall Gibbs free energy. However, the existence and the position of the barrier depend on the relative curvatures of the electronic energy (w/ solvation correction) and thermal corrections. One may estimate the high limit of the Gibbs free energy barrier, which is 19.2 kcal/mol on the quartet PES (estimated with no thermal corrections at all). The actual barrier should be significantly lower and the low limit of Gibbs free energy barrier on quartet PES is 6.0 kcal/mol (*G* of quartet **[py-Fe-CN-Cu']**$^{+}$, Table V-2). Another significant feature of Figure V-9 is that the curves cross each other, indicating a change of the ground state multiplicity when the N(py)-Fe bond is elongated and weakened during the dissociation.

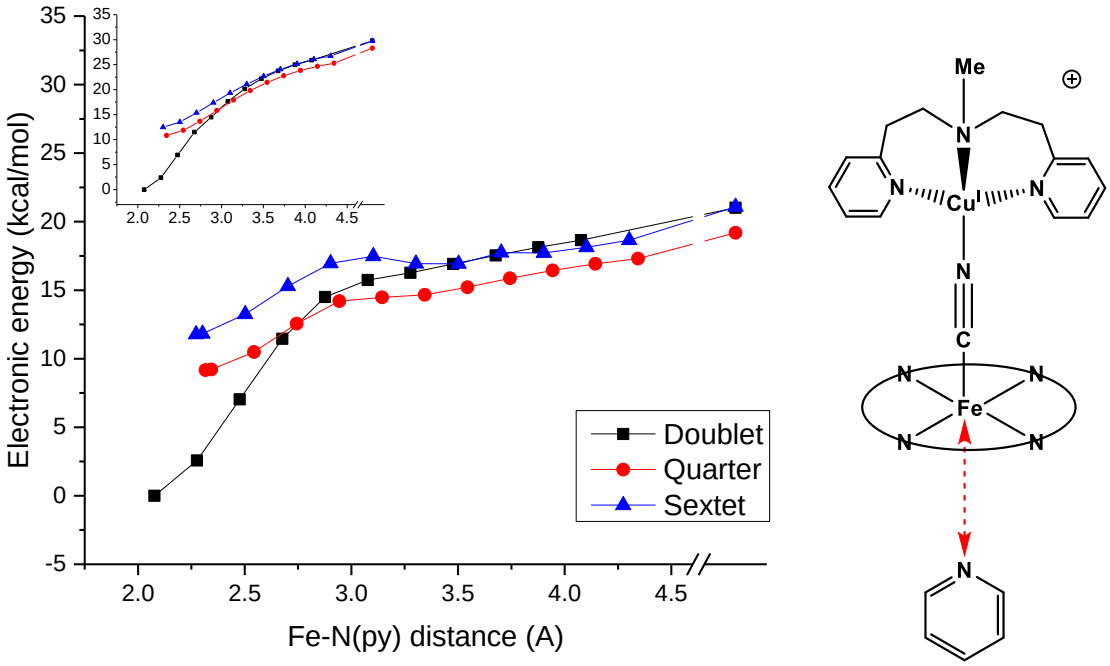

Figure V-9 The pyridine dissociation curves (the relaxed scan of the N(py)-Fe bond of **[py-Fe-CN-Cu']**$^{+}$) on PES of different multiplicities. The main panel contains solvation corrections while the inset panel does not. The pyridine was restrained to leave perpendicularly to the porphyrin. The thermal corrections are not available on most points (i.e. non-stationary points). There is a local maximal on the sextet curve, caused by the geometric variations on the Cu^{I} fragment in the restricted optimization; it does not indicate a transition state.

Summary. The occurrence of cyanide linkage isomerization depends on thermodynamic preferences and kinetic barriers. The carbon end of the cyanide is "soft" in the hard-soft acid-base theory and prefers an electron-rich "soft" metal center; the nitrogen end is "hard" and prefers a more oxidized "hard" metal. To make the isomerization possible, the initial

orientation of the bridging cyanide, as pre-determined by the reagent used, must be mismatched to gain the driving power. This isomerization involves shifting of the metals on both ends of the cyanide, and (partial) bond breakage processes contribute to the barriers. And the strength of involved metal-cyanide bonds depends on the spin-states and the oxidation-states of the metals, which may have the flexibility to go to different spin states to achieve lower barriers. Particularly for Holm's Fe^{III}-CN-Cu^{I} system, the initial linkage cyanide sequence is determined by the reagents **py-Fe-CN** and **Cu'**; the Cu^{I} is much softer than Fe^{III}, therefore the isomerization is thermodynamically favorable. The Cu^{I} is also a saturated d^{10} species which forms a weak N-Cu bond while Fe^{III} may go to the intermediate-spin and high-spin states to put its *d* electrons on the d_{z2} orbital to weaken the Fe-C bond. Loss of the axial pyridine facilitates this process as well. With an intermediate- or high-spin Fe^{III}, the barrier of the isomerization is reduced to a much lower number so that the reaction becomes possible. The counterpart Fe^{III}-CN-Cu^{II} complex may also have an intermediate- or high-spin Fe^{III} to weaken the Fe-C bond but the Cu^{II} has a stronger bond with the nitrogen and this adds to the overall barrier. Therefore, the linkage cyanide isomerization of the Fe^{III}-CN-Cu^{II} complex was not observed.

CHAPTER VI

MECHANISM OF REACTIONS RELATED TO THE BRIDGING THIOLATES ON THE MODELS OF HYDROGENASE

C-H bond activation

Introduction. The remarkable efficiency of [FeFe]-hydrogenase ([FeFe]-Hydrogenase) enzymes is related to an equally remarkable arrangement of components that provide a low energy pathway for H-H bond cleavage and formation. Many lines of evidence point to the function of an amine base, strategically placed in a dithiolate cofactor, as a shuttle for protons transferring to and from the Fe_d (the iron distal to the $[Fe_4S_4]$ sub-cluster that acts as a redox level switch to the two iron subsite), to assist the proton-coupled electron transfer processes.[54, 72, 215-221] Inspired by the important structural pendant base feature of [FeFe]-Hydrogenases, DuBois and co-workers devised a series of pendant amine base-containing diphosphine ligands that optimize mono-nickel and mono-iron complexes as sustainable, highly active base-metal catalysts for the H-H heterolytic formation and cleavage.[99, 101, 222-225] Additional studies have determined that the internal amine in such chelating diphosphine ligands installed on [FeFe]-Hydrogenase active site models can also

---

This chapter is primarily reproduced form two manuscripts with permission: Zheng, D.; Wang, N.; Wang, M.; Ding, S.; Ma, C.; Darensbourg, M. Y.; Hall, M. B.; Sun, L. *J. Am. Chem. Soc.* **2014,** *136*, 16817-16823. Crouthers, D. J.; Ding, S.; Denny, J. A.; Bethel, R. D.; Hsieh, C.-H.; Hall, M. B.; Darensbourg, M. Y. *Angew. Chem.* **2015,** *127*, 11254-11258. The author of this dissertation primarily contributed the computational studies.

act as a proton transfer relay and facilitate iron-catalyzed reduction of protons and oxidation of hydrogen.[226-232]

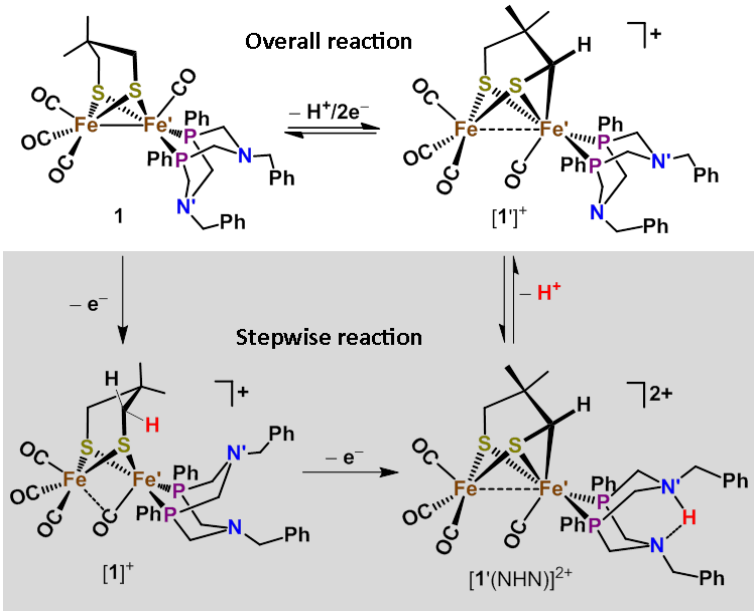

Figure VI-1 Summary of the oxidation reaction of the diiron complex. The top half summarizes the overall reaction of **1**, discovered in this work and the bottom, shaded area gives the observed intermediates.

In the process of catalytic activation of H_2 with transition metals, the σ-type (η^2-H_2)·M interaction can lead to both homolytic and heterolytic H-H cleavage, with the former being prominent with readily oxidizable (typically third row) transition metals; the latter occurs with electrophilic metals in the presence of external bases. Despite similar homolytic H-H and C-H bond energies, the steric encumbrance from carbon substituents, as well as the directionality of orbital overlap, has relegated activation of C(sp^3)-H bonds largely to noble metals under harsh conditions.[233] As functional group tolerance is a

requirement of most synthetic applications in organic chemistry, research into C–H activation under mild and sustainable conditions is a worthy and ongoing challenge to chemists.[234]

Herein we report an intramolecular iron-mediated C(sp^3)-H heterolysis in double oxidation of an [FeFe]-Hydrogenase model at ambient conditions, with an assist of pendant amine base of diphosphine ligand. Figure VI-1 shows the parent complex of this study, (μ-dmpdt)[$Fe(CO)_3$][Fe'(CO)($P^{Ph}_2N^{Bn}_2$)] (**1**, dmpdt = 2,2-dimethyl-1,3-propane-dithiolate; $P^{Ph}_2N^{Bn}_2$ = 1,5-dibenzyl-3,7-diphenyl-1,5-diaza-3,7-diphosphacyclooctane), along with products derived from oxidation and deprotonation. The reaction process is an account of the competition between two Lewis bases, the C-H σ-bond and the lone pair electrons of the pendant amine, for the Lewis acid site of iron. The ultimate path to stability requires a synchrony of molecular motions that creates a favorable structure with a 6-coordinate Fe^{II}, an Fe-C bond, and a protonated amine. DFT studies have identified a mechanistic pathway for the experimentally observed C-H activation with illustration of the roles played by the versatile pendant amine.

Summary of experiments. The structures of **1**, [**1**'(NHN)]$^{2+}$ and [**1**']$^{+}$ presented in Figure VI-1 were obtained from X-ray diffraction analyses; the structure of the single-oxidized [**1**]$^{+}$ was implicitly assigned according to IR spectrum, which shows a low CO vibrational frequency indicative of a bridging position and EPR spectral data along with computational studies which imply an unpaired electron on Fe'^{I} with hyperfine coupling from two phosphors. Two successive oxidations of **1** lead to the activation of the C-H bond on the bridging dithiolate and result in an Fe-C bond with the cleaved proton pinched

by the two amines of the $P^{Ph}_2N^{Bn}_2$ ligand, as one sees in [**1**'(NHN)]$^{2+}$. With added exogenous base, [**1**'(NHN)]$^{2+}$ loses the proton and coverts into [**1**']$^{+}$. A reference compound **2,** (μ-dmpdt)[Fe(CO)$_3$][Fe'(CO)($P^{Ph}_2C_5$)], with an amine-free cyclodiphosphine ligand,[99] does not show a comparable C-H bond activation.

The experiments raise a few questions: 1) How does the amine on the N_2P_2 ligand assist the C-H bond activation? 2) Why is the β-C-H bond on the dithiolate preferred for activation to create a S-C-Fe three-membered ring instead of other C-H bonds? 3) Finally, how does the dithiolate and the N_2P_2 ligand subtly change their conformations during the reaction. These questions are investigated by the following computational study.

Computational mechanistic study. Hereafter the designations of all computed species are given *in italic* to distinguish them from their experimental counterparts. The atoms that are directly involved in the β-C-H bond activation are marked with a prime: C', H', N' and Fe'.

For the parent complex **1**, the computational study reveals that ***1L*** (Figure VI-2) with the bridgehead of FeS_2C_3 ring pointing towards the Fe(CO)$_3$ moiety is 4.6 kcal/mol more stable than its counterpart ***1R*** featuring the bridgehead orientated to the Fe'(CO)(P_2N_2) unit. One-electron oxidation of ***1L*** directly produces ***[1]$^+$La*** with a geometry like that of ***1L***. Overcoming a few small barriers, ***[1]$^+$La*** converts into ***[1]$^+$Rb***, the most stable isomer of [**1**]$^+$. The ***[1]$^+$Rb*** features a bridgehead methyl pointing to the vacant site of rotated Fe'(CO)(P_2N_2) moiety with the apical CO beneath the S_2P_2 plane. The rotation of Fe'(CO)(P_2N_2) and (semi-)bridging carbonyl reduces the Fe-Fe' bond character on the SOMO. Concomitantly, the spin density resides on Fe', consistent with

the observed ^{31}P hyperfine couplings in the EPR spectrum of [**1**]$^{+}$. An oxidation state assignment of $Fe^{II}Fe'^{I}$ is given to ***[1]*$^{+}$*Rb***, similar to the precedent H_{ox} models.[1, 67-70, 235-237] A weak interaction between a hydrogen from the bridgehead methyl and the iron vacant site (*d*(Fe'-H) = 2.579 Å, *d*(C-H) = 1.103 Å) is realized and may contribute to the overall stabilization of ***[1]*$^{+}$*Rb***.[238]

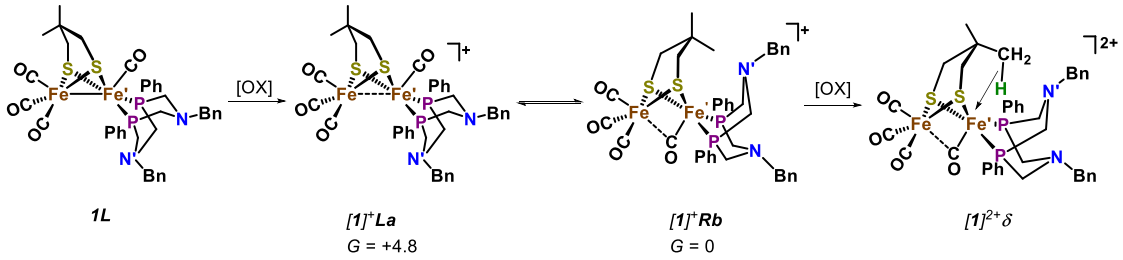

Figure VI-2 Key species in the two successive oxidation steps of the diiron complex. Energy values for the derivatives of **1** are given in kcal/mol.

Further oxidation of ***[1]*$^{+}$*Rb*** yields ***[1]*$^{2+}$*δ***, with concomitant formation of a 2-electron δ-agostic interaction[239-241] between the δ-C-H bond on the bridgehead methyl and Fe' (*d*(Fe'-H) = 1.844 Å, *d*(C-H) = 1.145 Å). Such a δ-agostic interaction in ***[1]*$^{2+}$*δ*** could not lead to the δ-C-H activation due to a relatively high barrier (13.0 kcal/mol) of ***TS1*** (Part I in Figure VI-3). The high barrier is likely attributed to a combination of poor positioning of the C-H bond relative to Fe' (poor overlap of orbitals), the introduction of steric strain into the originally relaxed $Fe'S_2C_3$ ring, and the lower availability of pendant amine (*d*(N'···H) = 2.388 Å in ***[1]*$^{2+}$*δ***, compared to *d*(N'···H') = 2.234 Å in ***[1]*$^{2+}$*β*** discussed later. In fact, there is an alternative pathway leading to the experimentally observed product [**1**'(NHN)]$^{2+}$ with a series of lower barriers.

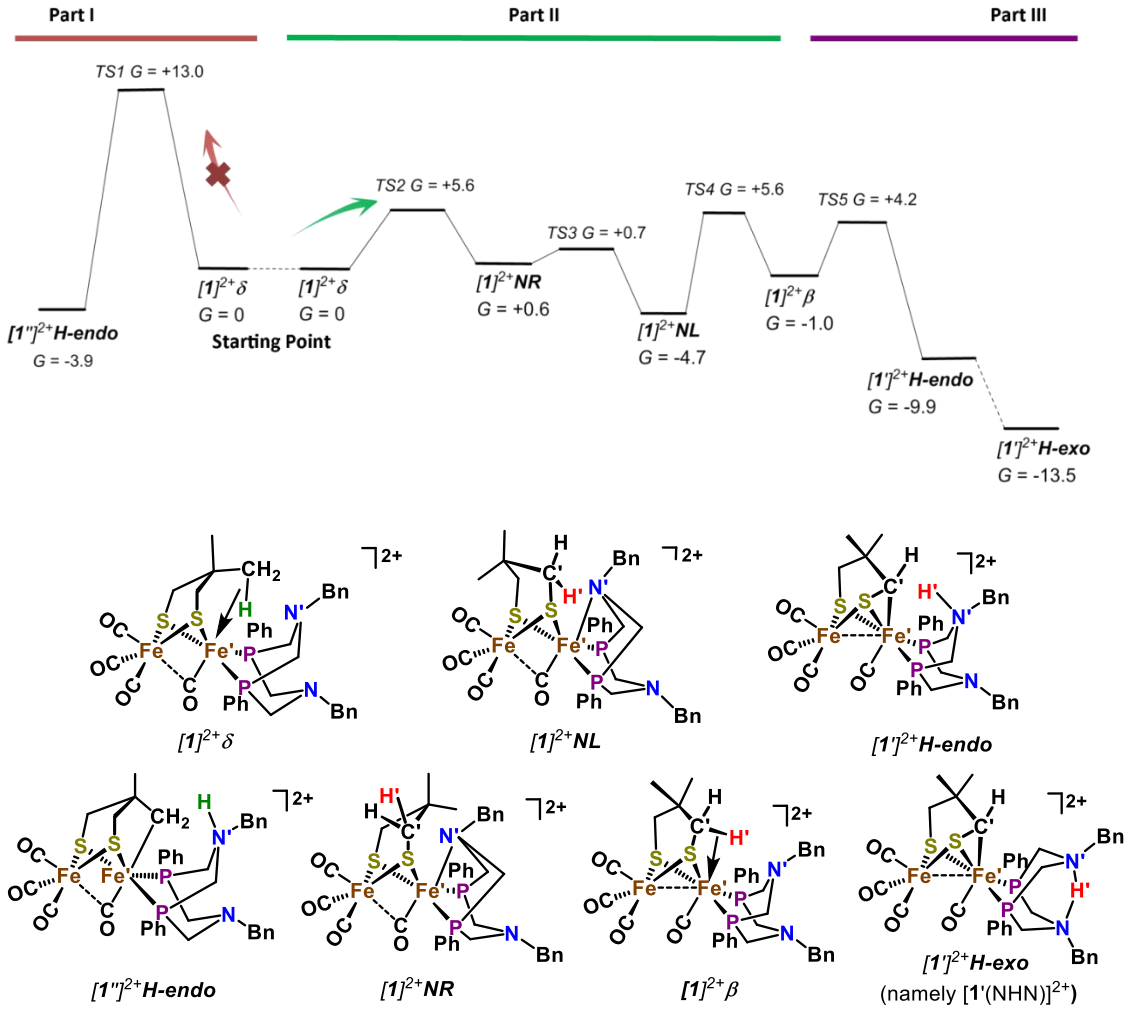

Figure VI-3 Energy profile of β-C-H bond activation and related intermediates. The energy profile (in kcal/mol) contains three parts: I. The direct activation of δ-C-H bond (The direction of reaction in part I is from "starting point" to left); II. The conversion between δ-agostic interaction and β-agostic interaction; III. The activation of β-C-H bond aided by the pendant amine base.

This lower energy path (Figure VI-3, Parts II and III) begins with the displacement of the δ-agostic interaction by a strained Fe'-N' interaction from the pendant amine,

overcoming a shallow barrier ***TS2*** of 5.6 kcal/mol to form $[\mathbf{1}]^{2+}\mathbf{NR}$. The dative bond between Fe' and N' (d(Fe'-N') = 2.234 Å) is not optimal due to the steric strain of the Fe'PCNCP ring; it is elongated compared to a bond between an Fe^{II} and analogous free amine (shorter by ~ 0.15 Å). Nevertheless, the pendant amine serves as a "placeholder" in $[\mathbf{1}]^{2+}\mathbf{NR}$, to occupy the vacant site and saturate the coordination potential of Fe'^{II}. The entire structure further stabilizes itself by swinging the $Fe'S_2C_3$ ring from the boat conformation in $[\mathbf{1}]^{2+}\mathbf{NR}$ to the chair in $[\mathbf{1}]^{2+}\mathbf{NL}$ through ***TS3***. A consequence of such boat-chair conversion is that the β-C'-H' bond on the dithiolate linker is brought close to Fe' in $[\mathbf{1}]^{2+}\mathbf{NL}$. At this stage, the "placeholder" pendant amine could be replaced by a β-agostic interaction as shown in $[\mathbf{1}]^{2+}\boldsymbol{\beta}$. During this replacement, the $Fe'S_2C_3$ ring distorts, as reflected in ***TS4***. The distortion helps the β-C'-H' bond approach Fe' sufficiently close that a σ-complex could be formed, in which the β-C'-H' bond length (d(C'-H') = 1.184 Å) is significantly elongated; the distortion also reorganizes the coordination environment, especially reducing the Fe'···H', Fe'···C', and N'···H' distances (d(Fe'···H') = 1.802 Å, d(Fe'···C') = 2.308 Å, d(N'···H') = 2.308 Å), in a way that leads to facile β-C'-H' bond heterolysis. Eventually, the β-C'-H' activation occurs in a concerted fashion; as the proton cleaved from the β-C'-H' bond transfers to the pendant amine, the residual electron pair on carbon forms the Fe'-C' bond, producing $[\mathbf{1'}]^{2+}\mathbf{H\text{-}endo}$. The proton at the internal amine could transfer from endo to exo position, forming a more stable species $[\mathbf{1'}]^{2+}\mathbf{H\text{-}exo}$, in which the proton is pinched and stabilized by two pendant amines of P_2N_2 ligand as shown in the crystal structure of $[\mathbf{1}'(NHN)]^{2+}$. Similar proton transfer has been reported by DuBois *et al.* for the mononuclear nickel complexes containing a P_2N_2 ligand.[95, 242] The

experimental results clearly show that the proton at the internal amine can be permanently removed by an extrinsic base to form the final product [**1**']$^+$.

Summary. Two-electron oxidation of the [FeFe]-Hydrogenase model (**1**) bearing a $P^{Ph}{}_2N^{Bn}{}_2$ ligand with pendant amine bases leads to an intramolecular iron-mediated C-H heterolysis. In fact, such a C-H bond activation cannot take place for the analogue, complex **2**, having a $P^{Ph}{}_2C_5$ without the built-in, pendant base. The contrasting oxidative reactivities of **1** and **2** clearly indicate that the pendant amine in the second coordination sphere plays a critical role in the C-H heterolysis. The pendant amine serves as a final proton shuttle, and also as a regulator of molecular transformation during the process of C-H heterolysis. The doubly oxidized product [**1**']$^+$ is an unique $Fe^{II}Fe^{II}$ mimic of [FeFe]-Hydrogenases with a rigid FeSC three-membered ring while having no (semi)-bridging CO. Computational results suggests a pathway involving the formation of a Fe$\cdots\eta^2$-CH β-agostic coordination intermediate, followed by the deprotonation of η^2-CH with the help of an internal amine base. Of particular interest, the C-H heterolysis under ambient conditions reveals that the [FeFe]-Hydrogenase mimics feature the capacity of stabilizing reactive anions, *i.e.* the carbanion in the present case or the hydride when H_2 is a substrate. These results shed light on the advantage of incorporation of a pendant amine base into a chelating diphosphine ligand, the platform for mononuclear nickel complexes in H-H heterolytic cleavage.[222, 225] Such strategy may be extended to C(sp^3)-H bond activation by iron using properly designed Lewis acid-base complexes.

Bridgehead isomerization

Introduction. Transition-metal sulfide clusters are presumed to have played an important role in energy metabolism even before the proliferation of life on planet Earth and before the paleoatmosphere became enriched in oxygen. An appealing hypothesis is that in the presence of CO, the simplest of iron-sulfur clusters, Fe_2S_2, developed and detached as molecular $[(\mu\text{-}S_2)(Fe(CO)_3)_2]$, or possibly its hydrogenated form, $[(\mu\text{-}HS)_2(Fe(CO)_3)_2]$, from a precursor mineral surface, such as iron pyrite.[243-246] These complexes could therefore be early abiotic analogues of the diiron hydrogenase ([FeFe]-Hydrogenase) active site, to be later replaced by biosynthetic paths required for protection of the organism from the toxic diatomic ligands in the [FeFe]-Hydrogenase active site. (Figure VI-4) In fact, $[(\mu\text{-}S_2)(Fe(CO)_3)_2]$ enjoys current fame as the synthetic precursor to a host of small molecules that are biomimetic analogues of the active site of [FeFe]-Hydrogenase, thus connecting the inorganic to the biological world, through organometallic chemistry. (Figure VI-4)

Studies of SH^- as a ligand are of importance to the bioinorganic chemistry of iron; however, examples and studies of isolated Fe-SH units are sparse.[247-248] Discrete hydrosulfido complexes can be synthesized through protonation of sulfido ligands, an example of which is the protonation of the reduced, anionic sulfido-bridged species $[(\mu\text{-}S)_2(Fe(CO)_3)_2]^{2-}$ to form $[(\mu\text{-}SH)_2(Fe(CO)_3)_2]$ (**3**).[249-250] Although the spectroscopic signatures (ν(CO) and NMR spectra) of $[(\mu\text{-}SH)_2(Fe(CO)_3)_2]$ have been known for decades, its X-ray crystal structure has never reported.

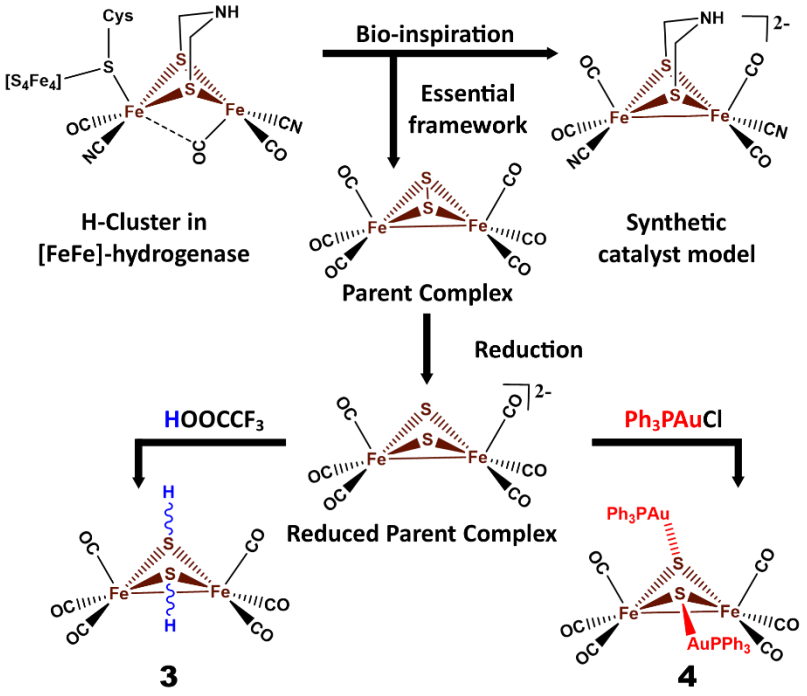

Figure VI-4 Diagram of the biological [FeFe]-hydrogenase active site and the organometallic active-site model of [FeFe]-hydrogenase. The two structures are connected through the possible primordial precursor $[(\mu\text{-}S_2)(Fe(CO)_3)_2]$. Current biomimetic syntheses utilize the reduced form of the persulfide.

Because of the well-known isolobal analogy between Ph_3PAu^+ and H^+, the former may serve as a surrogate for the latter, thus leading to experimental strategies particularly useful in the structural determination of many organometallic compounds containing transition-metal hydrides.[251-254] The Ph_3PAu^+ unit has also been used to model the protonation of metal-bound thiolates, with the generation of thiolate-bridged $M(\mu\text{-}SR)Au^I$ moieties.[255-256] In this study, the desired gold-phosphine analog of **3**, $[(\mu\text{-}SAuPPh_3)_2(Fe(CO)_3)_2]$ (**4**), was synthesized for comparisons.

Summary of experiments. Both **3** and **4** (Figure VI-4) were obtained by adding corresponding proton/gold phosphine precursors to the reduced parent complex $[(\mu\text{-}S)_2(Fe(CO)_3)_2]^{2-}$. The additions of $H^+/AuPPh_3^+$ withdraw the electron density from the Fe_2S_2 framework and cause the shifts of the CO vibrational frequencies, though to different extents, by ~ 50 cm^{-1} (H^+) and ~ 10 cm^{-1} ($Au\text{-}PPh_3^+$), respectively. The resulting complexes were crystalized and subject to the X-ray diffraction analyses to confirm their structures.

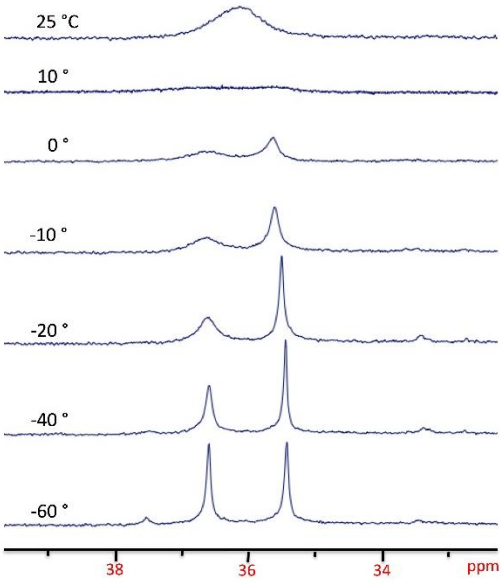

Figure VI-5 Variable-temperature ^{31}P NMR spectra of $[(\mu\text{-}SAuPPh_3)_2(Fe(CO)_3)_2]$ in d_8-toluene. The applied frequency is 121.4 MHz.

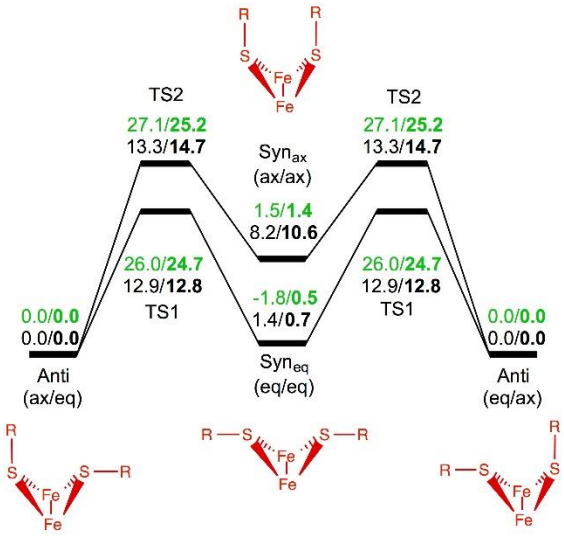

Figure VI-6 Energy profile of the transitions between the three isomers. Green numbers are for **3** and black numbers are for **4** (which the profile is scaled). The calculated electronic energies E_{ele} in vacuum are in plain text while the Gibbs free energies G after thermal and solvation corrections are in **bold** (solvent: benzene for **3** and toluene for **4**).

An interesting aspect of the geometry is the two added protons (whose positions were given by maximum electron density in X-ray diffraction) in **3** and the two gold phosphines in **4** adopted an *anti*-configuration, Figure VI-6. (The other two possible configurations are *syn*$_{eq}$ and *syn*$_{ax}$.) The ^{1}H NMR spectra of **3** in d_6-benzene solution display four signals (2 for *anti*-**3** and 1 for *syn*$_{eq}$- and *syn*$_{ax}$-**3** each).[249-250] The ratio is *anti*- : *syn*$_{eq}$- : *syn*$_{ax}$-**3** = 12:5:4 which indicates *anti*-**3** is most stable. No broadening of signals, *i.e.*, no tendency to isomerize, was observed upon heating to 70 °C. In contrast, the ^{31}P NMR spectra of **4** in d_8-toluene (Figure VI-5), show two discrete signals with an approximate ratio of 1:1 at - 60 °C. They are assigned to the axial and equatorial

phosphines of *anti*-**4**. These two peaks broaden as the temperature rises and finally achieves coalescence between 0 and 10 °C with an estimated barrier of 13.3 kcal/mol,[257] before merging into one signal at 25 °C. Application of strong acid, HBF_4, to **4** generates **3** by releasing the Au-PPh_3^+ fragment.

Mechanistic study. The NMR study above suggests different isomers of **3** coexist without isomerization at NMR timescale up to 70 °C and the bulkier Au-PPh_3^+ group is more prone to isomerize than the smaller proton. Computational study was used to investigate the factors differentiating their behaviors by exploring the isomerization mechanism with estimation of barriers.

According to a review by Toyota,[258] multiple mechanisms are possible for the inversion of pyramidal sulfur. Mueting and Mattson measured an E_{act} barrier of 29.0 kcal mol^{-1} for the isomerization between the syn_{eq} and *anti* isomers of [(μ-$SMe)_2(Fe(CO)_3)_2$] and concluded that Fe-S bond rupture and reformation occurred during the isomerization.[259] From recent computational studies for the same system, Lichtenberger and co-workers found that a simple inversion at sulfur could account for the lowest-energy pathway (E_{act} = 26.8 kcal/mol).[260] However, such barriers are high enough to prevent rapid exchange at ambient temperature.

Gibbs free energy of each isomer of **3** and **4** as well as the activation energy barrier for conversion between the isomers were estimated by DFT calculations. As described above, the small steric encumbrance of the SH unit, and an apparent high barrier to inversion at S, permits the observation of all three isomers of **3** by ^{1}H NMR spectroscopy. DFT calculations, with thermal and solvation corrections, found similar Gibbs free

energies (*G*) for these isomers, whereby the *syn*$_{ax}$-**3** and *syn*$_{eq}$-**3** isomers were less stable than *anti*-**3** by 1.4 and 0.5 kcal/mol, respectively (Figure VI-4). This result is qualitatively consistent with the experimental ratios determined by the NMR studies, in which the major product was found to be the *anti* isomer, followed by the *syn*$_{eq}$ and *syn*$_{ax}$ isomers (see above). As for **4**, the calculations indicated that *syn*$_{eq}$-**4** is slightly less stable than *anti*-**4** by 0.7 kcal/mol, whereas *syn*$_{ax}$-**4** is less stable by 10.6 kcal/mol (Figure IV-4). The high energy of *syn*$_{ax}$-**4** is attributable to the steric repulsion between the two bulky triphenylphosphine ligands, even though they were found (by computation) to interdigitate to minimize the repulsion.

As reported by Lichenberger and co-workers for the [(μ-SMe)$_2$(Fe(CO)$_3$)$_2$] complex,[260] our calculations for the interconversion of isomers of complexes **3** and **4** found for both, a transition state structure with a pseudo-trigonal-planar sulfur moiety, HSFe$_2$ or AuSFe$_2$. The activation energy barriers between the *anti* and the two *syn* isomers of **3** were calculated to be 24.7 (TS1-**3**, between *anti*-**3** and *syn*$_{ax}$-**3**) and 25.2 kcal mol^{-1} (TS2-**3**, between *anti*-**3** and *syn*$_{eq}$-**3**), whereas the transition states (TSs) for **4** are much more accessible, with Gibbs free energy barriers of 12.8 (TS1-**4**) and 14.7 kcal mol^{-1} (TS2-**4**), in agreement with the experimental observations. The intermediate, *syn*$_{eq}$ or *syn*$_{ax}$, of the exchange process of **4**, as reflected by ^{31}P NMR spectroscopy, depends on the order of the motions of the two moieties, via TS1 and TS2, respectively (Figure VI-4). The route featuring TS1, with a lower barrier, is slightly favored over the alternative route via TS2. The most accessible path for **4** qualitatively fits the experimental value, 13.3 kcal/mol. Because of the 1.9 kcal/mol difference between TS1 and TS2, the lifetime of P$_{ax}$ of *anti*-

4 is only approximately 1/30 of that of P_{eq}. Thus, the ^{31}P signal of P_{ax} is expected to broaden prior to that of P_{eq} as the temperature is raised. Therefore, the two signals at 36.6 and 35.4 ppm for **4** at low temperature can be assigned to the P_{ax} and P_{eq} atoms of *anti*-**4**, respectively. Other mechanistic trials for the conformation exchange in **4**, which involved the dissociation–association of PPh_3 or $AuPPh_3^+$, or concerted semaphore-like motions of both $AuPPh_3$ units, did not yield an acceptable route with a relatively low barrier.

The high barriers (TS1 and TS2) of **3** are due to the electronic reorganization required for inversion of a pyramidal sulfur atom to access the trigonal-planar, sp^2-type bonding from bonds that were largely of the p^3 type.[164, 258] However, despite its analogy to the proton, the gold-phosphine moiety in **4** is able to lower the planar barrier because it does not require the S atom to significantly rehybridize during the inversion as reflected. Indicated by NBO analyses, in the inversion TSs (TS1-**4** and TS2-**4**), the two Fe-S bonds continue to utilize mainly *p* contribution from the S atoms for bonding, whereas the Au dative bond to S changes readily from accepting the S 3*p* lone pair in the pyramidal ground state to accepting the 3*s* lone pair in the planar transition states. In conclusion, the gold perturbs the electronic structure of the Fe_2S moiety less in the motion to the transition states, and those transition states have low energies in turn.

Summary. The $[(\mu\text{-}SAuPPh_3)_2(Fe(CO)_3)_2]$ (**4**) complex, as an isolobal analogue of $[(\mu\text{-}SH)_2(Fe(CO)_3)_2]$ (**3**) and a molecular mimic of an aurolated or metalated FeS surface, was synthesized and characterized (with the large $AuPPh_3$ units found in the solid state in the *anti* orientation). The metallated sulfide-diiron species may be viewed as protected S-reactivity centers and the reactivity can be recovered by removing the $Au\text{-}PPh_3^+$ fragment.

Solution NMR spectroscopic studies of the latter found all possible isomers, *anti*, syn_{ax}, and syn_{eq}. The small calculated differences in Gibbs free energy are consistent with the experimental distribution of the three isomers at room temperature and reflect a high barrier to isomerization owing to substantial electronic reorganization at sulfur in the transition states. In contrast, the largely dative character of the $Fe_2S^- \rightarrow AuPPh_3^+$ bond enables such sulfur inversion to occur with less perturbation of electronic structure.

CHAPTER VII

MECHANISTIC PREDICTION OF A BIMETALLIC CARBON DIOXIDE REDUCTION CATALYST BY COMPUTATIONAL CHEMISTRY

Introduction

Carbon dioxide, CO_2, is the major product of cellular respiration and the combustion of fossil fuels. The massive production of CO_2 related to human activities since the industrial revolution has increased the atmosphere CO_2 level to 400 ppm, the first time in the past millions of years. The elevated concentration of CO_2 is believed to be related to some severe environmental challenges such as global warming[261] and ocean acidification.[262] Carbon dioxide, on the other hand, could act as a C_1 feedstock to regenerate fuels.[263-265] An environmentally friendly scheme is to couple the CO_2 reduction with the H_2O oxidation:[266-268]

$$H_2O = 2H^+ + 2e^- + 0.5O_2$$

$$CO_2 + 2H^+ + 2e^- = CO + H_2O$$

In this example, the carbon monoxide is the product of CO_2 reduction, one of many possibilities, and it may lead to various derivative products. The ideal power source to drive this reaction is renewable energy such as solar and wind electricity. Such sources of intermittent electricity may then be converted into storable chemical energy.

This chapter is reproduced from an unpublished manuscript: Ding, S.; Darensbourg, M. Y.; Hall, M. B. *Manuscript in preparation*, with the computational part, by the author of this dissertation, taken from the manuscript with permission: Lunsford, A. M.; Goldstein, K. F.; Cohan, M. A.; Denny, J. A.; Bhuvanesh, N.; Ding, S.; Hall, M. B.; Darensbourg, M. Y. Dalton Trans. **2017**, *46*, 5175-5182.

The typical products of CO_2 electrolysis are carbon monoxide, formic acid/formate, along with formaldehyde, methanol, and methane, depending on the number of electrons transferred.[269] In addition, CO_2 may also couple into oxalic acid and oxalate during reduction. A lot of heterogenous,[270] homogenous[271-274] and enzymic catalysts,[275] have been developed to promote this reaction.

Assisted by homogeneous molecular electrocatalysts, the formic acid/formate are produced through the hydride transfer to CO_2, and the hydride is generated by reducing a proton bound to the vacant site of the catalyst, Figure VII-1.[276-277] The competitive hydride transfer to H^+ happens at the same time and inevitably produces a side product, H_2, Figure VII-1. The other major product, CO, is generated by two successive protonations on one oxygen of a bound CO_2 to cleave the O-CO bond, Figure VII-1.[278] The product selectivity among CO, HCOOH, and H_2, is generally controlled by the potential applied[279] and the acidity of the proton source[280] [281-282] as mechanistically the proton and CO_2 compete for the vacant site of the catalyst or the hydride on the previous vacant site to initiate the corresponding catalytic cycles. Some ligands, like PCP-pincer ligand,[283-284] suppress the binding of CO_2 and shift the selectivity to HCOOH by modulating the nucleophilicity of the metal vacant site.

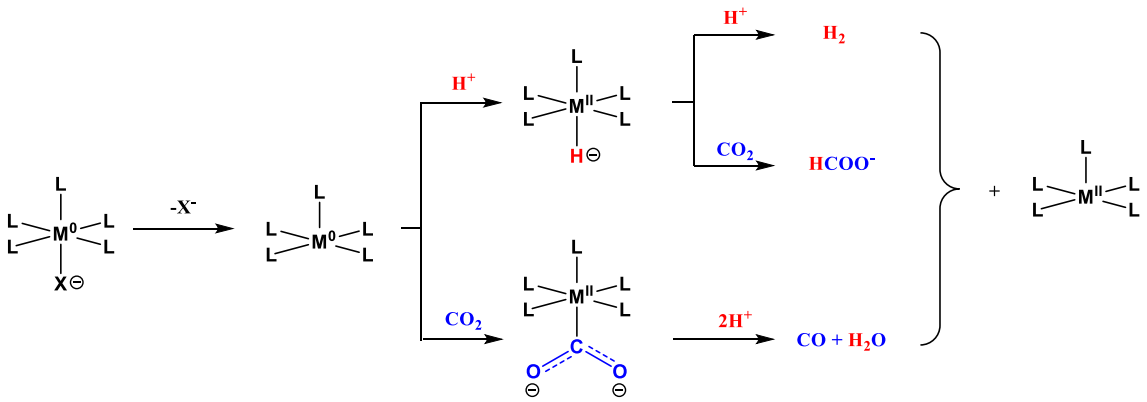

Figure VII-1 Schematic representation of competitive steps on the CO_2 reduction catalysts. Two substrates, CO_2 and H^+, compete for the vacant site and reduction power. Upon the formation of a hydride, these two substrates again compete for the hydride transfer. The reduction events may occur in-between and were omitted for simplicity.

The heterogenous molecular electrocatalysts for CO_2 reduction generally contain one or more mid-to-late transition metals. Classic catalysts use the second-row and third-row transition metals Pd, Ru, Os and Ir and they are bound to poly-pyridinyl ligands.[271] They feature at least one vacant site or a labile ligand that can easily leave to make a vacant site. On the other hand, abundant base metals Fe, Co, and Ni are also used to develop cheaper catalysts and the accompanying ligands are macrocyclic ligands such as porphyrin.[274] A few examples are presented in Figure VII-2.

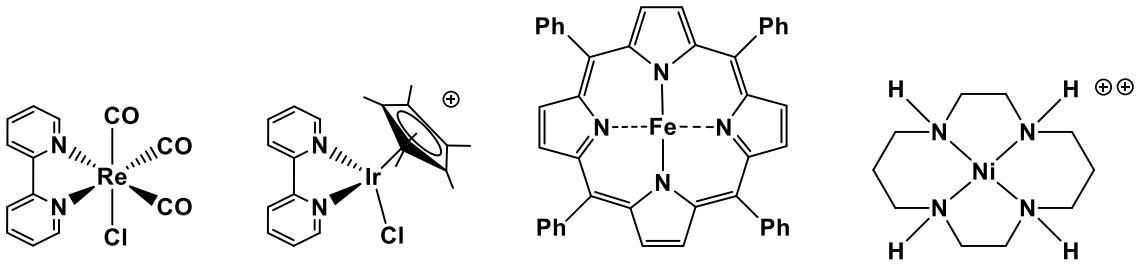

Figure VII-2 A few representative molecular electrocatalysts for CO_2 reduction. (bpy)Re(CO)$_3$Cl,[285] [(bpy)IrCp*Cl]$^-$,[286] Fe(Ph$_4$-porphorin),[287] and [Ni(cyclam)]$^{2+}$ [288].

A successful catalyst for CO_2 reduction is *fac*-(bpy)Re(CO)$_3$Cl (bpy = bipyridine) whose catalytic activity was discovered by Lehn and coworkers, Figure VII-2. It essentially opened the field of combining transition metals with poly-pyridyl ligands to design CO_2 reduction electrocatalysts. It is both an electrocatalyst[285] and photo-catalyst[289] (with sacrificed electron donors) for CO_2 reduction. Both one-electron and two-electron pathways[290] were proposed, *i.e.* either one or two reduction events are needed to cleave the labile chloride to create the vacant site on Re, depending on the solvent used. It was proven that two equivalents of reduction power must be introduced to the complex before the CO_2 can bind and be converted into the dianionic form CO_2^{2-}. The bipyridine is a redox-active ligand and can store the first equivalent of reduction power through its extended conjugation system while the Re can store a second equivalent of reduction power, before one molecule of CO_2 is fixed. After that, one oxygen is cleaved in the form of water through further protonations and reductions and the remaining CO is replaced by another molecule of CO_2 to conclude the catalytic cycle. A detailed mechanism is discussed in the following section.

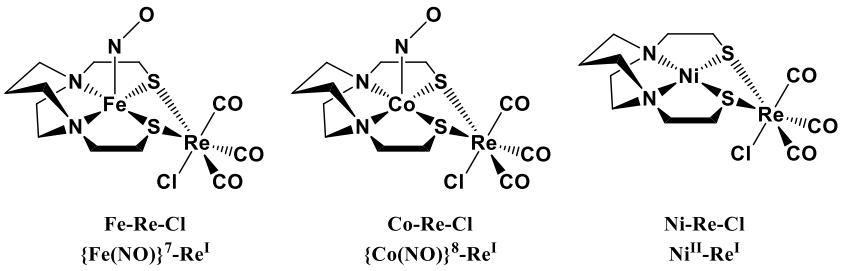

Figure VII-3 The bimetallic complexes as candidates for CO_2 reduction catalysts.

The bidentate metalloligands $M(N_2S_2)$ developed in our laboratory[106, 152] contain a redox center, either a transition metal Ni, or a transition metal Fe/Co with the redox non-innocent ligand NO, which can serve as an electron reservoir similar to bipyridine ligand. Therefore these $M(N_2S_2)$ metalloligands are expected to be able to replace the bipyridine to generate the bimetallic complexes: **Fe-Re-Cl**, **Co-Re-Cl**, and **Ni-Re-Cl**, Figure VII-3 as catalyst candidates.[291] In the bipyridine system calculated by Carter *et al.*, they have claimed CO_2 binding to **Re-Cl** is assisted by an external K^+ ion (*vide infra*).[292] Based on that, another optimistic expectation arises that the central metal in the metalloligand can help chelate and stabilize the bound CO_2[2].

In the following part of this chapter describes the full CO_2 reduction mechanism on these bimetallic complexes, including the key steps such as CO_2 binding, water formation by protonation and CO cleavage. The calculated energetics forms the foundation of the comparison of the roles of the traditional bipyridine ligand and the $M(N_2S_2)$ metalloligand. Besides, the mechanisms leading to alternative products H_2 and formic acid, are also explored.

Notes of methodology

The functional B3LYP is used in combination with 6-311++G(d,p) for all atoms except Re, for which, the pseudopotential ECP60MDF and the matching basis set cc-pVTZ-PP[88] are used. Different from the general methodology, all the optimizations in this chapter are done with the solvation model (acetonitrile) since the kinetics of the protonations are also evaluated. The solvent effects help stabilize charged species.

A mechanistic revisit to (bpy)Re(CO)$_3$Cl

The computational mechanism of CO_2 reduction under acidic conditions by (bpy)Re(CO)$_3$Cl (**Re-Cl**) was previously studied by Carter *et al.*[292-293] [294] We have recalculated this system so that it can be compared to that derive for our bimetallic complexes. A simplified version of the catalytic cycle is given in the following paragraphs.

The mono-core complex **Re-Cl** features a 6-coordinate Re^I with no available or vacant site(s) to process the substrate (either CO_2 or H^+); thus it must be reductively activated for catalytic activities. The reduction event, calculated to be at -2.07 V (*vs.* $Fc^{+/0}$) puts the electron on the bipyridine π orbital instead of the anti-bonding d_{z2} or d_{x2-y2} orbital of Re, Figure VII-4, consistent with the previous calculations from Carter *et al.*[292] Electron paramagnetic resonance (EPR) evidence shows a low spin density is present on Re.[295] The chloride cleavage is motivated by the enhanced electron density throughout the catalyst after reduction. The Cl^- removal from [**Re-Cl**]$^-$ (G = -29.0 kcal/mol, see Figure VII-5 for zero point in the catalytic cycle) has a net barrier of 10.0 kcal/mol and stabilizes the resultant **Re** (G = -34.2 kcal/mol) by 5.2 kcal/mol. If the first reduction and the loss of

Cl^- are coupled, then the redox potential can be lowered to - 1.84 V (exp. value: - 1.72 V,[296] converted from the original value reported vs. SCE. These redox potentials are adjusted to the reference couple $Fc^{+/0}$ by shifting - 0.38 V in acetonitrile[297]). The d_{z2} orbital of **Re** is also slightly stabilized by the departure of the axial ligand Cl^- and helps delocalize the added electron on the bipyridine, Figure VII-4. In Carter's calculation, an explicit cation K^+ is added to **Re-Cl** and the calculated redox potential for the ion pair/redox couple K^+[**Re-Cl**]$^{0/-}$ is - 1.79 V. The **Re** complex may de-activate itself by dimerization, which can be prevented by adding bulky groups to the bipyridine ligands.[298-299]

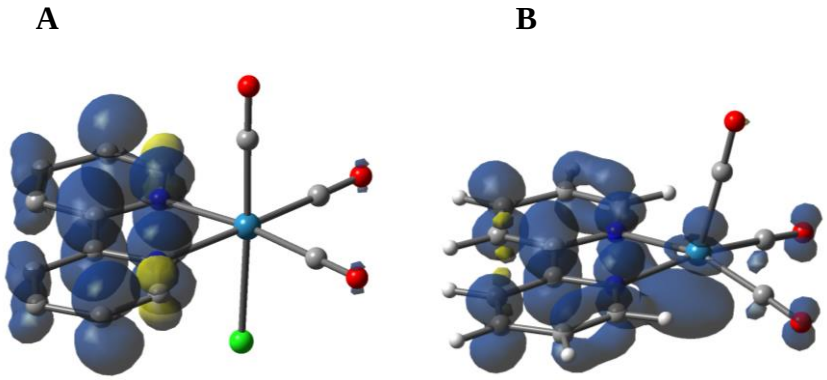

Figure VII-4 The spin density plots before and after the chloride removal from the monometallic catalyst. **A**) [**Re-Cl**]$^-$ and **B**) **Re**. The electron added to **Re-Cl** is localized on the bipyridine ligand. The removal of Cl^- from [**Re-Cl**]$^-$ helps stabilize this added electron by lowering the Re d_{z2} orbital and partial charge shifts from the bipyridine to Re.

Another reduction step on **Re** at -2.11V (exp.: - 2.09 V[296]) is required before the catalyst can accept the substrate. The two added electrons pair with each other in the singlet [**Re**]$^-$ and they are extensively shared by the bipyridine and Re. This delocalization

was confirmed by XANES[300] that suggests the Re in **[Re]**$^{-}$ behaves like Re^{0} despite its formal oxidation state of Re^{-I}. In contrast to our calculations, Carter's work shows the Cl^{-} dissociation occurs after the second reduction, rather than the first (they estimated ΔG =7.7 kcal/mol to remove the Cl^{-} ligand from the singly reduced catalyst, [**Re-Cl**]$^{-}$ accompanied by an explicit counter ion K^{+} in their modelling). And they coupled the thermodynamics of the Cl^{-} removal and the second reduction event, to give a - 2.06 V redox potential. The CO_2 can dock onto [**Re**]$^{-}$ over a barrier of 17.2 kcal/mol but the binding is thermodynamically unfavorable by 10.3 kcal/mol. Concomitantly, the charge transfers from [**Re**]$^{-}$ to CO_2 so that [**Re-CO$_2$**]$^{-}$ is best described as Re^{+}-CO_2^{2-} with a very bent O-C-O angle of 125.5°. The calculated thermodynamic data of CO_2 binding contrasts with Carter's reports as their explicit K^{+} cation stabilizes the bound, negatively charged CO^{2-}, which gives a thermodynamically favorable binding without a barrier.[292] Their calculations essentially reflect the CO_2 binding preference to the ion pair $K^{+}[(bpy)Re(CO)_3]^{-}$ instead of the activated form of catalyst $[(bpy)Re(CO)_3]^{-}$. The same favorable trend was reproduced with an explicit K^{+} counter ion in our calculations, when K+ directly assists the binding of CO_2, and the preference is ΔG = -5.8 Kcal/mol.

The protonation of [**Re-CO$_2$**]$^{-}$ by phenol (p*K*a = 29.14 in acetonitrile) is favored by - 6.4 kcal/mol with a negligible barrier which makes the CO_2 bind irreversibly. The identity of the protonation product **Re-CO$_2$H** was verified by $^{12/13}CO_2$ isotope shifts in IR spectra and these peaks grow with increased acid concentrations.[301] The **Re-CO$_2$H** may accept a third electron at the calculated potential of -2.17V, again using the bipyridine as the electron reservoir, to increase its affinity to the next incoming proton.

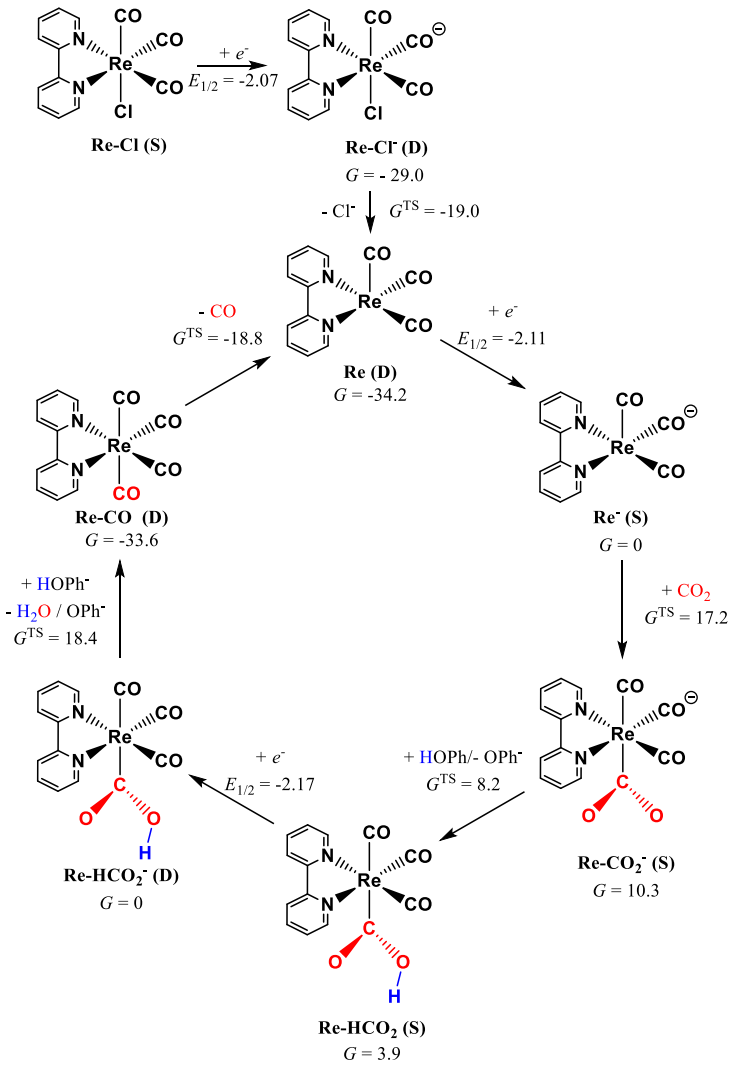

Figure VII-5 Calculated mechanism of electrocatalytic CO_2 reduction to CO as catalyzed by **Re-Cl**. The barrier of certain protonation steps may be lower than their immediate precursors as the proton donor (phenol unless otherwise specified) forms a favorable hydrogen bond with the catalyst, before the proton is transferred. All Gibbs free energies are calculated in solvation model (acetonitrile). Redox potential is given with respect to the $Fc^{+/0}$ couple (potential = 0 V) standard couple. The zero point is reset after each redox

event. The multiplicity of each species is denoted with a letter in the parentheses: singlet-S, doublet-D, and triplet-T.

A second proton is transferred from PhOH to the hydroxyl of **Re-CO_2H** and produces water, conjugate base OPh^- and (bpy)Re$(CO)_4$, **Re-CO**. Though highly thermodynamically favored with ΔG = -33.6 kcal/mol, this protonation also incurs a high barrier of 18.4 kcal/mol and is the rate-determining step, consistent with the evidence from H/D kinetic isotope experiment.[126] The **Re-CO** regenerates the more stable (by - 0.6 kcal/mol) species **Re** by cleaving one CO over a barrier of 14.8 kcal/mol and closes the E[ECEC] catalytic cycle. To reduce **Re-CO** to **[Re-CO]$^-$**, a more negative potential, -2.60 V is required but the carbonyl dissociation from **[Re-CO]$^-$** is almost barrierless (1.0 kcal/mol). These two steps are not recognized as a part of the catalytic cycle due to the very negative potential required. The mechanism is summarized in Figure VII-5.

Computational prediction of CO_2 reduction mechanism on Ni-Re-Cl

CV experiments and the activation of the bimetallic catalyst. The cyclic voltammograms of a 2 mM solution of **Co-Re-Cl**, **Fe-Re-Cl**, and **Ni-Re-Cl** in DMF are displayed in Figure VII-6 on initiating the scan in the positive direction and referenced to Fc/Fc^+ = 0.0 V.[291]

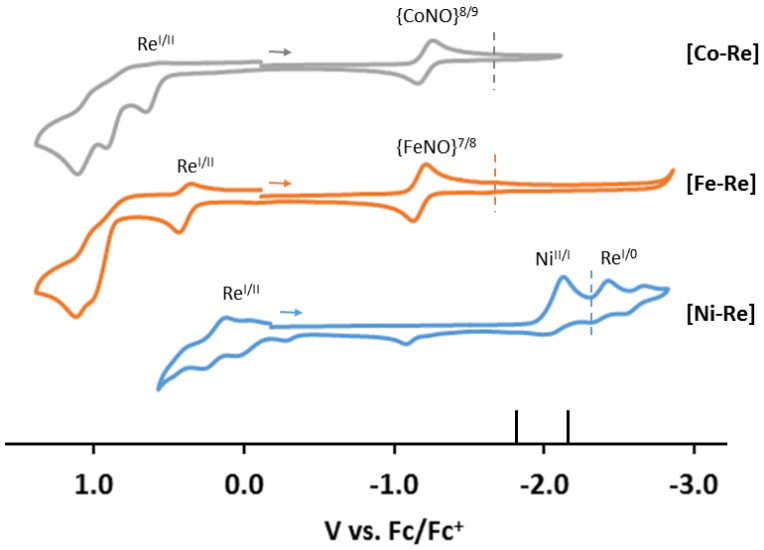

Figure VII-6 Overlay of the cyclic voltammograms of **Ni-Re-Cl**, **Fe-Re-Cl**, and **Co-Re-Cl**. All voltammograms were taken in DMF at a scan rate of 200 mV/s and referenced to $Fc^{+/0}$ = 0.0 V. The dotted line denotes the reduction potential of the free metalloligand and the solid black lines denote the reduction potential of **Re-Cl.**

Calculations examined the three complexes, at different redox levels and their spin density distributions to give electrochemistry assignments with calculated redox potentials. The oxidation and the first reduction events of **Ni-Re-Cl**, at experimental (*computed*) values of $E_{1/2}$ = 0.19 V (*0.36 V*) and E_p = - 2.12 V (*-2.07 V*) were assigned to the $Re^{I/II}$ and $Ni^{II/I}$ redox couples, respectively. The $Ni^{II/I}$ reduction event is followed by a cleavage of the chloride from **[Ni-Re]**$^-$ like the monometallic complex **Re-Cl**, with a calculated ΔG of – 6.9 kcal/mol; in contrast, ΔG = 3.1 kcal/mol for similar chloride cleavage from the original **Ni-Re-Cl**. According to our computations, this cleavage is presumed to be facilitated by the enhanced S-donating ability of the $[Ni^{I}N_2S_2]^-$ metallodithiolate ligand.

The added electron on Ni^{I} is accommodated on the highly destabilized d_{x2-y2} orbital of Ni^{I}, Figure VII-7. It is noteworthy that in our previous investigation of $Ni^{II}(N_2S_2)Fe^{II}(CO)Cp^{+}$, an intramolecular electron transfer to the $Fe^{II}(CO)Cp^{+}$ fragment followed the reduction of Ni^{II} to Ni^{I}. Concomitant dissociation of one S-Fe bond thus triggered the hemi-lability of the bridging dithiolate.[154] A similar hemi-lability was not detected in the calculations of **[Ni-Re]**$^{-}$, perhaps because the significant orbital splitting of the octahedral Re^{I} (d^6) with multiple carbonyls inhibits the intramolecular electron transfer. The added electron remains on Ni even after the chloride cleavage, Figure VII-7.

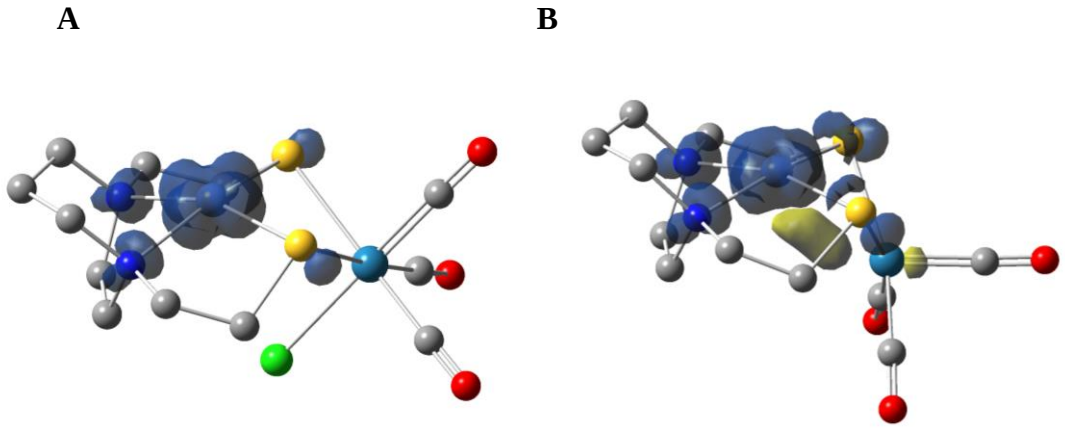

Figure VII-7 Spin density changes before and after chloride removal from the bimetallic catalyst. **A**) [**Ni-Re-Cl**]$^{-}$ and **B**) **Ni-Re** . The unpaired electron (the added electron) is primarily on Ni.

As indicated in Figures 7-6 and 7-8, the chloride dissociation renders the first reduction of **Ni-Re-Cl** irreversible or quasi-reversible and is a prerequisite for the second reduction event at E_p = - 2.43 V (- *2.54* V) assigned to the $Re^{I/0}$ couple, accessible only after Cl-Re bond cleavage. Otherwise, with an intact Cl-Re bond and fully saturated, six-

coordinate $Re^{I}(d^6)$, the estimated redox potential of the second reduction should be as negative as - 4.12 V. In this case the second added electron is assigned to the $Ni^{I/0}$ couple instead of the $Re^{I/0}$ couple.

The reduction events of **Co-Re-Cl** at $E_{1/2}$ = -1.21 V (- *1.05* V) and **Fe-Re-Cl** at $E_{1/2}$ = -1.17 V (- *1.16 V*) were assigned to $\{Co(NO)\}^{8/9}$ and $\{Fe(NO)\}^{7/8}$ couples, respectively. The buffering by the non-innocent NO ligand provides a soft landing for the incoming electron, such that the added electron on the metallodithiolate ligand no longer provides adequate aid (via enhanced S-donation) to chloride dissociation on the rhenium center. It is confirmed by the smaller red shifts of computational CO vibrational frequencies of $Re(CO)_3$ moiety after reduction. As a result, the Re in **[Fe-Re-Cl]**$^-$ and **[Co-Re-Cl]**$^-$ have lower electron density, as evidenced by higher CO frequencies calculated, and are less likely to dissociate the chloride. The chloride dissociation reaction has a calculated ΔG of -4.0 and -3.5 kcal/mol, for **[Fe-Re-Cl]**$^-$ and **[Co-Re-Cl]**$^-$ respectively. Though the calculated ΔG for chloride dissociation for these two complexes is marginal, it is assumed that the Cl-Re bond persists in **[Fe-Re-Cl]**$^-$ and **[Co-Re-Cl]**$^-$ as suggested by the reversibility of reduction events at ca.~ -1.2 V and the absence of further reduction events. Therefore, neither M(NO) nor the saturated Re^{I} may accept a second electron, consistent with the absence of further reduction events within the potential range we explored, Figure VII-6. Since **Fe-Re-Cl**, and **Co-Re-Cl** cannot be activated by the dissociation of the axial ligand Cl^- to generate the active site, they are less likely to be electrocatalysts.

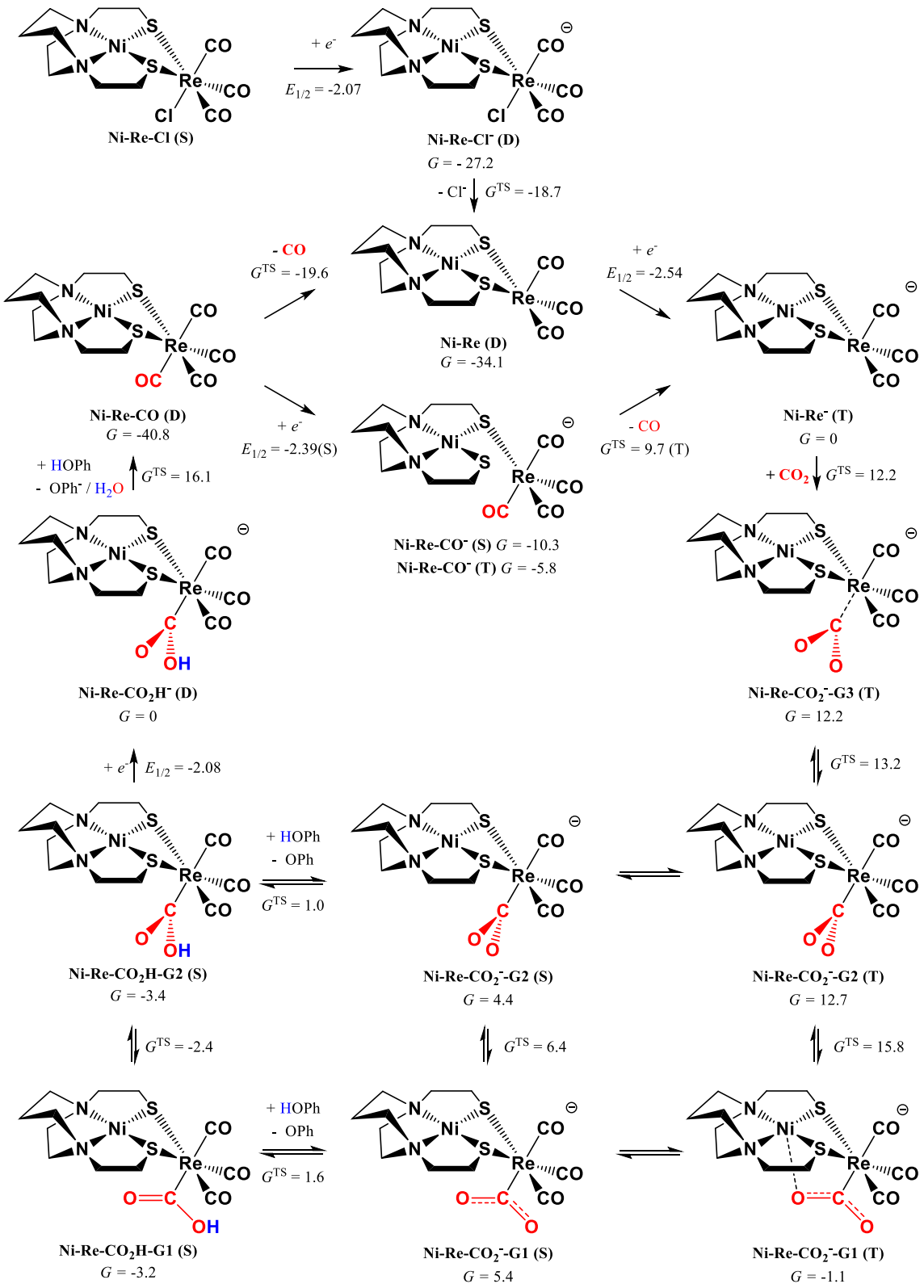
Ni-Re-Cl (S)
+ e-
E1/2 = -2.07
Ni-Re-Cl- (D)
G = - 27.2
- Cl-
GTS = -18.7
- CO
GTS = -19.6
Ni-Re (D)
G = -34.1
+ e-
E1/2 = -2.54
Ni-Re-CO (D)
G = -40.8
+ e-
E1/2 = -2.39(S)
- CO
GTS = 9.7 (T)
Ni-Re- (T)
G = 0
+ HOPh
- OPh- / H2O
GTS = 16.1
+ CO2
GTS = 12.2
Ni-Re-CO- (S) G = -10.3
Ni-Re-CO- (T) G = -5.8
Ni-Re-CO2H- (D)
G = 0
Ni-Re-CO2--G3 (T)
G = 12.2
+ e-
E1/2 = -2.08
GTS = 13.2
+ HOPh
- OPh
GTS = 1.0
Ni-Re-CO2H-G2 (S)
G = -3.4
Ni-Re-CO2--G2 (S)
G = 4.4
Ni-Re-CO2--G2 (T)
G = 12.7
GTS = -2.4
GTS = 6.4
GTS = 15.8
+ HOPh
- OPh
GTS = 1.6
Ni-Re-CO2H-G1 (S)
G = -3.2
Ni-Re-CO2--G1 (S)
G = 5.4
Ni-Re-CO2--G1 (T)
G = -1.1

Figure VII-8 The mechanism of electrocatalytic CO_2 reduction mediated by **Re-Ni-Cl**. For selected species, the energies of more than one spin state are presented, as certain steps may occur on a potential energy surface of a certain spin state. See the caption of Figure VII-5 for more information.

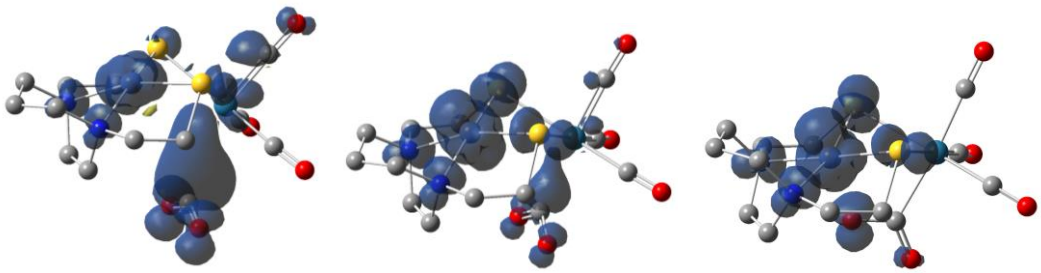

	G3 (T)	**G2 (T)**	**G1 (T)**
d(Re-C) / Å	3.013	2.345	2.217
d(Ni-O) / Å	4.582, 4.585	3.899, 3.947	2.036, 4.066
A(O-C-O) / °	141.6	124.4	119.6
Spin Density	0.901(Ni), 1.088 (NiN_2S_2), 0.264(Re), 0.582 (CO_2)	1.394(Ni), 1.821 (NiN_2S_2), -0.004(Re), 0.132 (CO_2)	1.445(Ni), 1.867 (NiN_2S_2), -0.051(Re), 0.128 (CO_2)

Figure VII-9 Spin density plots of triplet **[Ni-Re-CO_2]$^-$-G1/G2/G3** with selected geometric parameters.

The Cl^- loss of **[Ni-Re-Cl]**$^-$ has a barrier of 8.5 kcal/mol and generates **Ni-Re** by a Gibbs free energy drop of -6.9 kcal/mol, Figure VII-8. The resultant **Ni-Re** must accept another electron before it becomes active toward substrates. However, the doubly reduced [**Ni-Re**]$^-$ is triplet, with a formal oxidation state of $Ni^I(d^9)$-$Re^0(d^7)$. Each metal holds an unpaired electron as the two metals bridged by the thiolates are *de facto* independent spin

centers; this is not possible for **[Re]**$^{-}$ with the extensive conjugation network between bipyridine and Re. It is energetically disadvantageous to pair the electrons up in **[Ni-Re]**$^{-}$, with an energy rise of 11.2 kcal/mol, in the closed-shell singlet. The broken-symmetry singlet counterpart of the triplet is only slightly less stable than the triplet by 1.3 kcal/mol.

The binding of CO_2. The binding of CO_2 to the triplet **[Ni-Re]**$^{-}$ (G = 0 kcal/mol) involves a few steps of geometric reorganizations along with electron transfers, Figure VII-9. The linear CO_2 bends to 141.6° as it approaches Re^0 and accepts one unpaired alpha electron from Re^0, rendering the formal oxidation state of Ni^{I}-Re^{I}-$(CO_2)^{-}$, evidenced by the total spin density of 0.582 on CO_2 of the triplet intermediate **[Ni-Re-CO_2]**$^{-}$**-G3** (G = 12.2 kcal/mol). The Re-C distance is 3.013 Å, as the formal bond order of Re-C bond is 0.5. The C-Re bond distance continues to decrease when one beta electron is transferred from Ni^{I} to the now reduced CO_2^{-}, forming triplet **[Ni-Re-CO_2]**$^{-}$**-G2** (G = 12.7 kcal/mol) over a barrier of G = 13.2 kcal/mol. Two added electrons pair in CO_2^{2-} and the spin density remains on high-spin Ni^{II}, with spin densities of 1.394 for the Ni atom and 2.100 for the NiN_2S_2 moiety. So that the formal oxidation state assignment is Ni^{II}-Re^{I}-$(CO_2)^{2-}$. In the triplet intermediate **[Ni-Re-CO_2]**$^{-}$**-G2**, the C-Re distance and the O-C-O angle shrink to 2.345 Å and 124.4°, respectively, indicative of a full C-Re dative (or covalent) bond. The last step is to rotate CO_2 so that one of its oxygens is exactly below Ni to form the fifth dative bond to Ni and to mutually stabilize the high-spin Ni^{II} and the bound CO_2^{2-}. This step has a barrier at 15.8 kcal/mol but the resulting triplet **[Ni-Re-CO_2]**$^{-}$**-G1** is stable, G = - 1.1 kcal/mol and is recognized as the resting state after CO_2 binding. The triplet spin density remains on Ni^{II} while the C-Re distance and the O-C-O angle continue to decrease

to 2.217Å and 119.6°, respectively. The CS_2 analogue, **[Ni-Re-CS_2]$^-$-G1**, is predicted to be more stable, as the binding of CS_2 to the triplet **[Ni-Re]$^-$** is more favorable with ΔG = -7.2 kcal/mol.

As a summary, CO_2^{2-} in the triplet **[Ni-Re-CO_2]$^-$-G1** is recognized a bidentate μ_2-η^2 ligand, one of nine binding modes,[302] using its O and C to bind to the Ni and the Re respectively. This unique κ^2-binding mode makes CO_2 fixation to **[Ni-Re]$^-$** favored by -1.1 kcal/mol in contrast to unfavorable 10.3 kcal/mol for **[Re]$^-$** (without the assistance of an external K^+ cation). Another comparison is that the singlet counterpart of the triplet **[Ni-Re-CO_2]$^-$-G1** is 6.5 kcal/mol less stable, with a low-spin Ni^{II} and the absence of the Ni-O bond. The second metal center brought by the application of the N_2S_2 metalloligand assists the CO_2 up-take by establishing an extra dative bond to relieve the electron density on CO_2^{2-}. We describe this scenario as "cooperative metal-assisted" binding, Figure VII-8.

The protonation on the bound CO_2. The electron density depletion in the resting state, triplet **[Ni-Re-CO_2]$^-$-G1** by the Ni-O bond creates an obstacle for the successive protonation reaction. The barrier to protonate **[Ni-Re-CO_2]$^-$-G1** by phenol on the triplet potential energy surface is calculated to be G^{TS} = 13.3 kcal/mol. The singlet counterpart **[Ni-Re-CO_2]$^-$-G1** (G = 5.4 kcal/mol) features a low-spin Ni^{II} with the doubly occupied d_{z2} orbital. The Ni has no need for the donation from the oxygen to its d_{z2} and no longer has the Ni-O bond. The CO_2^{2-} unit thus has higher electron density and is more prone to be protonated. The barrier (G = 1.6 kcal/mol) for this protonation on the singlet **[Ni-Re-CO_2]$^-$-G1** is significantly lower; it is even lower than its immediate processor, with a

favorable hydrogen bond to pre-organize the proton donor (phenol) and the singlet **[Ni-Re-CO_2]$^-$-G1** before the proton transfer occurs. The same preference is also applicable to the singlet **[Ni-Re-CO_2]$^-$-G2**. These two singlet rotamers, may convert into each other freely with negligible barrier(s), before or after protonation. Therefore, the triplet **[Ni-Re-CO_2]$^-$-G1** may have spin crossover before the protonation occurs. The most stable species after protonation is determined to be singlet **Ni-Re-CO_2H-G2** (G = -3.4 kcal/mol), Figure VII-8.

We find that the **Ni-Re-CO_2H-G2** accepts an electron at -2.08 V to make the next proton up-take more thermodynamically feasible. Another phenol then attaches the hydroxy group on the resultant **[Ni-Re-CO_2H]$^-$** over a barrier of G = 16.1 kcal/mol. This step cleaves a water from the catalyst and creates a tetracarbonyl species **Ni-Re-CO** (doublet, Ni^{I}-Re^{I}) with a very exoergic ΔG of -40.8 kcal/mol. This very negative Gibbs free energy can be attributed to the formation of a stable product, H_2O, and the increase of the molarity during the reaction. The **Ni-Re-CO** may now kick off its extra carbonyl to regenerate the activated catalyst **Ni-Re** over a net barrier of 21.2 kcal/mol. Another option to finish the catalytic cycle is to reduce **Ni-Re-CO** at a potential of -2.39 V. The added electron forces one S-Re to dissociate. The reduced species **[Ni-Re-CO]$^-$** has a ground state of singlet, with a configuration of Ni^{II}-Re^{-I}, in which the trigonal bipyramidal Re^{-I} is heavily stabilized by the synergic back-bonding of four carbonyls. The triplet **[Ni-Re-CO]$^-$** is 4.5 kcal/mol higher than the singlet with a configuration of Ni^{I}-Re^{0} and Re adopts a square pyramidal geometry. It is energetically unfavorable to remove CO from singlet **[Ni-Re-CO]$^-$** as the loss of back-bonding makes Re^{-I} unstable. The CO

dissociation from the triplet **[Ni-Re-CO]**$^{-}$ is determined to have a barrier at G = 9.7 kcal/mol and regenerates **[Ni-Re]**$^{-}$; thus the net barrier from the singlet ground state is 20.0 kcal/mol, comparable to the barrier of direct CO dissociation form **Ni-Re-CO**. Therefore, the rate-determining step for CO_2 reduction catalyzed by **Ni-Re-Cl** should be CO dissociation/catalyst regeneration, in contrast to that of **Re-Cl**, the second protonation on the bound CO_2.

H_2 production mechanism

A competitive process with CO_2 reduction is H_2 evolution, by electroreduction of protons present in the solution. The complexes, **Re-Cl** and **Ni-Re-Cl**, share a Re-centered H_2 production mechanism, Figure VII-10. The vacant site on Re, after two equivalents of reduction and the Cl^- dissociation, may accept the incoming protons. However, the protonation by phenol on **[Re]**$^{-}$ and **[Ni-Re]**$^{-}$ is significantly hindered by a high kinetic barrier of 27.1 and 25.4 kcal/mol, respectively, regardless of the favorable thermodynamics. The proton acceptor, *i.e.* the Re atom, is not able to form a hydrogen bond with the proton donor to compensate the entropy penalty of a bimolecular reaction. The protonated, hydride-bearing species **Re-H** and **Ni-Re-H** both can accept another electron at -2.11 and -2.06V, respectively, before another proton from phenol is introduced to produce H_2 by proton-hydride coupling. The coupling, in the absence of the assistance of an intramolecular proton shuttle, is also characterized by high barriers of 24.2 and 26.0 kcal/mol, respectively for **[Re-H]**$^{-}$ and **[Ni-Re-H]**$^{-}$, with thermodynamic disadvantages of 6.9 and 15.4 kcal/mol, to generate H_2 σ-complexes. The release of H_2 from these σ-

complexes incurs a nominal barrier and regenerates the activated catalyst. In conclusion, the calculations predict that neither **Re-Cl** nor **Ni-Re-Cl**, could be an effective electrocatalyst for H_2 production.

A

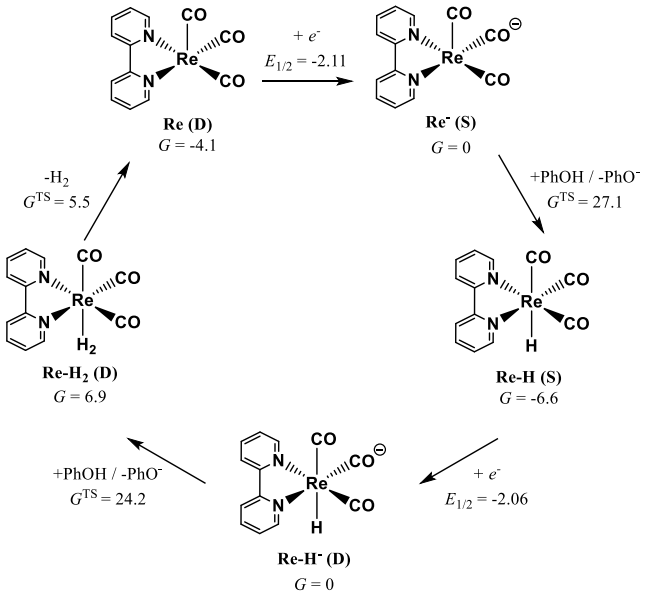

B

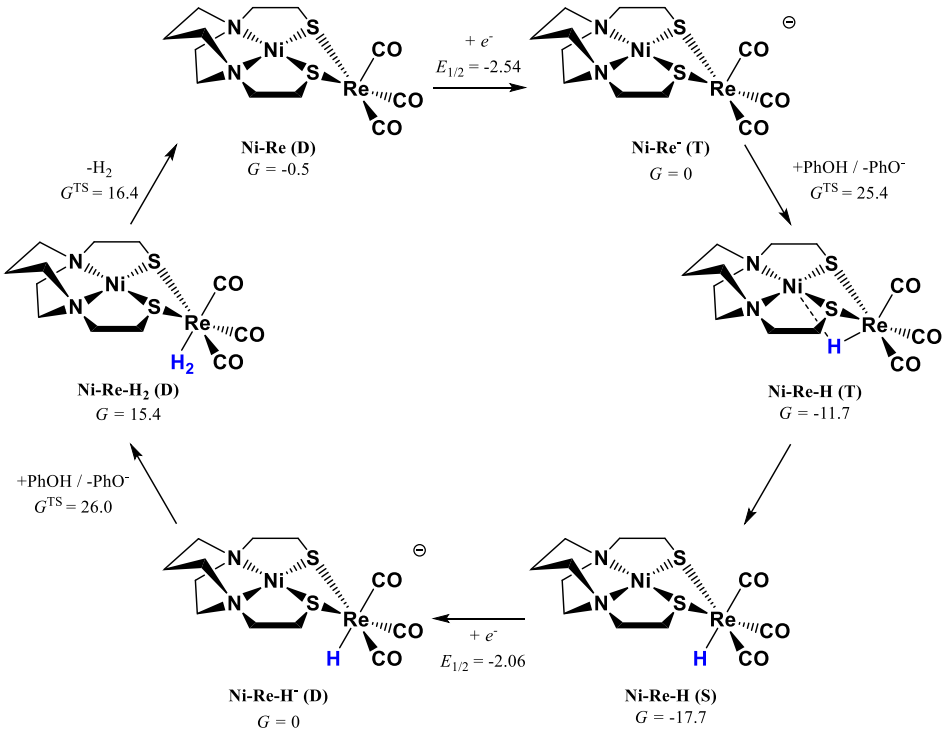

Figure VII-10 The competitive electrocatalytic H_2 production mechanism. **A**) Re-Cl and **B**) Ni-Re-Cl. The proton source is phenol, p*K*a = 29.14 in acetonitrile.

Hydride transfer CO_2 reduction mechanism by tetracarbonyl Ni-Re-CO

The kinetic difficulty inhibits the protonation either on **[Re]**$^-$ or **[Ni-Re]**$^-$ to generate a hydride. Therefore, it is unlikely for **[Re]**$^-$ or **[Ni-Re]**$^-$ to catalyze hydride transfer CO_2 reduction to produce formic acid. After one turn-over of electron-proton coupling CO_2 reduction to produce CO, the CO dissociation from the catalyst **Ni-Re-CO/[Ni-Re-CO]**$^-$ is the rate-determining step and the tetracarbonyl species should have a substantial existence in the reaction mixture. The most interesting feature in the singlet **[Ni-Re-CO]**$^-$ is that one of the hemi-labile Re-S bonds is dissociated to accommodate the

added electrons. The Re^{-I} in singlet **[Ni-Re-CO]**$^{-}$ is sufficiently electron rich enough to convert a proton into a hydride, *i.e.*, oxidation addition. The calculation reveals the direct protonation on Re of **[Ni-Re-CO]**$^{-}$ by phenol is favored by -8.8 kcal/mol, but it would incur a barrier of G = 22.2 kcal/mol. The protonation on S by phenol, which was previously treated as an intramolecular shuttle,[154] is unfavorable by 16.2 kcal/mol with an ever-higher, unrealistic barrier of G = 31.1 kcal/mol, while the intramolecular proton transfer from the sulfur to Re only has a negligible barrier. Taking the thermodynamics and kinetics into account, the sulfur may not help temporarily store the proton upon the S-Ru bond dissociation. The high barrier to protonate S is attributed to the unfavorable heat of reaction between a weak proton donor (phenol) and a moderate proton acceptor (neutral thiolate), in addition to the entropy penalty associated with a bimolecular reaction. The unfavorable Gibbs free energy is reflected by an extremely late transition state, in which the H-OPh distance is 2.195 Å. (This H-O distance of a free phenol is optimized to 0.963 Å.) In other words, the basicity of a pendant base must match the acidity of the applied acid before it can be a kinetically effective agent to shuttle protons, Figure VII-11.

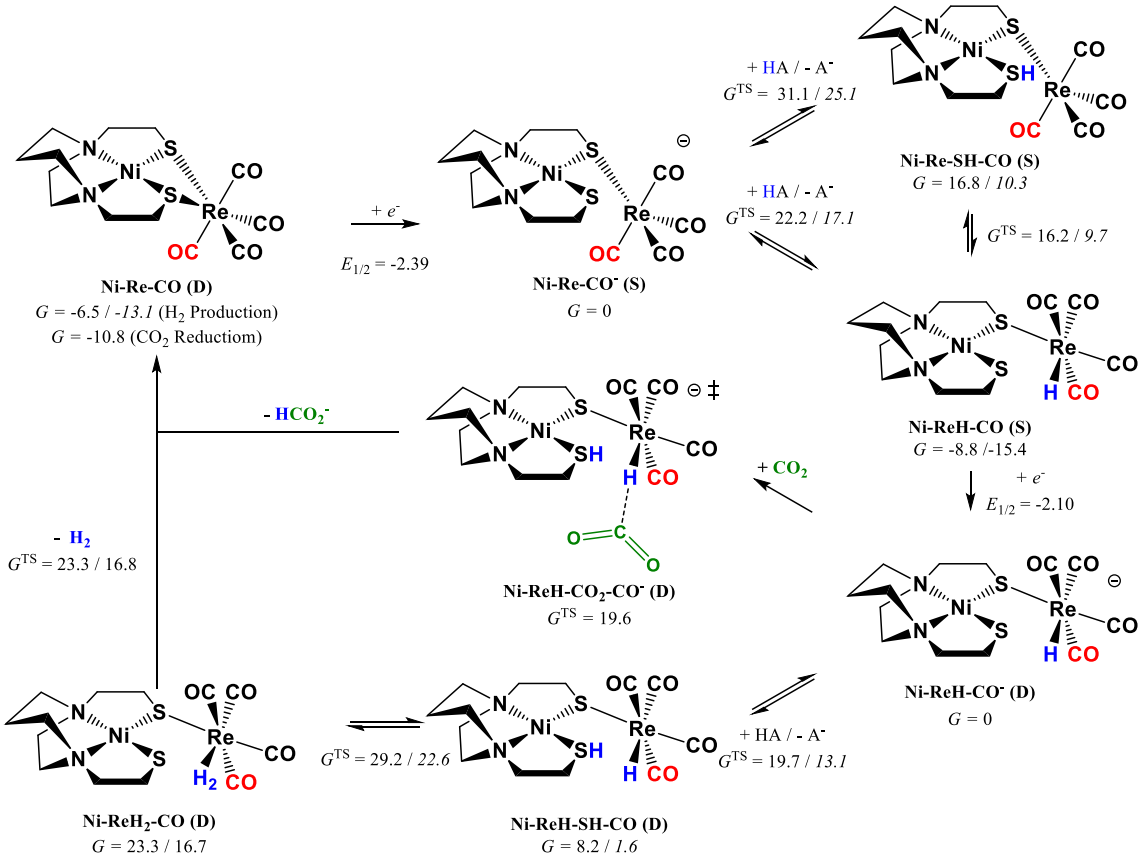

Figure VII-11 Electrocatalytic mechanism of CO_2 and H_2 productions facilitated by the tetracarbonyl complex **Ni-Re-CO**. Two different types of proton sources, phenol (p*K*a = 29.14) and acetic acid (p*K*a = 23.51) are used in calculations. The corresponding Gibbs free energies, if different, are denoted in plain (phenol) and in *italics* (acetic acid), respectively.

The hydride bearing **Ni-ReH-CO** (Ni^{II}-Re^{I}) is reduced again at -2.10 V before the hydride is transferred to another molecule of CO_2 over a barrier of G = 19.6 kcal/mol. The competing process is the hydride transfer to a proton to generate H_2, which must overcome

two barriers, G = 19.7 and 29.2 kcal/mol, for the second proton transfer as well as the proton-hydride coupling, respectively; therefore, it is kinetically infeasible.

With phenol as the proton source, the rate determining step is the protonation of Re for the formic acid production, and the proton-hydride coupling is rate-determining for H_2 production, respectively. The thermodynamics of the protonation process on **Ni-Re-CO** is indeed acid-dependent. The protonation on Re of **[Ni-Re-CO]**$^-$ by a slightly stronger acid, acetic acid (pKa = 23.51 in acetonitrile; phenol, pKa = 29.14), is favored by 15.4 kcal/mol with a barrier of 17.1 kcal/mol; the barrier is lower by 5.1 kcal/mol compared to that of phenol. The decrease of the barrier for hydride generation turns the hydride transfer to CO_2, which is independent on acidity of the proton source, into the rate determining step (G^{TS} = 19.6 kcal/mol) for formic acid production catalytic cycle. The second protonation on hydride-bearing species by acetic acid is also kinetically more feasible, with a barrier of 13.1 kcal/mol. However, the H_2 production is still less advantageous than the formic acid formation due to the higher barrier (G^{TS} = 22.6 kcal/mol) for the proton-hydride coupling. Using an ever-stronger acid may not help proton-hydride coupling as the net Gibbs free energy difference between the transition state and the precursor **Ni-ReH-SH-CO** is as high as 21.0 kcal/mol and is independent on the acid applied, unless a different mechanism appears with a stronger acid. The theoretical study indicates **[Ni-Re-CO]**$^-$ may serve as a hydride-transfer catalyst to reduce CO_2 by electrochemically produced hydride.

Summary

The capacity of the bimetallic complex **Ni-Re-Cl** to serve as an electrocatalyst for CO_2 reduction is investigated by computational chemistry in comparison with a monometallic electrocatalyst **Re-Cl**. Similar to **[Re]**$^-$, the Re in reduction-activated **[Ni-Re]**$^-$ acts as the reactive center for CO_2 binding and reduction, while the other metal, Ni, provides an auxiliary binding site to stabilize the bound CO_2, turning the bound CO_2 into a birdging bidentate ligand. Therefore, the unfavorable thermodynamics of CO_2 binding to **[Re]**$^-$ is inverted with **[Ni-Re]**$^-$**;** the CO_2-bound intermediate is predicted to be stable, before the proton donor phenol is added to push the catalytic cycle forward by cleaving one O of CO_2 in the form of H_2O, with CO remaining on the catalyst. The competitive H_2 production, on either **[Re]**$^-$ or **[Ni-Re]**$^-$, is inhibited by high barriers to protonate Re and Re-bound hydride; while the lack of the hydride bearing species throughout the catalytic cycle, on the other hand, rules out the possibility to reduce CO_2 by hydride transfer to ensure high selectivity.

The calculations find that carbon monoxide dissociation from **[Ni-Re-CO]**$^{0/-}$ regenerates **[Ni-Re]**$^{0/-}$ and is the rate-determining step for the catalytic cycle initiated from **[Ni-Re]**$^{0/-}$. However, the tetracarbonyl species **[Ni-Re-CO]**$^-$ may have its own catalytic cycle. The protonation on five-coordinate Re^{-I} of **[Ni-Re-CO]**$^-$ faces a lower barrier, especially if the proton donor capacity is elevated. The generated metal-hydride reduces another molecule of CO_2 by hydride transfer, while hydrogen evolution still suffers from the high barrier of intramolecular hydrogen-hydride coupling and is significantly slower.

The selectivity of CO actually is dependent on the acidity of the proton source and a stronger acid can accelerate the production of CO.

CHAPTER VIII

SUMMARY

Summary of projects

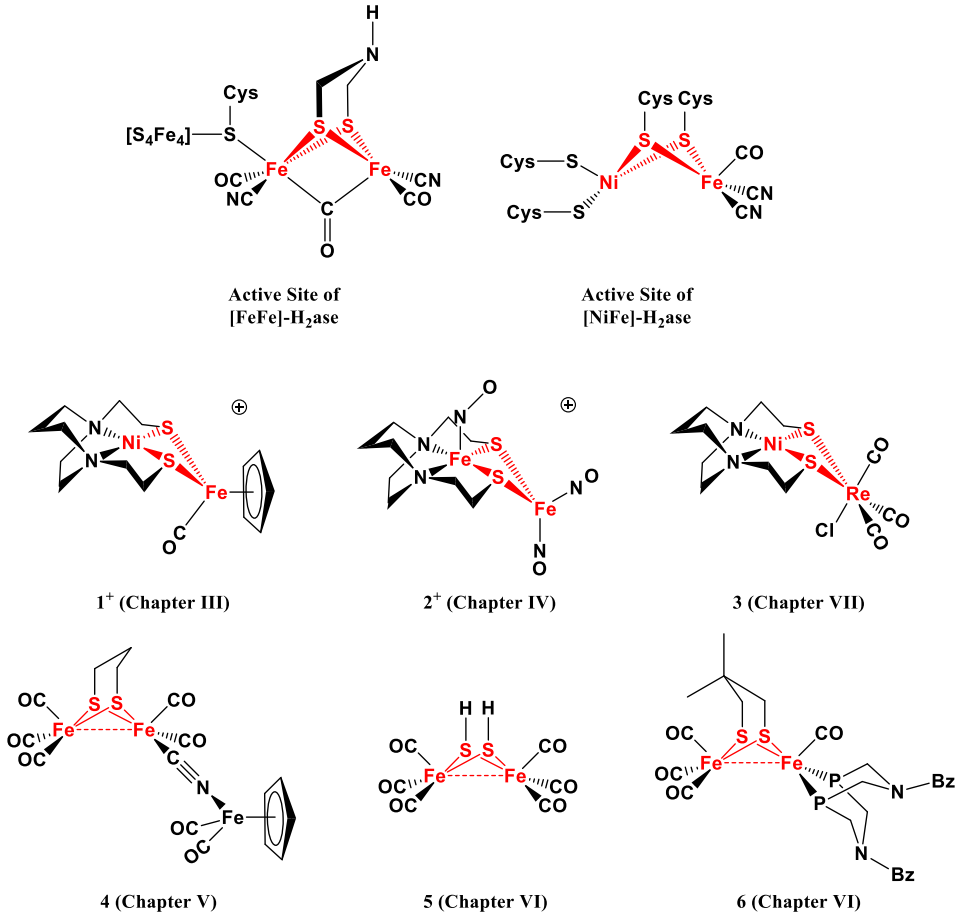

Figure VIII-1 The active sites of [FeFe]- and [NiFe]-hydrogenases and representative complexes from each chapter. *Nota bene* they share the M(μ-S)$_2$M' core.

This dissertation describes a collection of reaction mechanisms in organometallic chemistry, concerning chemical or electrochemical, catalytic or stoichiometric reactions.

Although seemingly quite separated, H_2 production, CO_2 reduction, C-H bond activation, and ligand conformation isomerization, the involved complexes and the corresponding mechanisms, have something in common.

As shown in Figure VIII-1, these organometallic complexes share the same M(μ-S)$_2$M' core. Two transition metals are connected by the two bridging thiolates, or a dithiolate, to form a unity. In this manner, the metals may cooperate with each other. (Such a constitution is originally inspired by the active sites of hydrogenases, Figure VIII-1.) The transition metals involved in these complexes are largely first-row Fe and Ni, which are considered, in the aspect of redox activity, to be "one electron" metals, *i.e.*, they can only hold one electron during reactions. By linking two of them, they may work synergistically to promote reactions involving two electrons. Our calculations indeed confirm the two successive redox events on the bimetallics are assigned two metals in alternate order. This is true for both two oxidation events in the C-H bond activation project (complex **6**), and two reduction events in the H_2 production electro-catalyst project (complexes $\mathbf{1}^+$ and $\mathbf{2}^+$).

On the other hand, the "hinge" binding of two metals, *i.e.*, the two bridging sulfurs/thiolates, are flexible. The flexibility is reflected in the capacity of binding various organometallic fragments to create a variety of bimetallic complexes, with various M-(μ-S)$_2$-M' hinge angles and M-M' distances. In some cases, the bridging thiolate can even dissociate, which is discussed next. In short, the M(μ-S)$_2$M' paradigm, must be the choice of Nature.

The ligand participation (*vs*. that of metals) is determined to be equivalently important in the reaction mechanisms presented in this dissertation. The reaction centers of the organometallics were traditionally believed to be the metals while the ligands were thought to act a supportive role, and largely treated as the "spectators". However, almost all my mechanistic studies implicate the direct participation of the ligands; they are "actor" ligands. The bridging thiolate dissociates to temporarily store a proton for the successive H_2 production (complex $\mathbf{1}^+$); the diatomic ligands CO and NO help buffer the electrons on the bound metal by π-back-bonding (complexes $\mathbf{2}^+$ and **3**); the strategically placed pendant amine helps remove the proton to finalize the C-H bond activation (complex **6**); not to mention the ligand isomerization reactions of complexes **4** and **5**.

A particularly interesting point is that the ligand participation is extended to the second coordination sphere in the project of the C-H bond activation (complex **6**). The implanted amine on the P_2N_2 ligand by no means has a direct contact (a dative bond) with the iron in complex **6**, due to steric constrains. However, the absence of such an assisting group would completely stop the reaction, in reminiscent of the natural strategically placed, pendant amine in the [FeFe]-hydrogenase, which is also responsible for the shuttling of protons.

The secret of the "actor" role of the ligands is largely unveiled by the computational chemistry, as these transient species directly demonstrating ligands at work are less available. The computational studies suggest metals and ligands, are at least of equivalent importance for the overall activity of the organometallic complexes. This further leads to a question, whether the groups in the protein matrix, which are seemingly

remote from the active sites, would ultimately affect the activities through subtle interactions.

The versatility of the computational tools

In this dissertation, the computations were used in a relatively versatile way (Figure VIII-2) in order to provide a multiple-point validation between the experimental and computational results. The calculations first generate the orbitals of the molecular system of interest and other properties of these molecules are derived from the orbitals.

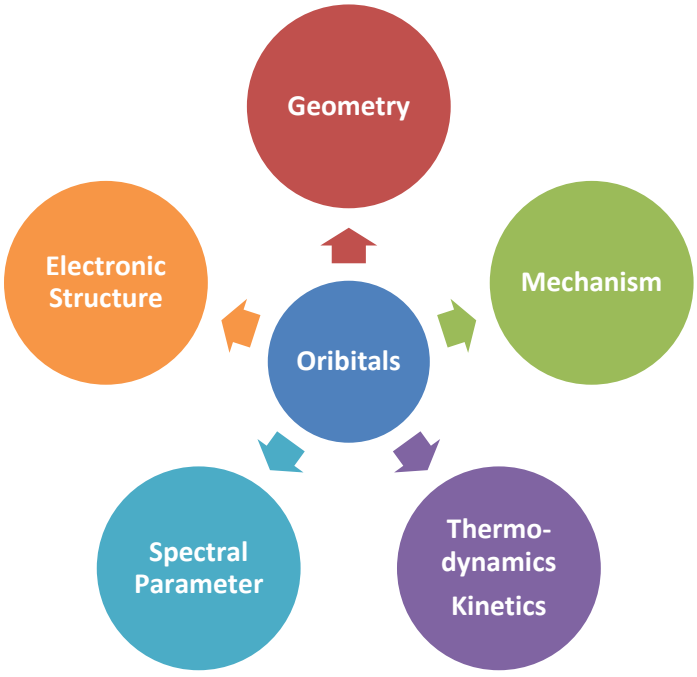

Figure VIII-2 The information made available by computational chemistry.

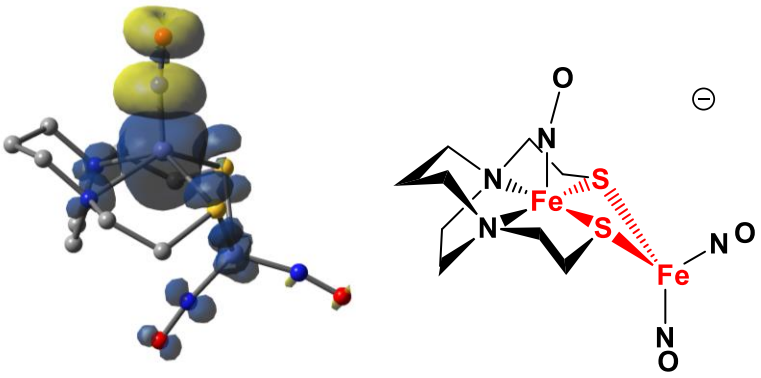

Figure VIII-3 The spin densities of a triplet $\{FeNO\}^8$ species. The blue shading indicates excess alpha spin densities on the Fe and the yellow shading indicates excess beta spin densities on the NO ligand in **2**. Note the electron rich $\{FeNO\}^8$ is linear.

- The electronic structure (*i.e.*, the composition of orbitals) depicts the interactions between atoms and fragments in the molecule. For example, we demonstrated the electronic structure of the $\{FeNO\}^8$ moiety of $\mathbf{2}^-$, the doubly reduced form of $\mathbf{2}^+$, has antiferromagnetically coupled high-spin Fe^{II} and high-spin NO^-, Figure VIII-3. This configuration leads to a linear NO, as the d_{z2} orbital which prefers a bent NO to overlap with NO's π^* orbital is only singly occupied. Conventional wisdom, *i.e.*, simple explanations regarding M-NO interactions conclude that the more reduced the M-NO fragment is, the more bent the M-N-O angle is. And this rule is correct, if based on the assumption the strong back-bonding of NO would render the M(NO) fragment to be low-spin. Careful analysis of the spin state of the $\{FeNO\}^8$ fragment led to the unexpected linear geometry predicted by computations. The conventional

approach of M-N-O angles is exemplified in the singlet $\{CoNO\}^8$, which is highly bent.

- The geometries are optimized and compared with structures from X-ray diffraction analyses. Most importantly, structures are calculated for transient species that cannot be or have not been captured or separated. For example, the optimization indicated the singly oxidized intermediate $\mathbf{6}^+$ has a bridging carbonyl (Figure VIII-4), which matches a low CO stretching frequency in the IR spectrum.

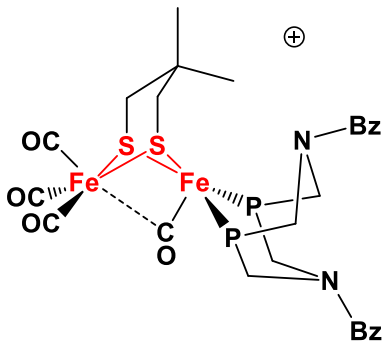

Figure VIII-4 The calculated geometry of $[Fe(CO)_3][(\mu\text{-}CO)Fe'(P_2N_2)]^+$ features a (semi-)bridging carbonyl.

- A sketch of the potential energy surface (PES) of the interested reaction is formed by calculating the Gibbs free energies of various relevant species. All the mechanisms presented in the dissertation, are essentially searches for the lowest barriers between the reactants and products. The illustrative example, in Figure VIII-5, contains multiple candidate transition states to isomerize the linkage cyanide in **4**, while the

carbon-bridged species (TS1 in Figure VIII-5) is calculated to be the most accessible one.

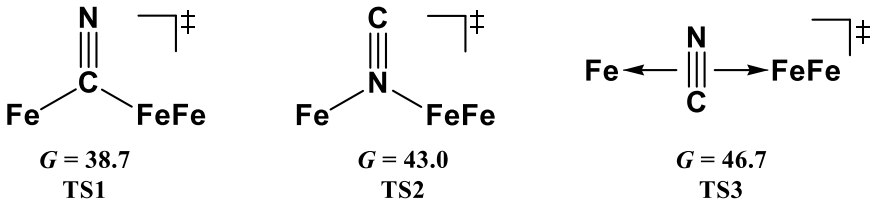

Figure VIII-5 Multiple candidate transition states connecting two cyanide linkage isomers.

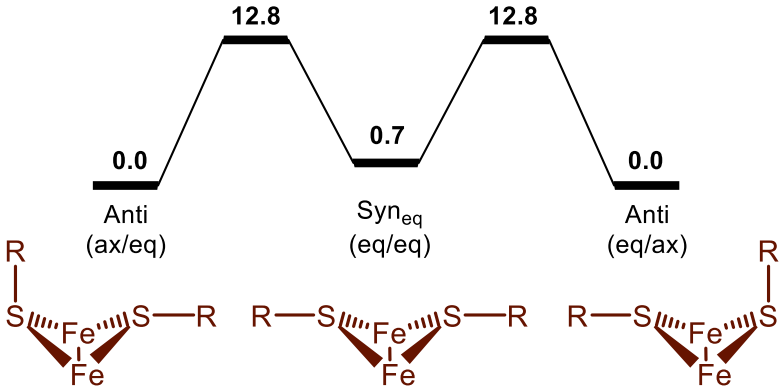

Figure VIII-6 The conformation exchange of the bridging heads.

- The calculated thermodynamic data (Gibbs free energies) can used to determine the reaction preferences, *i.e.*, whether a reaction should happen spontaneously; the acidities and redox potentials of species are further derived from it. The kinetic barrier heights can be estimated with optimized transition states, to show the rates of reactions. For example, the NMR coalescence kinetic experiments determined, for the axial-equatorial conformation exchange of **5,** the barrier is 13.3 kcal/mol. It validates the two-step mechanism with a calculated 12.8 kcal/mol barrier (Figure VIII-6).

- Various types of spectral results can be simulated with calculated parameters and compared to experimental counterparts to assist assignments, including IR (from molecular motions), EPR (from spin densities), Mossbauer and NMR (from electron density at nuclei), the spectra relating to compounds in Figure VIII-1. Representatively, the middle NO band of the IR spectrum of $\mathbf{2}^{+}$ was assigned to the Fe(NO) moiety with the visualized vibrational mode, Figure VIII-7, while the other two are assigned to the $Fe(NO)_2$ moiety.

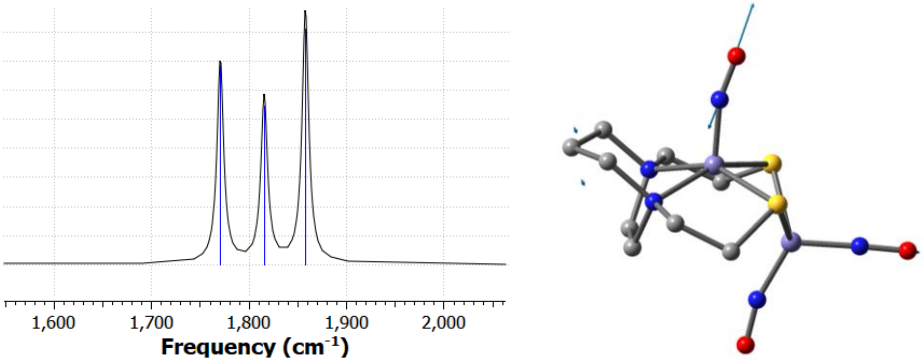

Figure VIII-7 The simulated IR spectrum of a tri-nitrosyl species. Wavenumbers are 1771, 1816 and 1858 cm^{-1} for three NO bands of $\mathbf{2}^{+}$, respectively. The displacement vector of the middle band (1816 cm^{-1}) is presented in the right panel with a major contribution from the NO of the Fe(NO) moiety.

Remaining difficulties and possible solutions

The computational chemistry, helps solve many problems but also leaves some behind. Here is an incomplete list.

- In the molecular modelling by quantum chemistry, the searches for intermediates and transition states, or anything without direct structural evidence, are largely initiated from experience or empiricism. The optimized structure is dependent on the input structure. In other words, the modelling would always provide a slice of the PES rather than the full picture. Mechanistic proposals based on educated guesses could safely include most chemically reasonable variants of the desired intermediates and reaction routes, but exceptions do exist. Therefore, what the computational chemistry does is to screen out reasonable mechanisms by denying those with barriers that are unreasonably too high. To obtain a full list of possible intermediates and transition states, the molecular dynamic simulations must be done. But a molecular dynamic simulation backed up by the quantum-chemistry level energetics will have forbiddingly high demands for resources.
- The barrier estimation in the conventional mechanistic study is only applicable to steps that do not involve electron transfers and proton transfers, as one sees in the H_2 production and CO_2 reduction projects. The proton transfer, essentially involves the separation of the proton and its carrier conjugate base, *i.e.*, the separation of charges of opposite signs. The charge-charge interaction is indeed shielded by the solvents such that a solvation model is needed in the optimization of the transition state, which increases the calculation time by a factor of two to five. Such a special procedure is only applied to a limited subset of selected protonations. The barrier of the electron transfer from the electrode to the electro-catalyst is more problematic, because it involves the reaction on the surface of the electrode. The simulation of surface

reactions needs special handling. An associated problem is the barrier of the electron-coupled proton transfer, since the electron transfer process is not kinetically modelled at all, the calculation is limited to the thermodynamic data.

- The bimetallic models, though providing mechanistic insight to the enzyme, are sometimes too simple to describe the real mechanism on the enzyme. In the C-H activation project, it is proved that the second coordination sphere facilitates the reaction to a large extent. The H_2 producing electro-catalysts, nominal models of Hydrogenase, lacks the delicate apparatus for electron and proton transportations, which are multiple amino acid residues in the hydrogenase. These electro-catalysts have to grab the electrons and protons by themselves, by shifting back and forth between the electrode and the bulk solution, like any other non-bio-inspired electro-catalyst. The same problem is also applicable to the cyanide linkage isomerization which we failed to reproduce on our model complexes. The isomerization, could have something to do with the protein matrix, completely overlooked in the molecular modelling. One possible fix to this problem is to add important amino-acid residues in the calculation as the "background". The ultimate solution is to have the full protein matrix, though most of the matrix should be simulated with molecular mechanics methods to save resources.
- The electronic structure of the ubiquitous fragment $Fe(NO)_x$ in the model complexes is still treated as a unity, rather than discrete components of metal and nitrosyl with clear partitioning of their shared electrons. The accurate description of the $M(NO)_x$ moiety essentially requires a multi-determinant wavefunction from high-level *ab*

initio calculations. However, the spin-polarization scheme by DFT calculations did a good job by giving the averaged electron distribution and is good enough for mechanistic studies, because errors are largely cancelled in the catalytic cycles.

- Computational algorithms, are not yet able to produce accurate spectral parameters independently. These parameters are generally semi-quantitative and are used in a relative fashion. The IR frequencies need to be scaled by an empirical factor, while the Mossbauer parameters have to be fitted by a calibration curve. Sometimes the spectrum parameters produced by computational chemistry, is not creditworthy enough to unambiguously assign subtle structure differences. For example, cyanide linkage isomers of **4** give very similar IR frequencies.
- It is somewhat difficult to apply the computational results to optimize the catalysts. The calculations presented in this dissertation are tightly related to the experimental evidence. On one hand, they mutually verify each other. On the other hand, the calculations may be too deeply rooted in the experiments, resulting in a collection of data points that is too sparse. The calculations can tell which step is rate-limiting, but can hardly offer suggestions to improve it, beyond the level of chemistry common sense. A database containing ample trial models generated from building fragments is needed to build a robust statistic model before useful suggestions can be provided.

Outlook

The goal of computational chemistry has long been expected to provide the state-of-the-art predictions since its birth. Unfortunately, it is far more successive in

reproducing the results from the wet lab, though such reproduction helps validate the computational methods utilized for further predictions. In addition, computational chemistry is also good at generating a sounder explanation to observed experimental phenomena by filling the gaps between pieces of experimental evidence.

The current omission of prediction power is partly caused by the limit of computational resources. The mechanistic study of a moderated-sized system (say, fifty atoms with two transition metals) would reasonably cost 100, 000 CPU hours and could easily span into a course of three months, even with modern super computers that can deal with multiple jobs parallelly. On top of that, heavy human interventions are required such that the calculations simply won't run as expected. With an optimistic estimation, only a half of the calculations come to the end with no surprises while others contain errors to be corrected, endless loops to be stopped, and unexpected results to be carefully reviewed. The huge cost to commit errors makes computational chemists conservative: they are only willing to spend time on experimentally proven systems. If they dare to invest more on a purely theoretical model, they become very vulnerable to the peer reviews that would probably open with the concern: whether it happens in the real world.

This can be changed; the change is happening indeed. The computation power is just increasing simply following Moore's law (the capacity of a computer doubles every eighteen months). A faster processor means less time wasted in waiting, more data and less disappointment. Beyond the evolution of the chips, the other trend is, the scientific computation is gradually switching from CPU-powered to GPU-powered. GPU,

specialized in parallel computing, can dramatically reduce the run-time by ten-fold, if not more (in comparison to CPU serial computing).

On the other hand, the machine learning is expected to increase the automation of data collection and analysis, which is more or less carried out manually now. Its development may liberate the computational chemists from daily trouble-shooting and make them focus on the chemical aspects of the outcomes.

The stronger than ever computational resources, in combination with automatic tools is drawing such a blueprint: in the near future, the computational chemists can systematically screen a large database of organometallic candidates that are designed, but not actually synthesized yet, to build a robust model without costing an arm and a leg: the accuracy of prediction is dependent on the accumulation of data points. Ultimately, the predictions can help reduce the burdens of our experimental peers. I believe It is the dawn, the moment before the sweet prediction power of computational chemistry can be harvested. The best time, is not behind, but is ahead.

REFERENCES

1. Born, M.; Oppenheimer, R. *Annalen der Physik* **1927,** *389*, 457-484.
2. Pauli, W., Exclusion Principle and Quantum Mechanics. In *Writings on Physics and Philosophy*, Enz, C. P.; von Meyenn, K., Eds. Springer Berlin Heidelberg: Berlin, Heidelberg, 1994; pp 165-181.
3. Slater, J. C. *Physical Review* **1929,** *34*, 1293-1322.
4. Lennard-Jones, J. E. *Transactions of the Faraday Society* **1929,** *25*, 668-686.
5. Boys, S. F. *Proceedings of the Royal Society of London. Series A. Mathematical and Physical Sciences* **1950,** *200*, 542-554.
6. Hehre, W. J.; Stewart, R. F.; Pople, J. A. *J. Chem. Phys.* **1969,** *51*, 2657-2664.
7. Harris, J. *Physical Review B* **1985,** *31*, 1770-1779.
8. Roothaan, C. C. J. *Reviews of Modern Physics* **1951,** *23*, 69-89.
9. Hartree, D. R. *Mathematical Proceedings of the Cambridge Philosophical Society* **2008,** *24*, 89-110.
10. Fock, V. *Zeitschrift für Physik* **1930,** *61*, 126-148.
11. St.-Amant, A.; Cornell, W. D.; Kollman, P. A.; Halgren, T. A. *J. Comput. Chem.* **1995,** *16*, 1483-1506.
12. Hohenberg, P.; Kohn, W. *Physical Review* **1964,** *136*, B864-B871.
13. Zhou, B.; Ligneres, V. L.; Carter, E. A. *J. Chem. Phys.* **2005,** *122*, 044103.
14. Kohn, W.; Sham, L. J. *Physical Review* **1965,** *140*, A1133-A1138.

15. Thomas, L. H. *Mathematical Proceedings of the Cambridge Philosophical Society* **2008,** *23*, 542-548.

16. Perdew, J. P.; Wang, Y. *Physical Review B* **1992,** *45*, 13244-13249.

17. Perdew, J. P.; Ruzsinszky, A.; Tao, J.; Staroverov, V. N.; Scuseria, G. E.; Csonka, G. I. *J. Chem. Phys.* **2005,** *123*, 062201.

18. Herman, F.; Van Dyke, J. P.; Ortenburger, I. B. *Phys. Rev. Lett.* **1969,** *22*, 807-811.

19. Herman, F.; Ortenburger, I. B.; Van Dyke, J. P. *Int. J. Quantum Chem* **1969,** *4*, 827-846.

20. Perdew, J. P.; Burke, K.; Ernzerhof, M. *Phys. Rev. Lett.* **1996,** *77*, 3865-3868.

21. Tao, J.; Perdew, J. P.; Staroverov, V. N.; Scuseria, G. E. *Phys. Rev. Lett.* **2003,** *91*, 146401.

22. Mori-Sánchez, P.; Cohen, A. J.; Yang, W. *J. Chem. Phys.* **2006,** *125*, 201102.

23. Becke, A. D. *J. Chem. Phys.* **1993,** *98*, 1372-1377.

24. Becke, A. D. *J. Chem. Phys.* **1993,** *98*, 5648-5652.

25. Adamo, C.; Barone, V. *J. Chem. Phys.* **1999,** *110*, 6158-6170.

26. Staroverov, V. N.; Scuseria, G. E.; Tao, J.; Perdew, J. P. *J. Chem. Phys.* **2003,** *119*, 12129-12137.

27. Gill, P. M. W.; Adamson, R. D.; Pople, J. A. *Mol. Phys.* **1996,** *88*, 1005-1009.

28. Leininger, T.; Stoll, H.; Werner, H.-J.; Savin, A. *Chem. Phys. Lett.* **1997,** *275*, 151-160.

29. Grimme, S.; Antony, J.; Ehrlich, S.; Krieg, H. *J. Chem. Phys.* **2010,** *132*, 154104.

30. Grimme, S.; Ehrlich, S.; Goerigk, L. *J. Comput. Chem.* **2011,** *32*, 1456-1465.

31. Mardirossian, N.; Head-Gordon, M. *Mol. Phys.* **2017**, 1-58.

32. Mardirossian, N.; Head-Gordon, M. *Journal of Chemical Theory and Computation* **2016,** *12*, 4303-4325.

33. Goerigk, L.; Grimme, S. *Wiley Interdisciplinary Reviews: Computational Molecular Science* **2014,** *4*, 576-600.

34. Davidson, E. R. *Chem. Rev.* **2000,** *100*, 351-352.

35. Lever, A. B. P. *Coord. Chem. Rev.* **2003,** *238*, 1.

36. Lubitz, W.; Ogata, H.; Rüdiger, O.; Reijerse, E. *Chem. Rev.* **2014,** *114*, 4081-4148.

37. Vignais, P. M.; Billoud, B. *Chem. Rev.* **2007,** *107*, 4206-4272.

38. Nicolet, Y.; Piras, C.; Legrand, P.; Hatchikian, C. E.; Fontecilla-Camps, J. C. *Structure* **1999,** *7*, 13-23.

39. Peters, J. W.; Lanzilotta, W. N.; Lemon, B. J.; Seefeldt, L. C. *Science* **1998,** *282*, 1853-1858.

40. Silakov, A.; Wenk, B.; Reijerse, E.; Lubitz, W. *Phys. Chem. Chem. Phys.* **2009,** *11*, 6592-6599.

41. Hatchikian, E. C.; Forget, N.; Fernandez, V. M.; Williams, R.; Cammack, R. *Eur. J. Biochem.* **1992,** *209*, 357-365.

42. Caserta, G.; Pecqueur, L.; Adamska-Venkatesh, A.; Papini, C.; Roy, S.; Artero, V.; Atta, M.; Reijerse, E.; Lubitz, W.; Fontecave, M. *Nat. Chem. Biol.* **2017,** *13*, 779-784.

43. Esselborn, J.; Lambertz, C.; Adamska-Venkatesh, A.; Simmons, T.; Berggren, G.; Noth, J.; Siebel, J.; Hemschemeier, A.; Artero, V.; Reijerse, E.; Fontecave, M.; Lubitz, W.; Happe, T. *Nat. Chem. Biol.* **2013,** *9*, 607-609.

44. Mulder, D. W.; Boyd, E. S.; Sarma, R.; Lange, R. K.; Endrizzi, J. A.; Broderick, J. B.; Peters, J. W. *Nature* **2010,** *465*, 248-251.

45. Berggren, G.; Adamska, A.; Lambertz, C.; Simmons, T. R.; Esselborn, J.; Atta, M.; Gambarelli, S.; Mouesca, J. M.; Reijerse, E.; Lubitz, W.; Happe, T.; Artero, V.; Fontecave, M. *Nature* **2013,** *499*, 66-69.

46. Siebel, J. F.; Adamska-Venkatesh, A.; Weber, K.; Rumpel, S.; Reijerse, E.; Lubitz, W. *Biochemistry* **2015,** *54*, 1474-1483.

47. Esselborn, J.; Muraki, N.; Klein, K.; Engelbrecht, V.; Metzler-Nolte, N.; Apfel, U. P.; Hofmann, E.; Kurisu, G.; Happe, T. *Chem. Sci.* **2016,** *7*, 959-968.

48. Reijerse, E. J.; Pham, C. C.; Pelmenschikov, V.; Gilbert-Wilson, R.; Adamska-Venkatesh, A.; Siebel, J. F.; Gee, L. B.; Yoda, Y.; Tamasaku, K.; Lubitz, W.; Rauchfuss, T. B.; Cramer, S. P. *J. Am. Chem. Soc.* **2017,** *139*, 4306-4309.

49. Sommer, C.; Adamska-Venkatesh, A.; Pawlak, K.; Birrell, J. A.; Rüdiger, O.; Reijerse, E. J.; Lubitz, W. *J. Am. Chem. Soc.* **2017,** *139*, 1440-1443.

50. Adamska, A.; Silakov, A.; Lambertz, C.; Rüdiger, O.; Happe, T.; Reijerse, E.; Lubitz, W. *Angew. Chem. Int. Ed.* **2012,** *51*, 11458-11462.

51. Mulder, D. W.; Guo, Y.; Ratzloff, M. W.; King, P. W. *J. Am. Chem. Soc.* **2017,** *139*, 83-86.

52. Siegbahn, P. E. M.; Tye, J. W.; Hall, M. B. *Chem. Rev.* **2007,** *107*, 4414-4435.

53. Cao, Z.; Hall, M. B. *J. Am. Chem. Soc.* **2001,** *123*, 3734-3742.

54. Fan, H.-J.; Hall, M. B. *J. Am. Chem. Soc.* **2001,** *123*, 3828-3829.

55. Liu, Z.-P.; Hu, P. *J. Am. Chem. Soc.* **2002,** *124*, 5175-5182.

56. Liu, Z.-P.; Hu, P. *J. Chem. Phys.* **2002,** *117*, 8177-8180.

57. Schwab, D. E.; Tard, C.; Brecht, E.; Peters, J. W.; Pickett, C. J.; Szilagyi, R. K. *Chem. Commun.* **2006**, 3696-3698.

58. Fiedler, A. T.; Brunold, T. C. *Inorg. Chem.* **2005,** *44*, 9322-9334.

59. Bruschi, M.; Greco, C.; Kaukonen, M.; Fantucci, P.; Ryde, U.; De Gioia, L. *Angew. Chem. Int. Ed.* **2009,** *48*, 3503-3506.

60. Torres, R. A.; Lovell, T.; Noodleman, L.; Case, D. A. *J. Am. Chem. Soc.* **2003,** *125*, 1923-1936.

61. Mouesca, J.-M.; Chen, J. L.; Noodleman, L.; Bashford, D.; Case, D. A. *J. Am. Chem. Soc.* **1994,** *116*, 11898-11914.

62. Marcus, R. A. *Reviews of Modern Physics* **1993,** *65*, 599-610.

63. Winter, A.; Zsolnai, L.; Hüttner, G. *Zeitschrift für Naturforschung B* **1982,** *37*, 1430-1436.

64. Felton, G. A. N.; Vannucci, A. K.; Chen, J.; Lockett, L. T.; Okumura, N.; Petro, B. J.; Zakai, U. I.; Evans, D. H.; Glass, R. S.; Lichtenberger, D. L. *J. Am. Chem. Soc.* **2007,** *129*, 12521-12530.

65. Greco, C.; Zampella, G.; Bertini, L.; Bruschi, M.; Fantucci, P.; De Gioia, L. *Inorg. Chem.* **2007,** *46*, 108-116.

66. Li, H.; Rauchfuss, T. B. *J. Am. Chem. Soc.* **2002,** *124*, 726-727.

67. Liu, T.; Darensbourg, M. Y. *J. Am. Chem. Soc.* **2007,** *129*, 7008-7009.

68. Justice, A. K.; Rauchfuss, T. B.; Wilson, S. R. *Angew. Chem. Int. Ed.* **2007,** *46*, 6152-6154.

69. Singleton, M. L.; Bhuvanesh, N.; Reibenspies, J. H.; Darensbourg, M. Y. *Angew. Chem. Int. Ed.* **2008,** *47*, 9492-9495.

70. Hsieh, C.-H.; Erdem, Ö. F.; Harman, S. D.; Singleton, M. L.; Reijerse, E.; Lubitz, W.; Popescu, C. V.; Reibenspies, J. H.; Brothers, S. M.; Hall, M. B.; Darensbourg, M. Y. *J. Am. Chem. Soc.* **2012,** *134*, 13089-13102.

71. Zaffaroni, R.; Rauchfuss, T. B.; Gray, D. L.; De Gioia, L.; Zampella, G. *J. Am. Chem. Soc.* **2012,** *134*, 19260-19269.

72. Carroll, M. E.; Barton, B. E.; Rauchfuss, T. B.; Carroll, P. J. *J. Am. Chem. Soc.* **2012,** *134*, 18843-18852.

73. Olsen, M. T.; Bruschi, M.; De Gioia, L.; Rauchfuss, T. B.; Wilson, S. R. *J. Am. Chem. Soc.* **2008,** *130*, 12021-12030.

74. Frisch, M. J.; Trucks, G. W.; Schlegel, H. B.; Scuseria, G. E.; Robb, M. A.; Cheeseman, J. R.; Scalmani, G.; Barone, V.; Mennucci, B.; Petersson, G. A.; Nakatsuji, H.; Caricato, M.; Li, X.; Hratchian, H. P.; Izmaylov, A. F.; Bloino, J.; Zheng, G.; Sonnenberg, J. L.; Hada, M.; Ehara, M.; Toyota, K.; Fukuda, R.; Hasegawa, J.; Ishida, M.; Nakajima, T.; Honda, Y.; Kitao, O.; Nakai, H.; Vreven, T.; Montgomery Jr., J. A.; Peralta, J. E.; Ogliaro, F.; Bearpark, M. J.; Heyd, J.; Brothers, E. N.; Kudin, K. N.; Staroverov, V. N.; Kobayashi, R.; Normand, J.; Raghavachari, K.; Rendell, A. P.; Burant, J. C.; Iyengar, S. S.; Tomasi, J.; Cossi,

M.; Rega, N.; Millam, N. J.; Klene, M.; Knox, J. E.; Cross, J. B.; Bakken, V.; Adamo, C.; Jaramillo, J.; Gomperts, R.; Stratmann, R. E.; Yazyev, O.; Austin, A. J.; Cammi, R.; Pomelli, C.; Ochterski, J. W.; Martin, R. L.; Morokuma, K.; Zakrzewski, V. G.; Voth, G. A.; Salvador, P.; Dannenberg, J. J.; Dapprich, S.; Daniels, A. D.; Farkas, Ö.; Foresman, J. B.; Ortiz, J. V.; Cioslowski, J.; Fox, D. J. *Gaussian 09*, Gaussian, Inc.: Wallingford, CT, USA, 2009.

75. Neese, F. *Wiley Interdisciplinary Reviews: Computational Molecular Science* **2012,** *2*, 73-78.
76. Brothers, S. M.; Darensbourg, M. Y.; Hall, M. B. *Inorg. Chem.* **2011,** *50*, 8532-8540.
77. Zhao, Y.; Truhlar, D. G. *Theor. Chem. Acc.* **2008,** *120*, 215-241.
78. Chai, J.-D.; Head-Gordon, M. *Phys. Chem. Chem. Phys.* **2008,** *10*, 6615-6620.
79. Krishnan, R.; Binkley, J. S.; Seeger, R.; Pople, J. A. *J. Chem. Phys.* **1980,** *72*, 650-654.
80. McLean, A. D.; Chandler, G. S. *J. Chem. Phys.* **1980,** *72*, 5639-5648.
81. Clark, T.; Chandrasekhar, J.; Spitznagel, G. W.; Schleyer, P. V. R. *J. Comput. Chem.* **1983,** *4*, 294-301.
82. Figgen, D.; Peterson, K. A.; Dolg, M.; Stoll, H. *J. Chem. Phys.* **2009,** *130*, 164108.
83. Li, X.; Frisch, M. J. *Journal of Chemical Theory and Computation* **2006,** *2*, 835-839.
84. Simons, J.; Joergensen, P.; Taylor, H.; Ozment, J. *The Journal of Physical Chemistry* **1983,** *87*, 2745-2753.

85. Peng, C.; Bernhard Schlegel, H. *Isr. J. Chem.* **1993,** *33*, 449-454.

86. Peng, C.; Ayala, P. Y.; Schlegel, H. B.; Frisch, M. J. *J. Comput. Chem.* **1996,** *17*, 49-56.

87. Yamaguchi, K.; Yamanaka, S.; Nishino, M.; Takano, Y.; Kitagawa, Y.; Nagao, H.; Yoshioka, Y. *Theor. Chem. Acc.* **1999,** *102*, 328-345.

88. Marenich, A. V.; Cramer, C. J.; Truhlar, D. G. *The Journal of Physical Chemistry B* **2009,** *113*, 6378-6396.

89. Eyring, H. *J. Chem. Phys.* **1935,** *3*, 107-115.

90. Foster, J. P.; Weinhold, F. *J. Am. Chem. Soc.* **1980,** *102*, 7211-7218.

91. Neese, F. *Inorg. Chim. Acta* **2002,** *337*, 181-192.

92. Can, M.; Armstrong, F. A.; Ragsdale, S. W. *Chem. Rev.* **2014,** *114*, 4149-4174.

93. Helm, M. L.; Stewart, M. P.; Bullock, R. M.; DuBois, M. R.; DuBois, D. L. *Science* **2011,** *333*, 863-866.

94. DuBois, D. L. *Inorg. Chem.* **2014,** *53*, 3935-3960.

95. Wilson, A. D.; Shoemaker, R. K.; Miedaner, A.; Muckerman, J. T.; DuBois, D. L.; DuBois, M. R. *Proc. Nat. Acad. Sci. U. S. A.* **2007,** *104*, 6951-6956.

96. Wilson, A. D.; Newell, R. H.; McNevin, M. J.; Muckerman, J. T.; Rakowski DuBois, M.; DuBois, D. L. *J. Am. Chem. Soc.* **2006,** *128*, 358-366.

97. Raugei, S.; Chen, S.; Ho, M.-H.; Ginovska-Pangovska, B.; Rousseau, R. J.; Dupuis, M.; DuBois, D. L.; Bullock, R. M. *Chem. Eur. J.* **2012,** *18*, 6493-6506.

98. Stewart, M. P.; Ho, M.-H.; Wiese, S.; Lindstrom, M. L.; Thogerson, C. E.; Raugei, S.; Bullock, R. M.; Helm, M. L. *J. Am. Chem. Soc.* **2013,** *135*, 6033-6046.

99. Liu, T.; Chen, S.; O'Hagan, M. J.; Rakowski DuBois, M.; Bullock, R. M.; DuBois, D. L. *J. Am. Chem. Soc.* **2012,** *134*, 6257-6272.

100. Liu, T.; DuBois, D. L.; Bullock, R. M. *Nat. Chem.* **2013,** *5*, 228-233.

101. Liu, T.; Wang, X.; Hoffmann, C.; DuBois, D. L.; Bullock, R. M. *Angew. Chem. Int. Ed.* **2014,** *53*, 5300-5304.

102. Ogata, H.; Nishikawa, K.; Lubitz, W. *Nature* **2015,** *520*, 571-574.

103. Dementin, S.; Burlat, B.; De Lacey, A. L.; Pardo, A.; Adryanczyk-Perrier, G.; Guigliarelli, B.; Fernandez, V. M.; Rousset, M. *J. Biol. Chem.* **2004,** *279*, 10508-10513.

104. Niu, S.; Hall, M. B. *Inorg. Chem.* **2001,** *40*, 6201-6203.

105. Ogo, S.; Ichikawa, K.; Kishima, T.; Matsumoto, T.; Nakai, H.; Kusaka, K.; Ohhara, T. *Science* **2013,** *339*, 682-684.

106. Denny, J. A.; Darensbourg, M. Y. *Chem. Rev.* **2015,** *115*, 5248-5273.

107. Nguyen, N. T.; Mori, Y.; Matsumoto, T.; Yatabe, T.; Kabe, R.; Nakai, H.; Yoon, K.-S.; Ogo, S. *Chem. Commun.* **2014,** *50*, 13385-13387.

108. Yang, D.; Li, Y.; Su, L.; Wang, B.; Qu, J. *Eur. J. Inorg. Chem.* **2015,** *2015*, 2965-2973.

109. Zhu, W.; Marr, A. C.; Wang, Q.; Neese, F.; Spencer, D. J. E.; Blake, A. J.; Cooke, P. A.; Wilson, C.; Schröder, M. *Proc. Nat. Acad. Sci. U. S. A.* **2005,** *102*, 18280-18285.

110. Canaguier, S.; Field, M.; Oudart, Y.; Pecaut, J.; Fontecave, M.; Artero, V. *Chem. Commun.* **2010,** *46*, 5876-5878.

111. Weber, K.; Erdem, Ö. F.; Bill, E.; Weyhermüller, T.; Lubitz, W. *Inorg. Chem.* **2014,** *53*, 6329-6337.

112. Reynolds, M. A.; Rauchfuss, T. B.; Wilson, S. R. *Organometallics* **2003,** *22*, 1619-1625.

113. Kim, K.; Matsumoto, T.; Robertson, A.; Nakai, H.; Ogo, S. *Chem. Asian. J.* **2012,** *7*, 1394-1400.

114. Kishima, T.; Matsumoto, T.; Nakai, H.; Hayami, S.; Ohta, T.; Ogo, S. *Angew. Chem. Int. Ed.* **2016,** *55*, 724-727.

115. Kure, B.; Sano, M.; Nakajima, T.; Tanase, T. *Organometallics* **2014,** *33*, 3950-3965.

116. Kim, K.; Kishima, T.; Matsumoto, T.; Nakai, H.; Ogo, S. *Organometallics* **2013,** *32*, 79-87.

117. Enemark, J. H.; Feltham, R. D. *Coord. Chem. Rev.* **1974,** *13*, 339-406.

118. Chiang, C.-Y.; Miller, M. L.; Reibenspies, J. H.; Darensbourg, M. Y. *J. Am. Chem. Soc.* **2004,** *126*, 10867-10874.

119. Chiang, C.-Y.; Lee, J.; Dalrymple, C.; Sarahan, M. C.; Reibenspies, J. H.; Darensbourg, M. Y. *Inorg. Chem.* **2005,** *44*, 9007-9016.

120. Hsieh, C.-H.; Ding, S.; Erdem, O. F.; Crouthers, D. J.; Liu, T.; McCrory, C. C. L.; Lubitz, W.; Popescu, C. V.; Reibenspies, J. H.; Hall, M. B.; Darensbourg, M. Y. *Nat. Commun.* **2014,** *5*.

121. Smee, J. J.; Miller, M. L.; Grapperhaus, C. A.; Reibenspies, J. H.; Darensbourg, M. Y. *Inorg. Chem.* **2001,** *40*, 3601-3605.

122. Fourmond, V.; Jacques, P. A.; Fontecave, M.; Artero, V. *Inorg. Chem.* **2010,** *49*, 10338-10347.

123. Felton, G. A. N.; Glass, R. S.; Lichtenberger, D. L.; Evans, D. H. *Inorg. Chem.* **2006,** *45*, 9181-9184.

124. Appel, A. M.; Helm, M. L. *ACS Catal.* **2014,** *4*, 630-633.

125. Wiese, S.; Kilgore, U. J.; Ho, M.-H.; Raugei, S.; DuBois, D. L.; Bullock, R. M.; Helm, M. L. *ACS Catal.* **2013,** *3*, 2527-2535.

126. Smieja, J. M.; Benson, E. E.; Kumar, B.; Grice, K. A.; Seu, C. S.; Miller, A. J. M.; Mayer, J. M.; Kubiak, C. P. *Proc. Nat. Acad. Sci. U. S. A.* **2012,** *109*, 15646-15650.

127. Cheng, T. Y.; Bullock, R. M. *J. Am. Chem. Soc.* **1999,** *121*, 3150-3155.

128. Surawatanawong, P.; Tye, J. W.; Darensbourg, M. Y.; Hall, M. B. *Dalton Trans.* **2010,** *39*, 3093-3104.

129. Marenich, A. V.; Ho, J.; Coote, M. L.; Cramer, C. J.; Truhlar, D. G. *Phys. Chem. Chem. Phys.* **2014,** *16*, 15068-15106.

130. Sun, N.; Liu, L. V.; Dey, A.; Villar-Acevedo, G.; Kovacs, J. A.; Darensbourg, M. Y.; Hodgson, K. O.; Hedman, B.; Solomon, E. I. *Inorg. Chem.* **2011,** *50*, 427-436.

131. Coetzee, J. F.; Padmanabhan, G. R. *J. Am. Chem. Soc.* **1965,** *87*, 5005-5010.

132. Artero, V.; Fontecave, M. *C. R. Chim.* **2008,** *11*, 926-931.

133. Luca, O. R.; Crabtree, R. H. *Chem. Soc. Rev.* **2013,** *42*, 1440-1459.

134. Brazzolotto, D.; Gennari, M.; Queyriaux, N.; Simmons, T. R.; Pécaut, J.; Demeshko, S.; Meyer, F.; Orio, M.; Artero, V.; Duboc, C. *Nat. Chem.* **2016**, DOI: 10.1038/nchem.2575.

135. Addison, A. W.; Rao, T. N.; Reedijk, J.; van Rijn, J.; Verschoor, G. C. *J. Chem. Soc., Dalton Trans.* **1984**, 1349-1356.

136. Hammond, G. S. *J. Am. Chem. Soc.* **1955,** *77*, 334-338.

137. Cook, T. R.; Dogutan, D. K.; Reece, S. Y.; Surendranath, Y.; Teets, T. S.; Nocera, D. G. *Chem. Rev.* **2010,** *110*, 6474-6502.

138. Mulder, David W.; Shepard, Eric M.; Meuser, Jonathan E.; Joshi, N.; King, Paul W.; Posewitz, Matthew C.; Broderick, Joan B.; Peters, John W. *Structure* **2011,** *19*, 1038-1052.

139. Niu, S.; Thomson, L. M.; Hall, M. B. *J. Am. Chem. Soc.* **1999,** *121*, 4000-4007.

140. Siegbahn, P. E. M. *Adv. Inorg. Chem.* **2004,** *Volume 56*, 101-125.

141. Pavlov, M.; Siegbahn, P. E. M.; Blomberg, M. R. A.; Crabtree, R. H. *J. Am. Chem. Soc.* **1998,** *120*, 548-555.

142. Evans, R. M.; Brooke, E. J.; Wehlin, S. A. M.; Nomerotskaia, E.; Sargent, F.; Carr, S. B.; Phillips, S. E. V.; Armstrong, F. A. *Nat. Chem. Biol.* **2016,** *12*, 46-50.

143. Ogata, H.; Nishikawa, K.; Lubitz, W. *Nature* **2015,** *520*, 571-574.

144. Simpson, F.; Burris, R. *Science* **1984,** *224*, 1095-1097.

145. Hoffman, B. M.; Lukoyanov, D.; Yang, Z.-Y.; Dean, D. R.; Seefeldt, L. C. *Chem. Rev.* **2014,** *114*, 4041-4062.

146. Hoffman, B. M.; Lukoyanov, D.; Dean, D. R.; Seefeldt, L. C. *Acc. Chem. Res.* **2013,** *46*, 587-595.

147. Lukoyanov, D.; Khadka, N.; Yang, Z.-Y.; Dean, D. R.; Seefeldt, L. C.; Hoffman, B. M. *J. Am. Chem. Soc.* **2016,** *138*, 10674-10683.

148. Lukoyanov, D.; Khadka, N.; Yang, Z.-Y.; Dean, D. R.; Seefeldt, L. C.; Hoffman, B. M. *J. Am. Chem. Soc.* **2016,** *138*, 1320-1327.

149. Lukoyanov, D.; Yang, Z.-Y.; Khadka, N.; Dean, D. R.; Seefeldt, L. C.; Hoffman, B. M. *J. Am. Chem. Soc.* **2015,** *137*, 3610-3615.

150. Tard, C.; Pickett, C. J. *Chem. Rev.* **2009,** *109*, 2245-2274.

151. Schilter, D.; Camara, J. M.; Huynh, M. T.; Hammes-Schiffer, S.; Rauchfuss, T. B. *Chem. Rev.* **2016,** *116*, 8693-8749.

152. Denny, J. A.; Darensbourg, M. Y. *Coord. Chem. Rev.* **2016,** *324*, 82-89.

153. Jørgensen, C. K. *Coord. Chem. Rev.* **1966,** *1*, 164-178.

154. Ding, S.; Ghosh, P.; Lunsford, A. M.; Wang, N.; Bhuvanesh, N.; Hall, M. B.; Darensbourg, M. Y. *J. Am. Chem. Soc.* **2016,** *138*, 12920-12927.

155. Ghosh, P.; Ding, S.; Chupik, R. B.; Hsieh, C.-H.; Bhuvanesh, N.; Hall, M. B.; Darensbourg, M. Y. *Chem. Sci.* **2017**, DOI: 10.1039/C7SC03378H.

156. Hsieh, C.-H.; Ding, S.; Erdem, O. F.; Crouthers, D. J.; Liu, T.; McCrory, C. C. L.; Lubitz, W.; Popescu, C. V.; Reibenspies, J. H.; Hall, M. B.; Darensbourg, M. Y. *Nat. Commun.* **2014,** *5*, 3684.

157. Jeffrey, J. C.; Rauchfuss, T. B. *Inorg. Chem.* **1979,** *18*, 2658-2666.

158. Hsieh, C.-H.; Darensbourg, M. Y. *J. Am. Chem. Soc.* **2010,** *132*, 14118-14125.

159. Hsieh, C.-H.; Chupik, R. B.; Pinder, T. A.; Darensbourg, M. Y. *Polyhedron* **2013,** *58*, 151-155.

160. Pulukkody, R.; Darensbourg, M. Y. *Acc. Chem. Res.* **2015,** *48*, 2049-2058.

161. Lyaskovskyy, V.; de Bruin, B. *ACS Catalysis* **2012,** *2*, 270-279.

162. Geiger, W. E.; Ohrenberg, N. C.; Yeomans, B.; Connelly, N. G.; Emslie, D. J. H. *J. Am. Chem. Soc.* **2003,** *125*, 8680-8688.

163. Hay, B. P.; Hancock, R. D. *Coord. Chem. Rev.* **2001,** *212*, 61-78.

164. Hall, M. B. *Inorg. Chem.* **1978,** *17*, 2261-2269.

165. Crouthers, D. J.; Ding, S.; Denny, J. A.; Bethel, R. D.; Hsieh, C.-H.; Hall, M. B.; Darensbourg, M. Y. *Angew. Chem.* **2015,** *127*, 11254-11258.

166. Ogo, S.; Kabe, R.; Uehara, K.; Kure, B.; Nishimura, T.; Menon, S. C.; Harada, R.; Fukuzumi, S.; Higuchi, Y.; Ohhara, T.; Tamada, T.; Kuroki, R. *Science* **2007,** *316*, 585-587.

167. Barton, B. E.; Whaley, C. M.; Rauchfuss, T. B.; Gray, D. L. *J. Am. Chem. Soc.* **2009,** *131*, 6942-6943.

168. Barton, B. E.; Rauchfuss, T. B. *J. Am. Chem. Soc.* **2010,** *132*, 14877-14885.

169. Brazzolotto, D.; Gennari, M.; Queyriaux, N.; Simmons, T. R.; Pécaut, J.; Demeshko, S.; Meyer, F.; Orio, M.; Artero, V.; Duboc, C. *Nat. Chem.* **2016,** *8*, 1054-1060.

170. Hoffmann, R.; Chen, M. M. L.; Thorn, D. L. *Inorg. Chem.* **1977,** *16*, 503-511.

171. Connelly, N. G.; Emslie, D. J. H.; Metz, B.; Orpen, A. G.; Quayle, M. J. *Chem. Commun.* **1996**, 2289-2290.

172. Connelly, N. G.; Emslie, D. J. H.; Geiger, W. E.; Hayward, O. D.; Linehan, E. B.; Orpen, A. G.; Quayle, M. J.; Rieger, P. H. *J. Chem. Soc., Dalton Trans.* **2001**, 670-683.

173. Barton, B. E.; Rauchfuss, T. B. *Inorg. Chem.* **2008,** *47*, 2261-2263.

174. Wang, W.; Rauchfuss, T. B.; Zhu, L.; Zampella, G. *J. Am. Chem. Soc.* **2014,** *136*, 5773-5782.

175. Heiden, Z. M.; Zampella, G.; De Gioia, L.; Rauchfuss, T. B. *Angew. Chem. Int. Ed.* **2008,** *47*, 9756-9759.

176. Esselborn, J.; Lambertz, C.; Adamska-Venkatesh, A.; Simmons, T.; Berggren, G.; Noth, J.; Siebel, J.; Hemschemeier, A.; Artero, V.; Reijerse, E.; Fontecave, M.; Lubitz, W.; Happe, T. *Nat. Chem. Biol.* **2013,** *9*, 607-609.

177. Zhu, N.; Vahrenkamp, H. *Chem. Ber.* **1997,** *130*, 1241-1252.

178. Erdem, Ö. F.; Stein, M.; Kaur-Ghumaan, S.; Reijerse, E. J.; Ott, S.; Lubitz, W. *Chem. Eur. J.* **2013,** *19*, 14566-14572.

179. Baraban, J. H.; Changala, P. B.; Mellau, G. C.; Stanton, J. F.; Merer, A. J.; Field, R. W. *Science* **2015,** *350*, 1338-1342.

180. Ramabhadran, R. O.; Hua, Y.; Flood, A. H.; Raghavachari, K. *The Journal of Physical Chemistry A* **2014,** *118*, 7418-7423.

181. Shriver, D. F.; Shriver, S. A.; Anderson, S. E. *Inorg. Chem.* **1965,** *4*, 725-730.

182. Brown, D. B.; Shriver, D. F.; Schwartz, L. H. *Inorg. Chem.* **1968,** *7*, 77-83.

183. House, J. E.; Bailar, J. C. *Inorg. Chem.* **1969,** *8*, 672-673.

184. Brown, D. B.; Shriver, D. F. *Inorg. Chem.* **1969,** *8*, 37-42.

185. Reguera, E.; Bertrán, J. A.; Nuñez, L. *Polyhedron* **1994,** *13*, 1619-1624.

186. Coronado, E.; Giménez-López, M. C.; Levchenko, G.; Romero, F. M.; García-Baonza, V.; Milner, A.; Paz-Pasternak, M. *J. Am. Chem. Soc.* **2005,** *127*, 4580-4581.

187. Coronado, E.; Giménez-López, M. C.; Korzeniak, T.; Levchenko, G.; Romero, F. M.; Segura, A.; García-Baonza, V.; Cezar, J. C.; de Groot, F. M. F.; Milner, A.; Paz-Pasternak, M. *J. Am. Chem. Soc.* **2008,** *130*, 15519-15532.

188. Dumont, M. F.; Risset, O. N.; Knowles, E. S.; Yamamoto, T.; Pajerowski, D. M.; Meisel, M. W.; Talham, D. R. *Inorg. Chem.* **2013,** *52*, 4494-4501.

189. Nelson, K. J.; Miller, J. S. *Inorg. Chem.* **2008,** *47*, 2526-2533.

190. Arai, M.; Miyake, M.; Yamada, M. *The Journal of Physical Chemistry C* **2008,** *112*, 1953-1962.

191. Shatruk, M.; Avendano, C.; Dunbar, K. R., Cyanide-Bridged Complexes of Transition Metals: A Molecular Magnetism Perspective. In *Prog. Inorg. Chem.*, John Wiley & Sons, Inc.: 2009; pp 155-334.

192. Shatruk, M.; Dragulescu-Andrasi, A.; Chambers, K. E.; Stoian, S. A.; Bominaar, E. L.; Achim, C.; Dunbar, K. R. *J. Am. Chem. Soc.* **2007,** *129*, 6104-6116.

193. Shatruk, M.; Chambers, K. E.; Prosvirin, A. V.; Dunbar, K. R. *Inorg. Chem.* **2007,** *46*, 5155-5165.

194. Avendano, C.; Karadas, F.; Hilfiger, M.; Shatruk, M.; Dunbar, K. R. *Inorg. Chem.* **2010,** *49*, 583-594.

195. Bartlett, B. M.; Harris, T. D.; DeGroot, M. W.; Long, J. R. *Z. Anorg. Allg. Chem.* **2007,** *633*, 2380-2385.

196. Geiss, A.; Vahrenkamp, H. *Inorg. Chem.* **2000,** *39*, 4029-4036.

197. Bignozzi, C. A.; Chiorboli, C.; Indelli, M. T.; Scandola, F.; Bertolasi, V.; Gilli, G. *J. Chem. Soc., Dalton Trans.* **1994**, 2391-2395.

198. Corsi, D. M.; Murthy, N. N.; Young, V. G.; Karlin, K. D. *Inorg. Chem.* **1999,** *38*, 848-858.

199. Shores, M. P.; Sokol, J. J.; Long, J. R. *J. Am. Chem. Soc.* **2002,** *124*, 2279-2292.

200. Berseth, P. A.; Sokol, J. J.; Shores, M. P.; Heinrich, J. L.; Long, J. R. *J. Am. Chem. Soc.* **2000,** *122*, 9655-9662.

201. Yang, J. Y.; Shores, M. P.; Sokol, J. J.; Long, J. R. *Inorg. Chem.* **2003,** *42*, 1403-1419.

202. Espenson, J. H.; Bushey, W. R. *Inorg. Chem.* **1971,** *10*, 2457-2463.

203. Frank, S. N.; Anson, F. C. *Inorg. Chem.* **1972,** *11*, 2938-2948.

204. Rievaj, M.; Bustin, D.; Riccieri, P.; Zinato, E. *Inorg. Chim. Acta* **1995,** *228*, 153-158.

205. Bustin, D. I.; Rievaj, M.; Mocák, J. *Inorg. Chim. Acta* **1978,** *27*, 59-66.

206. Rievaj, M.; Bustin, D. *Chem. Zvesti* **1984**.

207. Heatherington, A.; Oon, S. M.; Vargas, R.; Kane-Maguire, N. A. P. *Inorg. Chim. Acta* **1980,** *44*, L279-L282.

208. Sakaguchi, U.; Tomioka, K.; Yoneda, H. *Inorg. Chim. Acta* **1985,** *101*, 23-29.

209. Mock, M. T.; Kieber-Emmons, M. T.; Popescu, C. V.; Gasda, P.; Yap, G. P. A.; Riordan, C. G. *Inorg. Chim. Acta* **2009,** *362*, 4553-4562.

210. Lim, B. S.; Holm, R. H. *Inorg. Chem.* **1998,** *37*, 4898-4908.

211. Scott, M. J.; Holm, R. H. *J. Am. Chem. Soc.* **1994,** *116*, 11357-11367.

212. Iwata, S.; Ostermeier, C.; Ludwig, B.; Michel, H. *Nature* **1995,** *376*, 660-669.

213. Tsukihara, T.; Aoyama, H.; Yamashita, E.; Tomizaki, T.; Yamaguchi, H.; Shinzawa-Itoh, K.; Nakashima, R.; Yaono, R.; Yoshikawa, S. *Science* **1995,** *269*, 1069-1074.

214. Truhlar, D. G.; Garrett, B. C. *Acc. Chem. Res.* **1980,** *13*, 440-448.

215. Barton, B. E.; Olsen, M. T.; Rauchfuss, T. B. *J. Am. Chem. Soc.* **2008,** *130*, 16834-16835.

216. Camara, J. M.; Rauchfuss, T. B. *Nat. Chem.* **2012,** *4*, 26-30.

217. Capon, J.-F.; Gloaguen, F.; Pétillon, F. Y.; Schollhammer, P.; Talarmin, J. *Coord. Chem. Rev.* **2009,** *253*, 1476-1494.

218. Tschierlei, S.; Ott, S.; Lomoth, R. *Energy & Environmental Science* **2011,** *4*, 2340-2352.

219. Wang, N.; Wang, M.; Chen, L.; Sun, L. *Dalton Trans.* **2013,** *42*, 12059-12071.

220. Olsen, M. T.; Barton, B. E.; Rauchfuss, T. B. *Inorg. Chem.* **2009,** *48*, 7507-7509.

221. Camara, J. M.; Rauchfuss, T. B. *J. Am. Chem. Soc.* **2011,** *133*, 8098-8101.

222. DuBois, D. L.; Bullock, R. M. *Eur. J. Inorg. Chem.* **2011,** *2011*, 1017-1027.

223. Helm, M. L.; Stewart, M. P.; Bullock, R. M.; DuBois, M. R.; DuBois, D. L. *Science* **2011,** *333*, 863-866.

224. Liu, T.; DuBois, D. L.; Bullock, R. M. *Nat. Chem.* **2013,** *5*, 228-233.

225. Rakowski DuBois, M.; DuBois, D. L. *Chem. Soc. Rev.* **2009,** *38*, 62-72.

226. Wang, N.; Wang, M.; Zhang, T.; Li, P.; Liu, J.; Sun, L. *Chem. Commun.* **2008**, 5800-5802.

227. Wang, N.; Wang, M.; Liu, J.; Jin, K.; Chen, L.; Sun, L. *Inorg. Chem.* **2009,** *48*, 11551-11558.

228. Ezzaher, S.; Capon, J.-F.; Gloaguen, F.; Pétillon, F. Y.; Schollhammer, P.; Talarmin, J.; Kervarec, N. *Inorg. Chem.* **2009,** *48*, 2-4.

229. Lounissi, S.; Zampella, G.; Capon, J.-F.; De Gioia, L.; Matoussi, F.; Mahfoudhi, S.; Pétillon, F. Y.; Schollhammer, P.; Talarmin, J. *Chem. Eur. J.* **2012,** *18*, 11123-11138.

230. Wang, Y.; Ahlquist, M. S. G. *Dalton Trans.* **2013,** *42*, 7816-7822.

231. Wang, Y.; Wang, M.; Sun, L.; Ahlquist, M. S. G. *Chem. Commun.* **2012,** *48*, 4450-4452.

232. Wang, N.; Wang, M.; Wang, Y.; Zheng, D.; Han, H.; Ahlquist, M. S. G.; Sun, L. *J. Am. Chem. Soc.* **2013,** *135*, 13688-13691.

233. Bercaw, J. E.; Labinger, J. A. *Proc. Nat. Acad. Sci. U. S. A.* **2007,** *104*, 6899-6900.

234. Wencel-Delord, J.; Droge, T.; Liu, F.; Glorius, F. *Chem. Soc. Rev.* **2011,** *40*, 4740-4761.

235. Justice, A. K.; De Gioia, L.; Nilges, M. J.; Rauchfuss, T. B.; Wilson, S. R.; Zampella, G. *Inorg. Chem.* **2008,** *47*, 7405-7414.

236. Herold, S.; Lippard, S. J. *J. Am. Chem. Soc.* **1997,** *119*, 145-156.

237. Thomas, C. M.; Darensbourg, M. Y.; Hall, M. B. *J. Inorg. Biochem.* **2007,** *101*, 1752-1757.

238. Munery, S.; Capon, J.-F.; De Gioia, L.; Elleouet, C.; Greco, C.; Pétillon, F. Y.; Schollhammer, P.; Talarmin, J.; Zampella, G. *Chem. Eur. J.* **2013,** *19*, 15458-15461.

239. Antberg, M.; Dahlenburg, L. *Angewandte Chemie International Edition in English* **1986,** *25*, 260-261.

240. Baker, M. V.; Field, L. D. *Aust. J. Chem.* **2000,** *52*, 1005-1012.

241. Ohki, Y.; Hatanaka, T.; Tatsumi, K. *J. Am. Chem. Soc.* **2008,** *130*, 17174-17186.

242. O'Hagan, M.; Ho, M.-H.; Yang, J. Y.; Appel, A. M.; DuBois, M. R.; Raugei, S.; Shaw, W. J.; DuBois, D. L.; Bullock, R. M. *J. Am. Chem. Soc.* **2012,** *134*, 19409-19424.

243. Wächtershäuser, G. *Prog. Biophys. Mol. Biol.* **1992,** *58*, 85-201.

244. Wächtershäuser, G. *Philosophical Transactions of the Royal Society B: Biological Sciences* **2006,** *361*, 1787-1808.

245. Cody, G. D.; Boctor, N. Z.; Filley, T. R.; Hazen, R. M.; Scott, J. H.; Sharma, A.; Yoder, H. S. *Science* **2000,** *289*, 1337-1340.

246. McGlynn, S. E.; Mulder, D. W.; Shepard, E. M.; Broderick, J. B.; Peters, J. W. *Dalton Trans.* **2009**, 4274-4285.

247. Kuwata, S.; Hidai, M. *Coord. Chem. Rev.* **2001,** *213*, 211-305.

248. Tsou, C.-C.; Chiu, W.-C.; Ke, C.-H.; Tsai, J.-C.; Wang, Y.-M.; Chiang, M.-H.; Liaw, W.-F. *J. Am. Chem. Soc.* **2014,** *136*, 9424-9433.

249. Seyferth, D.; Henderson, R. S. *J. Organomet. Chem.* **1981,** *218*, C34-C36.

250. Seyferth, D.; Womack, G. B.; Henderson, R. S.; Cowie, M.; Hames, B. W. *Organometallics* **1986,** *5*, 1568-1575.

251. Stone, F. G. A. *Angewandte Chemie International Edition in English* **1984,** *23*, 89-99.

252. Raubenheimer, H. G.; Schmidbaur, H. *Organometallics* **2012,** *31*, 2507-2522.

253. Hoffmann, R. *Angewandte Chemie International Edition in English* **1982,** *21*, 711-724.

254. Evans, D. G.; Michael, D.; Mingos, P. *J. Organomet. Chem.* **1982,** *232*, 171-191.

255. Fritsch, E.; Polborn, K.; Robl, C.; Sünkel, K.; Beck, W. *Z. Anorg. Allg. Chem.* **1993,** *619*, 2050-2060.

256. Ruiz, J.; Rodríguez, V.; Vicente, C.; Martí, J. M.; López, G.; Pérez, J. *Inorg. Chem.* **2001,** *40*, 5354-5360.

257. Kessler, H. *Angewandte Chemie International Edition in English* **1970,** *9*, 219-235.

258. Toyota, S. *Rev. Heteroatom Chem.* **1999,** *21*, 139-162.

259. Mueting, A.; Mattson, B. M. *J. Inorg. Nucl. Chem.* **1981,** *43*, 749-751.

260. In-noi, O.; Haller, K. J.; Hall, G. B.; Brezinski, W. P.; Marx, J. M.; Sakamoto, T.; Evans, D. H.; Glass, R. S.; Lichtenberger, D. L. *Organometallics* **2014,** *33*, 5009-5019.

261. Hansen, J.; Sato, M.; Hearty, P.; Ruedy, R.; Kelley, M.; Masson-Delmotte, V.; Russell, G.; Tselioudis, G.; Cao, J.; Rignot, E.; Velicogna, I.; Tormey, B.;

Donovan, B.; Kandiano, E.; von Schuckmann, K.; Kharecha, P.; Legrande, A. N.; Bauer, M.; Lo, K. W. *Atmos. Chem. Phys.* **2016,** *16*, 3761-3812.

262. Gaylord, B.; Kroeker, K. J.; Sunday, J. M.; Anderson, K. M.; Barry, J. P.; Brown, N. E.; Connell, S. D.; Dupont, S.; Fabricius, K. E.; Hall-Spencer, J. M.; Klinger, T.; Milazzo, M.; Munday, P. L.; Russell, B. D.; Sanford, E.; Schreiber, S. J.; Thiyagarajan, V.; Vaughan, M. L. H.; Widdicombe, S.; Harley, C. D. G. *Ecology* **2015,** *96*, 3-15.
263. Olah, G. A.; Goeppert, A.; Prakash, G. K. S. *The Journal of Organic Chemistry* **2009,** *74*, 487-498.
264. Centi, G.; Perathoner, S. *Catal. Today* **2009,** *148*, 191-205.
265. Graves, C.; Ebbesen, S. D.; Mogensen, M.; Lackner, K. S. *Renewable and Sustainable Energy Reviews* **2011,** *15*, 1-23.
266. Du, D.; Lan, R.; Humphreys, J.; Tao, S. *J. Appl. Electrochem.* **2017,** *47*, 661-678.
267. Yagi, M.; Kaneko, M. *Chem. Rev.* **2001,** *101*, 21-36.
268. Rüttinger, W.; Dismukes, G. C. *Chem. Rev.* **1997,** *97*, 1-24.
269. Qiao, J.; Liu, Y.; Hong, F.; Zhang, J. *Chem. Soc. Rev.* **2014,** *43*, 631-675.
270. Zhu, D. D.; Liu, J. L.; Qiao, S. Z. *Adv. Mater.* **2016,** *28*, 3423-3452.
271. Elgrishi, N.; Chambers, M. B.; Wang, X.; Fontecave, M. *Chem. Soc. Rev.* **2017,** *46*, 761-796.
272. Taheri, A.; Berben, L. A. *Chem. Commun.* **2016,** *52*, 1768-1777.
273. Bonin, J.; Maurin, A.; Robert, M. *Coord. Chem. Rev.* **2017,** *334*, 184-198.
274. Takeda, H.; Cometto, C.; Ishitani, O.; Robert, M. *ACS Catal.* **2017,** *7*, 70-88.

275. Schlager, S.; Dibenedetto, A.; Aresta, M.; Apaydin, D. H.; Dumitru, L. M.; Neugebauer, H.; Sariciftci, N. S. *Energy Technology* **2017,** *5*, 812-821.

276. Mondal, B.; Neese, F.; Ye, S. *Inorg. Chem.* **2015,** *54*, 7192-7198.

277. Mondal, B.; Neese, F.; Ye, S. *Inorg. Chem.* **2016,** *55*, 5438-5444.

278. Song, J.; Klein, E. L.; Neese, F.; Ye, S. *Inorg. Chem.* **2014,** *53*, 7500-7507.

279. Machan, C. W.; Sampson, M. D.; Kubiak, C. P. *J. Am. Chem. Soc.* **2015,** *137*, 8564-8571.

280. Ishida, H.; Tanaka, H.; Tanaka, K.; Tanaka, T. *J. Chem. Soc., Chem. Commun.* **1987**, 131-132.

281. Hitoshi, I.; Koji, T.; Toshio, T. *Chem. Lett.* **1985,** *14*, 405-406.

282. Ishida, H.; Tanaka, K.; Tanaka, T. *Organometallics* **1987,** *6*, 181-186.

283. Kang, P.; Cheng, C.; Chen, Z.; Schauer, C. K.; Meyer, T. J.; Brookhart, M. *J. Am. Chem. Soc.* **2012,** *134*, 5500-5503.

284. Kang, P.; Meyer, T. J.; Brookhart, M. *Chem. Sci.* **2013,** *4*, 3497-3502.

285. Hawecker, J.; Lehn, J.-M.; Ziessel, R. *J. Chem. Soc., Chem. Commun.* **1984**, 328-330.

286. Caix, C.; Chardon-Noblat, S.; Deronzier, A. *J. Electroanal. Chem.* **1997,** *434*, 163-170.

287. Costentin, C.; Drouet, S.; Robert, M.; Savéant, J.-M. *Science* **2012,** *338*, 90-94.

288. Collin, J. P.; Jouaiti, A.; Sauvage, J. P. *Inorg. Chem.* **1988,** *27*, 1986-1990.

289. Hawecker, J.; Lehn, J.-M.; Ziessel, R. *J. Chem. Soc., Chem. Commun.* **1983**, 536-538.

290. Sullivan, B. P.; Bolinger, C. M.; Conrad, D.; Vining, W. J.; Meyer, T. J. *J. Chem. Soc., Chem. Commun.* **1985**, 1414-1416.

291. Lunsford, A. M.; Goldstein, K. F.; Cohan, M. A.; Denny, J. A.; Bhuvanesh, N.; Ding, S.; Hall, M. B.; Darensbourg, M. Y. *Dalton Trans.* **2017,** *46*, 5175-5182.

292. Keith, J. A.; Grice, K. A.; Kubiak, C. P.; Carter, E. A. *J. Am. Chem. Soc.* **2013,** *135*, 15823-15829.

293. Riplinger, C.; Sampson, M. D.; Ritzmann, A. M.; Kubiak, C. P.; Carter, E. A. *J. Am. Chem. Soc.* **2014,** *136*, 16285-16298.

294. Riplinger, C.; Carter, E. A. *ACS Catal.* **2015,** *5*, 900-908.

295. Scheiring, T.; Klein, A.; Kaim, W. *Journal of the Chemical Society, Perkin Transactions 2* **1997**, 2569-2572.

296. Smieja, J. M.; Kubiak, C. P. *Inorg. Chem.* **2010,** *49*, 9283-9289.

297. Pavlishchuk, V. V.; Addison, A. W. *Inorg. Chim. Acta* **2000,** *298*, 97-102.

298. Benson, E. E.; Kubiak, C. P. *Chem. Commun.* **2012,** *48*, 7374-7376.

299. Johnson, F. P. A.; George, M. W.; Hartl, F.; Turner, J. J. *Organometallics* **1996,** *15*, 3374-3387.

300. Benson, E. E.; Sampson, M. D.; Grice, K. A.; Smieja, J. M.; Froehlich, J. D.; Friebel, D.; Keith, J. A.; Carter, E. A.; Nilsson, A.; Kubiak, C. P. *Angew. Chem. Int. Ed.* **2013,** *52*, 4841-4844.

301. Sampson, M. D.; Froehlich, J. D.; Smieja, J. M.; Benson, E. E.; Sharp, I. D.; Kubiak, C. P. *Energy & Environmental Science* **2013,** *6*, 3748-3755.

302. Gibson, D. H. *Chem. Rev.* **1996,** *96*, 2063-2096.

APPENDIX A

RESUME

Career Highlights

- A well-trained computational chemist with solid mathematics and physics background.
- Excellence in research with nine publications and twelve presentations.
- Recognition by most competitive fellowships and the invitation to Nobel Laureate meeting.
- Team-oriented player with extensive collaboration and mentoring experience.
- History-proven self-motivation to develop problem solving skills adapted to new challenges.

Education

Texas A & M University, College Station, Texas, USA Sept. 2017

Doctor of Philosophy in Bio-Inorganic and Computational Chemistry, GPA: 3.82/4.
Dissertation: Computational modelling of organometallic compounds inspired by hydrogenase.
Advisors: Drs. Michael B. Hall and Marcetta Y. Darensbourg

Fudan University, Shanghai, China Jul. 2012

Bachelor of Science in Chemistry (Major) & Economics (Minor), GPA 3.74/4, Ranked 1/~100.
Thesis: Carbon-based solid acid
Advisor: Dr. Yinhong Yue

Experience and Leadership

Research Assistant Sep. 2012-Present

- Modelling of homogeneous/solvated organometallic hydrogenase mimics with correlations.
- Collaborated with experimentalists to assign and interpret spectral and electro-chemical results.
- Built mechanisms of H_2 production and C-H activation *etc.* with structure-function analysis.
- Nine publications, most in the top journals (IF ~ 10) with more anticipated.

Academic and Research Mentor Sep. 2013-Present

- Offered supplementary advice to two junior graduate students to promote their research.
- Managed to train undergraduates and graduates in computational chemistry.
- Demonstrated public speaking skills to four graduate students preparing seminars.

Reviewer for Chemistry Journals Sep. 2012-Present

- Served the chemistry community with dedication by reviewing 39 submitted manuscripts and proposals with my advisors for top journals. (*Nature*, 2; *Science*, 1; *Nat. Chem.*, 1; *Nat. Chem. Biol.*, 1; *J. Am. Chem. Soc.*, 9; *Angew. Chem. Int. Ed.*, 5).

Teaching Assistant Chem 641 Structural Inorganic Chemistry Jan. 2015-May. 2016

- Provided out-of-classroom instructions to graduate students to extent their knowledge base.
- Monitored weekly computational labs and maintained trouble-shooting sessions.
- Designed problem and answer set and organized reviews.

Guest Lecturer Chem 362/462 Descriptive / Inorganic Chemistry Jan. 2014- Dec. 2016

- Preparing and giving two workshops: "Crystal database" and "Molecular modelling"..
- Trained students for chemical informatics: Mercury and CSD structure database.
- Instructed students in the poster contest, later won the "special display" honor.

Lab Instructor Chem 238/318 Organic / Quantitative Chemistry Lab Sep. 2012-May. 2014

- Guided students to acquire hands-on experience in the intermediate-level lab courses.

Undergraduate Research Assistant Sep. 2010-Jun. 2012

- Two publications. Synthesized and characterized strong inorganic solid acids.
- Experience with powder/crystal XRD, TG, GC-MS, HPLC and Elementary analysis.

Scientific Skills

- Intensive training in mathematics (calculus, linear algebra, statistics) and physics.
- In-depth knowledge of Quantum Chemistry and its derivative computational tools.
- Expertise in the transition metal-containing organometallic systems.
    - First-row transition metal hydrogenase mimics and relevant electro-catalysts.
    - Systems with high static correlations and multi-reference properties.
    - Non-innocent and/or bridging ligand containing systems.
- Capacity of performing various computational tasks and analysis of data.
    - Density Functional Theory and post-HF ab initio methods.
    - Electronic and geometric structure tuning of systems with strong correlation.
    - Property predictions: free-energy, electrochemical and spectral.
    - Construction of mechanisms of chemical and electrochemical reactions.
- Skills of processing, assigning and simulating of spectra (IR, EPR, NMR, UV-Vis, Mossbauer).
- Proficiency in interpretation and understanding electro-chemical scans and behaviors.

Computer Skills

- Scientific calculation: Unix/Linux-base cluster usage and configuration.
- Programming: Object-oriented programming (C++) and script programming (Bash).
- Computational chemistry: Gaussian and Orca; AGUI, Chemcraft, Chemoffice
- Cheminformatics: Crystal (CCDC / Mercury), Protein (PBD / PyMol), Chemfinder.
- Spectra/data processing and simulation: Origin, Spincount, WinNMR.
- Designer: Adobe Creative suit (Acrobat, Dreamweaver, Flash, Illustrator and Photoshop).

Outreach

- Activity organizer and volunteer in TAMU chemistry open-house
- Peer mentor for prospective graduate student visitation weekend.
- Volunteer receptionist for new students and scholars for CSSA.

Peer-reviewed Publications

1. Ghosh, P.; Ding, S.; Chupik, R. B.; Quiroz, M.;Hsieh, C.-H.; Bhuvanesh, N.;Hall, M. B.; Darensbourg M. Y.; *Chem. Sci.*, **2017**, DOI: 10.1039/C7SC03378H.
2. Ding, S.; Ghosh, P.; Darensbourg, M. Y.; Hall, M. B.; *Proc. Natl. Acad. Sci.*, **2017**, DOI: 10.1073/pnas.1710475114.
3. Lunsford, A. M.; Goldstein, K. F.; Cohan, M. A.;Denny, J. A.; Bhuvanesh, N.; Ding, S.; Hall, M. B.; Darensbourg, M. Y. *Dalton Trans*, **2017**, *46*, 5175.
4. Ding, S.; Ghosh, P.; Lunsford, A. M.; Wang, N.; Bhuvanesh, N.; Hall, M. B.; Darensbourg, M. Y. *J. Am. Chem. Soc.*, **2016**, *138*, 12920.
5. Lunsford, A. M.; Beto, C. C.; Ding, S.; Erdem, O. F.; Wang, N.; Bhuvanesh, N.; Hall, M. B.; Darensbourg, M. Y. *Chem. Sci.*, **2016**, *7*, 3710.
6. Ding, S; Hall, M. B. *Struct. Bond*., **2016**, *169*, 199.
7. Crouthers, D. J.; Ding, S.; Denny J. A.; Bethel, R. D.; Hsieh, C.-H.; Hall, M. B.; Darensbourg, M. Y. *Angew. Chem. Int. Ed.*, **2015**, *54*, 11102.
8. Zheng, D.; Wang, N.; Wang, M.; Ding, S.; Ma, C.; Darensbourg, M.; Hall, M.; Sun, L. *J. Am. Chem. Soc.*, **2014**, *136*, 16817. (Cover article)
9. Hsieh, C-H.; Ding, S.; Erdem, O. F.; Crouthers, D. J.; Lubitz, W.; Popescu. C. V.; Reibenspies, J. H.; Hall, M. B.; Darensbourg, M. Y. *Nat. Commun.*, **2014***, 5,* 3684.
10. Liu, K.; Wang, X.; Ding, S.; Li, Y; Hua; W.; Yue, Y.; Gao, Z. *J. Mol. Catal. A*, **2013**, *380*, 84.
11. Ding, S.; Hua, W.; Yue, Y.; Gao Z. *J. Fudan U. (Sci. Vol.)*, **2012**, *51*, 608.

Selected Presentations

- Max-Planck Institute for chemical energy conversion, Muelheim, Germany, **2017**. (Oral)
- Dow-TAMU graduate symposium, Award Ceremony, College Station, TX, **2017**. (Oral)
- 253rd American Chemical Society National Meeting, San Francisco, CA, **2017**. (Oral)
- Gordon Conference: 11th Inorganic Reaction Mechanisms, Galveston, TX, **2017**. (Poster)
- 251st American Chemical Society National Meeting, San Diego, CA, **2016**. (Poster)
- 56th Sanibel Symposium, St Simons Island, GA, **2016**. (Oral)
- Gordon Conference: 10th Inorganic Reaction Mechanisms, Galveston, TX, **2015**. (Poster)
- 248th American Chemical Society National Meeting, San Francisco, CA, **2014**. (Poster)

Selected Awards and Recognition

- Invitation to the 67th Lindau Nobel Laurates meeting (International selection) 2017
- ACS Division of Inorganic Chemistry Student Travel Award (National-wide) 2017
- OGAPS Graduate Student Research and Presentation Travel Award (University-wide) 2017
- Dow Chemical Scholar Award 2017
- Marcetta Y. and Donald J. Darensbourg Graduate Student Travel Scholarship 2017
- A. E. Martell Graduate Student Enrichment Award. 2014
- Welch Fellowship for International Graduate Students. 2012
- DuPont Fellowship. 2011
- Thermo-Fisher Fellowship. 2011
- National Fellowship of People's Republic of China. (National-wide, 1 out of 1500) 2010